Synthesis, structure and mechanism of polyoxometalate self-assembly:
Towards designed nanoscale architectures

Elizabeth Frances Wilson

A thesis submitted to the University of Glasgow

for the degree of Doctor of Philosophy

Department of Chemistry

July 2009

Acknowledgements

This project was carried out between August 2006 and July 2009 in the Department of Chemistry at the University of Glasgow. During my time at Glasgow, many people have offered their support and guidance and kept me sane whilst completing this work! In particular I would like to acknowledge:

Prof. Lee Cronin for giving me the chance of a new start in my chemistry studies and for always encouraging me to be bold and 'suspend my disbelief' when carrying out my experiments!

Dr. De-Liang Long for all your help with synthesis and crystallography over the past three years.

Dr. Bob Peacock for being wonderful in giving me limitless advice about UV experiments and putting up with my annoying diffuse reflectance questions. Thanks so much for all your help.

Dr. Carsten Streb(belhoff!) What can I say? Thank you for your constant support and advice, for thorough proof-reading of this thesis, for putting up with me when I've been stressed and worried about everything, and for being my rock.

Dr. Hamera Abbas for getting me started in all this, for your support in times of mass spec horror and for being a good friend throughout.

Dr. Chris Ritchie for all your marvellous advice and discussions about polyoxometalate synthesis. What a star you are Crystal Richards!

Dr. Haralampos Miras for all your help and advice over the past three years, for putting up with my annoying questions, and for bearing the pain of the mass spec with me! You've been a great support, so thanks for that.

Dr. Bridgette Duncombe for all of your mass spec advice and for your friendship and encouragement throughout.

Dr. Geoff Cooper for all your synthetic advice and technical know-how in the production of this thesis. Also thanks so much for your friendship over the past four years, good times in the mountaineering club, and in the downstairs office, and I guess I should add, introducing me to the Hoff!

"It is difficult to say what is impossible, for the dream of yesterday is the hope of today and the reality of tomorrow"

Robert H. Goddard

Dedicated to my family
and to Carsten
Thank you for believing in me

TABLE OF CONTENTS

TABLE OF COMPOUNDS

Compound	Formula
1	$((n\text{-}C_4H_9)_4N)_{2n}(Ag_2Mo_8O_{26})_n$
2	$((n\text{-}C_4H_9)_4N)_3[MnMo_6O_{18}((OCH_2)_3CNH_2)_2]$
3	$Cs_{4.67}Na_{0.33}[IMo_6O_{24}]\cdot ca7H_2O$
4	$Na_4((HOCH_2CH_2)_3NH)_2[TeMo_6O_{24}]\cdot ca10H_2O$
5	$(DIP\text{-}1)[PW_{12}O_{40}]\cdot5DMSO\cdot ca1H_2O$
6	$(DIP\text{-}2)[PW_{12}O_{40}]\cdot5DMSO\cdot ca4H_2O$
7	$(IPblue)_3[PW_{12}O_{40}]\cdot4DMSO$

PUBLICATIONS

The following articles and communications were published as a result of work undertaken over the course of this PhD programme.

"Nucleation Mechanisms of Molecular Oxides: A Study of the Assembly-Dissassembly of $[W_6O_{19}]^{2-}$ Using Theory and Mass Spectrometry", L. Vilà-Nadal, A. Rodríguez-Fortea, L.-K. Yan, E. F. Wilson, L. Cronin, J. M. Poblet, *Angew. Chem. Int. Ed.* **2009**, *48*, 5452-5456.

"Discovery of Heteroatom-"Embedded" Te⊂{$W_{18}O_{54}$} Nanofunctional Polyoxometalates by Use of Cryospray Mass Spectrometry", J. Yan, D.–L. Long, E. F. Wilson, L. Cronin, *Angew. Chem. Int. Ed.* **2009**, *48*, 4376-4380.

"Near to the solution. MS in coordination chemistry", E. F. Wilson, C. Streb, *Nachr. Chem.* **2009**, *57*, 426-429.

"Unravelling the Complexities of Inorganic and Supramolecular Self-Assembly in Solution with Electrospray and Cryospray Mass Spectrometry", H. N. Miras, E. F. Wilson (joint first author), L. Cronin, *Chem. Commun.* **2009**, *11*, 1297-1311.

"Probing the Self-Assembly of Inorganic Cluster Architectures in Solution with Cryospray Mass Spectrometry: Growth of Polyoxomolybdate Clusters and Polymers Mediated by Silver(I) Ions", E. F. Wilson, H. Abbas, B. J. Duncombe, C. Streb, D.-L. Long, L. Cronin, *J. Am. Chem. Soc.* **2008**, *130*, 13876-13884.

"Capture of Periodate in a {$W_{18}O_{54}$} Cluster Cage Yielding a Catalytically Active Polyoxometalate $[H_3W_{18}O_{56}(IO_6)]^{6-}$Embedded with High-Valent Iodine", D.-L. Long, Y.-F. Song, E. F. Wilson, P. Kögerler, S.-X. Guo, A. M. Bond, J. S. J. Hargreaves, L. Cronin, *Angew. Chem. Int. Ed.* **2008**, *47*, 4384-4387.

ABBREVIATIONS

In addition to standard notation, the following abbreviations were used in this thesis:

POM	Polyoxometalate
DIP	2,3-Dihydro-1*H*-imidazo[1,2-*f*]phenanthridinium
IP	1*H*-Imidazo[1,2-*f*]-phenanthridinium
ESI-MS	Electrospray mass spectrometry
CSI-MS	Cryospray mass spectrometry
H-bonding	Hydrogen-bonding
FAB-MS	Fast atom bombardment mass spectrometry
MALDI-MS	Matrix assisted laser desorption ionisation mass spectrometry
XRD	X-ray diffractometry
NMR	Nuclear magnetic resonance spectroscopy
DCC	*N,N'*-dicyclohexylcarbodimide
TBA	Tetra-*n*-butyl ammonium
NBS	*N*-bromosuccinimide
TEAH$^+$	Protonated triethanolamine
TRIS	Tris(hydroxylmethyl)aminomethane
(DIP-1)Br$_3$	1-[2-(2-amino-ethylamino)ethyl]-2,3-dihydro-1*H*-imidazo[1,2-*f*]phenanthridinium tribromide
(DIP-2)Br$_3$	*cis*-1,3,5-tri(2,3-dihydro-1*H*-imidazo[1,2-*f*]phenanthridinium) cyclohexane tribromide
cis-TACH	*cis*-1,3,5-triaminocyclohexane
(IPblue)Cl	1*H*-Imidazo[1,2-*f*]phenanthridinium chloride
UV/vis	Ultraviolet-visible
SEM	Scanning electron microscopy
EDX	Energy-dispersive X-ray spectroscopy
EA	Elemental analysis
TGA	Thermogravimetric analysis
IR	Fourier-transform infrared spectroscopy
FAAS	Flame atomic absorption spectrometry

ABSTRACT

Cryospray (CSI-) and electrospray mass spectrometry (ESI-MS) techniques have been utilised to investigate the key features of the 'in-solution', self-assembly processes by which complex polyoxometalate systems, such as $((n\text{-}C_4H_9)_4N)_{2n}(Ag_2Mo_8O_{26})_n$ and $((n\text{-}C_4H_9)_4N)_3[MnMo_6O_{18}((OCH_2)_3CNH_2)_2]$, are formed.

CSI-MS monitoring of the rearrangement of molybdenum Lindqvist anions, $[Mo_6O_{19}]^{2-}$, in the presence of silver(I) ions, into a silver-linked β-octamolybdate structure, has allowed elucidation of the role of small isopolyoxomolybdate fragments and Ag^I ions in the assembly process. The observation of higher mass fragments, each with increasing organic cation contribution concomitant with their increasing metal nuclearity, has supported the previously proposed hypothesis that the organic cations have a structure-directing role in promoting the mode of POM structure growth in solution. The combined use of UV/vis spectroscopy and real-time CSI-MS monitoring of the reaction solution allowed correlation between the decreasing Lindqvist anion concentration and increasing β-octamolybdate anion concentration. Furthermore, UV/vis spectroscopy was used to show that the rate of decrease in Lindqvist anion concentration, and therefore, the inter-conversion of Lindqvist into β-octamolybdate anions, decreases as the carbon chain length of the alkylammonium cations in the system increases.

This approach was extended to use ESI-MS monitoring in examining the formation of the more complex, organic-inorganic, Mn-Anderson polyoxomolybdate structure $((n\text{-}C_4H_9)_4N)_3[MnMo_6O_{18}((OCH_2)_3CNH_2)_2]$. In this investigation, ESI-MS was used to monitor the real-time, 'in-solution' rearrangements of α-octamolybdate anions, $[\alpha\text{-}Mo_8O_{26}]^{4-}$, and coordination of manganese(III) cations and tris(hydroxymethyl)aminomethane (TRIS) groups in the formation of the Mn-Anderson-TRIS structure. These investigations have led to the proposal that the rearrangement of $[\alpha\text{-}Mo_8O_{26}]^{4-}$ anions occurs first through decomposition to $[Mo_4O_{13}]^{2-}$ cluster species, i.e. half-fragments of the octamolybdate anion; followed by decomposition to smaller, stable isopolyoxomolybdate fragment ions such as dimolybdate and trimolybdate fragment ions. It has then been proposed these fragments subsequently coordinate with the tripodal TRIS

ligands, manganese ions, and further molybdate anionic units to form the final, derivatized Mn-Anderson-TRIS cluster.

Investigations into the encapsulation of the high oxidation state heteroanion templates $\{I^{VII}O_6\}$ and $\{Te^{VI}O_6\}$ within polyoxomolybdate clusters, have led to the isolation and characterization of two new, molybdenum Anderson-based POM architectures, i.e. $Cs_{4.67}Na_{0.33}[IMo_6O_{24}] \cdot ca7H_2O$ and $Na_4((HOCH_2CH_2)_3NH)_2[TeMo_6O_{24}] \cdot ca10H_2O$. The use of coordinating caesium and sodium cations allowed the formation of a closely-packed structure composed of the periodate-centred Anderson clusters arranged into two layers, which then form a repeating ABAB pattern through the lattice. In contrast, the main building-blocks of the tellurium-based cluster system features the $[TeMo_6O_{24}]^{6-}$ anions and two coordinated cation arrangements, each composed of a $\{Na_2\}$ dimer and coordinated $TEAH^+$ cation. The presence of this structural motif, and its inter-connection with adjacent clusters, has led to chain-like packing arrangements within the greater lattice structure.

The introduction of three aromatic, phenanthridinium-based cations into polyoxometalate systems has led to the isolation and characterization of three new POM architectures with emergent photoactivity. The polyoxometalate framework in each is composed of tungsten Keggin clusters, i.e. $[PW_{12}O_{40}]^{3-}$, which are introduced into the systems as pre-formed building-blocks. Two of the compounds use derivatives of Dihydro-Imidazo-Phenanthridinium (DIP) molecules as cations, i.e. $(DIP-1)[PW_{12}O_{40}] \cdot 5DMSO \cdot ca1H_2O$ and $(DIP-2)[PW_{12}O_{40}] \cdot 5DMSO \cdot ca4H_2O$, whereas the final compound uses an Imidazo-Phenanthridinium (IP) molecule as the cationic unit, i.e. $(IPblue)_3[PW_{12}O_{40}] \cdot 4DMSO$. The use of these cations, which have different steric bulk, geometry and charge states, has led to the formation of interesting packing arrangements within the lattice structures of all three compounds. Additionally, further characterization of these compounds has revealed they all possess emergent photoactivity, in the form of intermolecular charge transfer bands in the solid state. Some degree of intermolecular charge transfer in the solution state has also been detected for the DIP-2-based structure.

1 Introduction

1.1 Supramolecular chemistry in Nature and beyond

It was Jean-Marie Lehn, winner of the 1987 Nobel Prize, who proposed the definition of supramolecular chemistry as "the chemistry of molecular assemblies and of the intermolecular bond."[1] This broad-based definition, which can be expressed in a simpler form as the "chemistry of the non-covalent bond", is particularly appropriate as this field of chemistry spans not only the areas of organic and inorganic chemistry manipulated by man in the laboratory, but also the biochemical structures of Nature herself.[2]

In essence, the definition refers to supramolecular structures built up from smaller molecular building-blocks which are arranged into macromolecular arrangements using non-covalent bonds, for example, metal-ligand coordination interactions, hydrogen bonds and dipolar interactions.

A key feature of such systems, both biological e.g. the tertiary structures of proteins, and man-made e.g. crown ethers and cryptands, is their ability to form these complex supramolecular structures independently from any external direction. This phenomenon, which is governed by the intermolecular interactions between pre-formed building-blocks of certain size, shape, symmetry, and with specific binding sites, has become known as 'self-assembly'.

This phenomenon has attracted increasing interest in recent years in many areas of synthetic chemistry, both organic and inorganic, as researchers strive to control and utilise this so-called 'bottom-up' synthetic approach in order to create functional supramolecular structures on the nanometre scale. Research into this synthetic approach is being fuelled, not only by a desire to mimic the elegant and efficient nature of complex supramolecular structure synthesis in Nature, but also due to current technological limitations which may well see 'top-down' synthetic approaches such as lithography limited to the tens of nanometre size scale and unable to produce, for example, the desired molecular electronic devices for the next generation of data storage and transfer.[2]

The field of polyoxometalate chemistry lies within this realm of inorganic supramolecular chemistry research, and is now the subject of intensive investigation by research groups the world over. The following sections will provide an introduction to this research area and to the relatively new application of mass spectrometry techniques in elucidating the self-assembly processes within polyoxometalate chemistry.

1.2 Polyoxometalates

1.2.1 The development of polyoxometalate chemistry

Polyoxometalate (POM) structures can be defined in general terms as molecular metal-oxide clusters formed through condensation reactions of early transition metal-oxygen anions. The early transition metals in question are those found in groups 5 and 6 of the periodic table, usually with the metal centres in their highest oxidation states. For example, the majority of POM structures currently known are composed of aggregations of molybdenum or tungsten oxoanions. This broad definition will be explained in more detail in section 1.2.2, however, to place the development of research into this field of chemistry in context, it is first of interest to consider the history and the rapidly growing research area concerning these intriguing inorganic structures.

The first polyoxometalate compound, now known to be $(NH_4)_3[PMo_{12}O_{40}]$, was discovered by Berzelius in 1826 and was produced as a yellow precipitate on acidification of ammonium molybdate solution with phosphoric acid.[3] However, the analytical composition of polyoxometalate compounds such as this, were not precisely determined until 1862 when Marignac investigated the tungstosilicate salts.[4, 5] By the beginning of the 20th century many different heteropolyacids, e.g. of the form $H_3PW_{12}O_{40}$, and a large number of their salts had been isolated. However, before the advent of X-ray diffraction methods, discovered by Laue in 1912[6] and developed by W. L. Bragg and W. H. Bragg,[7] only theoretical insights into the possible structural compositions of these heteropolyanions could be presented.

The first of such theories was built around Werner's coordination theory, and further developed by Miolati and then Rosenheim in 1908.[8] This theory was then superseded by the work of Pauling in 1929,[9] however, it was not until 1933 and Keggin's work in solving the powder X-ray diffraction pattern of $H_3PW_{12}O_{40}$, that definitive evidence for the structural composition of this heteropolyacid could be reported.[10, 11]

Since that time, and with the development of more advanced single crystal X-ray diffraction techniques and analysis software, the intensity of research in the field of POM chemistry has seen a rapid growth, with research now being carried out worldwide. The heightened interest in this research is due to the great structural and electronic diversity of POM systems and their subsequent potential uses in many other fields of scientific work. For example, some of the properties of POMs of main importance in potential applications are their redox properties, photochemical activities, ionic charge, and conductivity.[12] The main application of POMs is in the field of oxidation catalysis, however, some other examples of POM applications include: (i) medicine, e.g. targeting of antiviral chemotherapy;[13, 14] (ii) coatings e.g. corrosion-resistant coatings; (iii) sensors; (iv) sorbents of gases;[12] (v) electrooptics; (vi) electrochemistry/electrodes;[15] (vii) dyes/pigments; (viii) nuclear waste processing.[12]

1.2.2   The structure and synthesis of polyoxometalates

Polyoxometalates (POMs) are clusters of early transition metal-oxygen anions where the transition metals (e.g. V, Nb, Ta, Mo, W) are usually in their highest oxidation states, i.e. metal cations existing as d^0 species.[13, 14] These soluble metal-oxide clusters can be considered as aggregates of $\{MO_x\}$-type building-block units where the metal, M, (also known as the *addenda* atom) is best visualised positioned at the centre of a polyhedron with coordinated oxygen ligands (x = 4 - 7) defining the vertices.[16] The overall structure of a POM can be represented by aggregated sets of such polyhedra with corner or edge-sharing modes as shown in Figure 1. Face sharing of polyhedra is also possible, but is rarely seen.[17]
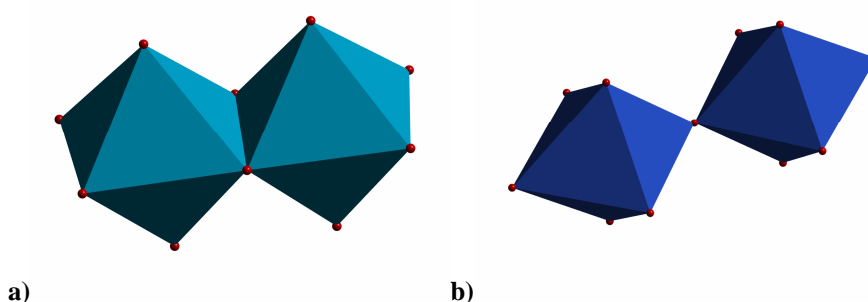
Figure 1: Example of {MO$_x$} polyhedra where M = group 5 or 6 transition metal such as Mo or W, linked through a) edge-sharing, and b) corner-sharing modes.

In general terms, the synthesis of these polyoxometalate clusters can be achieved through acidification of aqueous solutions of oxoanions e.g. MoO$_4^{2-}$, with or without the presence of a templating heteroatom (see section 1.2.3). The subsequent condensation reactions, of the form shown below, therefore, lead to the isolation of larger negatively charged polyoxoanion clusters in solution.

$$xMO_4^{n-} + zH^+ \rightarrow [M_xO_y]^{m-} + z/2\ H_2O$$

However, other synthetic variables in the reaction systems also play a large part in directing the condensation of these metal-oxide fragments. Examples of these other variables include: (i) the concentration and type of metal-oxide anions present; (ii) the pH and type of acid used, (iii) the type and concentration of heteroatom present; (iv) introduction of any additional ligands; (v) the use of reducing agent, e.g. as in Mo systems; (vi) the temperature of the reaction mixture; (vii) the solvent used.

It is the interplay between all of these experimental factors, along with other thermodynamic effects such as entropy and enthalpy, which then governs the self-assembly of specific polyoxoanion clusters in these reaction systems.[16, 18] Indeed these self-assembly processes have allowed the isolation of discrete clusters with a huge variety of nuclearities, from just two coordinated metal atoms, e.g. ((n-C$_4$H$_9$)$_4$N)$_2$[Mo$_2$O$_7$], up to 368 coordinated metal atoms in one discrete cluster.[17, 19] However, as these POM syntheses are often carried out in 'one-pot' reactions the actual mechanisms of the self-assembly processes leading to the formation of high nuclearity clusters have not yet been conclusively elucidated.[20] If these mechanisms can be fully understood, and control of

these mechanisms introduced to the POM syntheses, this presents the exciting prospect of controlled bottom-up synthetic routes to potentially useful new POM structures.

1.2.3 Classification of polyoxometalate structures

Polyoxometalate structures can be classified into two main families, i.e. the isopolyoxometalates, and the heteropolyoxometalates. Isopolyoxometalate anions consist only of the metal cation and oxide anion framework structure, e.g. $[Mo_7O_{24}]^{6-}$, therefore, are often much more unstable, and are fewer in number, than their heteropolyanion counterparts. In contrast, heteropolyoxometalate anions contain one or more p-, d- or f-block 'heteroatoms' coordinated with the metal-oxide cluster. When these heteroatoms template the formation of the complete polyoxoanion structure, e.g. the central P^V heteroatom within the $[PW_{12}O_{40}]^{3-}$, they may be referred to as 'primary' or 'central' heteroatoms; whereas those coordinated within the outer metal-oxide framework, e.g. the Cr^{III} in $[CrSiW_{11}(H_2O)O_{39}]^{5-}$, may be referred to as 'secondary' or 'peripheral' heteroatoms. It is due to the wide variety of heteroatoms which may be incorporated into these heteropolyoxometalate structures that there are many more of these structures known than for the isopolyoxometalates.

The following sections will examine, in more detail, some of the most important polyoxometalate structures from each of these families of polyoxometalates. The relatively new application of mass spectrometry techniques, to examine the formation of polyoxometalate structures in solution, will then also be discussed.

1.3 Isopolyoxometalates $[H_xM_yO_z]^{n-}$

Isopolyanions are classified by the assignment of the general formula $[H_xM_yO_z]^{n-}$ and consist only of the d^0 group 5 or 6 metal (M) cation and the oxide anion framework.[18] Therefore, these structures have often been found to be much more unstable than their heteropolyanion counterparts. Nevertheless, these architectures have interesting physical

properties, e.g. high charges and strongly basic oxygen surfaces, which makes them interesting as building-block units for larger polyoxometalate structures.[20]

1.3.1   The Lindqvist polyoxoanion $[M_6O_{19}]^{n-}$

A prominent example of an isopolyoxometalate structure common to all group 5 and 6 metal centres capable of forming polyoxometalates is the hexametalate, Lindqvist structure of general formula $[M_6O_{19}]^{n-}$.   The compounds $[Nb_6O_{19}]^{8-}$, $[Ta_6O_{19}]^{8-}$, $[Mo_6O_{19}]^{2-}$, and $[W_6O_{19}]^{2-}$ have all been isolated and the symmetry in all these clusters is approximately O_h.[18] The only caveat to this rule is that the hexametalate polyoxovanadate structure has, to   date,   only   been   isolated   as   polyalkoxovanadium   clusters   such   as $((C_4H_9)_4N)[V^V_6O_{12}(OCH_3)_7]$,[21] $[V^{IV}_4V^V_2O_7(OCH_3)_{12}]$[22],   and $Ba[V^V_6O_7(OH)_3((OCH_2)_3CCH_3)_3]$[23] where the $\{V_6O_{19}\}$ cluster core can be stabilized by the coordinating alkoxo ligands; or when other complementary ligands such as metal[24, 25] and organometallic[26] complexes are ligated to the $\{V_6O_{19}\}$ core through the oxygen bridges and so stabilize the cluster formation.

Looking in more detail at the structure of a conventional Lindqvist anion such as $[Mo_6O_{19}]^{2-}$, each fully oxidized (d^0) metal centre bears one terminal oxygen ligand and shares an additional four μ_2-bridging oxo ligands with the adjacent metal centres. The terminal oxygen ligands have shorter bond lengths, e.g. ~1.7 Å in both $[Mo_6O_{19}]^{2-}$ and $[W_6O_{19}]^{2-}$, in comparison with the μ_2-bridging oxo ligands, e.g. ~1.9 Å in both $[Mo_6O_{19}]^{2-}$ and $[W_6O_{19}]^{2-}$.   This coordination arrangement leads to consideration of the overall structure as being composed of six distorted, edge-sharing octahedra (see Figure 2).
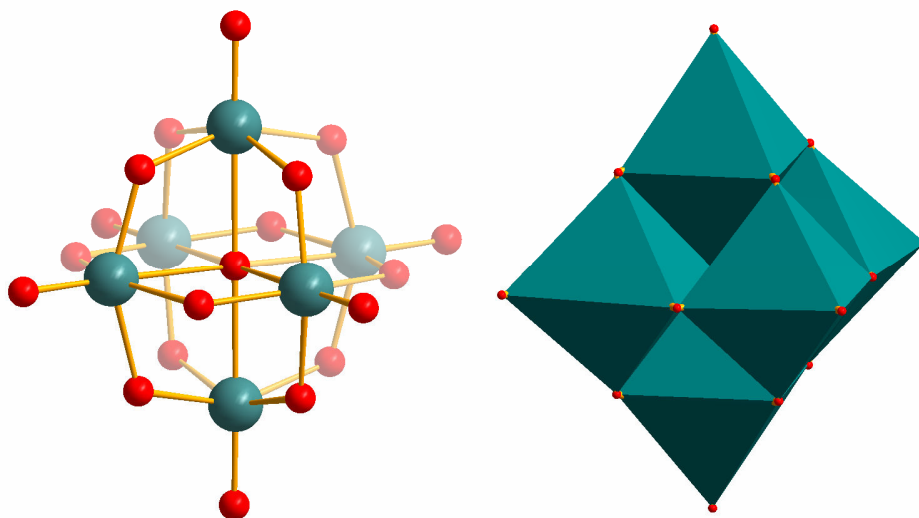
Figure 2: Structural representations of the $[M_6O_{19}]^{n-}$ Lindqvist anion, where M = V^{5+}, Nb^{5+}, Ta^{5+}, Mo^{6+}, W^{6+}, and n = 8 (group 5 metal centres) or n = 2 (group 6 metal centres). Left: Ball-and-stick representation. Right: Polyhedral representation showing the six edge-sharing octahedra which lend the cluster its overall octahedral symmetry. Colour scheme: Mo, teal (polyhedra); O, red.

In the $[Mo_6O_{19}]^{2-}$ cluster it is the weakly basic and strongly electronegative terminal oxygen atoms on this fully oxidised POM cluster which form the binding sites. The high local electron density of these sites is known to attract electrophilic secondary transition metals such as copper, cobalt and nickel which form complex counterions around the anion.[27, 28] Indeed, it was in an attempt to exploit the nucleophilic binding sites of the Lindqvist anion, that the coordination of silver(I) cations with this anion was investigated by Cronin *et al.* It was discovered, however, that the introduction of silver ions to this system leads into to the isolation of various silver-linked $[\beta\text{-}Mo_8O_{26}]^{4-}$ architectures as described in section 1.3.4.1. In comparison, coordination of the $[W_6O_{19}]^{2-}$ cluster to complexes of other transition metals has not been observed.

Organoimido derivatives of both $[Mo_6O_{19}]^{2-}$ and $[W_6O_{19}]^{2-}$ polyoxoanions have been synthesized using either direct or indirect methods.[29] Such derivatisations have been pursued with reactions using phosphinimines,[30, 31] isocyanates,[32, 33] or aromatic amines with *N,N'*-dicyclohexylcarbodimide (DCC).[34-36] An example of an arylimido derivative of {Mo_6O_{19}} produced using an indirect method is shown in Figure 3. The synthesis involves the rearrangement of the $[\alpha\text{-}Mo_8O_{26}]^{4-}$ anion (see section 1.3.4.2) in the presence

of 4-bromoaniline hydrochloride and DCC in anhydrous acetonitrile to produce the product $[Mo_6O_{18}(p\text{-}BrC_6H_4)]^{2-}$ cluster.[37]
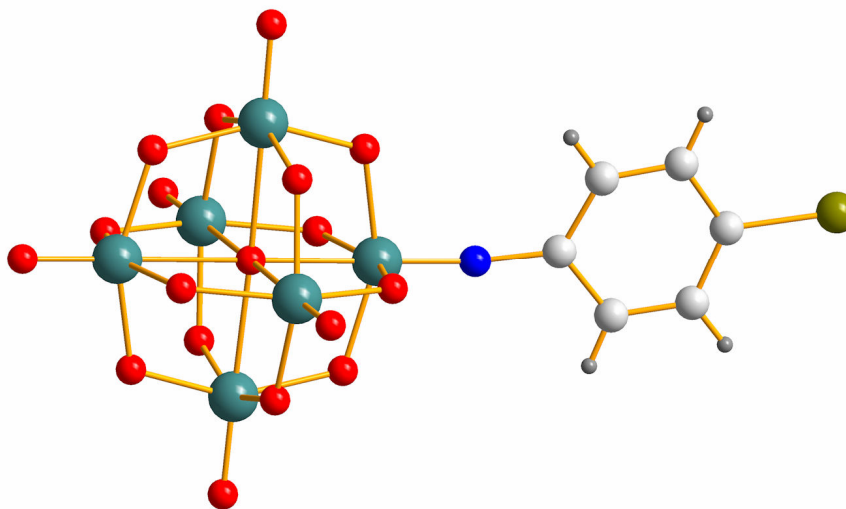
Figure 3: Structural representation of the arylimido $\{Mo_6O_{19}\}$ derivative $[Mo_6O_{18}(p\text{-}BrC_6H_4)]^{2-}$, synthesized through the rearrangement of $[\alpha\text{-}Mo_8O_{26}]^{4-}$ in the presence of 4-bromoaniline hydrochloride and DCC in anhydrous acetonitrile.[37] Colour scheme: Mo, teal; O, red; N, blue; C, light grey; Br, green; H, dark grey.

1.3.2   Decavanadate polyoxoanion $[V_{10}O_{28}]^{6-}$

Aqueous solutions containing metavanadate anions, $(VO_3)^-$, can be acidified to pH 6 or below in order to produce orange solutions containing the decavanadate anion $[V_{10}O_{28}]^{6-}$.[18, 38] Further studies have established that the decavanadate anion can be protonated in multiple steps such that $[H_nV_{10}O_{28}]^{(6-n)-}$ where $n = 2$, 3 or 4, is formed depending on the acidity of the solution.[39-43]

The structure of the $[V_{10}O_{28}]^{6-}$ anion can be described as a planar rectangular array of six edge-sharing $\{VO_6\}$ octahedra with an additional two pairs of edge-sharing octahedra positioned both above and below the plane of the rectangular array.[38] However, these octahedra are distorted in order maintain approximate valence balance between the terminal oxo and bridging oxo ligands, i.e. the approximate V-O (terminal) bond length is 1.60 Å, whilst the approximate V-O (central) bond length is 2.32 Å.[18] See Figure 4.
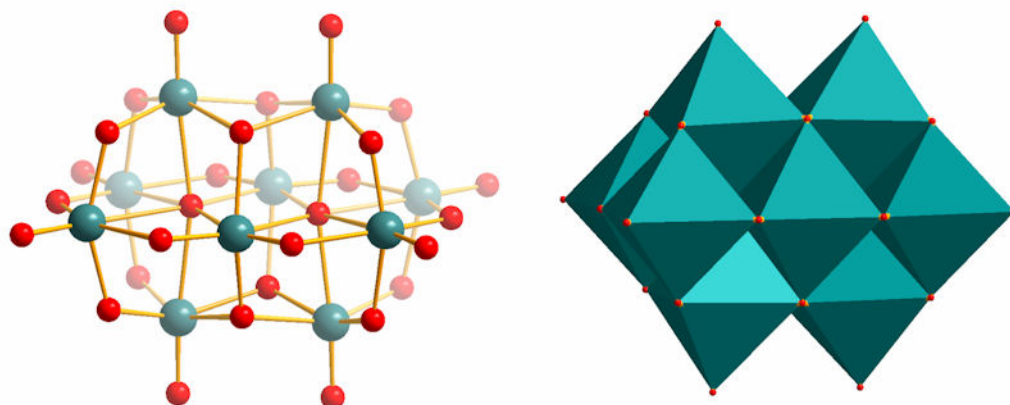
Figure 4: Structural representations of the $[V_{10}O_{28}]^{6-}$ decavanadate anion. Left: Ball-and-stick representation where the differences in V-O (terminal) and V-O (bridging) bond lengths can be clearly observed. Right: Polyhedral representation showing the six edge-sharing $\{VO_6\}$ octahedra which make up the central rectangular array and the two further pairs of edge-sharing octahedra which coordinate to both the top and bottom of the central plane. Colour scheme: V, teal (polyhedra); O, red.

1.3.3 Heptametalate polyoxoanion $[M_7O_{24}]^{6-}$

Heptametalate polyoxomolybdates[44-47] and polyoxotungstates[48-50] of general formula $[M_7O_{24}]^{6-}$ where M = Mo(VI) or W(VI), can both be isolated in the solid state. The heptamolybdate (paramolybdate) anion can be crystallized following acidification of aqueous molybdate solution to within the pH range of approximately 3 to 5.5;[18] whereas the heptatungstate (paratungstate A) anion is crystallized from aqueous tungstate solutions acidified to a pH of approximately 6.0.[48-50]

The structures of $[Mo_7O_{24}]^{6-}$ and $[W_7O_{24}]^{6-}$ are isostructural with similar dimensions and these structures can be considered to be composed of seven edge-sharing $\{MO_6\}$ octahedra. Each octahedron is distorted by the metal centre being displaced towards the periphery of the anion. A convenient description of the coordination arrangement of these octahedra is to consider the previously described $[V_{10}O_{28}]^{6-}$ structure after removal of three $\{MO_6\}$ octahedra from the central rectangular array of octahedra (see Figure 5).

It is also interesting to note that the $[Mo_7O_{24}]^{6-}$ anion has proved to be a useful building-block unit in the assembly of larger POM architectures.[51-56] A prominent example is the

$[Mo_{36}O_{112}(H_2O)_{18}]^{8-}$ cluster which may be considered to be composed of two 18-molybdate centred subunits related through a centre of inversion, each of which contains a $\{Mo_7O_{24}\}$ building-block surrounded by edge- and corner-sharing $\{MoO_6\}$ octahedra.[51, 52, 56, 57]
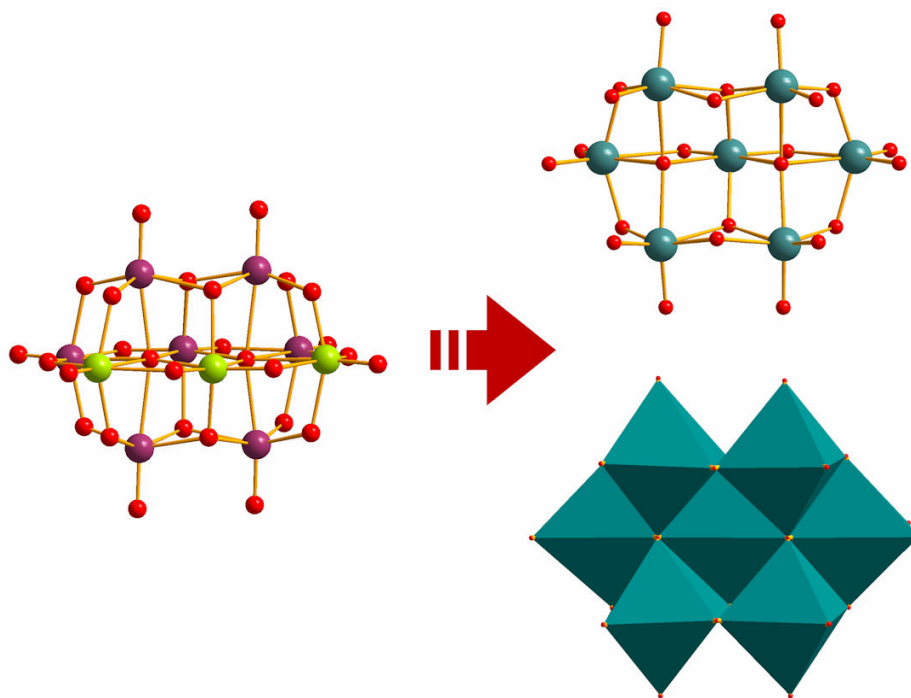
Figure 5: Left: Structural representation of the $[V_{10}O_{28}]^{6-}$ decavanadate anion. The three metal *addenda*, which can be considered to be removed in order to form the $[M_7O_{24}]^{6-}$ framework where M = Mo(VI) or W(VI), are highlighted in green. Top Right: Ball-and-stick representation of the $[Mo_7O_{24}]^{6-}$ anion. Bottom Right: Polyhedral representation showing the seven edge-sharing $\{MoO_6\}$ octahedra of the $[Mo_7O_{24}]^{6-}$ anion. Colour scheme: V, purple and light green; Mo, teal (polyhedra); O, red.

1.3.4 Octamolybdate polyoxoanion $[Mo_8O_{26}]^{4-}$

There have been eight isomeric forms of the octamolybdate polyoxoanion isolated to date, i.e. α-isomer, β-isomer, γ-isomer, δ-isomer, ε-isomer, ζ-isomer, η-isomer, and θ-isomer.[58-65] This current description of the octamolybdate structure, however, will focus on the two most prominent isomeric forms, $[α-Mo_8O_{26}]^{4-}$ and $[β-Mo_8O_{26}]^{4-}$.

1.3.4.1   β-octamolybdate polyoxoanion

The β-octamolybdate isomer, $[\beta\text{-Mo}_8\text{O}_{26}]^{4-}$ can be isolated following acidification of aqueous molybdate solutions to approximately pH 2 to 3.[18, 19, 66-70] It is composed of eight distorted octahedra sharing corners and edges. The cluster framework can be visualised by, once again, referring back to the decavanadate structure. If one considers removal of two $\{\text{MO}_6\}$ octahedra from the $\{\text{V}_{10}\text{O}_{28}\}$ cluster framework this then creates the octanuclear arrangement found in the $[\beta\text{-Mo}_8\text{O}_{26}]^{4-}$ anion (see Figure 6).
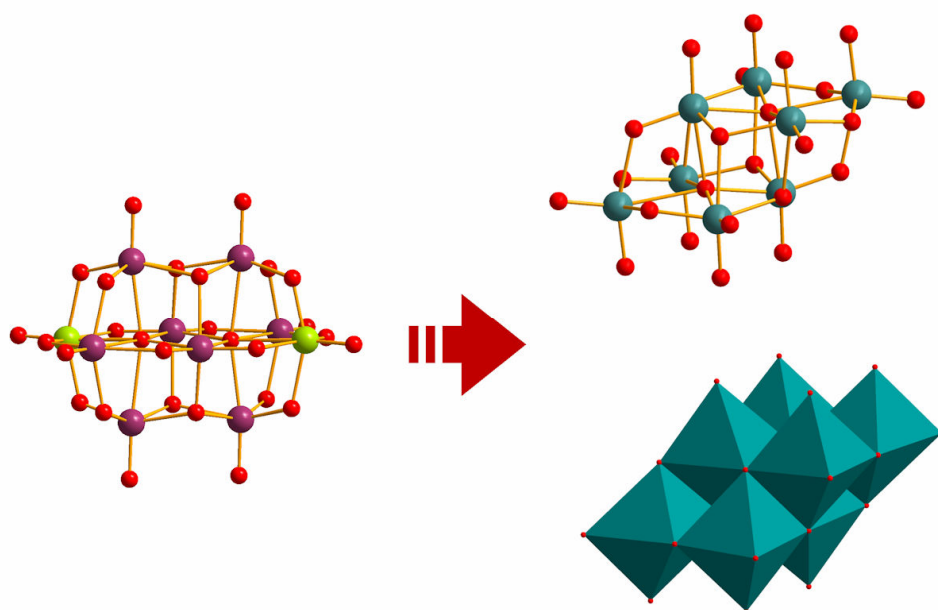
Figure 6: Left: Structural representation of the $[\text{V}_{10}\text{O}_{28}]^{6-}$ decavanadate anion. The two metal addenda, which can be considered to be removed in order to form the framework observed in $[\beta\text{-Mo}_8\text{O}_{26}]^{4-}$, are highlighted in green. Top Right: Ball-and-stick representation of the $[\beta\text{-Mo}_8\text{O}_{26}]^{4-}$ anion. Bottom Right: Polyhedral representation showing the eight corner- and edge-sharing $\{\text{MoO}_6\}$ octahedra of the $[\beta\text{-Mo}_8\text{O}_{26}]^{4-}$ anion. Colour scheme: V, purple and light green; Mo, teal (polyhedra); O, red.

The $[\beta\text{-Mo}_8\text{O}_{26}]^{4-}$ anion has been used extensively to coordinate through its terminal oxygen binding sites to many first row transition metal complexes. Examples include coordination to various Co, Ni, Cu and Zn complexes, allowing the formation of various architectures and 2-D and 3-D networks.[65, 71-79] The $[\beta\text{-Mo}_8\text{O}_{26}]^{4-}$ anion has also been reported to bind imidazole ligands through these terminal oxygen binding sites.[79]

Another prominent example of the coordination behaviour adopted by the $[\beta\text{-Mo}_8\text{O}_{26}]^{4-}$ anion is its ability to coordinate various silver(I) cations using its terminal oxygen ligands

to enable it to behave as a bi-, tetra-, or hexadentate ligand.[70, 80-82] Work in this area by Cronin *et al* revealed that reaction of the molybdenum Lindqvist anion, $[Mo_6O_{19}]^{2-}$, with silver(I) cations in a variety of coordinating solvents, led to the isolation of various architectures involving, specifically the aggregation of $(Ag\{Mo_8\}Ag)$ synthons (see Figure 7).[81, 83]
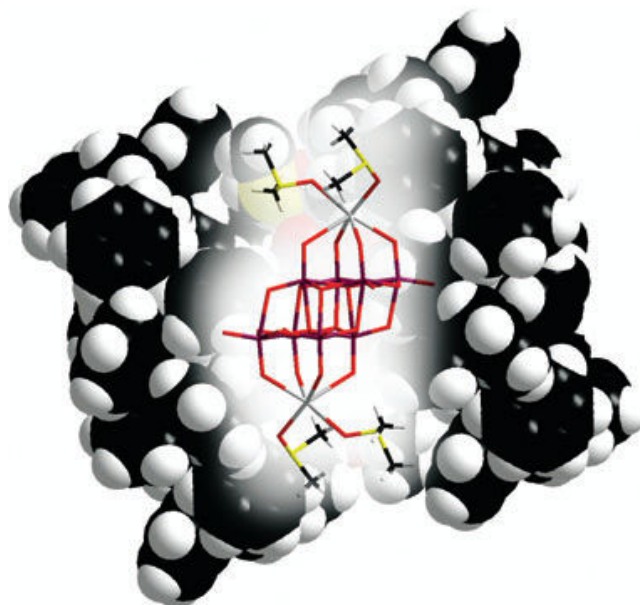
Figure 7: Representation of the $(Ph_4P)_2[Ag_2Mo_8O_{26}((CH_3)_2SO)_4]$ structure isolated by the reaction of Ph_4P^+ and silver(I) cations with $[Mo_6O_{19}]^{2-}$ anions in DMSO solution.[81] The $(Ag\{Mo_8\}Ag)$ synthon unit, coordinated with four DMSO solvent molecules, is shown in ball-and-stick representation. The sterically bulky Ph_4P^+ which surrounds, and allows the isolation of, this 'monomeric' building unit is shown as a space-filling representation. This space-filling representation is then faded in the centre for clarity. Colour scheme: Mo, purple; Ag, grey; O, red; S, yellow; C, black; H, white.

The use of rigid, sterically bulky cations such as tetraphenylphosphonium ions in DMSO solvent allowed isolation of the structure $(Ph_4P)_2[Ag_2Mo_8O_{26}((CH_3)_2SO)_4]$ which is composed of 'monomers' of this $(Ag\{Mo_8\}Ag)$ building-block.[81] In comparison the use of varying chain length alkylammonium cations, i.e. tetrapropyl-, tetrabutyl-, tetrahexyl-, and tetraheptylammonium ions; in a range of solvents such as acetonitrile, DMSO and DMF, led to the isolation of a variety of architectures ranging from chains, to grids and 2D-networks (see Figure 8). The generation of these different POM architectures was shown to be governed mainly by the steric requirements of the organic cations or coordinated solvent molecules.[81, 82] Another important feature of these results was the identification of the unusual $\{Ag_2\}$ dimers positioned between the $\{Mo_8\}$ cluster units, which are a result of the repeating $(Ag\{Mo_8\}Ag)$ building-block units within these structures. This linking motif is uncommon in POM chemistry and is a rare example of d^{10}

(i.e. filled d-shell) bridging units which are held together by significant argentophilic interactions, i.e. where the Ag-Ag distance is less than the sum of the van der Waals radii (3.44 Å).[82]
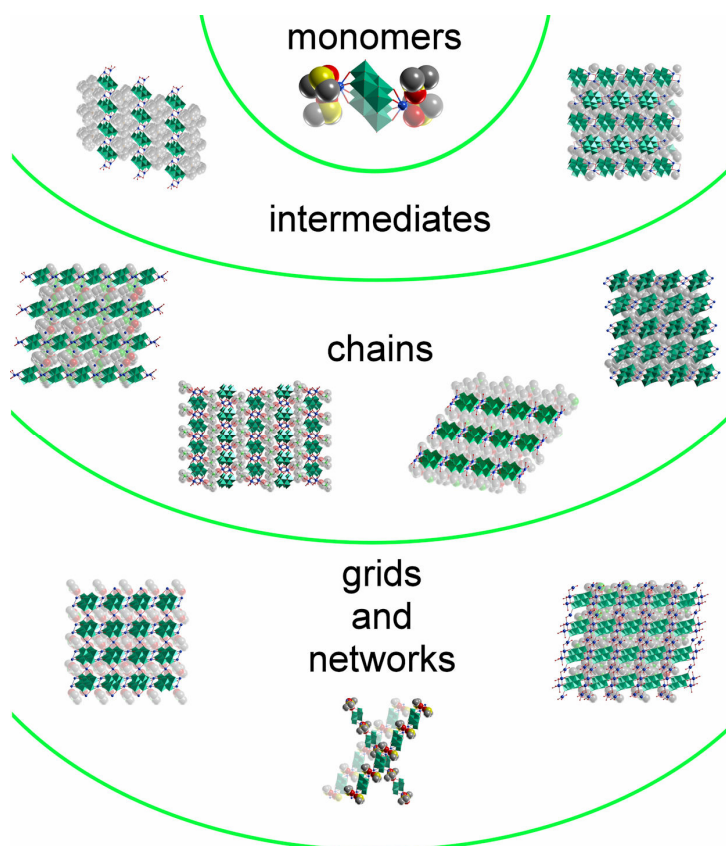
Figure 8: A summary of the variety of silver-linked β-octamolybdate architectures isolated when reacting $[Mo_6O_{19}]^{2-}$ anions with silver(I) cations in the presence of tetraphenylphosphonium cations or different chain length alkylammonium cations, and by varying the solvent system used.[81, 82] The 'monomer' (Ag{Mo_8}Ag) building block and the four coordinated DMSO solvent molecules of the compound $(Ph_4P)_2[Ag_2Mo_8O_{26}((CH_3)_2SO)_4]$ is shown at the top of this figure. The 'intermediates' section of the figure shows structures which are intermediate between the monomer and polymeric chain structures. In these compounds the silver cations act as linkers between adjacent {Mo_8} clusters through the formation of long-range (*ca* 2.8 Å) Ag-O contacts, however, there are no significant argentophilic interactions between the silver cations of neighbouring (Ag{Mo_8}Ag) synthons. The 'chains' section shows the structures composed of polymeric, infinite chains, i.e. (Ag{Mo_8}Ag)_∞, where the silver cations engage in both the long range Ag-O contacts described above, and argentophilic interactions. The 'grids and networks' section illustrates the structures formed *via* further silver(I) cations coordinating between adjacent (Ag{Mo_8}Ag)_∞ chains. Colour scheme: Mo, teal polyhedra; Ag, blue; O, red; C, grey; S, yellow. Non-coordinating solvent molecules and H atoms are omitted for clarity.

1.3.4.2   α-octamolybdate polyoxoanion

The $[\alpha\text{-Mo}_8\text{O}_{26}]^{4-}$ anion can be isolated from aqueous molybdate solutions following acidification to pH 3-4, *via* precipitation using organic cations such as tetrabutylammonium ions. The structure of this octamolybdate isomer was first reported by Fuchs and Hartl in 1976[84] and can be seen to be related to the Anderson structure, discussed later in section 1.4.1. It consists of a ring of six edge-sharing octahedra, with the central octahedron left vacant. This octahedral vacancy is capped on opposite faces by two tripodal, corner-sharing tetrahedra. Therefore, the overall structure has an approximate D_{3d} symmetry. It should also be noted that, once again, all the {MoO_6} octahedra and {MoO_4} tetrahedra are distorted and have short Mo-O (terminal) bond lengths.[18, 60] See Figure 9.
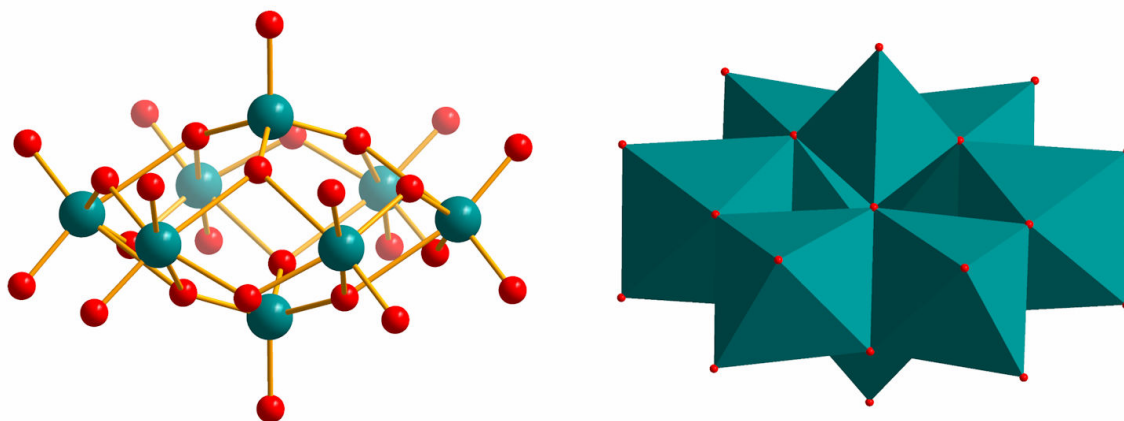
Figure 9: Representation of the $[\alpha\text{-Mo}_8\text{O}_{26}]^{4-}$ anion. Left: Ball-and-stick representation. Right: Polyhedral representation showing clearly one of the trigonal, corner-sharing {MoO_4} tetrahedra capping one face of the central vacant octahedron. Colour scheme: Mo, teal (polyhedra); O, red.

While it has been established, using IR and Raman studies, that $[\beta\text{-Mo}_8\text{O}_{26}]^{4-}$ is the predominant ocatamolybdate isomer in aqueous molybdate solution at pH 2,[85, 86] it has been found that it is the α-isomer which dominates at pH 2.7,[86] and both isomers are present at pH 3-4. Also in 1976 Klemperer and Shum showed that these isomers undergo a facile isomerization in acetonitrile, with the β-isomer, which contains only Mo centres in octahedral coordination environments, being favoured in the presence of small counterions such as potassium or tetramethylammonium cations.[19]

Another interesting feature of the $[\alpha\text{-Mo}_8\text{O}_{26}]^{4-}$ anion is that, on dissolution of ((*n*-C_4H_9)_4N)_4[α-Mo_8O_26] in acetonitrile and stoichiometric addition of (*n*-C_4H_9)_4NOH, the [α-

$Mo_8O_{26}]^{4-}$ anion has been found to decompose in solution and rearrange into $[Mo_2O_7]^{2-}$ anions. These dimolybdate anions were crystallized from this solution as ((n-$C_4H_9)_4N)_2[Mo_2O_7]$, and the $[Mo_2O_7]^{2-}$ units were found to be composed of two corner-sharing {MoO_4} tetrahedra. In analogy with the work of Klemperer and Shum[19] discussed above, addition of small counterions to this system once again precluded the rearrangement of the $[\alpha$-$Mo_8O_{26}]^{4-}$ anions into a POM structure containing tetrahedrally coordinated molybdenum centres. i.e. In this case, instead of producing the dimolybdate anion, only $[Mo_7O_{24}]^{6-}$ anion systems could be isolated.[87]

Although $[\alpha$-$Mo_8O_{26}]^{4-}$ anions have been reported to coordinate to copper centres using their terminal oxygen ligands as binding sites[65, 72] there are far fewer examples in the literature of such coordination than for the β-isomer. However, $[\alpha$-$Mo_8O_{26}]^{4-}$ anions are commonly used as facile precursors in the formation of other POM structures such as organoimido-functionalized $[Mo_6O_{19}]^{2-}$ architectures[36, 37, 88-90] (discussed previously in section 1.3.1), and tris(alkoxo)-functionalized molybdenum Anderson structures[91-96] (see section 1.4.1).

1.4 Heteropolyoxometalates $[X_xM_yO_z]^{n-}$

Heteropolyanions can be assigned the general formula $[X_xM_yO_z]^{n-}$ where $x \leq y$, and contain one or more p-, d- or f-block 'heteroatoms' (X), e.g. TeO_6^{6-}, IO_6^{5-}, SO_4^{2-}, PO_4^{3-}; along with the basic metal-oxide anion framework. These heteroatoms can be coordinated in either a non-solvent accessible environment, or on the surface of the POM structure. A large variety of elements are known to function as these heteroatoms hence there are a greater number of these structures to synthesize and study than the isopolyoxometalates. Also, as the structural and electronic properties are easier to synthetically modify than those of the isopoly compounds, this type of POM structure has been the focus of intensive study in the hope of new application discovery.[20]

1.4.1   The Anderson polyoxoanion [$H_x(XO_6)M_6O_{18}$]$^{n-}$

The Anderson polyoxoanion structure can be assigned the general formula [$H_x(XO_6)M_6O_{18}$]$^{n-}$ where x = 0-6, n = 2-6 and 8, M = Mo or W, and X = a central heteroatom.[18, 97-100] This polyoxometalate anion is composed of six edge-sharing {MoO_6} or {WO_6} octahedra surrounding a central, edge-sharing heteroatom octahedron i.e. {XO_6}, leading to the planar arrangement shown in Figure 10. The overall structure, therefore, has approximate D_{3d} symmetry.
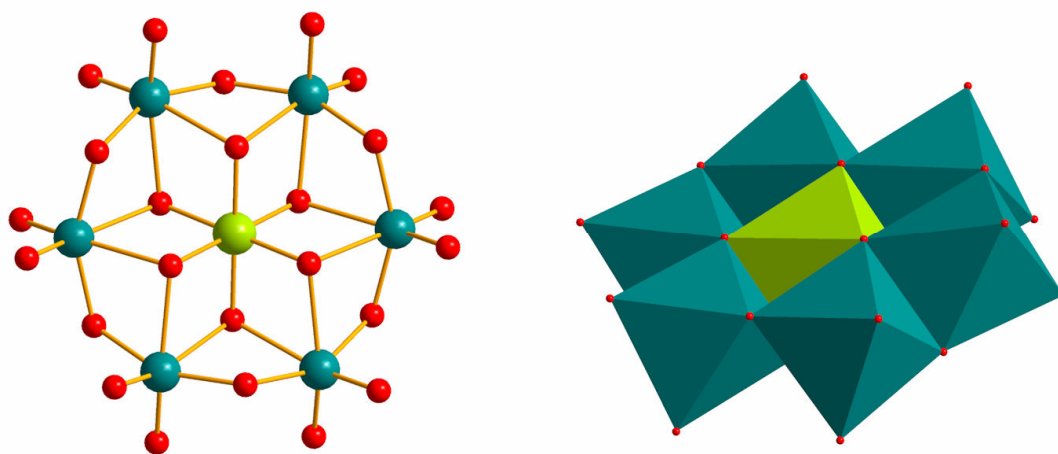
Figure 10: Representation of the molybdenum Anderson [$Te^{VI}Mo_8O_{24}$]$^{6-}$ anion. Left: Ball-and-stick representation showing the octahedral coordination environment of the central heteroatom. Right: Polyhedral representation showing the seven edge-sharing octahedra forming a planar arrangement. Colour scheme: Mo, teal (polyhedra); Te, light green (central polyhedron); O, red.

The first Anderson structure to be identified was that of [$Te^{VI}Mo_6O_{24}$]$^{6-}$,[101] however, since that time numerous other examples of Anderson structures containing heteroatoms in a range of oxidation states from +2 to +7 have been identified. Some molybdate examples include: [$Mn^{II}(OH)_6Mo_6O_{18}$]$^{4-}$, [$Co^{II}(OH)_6Mo_6O_{18}$]$^{4-}$, [$Cr^{III}(OH)_6Mo_6O_{18}$]$^{3-}$ [$Al^{III}(OH)_6Mo_6O_{18}$]$^{3-}$, [$Mn^{IV}(OH)_6Mo_6O_{18}$]$^{2-}$, [$Te^{VI}O_6Mo_6O_{18}$]$^{6-}$, and [$I^{VII}O_6Mo_6O_{18}$]$^{5-}$.[18, 102] While the more limited range of tungsten examples includes: [$Ni^{II}(OH)_6W_6O_{18}$]$^{4-}$, [$Mn^{IV}O_6W_6O_{18}$]$^{8-}$, [$Ni^{IV}O_6W_6O_{18}$]$^{8-}$, [$Te^{VI}O_6W_6O_{18}$]$^{6-}$, [$I^{VII}O_6W_6O_{18}$]$^{5-}$.[18]

The anions with high oxidation state heteroatoms such as Te^{VI} and I^{VII} can be seen to have unprotonated structures and are sometimes referred to as A-type Anderson structures.[18,

[103] The lower oxidation state examples, e.g. oxidation state of +2 or +3, are sometimes referred to as B-type Anderson structures, and these anions generally have non-acidic protons bound to the oxygen ligands of the central $\{XO_6\}$ octahedron. However, there is one reported B-type structure, $[H_6Pt^{IV}Mo_6O_{24}]^{2-}$, where four of the central μ_3-bridging oxo ligands and two of the μ_2-bridging oxo ligands are protonated.[104]

In general the Anderson polyoxometalate structures discussed above may be isolated from aqueous molybdate or tungstate solutions following acidification to within pH 3-4, however, the $\{X^{II}Mo_6\}$ salts where X = Mn and Cu, have been found to be unstable and cannot be recrystallized.[18, 98, 105-107]

There are examples of both molybdenum Anderson and tungsten Anderson clusters undergoing further coordination with transition metal complexes e.g. Cu and Ag;[108-111] and lanthanide cations, e.g. La, Ce and Pr.[112, 113] However, prominent examples of further functionalization of B-type molybdenum Anderson structures involve their ability to coordinate a wide variety of tris(alkoxo) ligands, i.e. $RC(CH_2OH)_3$ where R = a chosen substituent group, e.g. alkyl, aryl, nitro etc. This has led to the isolation of many organic-inorganic hybrid compounds[91-94, 96, 109] through the use of an indirect method of synthesis. This method involves the rearrangement of $[\alpha\text{-}Mo_8O_{26}]^{4-}$ cluster anions, in the presence of the heteroatom acetate salt, e.g. $Mn^{III}(CH_3CO_2)_3$, and the tris(alkoxo) ligand of choice, e.g. $CH_3C(CH_2OH)_3$, in order to isolate the derivatized Anderson cluster. See Figure 11.

These structures have been found to adopt two different coordination arrangements of the tris(alkoxo) ligands, which appear to be related to the two different protonation arrangements observed for B-type Anderson clusters.[91] The first type involves coordination of each tris(alkoxo) ligand directly above and below the central $\{XO_6\}$ octahedron, as shown on the left of Figure 11. Each tris(alkoxo) ligand can, therefore, be considered to effectively replace the three bridging hydroxide ligands surrounding the central heteroatom unit on each face of the Anderson cluster.[114] In the second mode of coordination the tris(alkoxo) ligands are coordinated above the tetrahedral cavities off to either side of the central heteroatom unit, as shown on the right of Figure 11. This coordination arrangement can be related to the unusual protonation environment of the B-type Anderson cluster $[H_6Pt^{IV}Mo_6O_{24}]^{2-}$ described earlier, i.e. each of the tris(alkoxo)

ligands can be considered to replace the two μ_3-bridging hydroxide ligands and one μ_2-bridging hydroxide ligand on opposite faces of the cluster.[91]
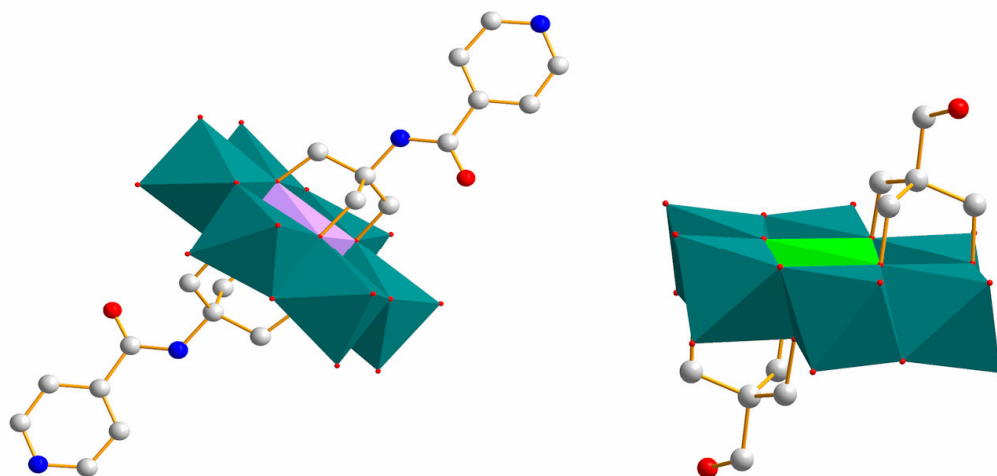
Figure 11: Representation of the two different coordination modes of tris(alkoxo) ligands with B-type Anderson clusters. Left: This cluster, [Mn^{III}Mo$_6$O$_{18}$((OCH$_2$)$_3$CNHCO(4-C$_5$H$_4$N))$_2$]$^{3-}$,[114] is an example of the first coordination mode. I.e. The two tris(alkoxo) ligands, (HOCH$_2$)$_3$CNHCO(4-C$_5$H$_4$N), are coordinated directly over opposing faces of the central {Mn^{III}O$_6$} octahedron of the {Mn^{III}Mo$_6$} Anderson cluster. Right: This cluster, [H$_2$Ni^{II}Mo$_6$O$_{18}$((OCH$_2$)$_3$CCH$_2$OH)$_2$]$^{2-}$,[91] is an example of the second coordination mode of tris(alkoxo) ligands with a B-type Anderson cluster. Each tris(alkoxo) ligand is coordinated to the Anderson cluster over the tetrahedral cavity adjacent to the central heteroatom octahedron. Colour scheme: Mo, teal polyhedra; Mn, light purple (central polyhedron); Ni, light green (central polyhedron); O, red; N, blue; C, grey. H atoms are omitted for clarity.

1.4.2   The Keggin anion [XM$_{12}$O$_{40}$]$^{n-}$

The structure of the Keggin anion, general formula [XM$_{12}$O$_{40}$]$^{n-}$ where M = W or Mo, and X = a central heteroatom; was first proposed for phosphotungstic acid by J. F. Keggin in 1933 on the basis of X-ray powder diffraction data.[10, 11] The structure was later confirmed using single crystal X-ray and neutron diffraction data.[115] It is based on a central {XO$_4$} heteroatom tetrahedron, around which are arranged twelve {MO$_6$} octahedra where M = W or Mo. These twelve {MO$_6$} octahedra are arranged into four groups of three edge-sharing octahedra, i.e. {M$_3$O$_{13}$} units, which are linked *via* corner-sharing to each other and to the central heteroatom tetrahedron (see Figure 12). This leads

to the structure having overall T_d symmetry for the tungsten Keggin anions. However, the molybdenum Keggin anions have an overall symmetry closer to the chiral group T due to small displacements of the Mo atoms from the mirror planes of the $\{M_3O_{13}\}$ units.[18]
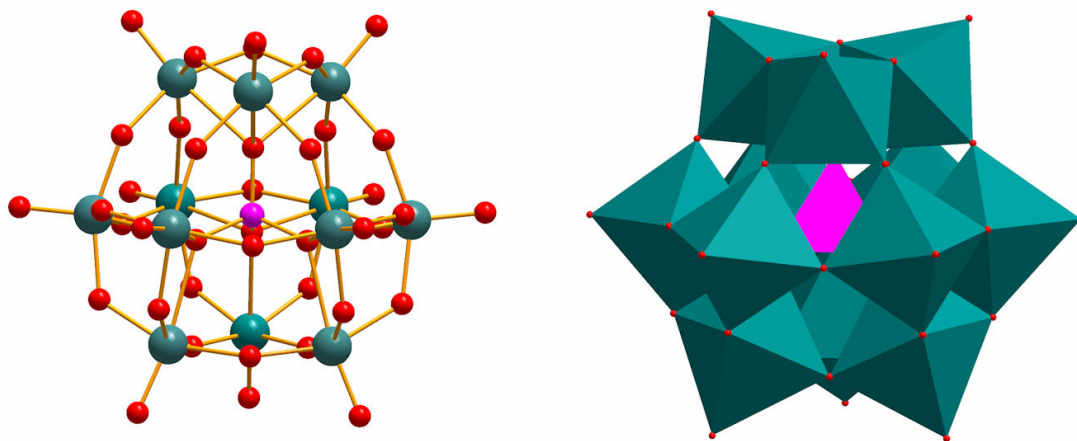
Figure 12: Representation of the $[\alpha\text{-PW}_{12}O_{40}]^{3-}$ Keggin anion. Left: Ball-and-stick representation showing the tetrahedral coordination of the central heteroatom. Right: Polyhedral representation showing the twelve $\{WO_6\}$ octahedra arranged into three edge-sharing $\{W_3O_{13}\}$ units. These $\{W_3O_{13}\}$ units can be seen to link, *via* corner-sharing, to each other and the central tetrahedron (highlighted in pink). Colour scheme: W, teal (polyhedra); P, pink (central tetrahedron); O, red.

The structure of the first identified Keggin anion $[PW_{12}O_{40}]^{3-}$, which is shown in Figure 12, is customarily referred to as the α-isomer. However, there are four further isomers, as reported by Baker and Figgis, which are assigned the nomenclature: β-, γ-, δ-, and ε-isomeric forms. These other isomers are related to the α-isomer by rotation through 60° of one, two, three and four of the $\{M_3O_{13}\}$ units.[116] The α-isomer is, however, the most stable isomer of the five, due to the increasing number of coulombically-unfavourable octahedral edge-shared contacts in the other isomers.[117-119] Indeed it has been found that the β-isomers spontaneously isomerize to the more stable α-form, a process whose rate varies from seconds for $\{\beta\text{-PMo}_{12}\}$ at room temperature to hours for $\{\beta\text{-SiW}_{12}\}$ at 150°C.[18]

It is important to note that the majority of heteropolyoxotungstates adopt either the Keggin anion structure, or structures derived from this Keggin anion. These so-called lacunary Keggin derivatives will be discussed in section 1.4.2.1. In comparison there are fewer heteropolyoxomolybdates based on Keggin or Keggin-derived building-blocks. Common

examples of heteropolyoxotungstates with the $[\alpha\text{-}XW_{12}O_{40}]^{n\text{-}}$ structure include those where $X = Al^{III}$, Si^{IV}, Ge^{IV}, P^{V}, As^{V}, Fe^{III}, Co^{II}. (Also an isopolyoxotungstate where $X = (H^{+})_{2}$ can be formed, which is known as α-metatungstate). Some examples of heteropolyoxomolybdates with the $[\alpha\text{-}XMo_{12}O_{40}]^{n\text{-}}$ structure include those where $X = Si^{IV}$, Ge^{IV}, P^{V}, As^{V}.[18]

1.4.2.1 Lacunary structures derived from the Keggin polyoxoanion

A particularly important feature of heteropolytungstates with the Keggin structure, e.g. $[SiW_{12}O_{40}]^{4\text{-}}$, is their ability to form lacunary structures, where one or more $\{WO_{6}\}$ octahedra are removed from the cluster shell and can subsequently be replaced by other coordinating peripheral heteroatoms, e.g. $[Ru^{III}SiW_{11}O_{39}(H_2O)]^{5\text{-}}$.[120]

Such complexes have been prepared in aqueous and non-aqueous solutions. For example, these lacunary polyoxoanion complexes have been prepared *via* acidification of aqueous mixtures containing both the heteroatom and $WO_4^{2\text{-}}$ ions; whereas in other cases such complexes have been prepared through partial hydrolysis of the 'parent' Keggin anion in aqueous solution whilst in the presence of the secondary heteroatom. This partial hydrolysis method requires the addition of base and careful control of the other reaction conditions to induce hydrolytic cleavage of W-O bonds in order to selectively remove one, two or three tungsten centres from the parent anion.[18, 121] In more detail, the W^{VI} centres are selectively removed with their terminal oxo ligands as $[WO]^{4+}$ units, along with the remaining μ_2-bridging oxo ligands coordinated to these metal centres. This process leads to the production of undecatungstate ($\{W_{11}\}$), decatungstate ($\{W_{10}\}$), and nonatungstate ($\{W_9\}$) heteropolyanion lacunary structures (see Figure 14). The most stable of these lacunary heteropolyanions are those of the silicotungstates.[121]

Due to the existence of four different isomers (α, β, γ, ε) for the parent Keggin anion, and due to the variation in location of the metal centres removed, this leads to an increasingly large number of 'positional isomers' as the number of removed metal centres increases. Additionally, variations in the orientation of the central tetrahedral heteroatom unit relative to the encapsulating metal-oxide framework can lead to further isomeric forms of these

lacunary structures. For example, in the lacuna $[PW_9O_{34}]^{9-}$ the central tetrahedral $[PO_4]^{3-}$ unit can be found in two different orientations with respect to the surrounding tungsten oxide framework, leading to two different, stable isomers denoted $[A\text{-}PW_9O_{34}]^{9-}$ and $[B\text{-}PW_9O_{34}]^{9-}$.[18, 121]

It is pertinent to note at this point that the formation of these A- and B-type isomers may be described in an alternative manner which considers the particular metal centres which are removed from the tungsten oxide framework. This description allows the formation of the A-type isomer to be explained *via* the removal of three tungsten centres from three different $\{W_3O_{13}\}$ edge-sharing units, whilst the B-type isomer is formed *via* the removal of three tungsten centres, all of which make up one of these $\{W_3O_{13}\}$ edge-sharing units (see Figure 13).[122]

$[\alpha\text{-}PW_{12}O_{40}]^{3-}$
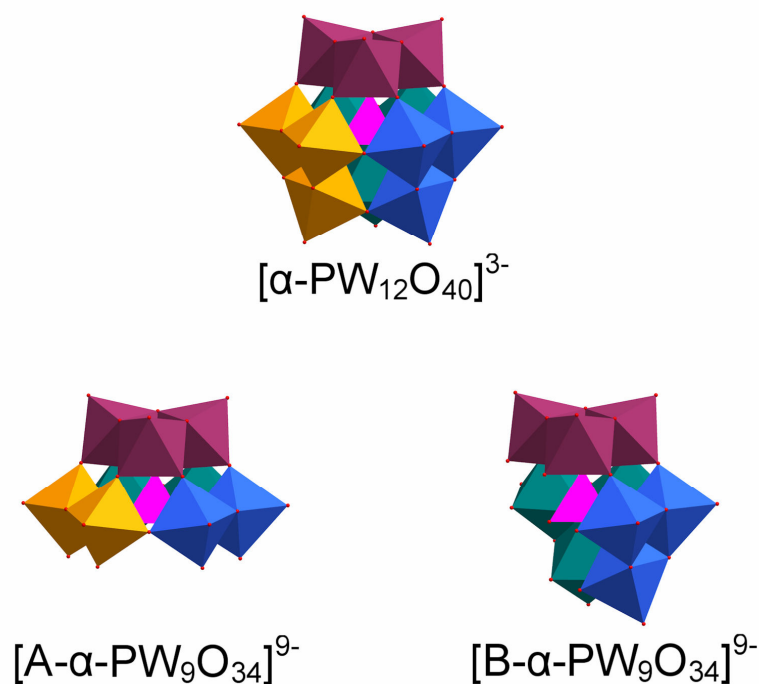
$[A\text{-}\alpha\text{-}PW_9O_{34}]^{9-}$ $[B\text{-}\alpha\text{-}PW_9O_{34}]^{9-}$

Figure 13: Representation of the A- and B-type isomers of $[\alpha\text{-}PW_9O_{34}]^{9-}$ with respect to the $[\alpha\text{-}PW_{12}O_{40}]^{3-}$ Keggin anion. Each of the four groups of $\{W_3O_{13}\}$ edge-sharing units, which make up the metal-oxide framework, is highlighted with different colour polyhedra. The central PO_4^{3-} heteroanion is shown as a pink tetrahedron. Bottom Left: The A-type $\{PW_9\}$ isomer is formed by removal of three tungsten centres from three different $\{W_3O_{13}\}$ edge-sharing units. Bottom Right: The B-type $\{PW_9\}$ isomer is formed by removal of three tungsten centres from one $\{W_3O_{13}\}$ edge-sharing unit. The resulting non-coordinated oxygen ligand of the PO_4^{3-} heteroanion is evident. Colour scheme: W, teal, purple, blue and orange polyhedra; P, pink tetrahedron; O, red.

Given these descriptions of the {XM$_9$} isomer formation it can be clearly observed that further coordination of these anions is greatly influenced by the resulting orientation of the central heteroatom tetrahedron. This is because in the B-type isomer one of the oxygen ligands of the {XO$_4$} tetrahedron is accessible for further coordination with peripheral heteroatoms such as transition metals;[123] whereas in the A-type isomer all the oxygen ligands of the {XO$_4$} tetrahedron form coordinative bonds with the tungsten oxide framework, leaving only the terminal oxo ligands of the tungsten oxide framework itself to form further coordinative interactions.[124] See Figure 13 and 14, top two figures.
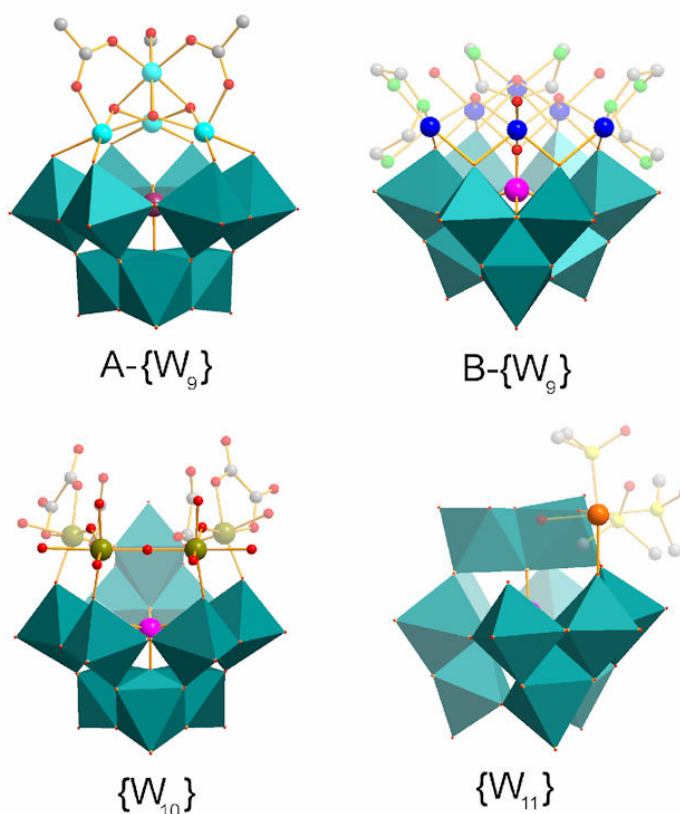
Figure 14: Illustrations of some examples of lacunary Keggin frameworks. Top Left: An A-type α-isomer of {SiW$_9$} coordinated to four peripheral Co^{II} centres whose coordination spheres are filled with μ$_2$-bridging acetate and hydroxyl ligands, i.e. [(A-α-SiW$_9$O$_{34}$)Co$_4$(OH)$_3$(CHCO$_2$)$_3$]$^{8-}$.[124] Top Right: The B-type α-isomer of {PW$_9$} coordinated to six peripheral Ni^{II} centres whose coordination spheres are filled with diethylenetriamine (dien) ligands, bridging hydroxyl ligands and water molecules, i.e. [Ni$_6$(μ$_3$-OH)$_3$(H$_2$O)$_2$(dien)$_3$(B-α-PW$_9$O$_{34}$].[123] Bottom Left: The α-isomer of {PW$_{10}$} coordinated to four peripheral Ti^{IV} centres whose coordination spheres are filled with oxalate (ox) ligands, bridging oxygen ligands, and water molecules, i.e. [[(Ti(ox)(H$_2$O)$_4$(μ-O)$_3$]α-PW$_{10}$O$_{37}$]$^{7-}$.[125] Bottom Right: The α-isomer of {GeW$_{11}$} coordinated to one peripheral Ru^{II} centre whose coordination sphere is filled with DMSO molecules and one water molecule, i.e. [Ru^{II}(DMSO)$_3$(H$_2$O)α-GeW$_{11}$O$_{39}$]$^{6-}$.[126] Colour scheme: W, teal (polyhedra); Si, purple; P, pink; Co, light blue; Ni, dark blue; Ti, dark yellow; Ru, orange; O, red; N, light green; C, grey; S, yellow. H atoms are omitted for clarity.

The ability to selectively synthesize then further coordinate such multidentate, lacunary POM anions to form larger, more complex POM architectures is very important in the design and synthesis of new POM materials. This area is currently of high research interest because these new POM architectures, due to the nature of their coordinated groups may have, for example, interesting electronic,[127] magnetic[128, 129] or catalytic properties.[130, 131]

1.4.3   The Wells-Dawson polyoxoanion $[X_2M_{18}O_{62}]^{n-}$

The Wells-Dawson, or simply Dawson polyoxoanion[132, 133] can be assigned the general formula $[X_2M_{18}O_{62}]^{n-}$ where M = W or Mo, and X = a central heteroatom such as P^V, As^V, S^{VI}, which forms two tetrahedral heteroanion units, e.g. PO_4^{3-}, within the metal-oxide framework. The tungsten Dawson anion may be synthesized through the reflux of aqueous sodium tungstate solution with excess H_3XO_4, then isolated either by using potassium or ammonium cations, or using ether extraction to isolate the free acid. The molybdenum Dawson can be synthesized through direct dimerisation of $\{XMo_9\}$ anions (one of the few molybdenum lacuna which can be recrystallized) in acidic solution,[18]

i.e. $2[XMo_9O_{31}(OH_2)_3]^{3-} \rightleftharpoons [X_2Mo_{18}O_{62}]^{6-} + 6H_2O$
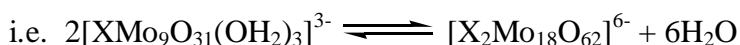
There are, to date, six known isomers of the $[X_2M_{18}O_{62}]^{n-}$ Dawson structure which are assigned the following prefixes: α, α*, β, β*, γ, and γ*.[134, 135] However, the most stable of these isomers, and that with the highest symmetry (D_{3h} for $\{X_2W_{18}\}$ and D_3 for $\{X_2Mo_{18}\}$), is the α-isomer. The other isomers, in analogy with the Keggin anion described previously, are related to the α-isomer through 60° rotations of the two $\{M_3O_{13}\}$ caps and/or the two $\{M_6O_{27}\}$ belts.[18, 135]

The structural composition of the α-isomer can most conveniently be described as two A-type α-$\{XM_9\}$ units coordinated together, indeed this dimerisation takes place directly in the synthesis of $\{X_2Mo_{18}\}$. However, in order to visualise the formation of the different

isomeric species it is also helpful to consider the structure as being composed of two capping $\{M_3O_{13}\}$ units and two central $\{M_6O_{27}\}$ belts. Each $\{M_3O_{13}\}$ unit is composed of three edge-sharing octahedra which then coordinate through corner-sharing to the $\{M_6O_{27}\}$ belt below. One of the oxo ligands of the encapsulated XO_4^{n-} heteroanion also acts as a μ_4-bridging oxo ligand and coordinates to this $\{M_3O_{13}\}$ capping unit. Each $\{M_6O_{27}\}$ belt is composed of three edge-sharing dioctahedra which are then coordinated together through corner-sharing linkages, into a planar arrangement. The three remaining oxo ligands of the encapsulated XO_4^{n-} heteroanion then act as μ_3-bridges and coordinate to these dioctahedra. Six corner-sharing interactions involving each octahedron in the belt coordinate it to the neighbouring $\{M_6O_{27}\}$ belt. See Figure 15.
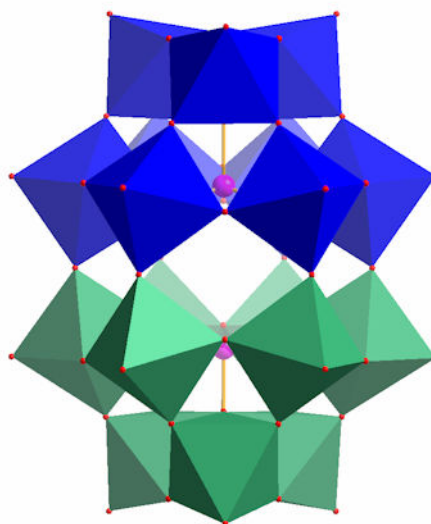
Figure 15: Representation of the $[\alpha\text{-}X_2M_{18}O_{62}]^{n-}$ Dawson anion where M = W or Mo, and X = a central heteroatom such as P^V, As^V, S^{VI}, which forms two tetrahedral heteroanion units, e.g. PO_4^{3-}, within the metal-oxide framework. The two A-α-$\{XM_9\}$ cluster units, which coordinate together through corner-sharing interactions, are highlighted using different coloured polyhedra. It is the aggregation of these A-type, α-$\{XM_9\}$ isomer subunits which dictates the formation of the α-Dawson isomer. In this illustration the metal-oxide octahedra of the cluster shell are shown as blue and green polyhedra, the two central heteroatoms are shown in purple, and oxygen ligands in red.

Dawson polyoxoanions can undergo further coordination to transition metals using their terminal oxo ligands as binding sites so allowing the construction of more complex POM architectures.[136, 137] Also they can undergo partial hydrolysis in a similar fashion to the Keggin anion described previously, leading to the isolation of Dawson-based lacunary structures (see section 1.4.3.1).

To date, the most intensively researched Dawson structure is $\{P_2W_{18}\}$ which has been used in the construction of thin-films with photo- and electrochromic,[138] and optoelectronic properties;[139] in heterogeneous catalysis[140-142]; and in biomedical applications.[143, 144] However, recently there has been interest in constructing new Dawson-like POM frameworks which, due to the reduced or oxidised nature of the encapsulated templates, may also possess interesting electronic properties. It is hoped that the development of such materials could lead to the production of a POM-based device.

Some examples of such research have recently been carried out by Cronin *et al.* In 2004 the α- and β-isomers of a molybdenum Dawson-like cluster encapsulating two pyramidal sulfite ions were produced, which exhibit unusual thermochromic behaviour.[145] The production of the related, tungsten-based Dawson-like cluster $[W^{VI}_{18}O_{56}(S^{IV}O_3)_2(H_2O)_2]^{8-}$ was reported in 2005, and this cluster anion was found to act like a molecular switch by undergoing an unusual electron-transfer reaction on heating. This reaction takes place *via* a structural rearrangement of the cluster framework which allows the two pyramidal sulfite ions to release up to four electrons to the cluster surface, producing the blue, sulfate-based, mixed-valence cluster $[\alpha\text{-}W^{VI}_{14}W^{V}_4O_{54}(S^{VI}O_4)_2]^{8-}$.[146]

Then in 2008, following the incorporation of the unusual octahedral-template $\{WO_6\}$ within the Dawson-like isopolyoxotungstate $[H_4W_{19}O_{62}]^{6-}$,[147] it was decided to investigate the replacement of this octahedral template with other encapsulated $\{XO_6\}$ heteroanion species where the heteroatom X is in a high oxidation state, e.g. I^{VII} or Te^{VI}. This research has recently led to the production of the catalytically active $[H_3W_{18}O_{56}(I^{VII}O_6)]^{6-}$ and $[H_3W_{18}O_{56}(Te^{VI}O_6)]^{7-}$ Dawson-like clusters.[148, 149] In addition it has been found that the encapsulated tellurate $\{Te^{VI}O_6\}$ heteroanion template in the latter cluster can be reduced using sodium dithionite to the tellurite anion $\{Te^{IV}O_3\}$, so enabling the isolation of the new cluster anion $[H_3W_{18}O_{57}(Te^{IV}O_3)]^{5-}$ (see Figure 16).[149]
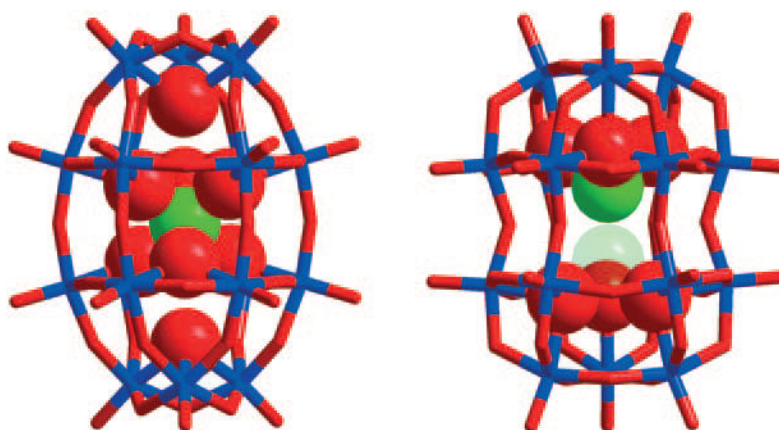
Figure 16: Left: Representation of the $[H_3Te^{VI}W_{18}O_{62}]^{7-}$ Dawson-like anion.[149] The metal-oxide framework is shown as a wire-frame representation and the $\{Te^{VI}O_6\}$ heteroanion unit as a space-filling model. The two oxo ligands which are lost on oxidation are also shown in space-filling format. Right: Representation of the $[H_3Te^{IV}W_{18}O_{60}]^{5-}$ Dawson-like anion.[149] Once again the metal-oxide framework is shown as a wire-frame representation and the $\{Te^{IV}O_3\}$ heteroanion, which is delocalised over two positions in the cluster as illustrated by the faded pyramidal unit, is shown as a space-filling model. Colour scheme: W, blue; Te, green; O, red. H atoms are omitted for clarity.

1.4.3.1   Lacunary structures derived from the Dawson polyoxoanion

The tungsten Dawson polyoxoanions $[X_2W_{18}O_{62}]^{6-}$ where $X = P^V$ or As^V, are stable in solution up to approximately pH 6. However, raising the pH above this level through the addition of base leads to partial hydrolysis of these clusters to yield lacunary Dawson species where one or more metal centres are removed in a controlled manner. This partial hydrolysis of the Dawson cluster is similar to that seen in the formation of the lacunary Keggin derivatives discussed previously. In the case of the Dawson clusters, however, all the stable lacunary species are derived from the α-isomer of the $\{X_2W_{18}\}$ anion. [18, 121, 150]

There are three stable lacunary species that can be produced in this way: $[\alpha_1\text{-}, \alpha_2\text{-}X_2W_{17}O_{61}]^{10-}$, $[\alpha\text{-}X_2W_{15}O_{56}]^{12-}$, and $[\alpha\text{-}H_2X_2W_{12}O_{48}]^{12-}$. The lacunary cluster $[\alpha\text{-}HAs_2W_{16}O_{59}]^{11-}$ has also been synthesized, however, no phosphate analogue is currently known.[121, 150]

The formation of these Dawson-derived lacuna can be explained by reference to the earlier description of the 'parent' Dawson cluster as being derived from two capping $\{M_3O_{13}\}$ units and two $\{M_6O_{27}\}$ belts. Using this description, the $[\alpha_1-X_2W_{17}O_{61}]^{10-}$ lacuna is formed *via* removal of one tungsten centre from one of the $\{W_6O_{27}\}$ belts, whilst the $[\alpha_2-X_2W_{17}O_{61}]^{10-}$ lacuna is formed through removal of one of the tungsten centres from a $\{W_3O_{13}\}$ cap. An entire $\{W_3O_{13}\}$ cap is removed from the 'parent' Dawson cluster to form the $[\alpha-X_2W_{15}O_{56}]^{12-}$ species. The $[\alpha-H_2X_2W_{12}O_{48}]^{12-}$ lacuna is formed *via* the removal of six adjacent tungsten atoms that form a longitudinal third of the polyanion, i.e. through the removal of one tungsten centre from each $\{W_3O_{13}\}$ cap and two adjacent tungsten centres from each of the two $\{W_6O_{27}\}$ belts.

These lacunary Dawson clusters can act as multidentate ligands and coordinate with a wide variety of transition metal and lanthanide ions, allowing the construction of many mixed-metal polyoxoanions as well as larger, more complex POM structures.[121, 150-156] Some examples of the extended coordination ability of these Dawson-lacuna are shown in Figure 17.

$\{P_2W_{17}\}$ $\{P_2W_{15}\}$ $\{P_2W_{12}\}$
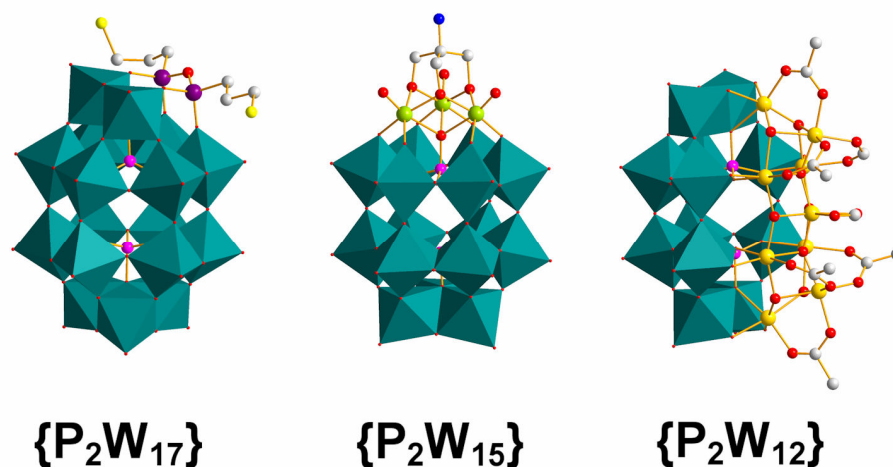
Figure 17: Illustrations of some examples of lacunary Dawson frameworks. Left: An α_2-$\{P_2W_{17}\}$ lacuna functionalized with an organosilyl group $(O[Si(CH_2)_3SH]_2)$ *via* the four oxygen atoms in the mono-lacunary site of the cluster, i.e. $[\alpha_2-P_2W_{17}O_{61}(O[Si(CH_2)_3SH]_2)]^{6-}$.[157] Centre: A $\{V_3O_{13}\}$ cap is coordinated in the vacant cap position of an α-$\{P_2W_{15}\}$ lacuna. The bridging oxo ligands of this cap are then replaced by the three alkoxo ligands of a coordinating tris(hydroxymethyl)aminomethane group, i.e. $[(H_2NC(CH_2O)_3)PV_3W_{15}O_{59}]^{6-}$.[158] Right: Six peripheral Fe[III] centres are coordinated into the six vacancies of an α-$\{P_2W_{12}\}$ isomer. Three further Fe[III] centres are then coordinated through bridging oxygen ligands to these Fe centres. The coordination spheres of these Fe centres are filled with bridging acetate ligands, i.e. $[H_4P_2W_{12}Fe^{III}_9O_{56}(OAc)_7]^{6-}$.[155] Colour scheme: W, teal polyhedra; P, pink; Si, purple; V, light green; Fe, dark yellow; O, red; N, blue; C, grey; S, yellow. H atoms are omitted for clarity.

Of particular note from these examples is the $[(H_2NC(CH_2O)_3)PV_3W_{15}O_{59}]^{6-}$ cluster (centre of Figure 17) which represents a tris(alkoxo) derivative of a mixed-metal Dawson lacuna.[158] The first of such structures to be isolated, i.e. $[RC(CH_2O)_3V_3P_2W_{15}O_{59}]^{6-}$ where R = CH_3, NO_2, CH_2OH; were reported by Hill *et al* in 1993.[151] Since that time, research into these derivatized Dawson clusters has increased in the hope of introducing further functionality to these structures, and has recently led to the isolation of a tetrameric assembly of these clusters,[158] as illustrated on the left of Figure 18. Also, as an extension of their research into these triester clusters, Hasenknopf, Lacôte and Thorimbert *et al* have recently reported the isolation of an amide derivatized mixed-metal Dawson lacuna,[159] through the reaction of various amide derivatives of 2-amino-2-ethyl-1,3-propanediol with $\{P_2V_3W_{15}\}$ in dimethylacetamide (see the right of Figure 18).
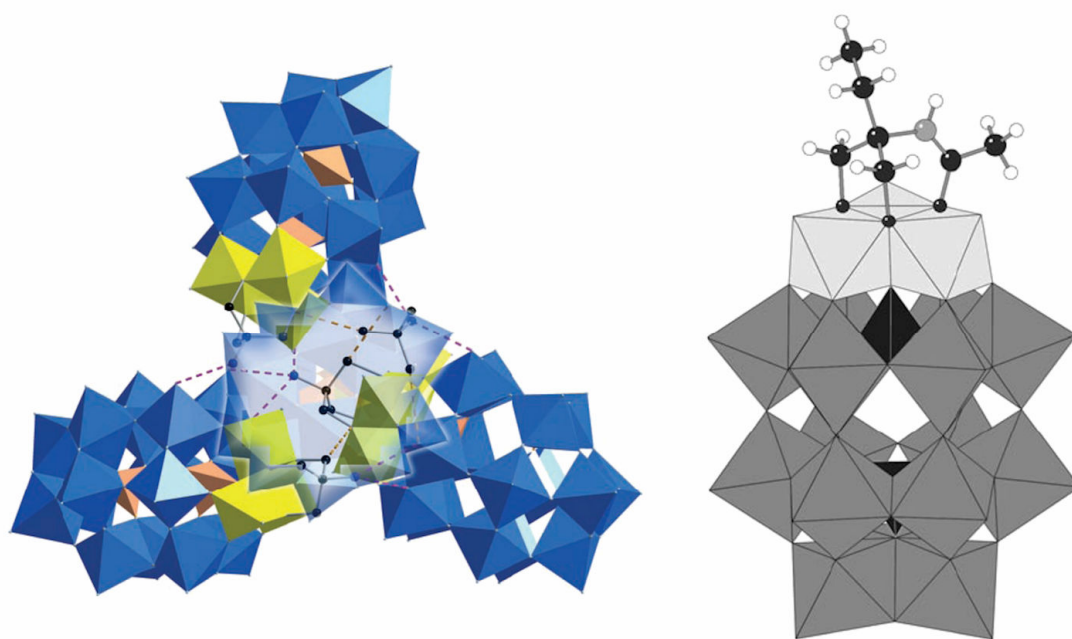
Figure 18: Left: Illustration of the H-bonded tetrameric assembly of four $[H_2NC(CH_2O)_3P_2V_3W_{15}O_{59}]^{6-}$ clusters.[158] One lobe of this distorted tetrahedral structure is made transparent to highlight the H-bonding interactions. Colour scheme: $\{WO_6\}$, blue polyhedra; $\{VO_6\}$, yellow polyhedra; $\{PO_4\}$, orange polyhedra; C black; N, blue; N-H···O hydrogen-bonding interactions, purple dotted lines; C-H···O short contact distances, golden dotted lines. Right: Structural representation of $[P_2V_3W_{15}O_{59}((OCH_2)_2C(Et)NHCOCH_3)]^{5-}$,[159] i.e. an amide derivatized $\{P_2V_3W_{15}\}$ Dawson lacuna. Colour scheme for polyhedra: W, dark gray; V, light gray; P, black. Colour scheme for ball-and-stick models: C, black; N, gray; H, white; O, small black.

1.5 Molybdenum blue and Keplerate Structures

The molybdenum blue and Keplerate structures will be discussed within this section as they comprise a class of highly reduced molybdenum-based polyoxoanions, which are constructed using the ubiquitous pentagonal $\{(Mo)Mo_5\}$ building-block units, as explained below.

1.5.1 Molybdenum blues

The term 'molybdenum blue' was first eluded to by Scheele in 1778,[160] then by Berzelius in 1826,[3] and refers to the amorphous blue material precipitated from solution following the reduction of acidified molybdate(VI) solutions using a wide variety of reducing agents. Indeed it is this reaction which forms the basis of the 'molybdenum blue test' to qualitatively determine the presence of molybdenum.[161]   Until relatively recently, however, the composition of this compound was unknown, and was only determined in 1998 through work by Müller *et al*.[162]

In this important piece of work it was illustrated that the anion of the crystalline compound isolated, i.e. $[Mo_{154}(NO)_{14}O_{420}(OH)_{28}(H_2O)_{70}]^{14-}$, is archetypical for these 'molybdenum blue' compounds. Through comparisons between the spectroscopic and powder X-ray diffraction data of this compound with the molybdenum blue precipitates, the authors suggested that the molybdenum blue materials were most probably forms of molecular molybdenum trioxide, with varying degrees of protonation and reduction and the probable formula $[(MoO_3)_{154}(H_2O)_{70}H_x]^{y-}$.[162]   This formula is related to that for the anion $[Mo_{154}(NO)_{14}O_{420}(OH)_{28}(H_2O)_{70}]^{14-}$ described above, through replacement of the 14 $\{MoNO\}^{3+}$ groups with $\{MoO\}^{4+}$ groups. This is not without precedent as previous comparable cluster pairs have been identified, e.g. $[Mo_{36}(NO)_4O_{108}(H_2O)_{16}]^{12-}$ and $[Mo_{36}O_{112}(H_2O)_{16}]^{8-}$.[163-165]

The structure of the $[Mo_{154}(NO)_{14}O_{420}(OH)_{28}(H_2O)_{70}]^{14-}$ anion can be explained with reference to the smaller building-block units from which it is composed, i.e. $\{Mo_8\}$, $\{Mo_2\}$ and $\{Mo_1\}$ units. In this context, the composition of these building-blocks units is

explained herewith. The $\{Mo_8\}$ building-block unit consists of a central, pentagonal $\{MoO_6(NO)\}$ bipyramid which shares each of its five equatorial edges with five $\{MoO_6\}$ octahedra, leading to the creation of the $\{(Mo)Mo_5\}$ pentagonal building-block referred to previously. Two additional corner-sharing $\{MoO_6\}$ octahedra are then coordinated to this pentagonal unit. This gives the $\{Mo_8\}$ building-block in this structure its characteristic curved appearance (see highlighted polyhedra, left-hand side of Figure 19). In discussing the construction of this building-block it is interesting to note that the pentagonal $\{(Mo)Mo_5\}$ unit can also be identified in the composition of both the fully oxidized $[Mo_{36}O_{112}(H_2O)_{18}]^{8-}$ cluster[51, 52, 56, 57] (where the central pentagonal bipyramid is $\{MoO_7\}$), and the partially reduced $\{Mo_{57}\}$ clusters, of the type $[Mo^{VI}_{51}Mo^{V}_6Fe_6(NO)_6O_{174}(OH)_3(H_2O)_{24}]^{15-}$.[164]

The remaining building-block units in this structure, i.e. the $\{Mo_2\}$ and $\{Mo_1\}$ units, are described as follows: the $\{Mo_2\}$ building-block unit consists of two corner-sharing $\{MoO_6\}$ octahedra (see red polyhedra, right-hand side of Figure 19); whilst the $\{Mo_1\}$ building-block refers to just one $\{MoO_6\}$ octahedral unit (see green polyhedra, right-hand side of Figure 19).

Using these building-block units the formula of the cluster anion $[Mo_{154}(NO)_{14}O_{420}(OH)_{28}(H_2O)_{70}]^{14-}$, otherwise referred to as $\{Mo_{154}\}$, can be re-written as $[\{Mo_2\}\{Mo_8\}\{Mo_1\}]_n$ or $[\{Mo^{VI}_2O_5(H_2O)_2\}\{Mo^{VI/V}_8XO_{25}(OH)_2(H_2O)_3Mo^{VI/V}\}]_n$ where n = 14 and X = NO. The arrangement of the building-blocks within this tetradecameric cluster is illustrated in Figure 19. The 14 $\{Mo_8\}$ units are arranged around the periphery of the wheel-like structure, both above and below the equatorial plane of the cluster and are coordinated together by the 14 $\{Mo_1\}$ units. This coordination arrangement is further reinforced by the 14 $\{Mo_2\}$ units forming corner-sharing linkages between the $\{Mo_8\}$ building-blocks (see Figure 19).[16]
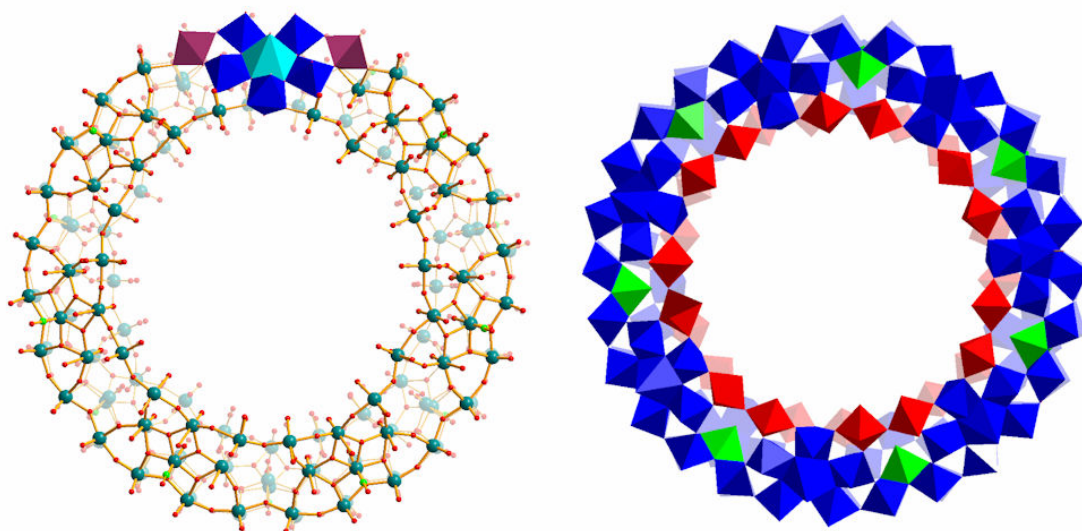
Figure 19: Structural representation of the $[Mo_{154}(NO)_{14}O_{420}(OH)_{28}(H_2O)_{70}]^{14-}$ anion, archetypical of the 'molybdenum blue' species.[16, 162] Left: The majority of the cluster is shown in ball-and-stick representation where the colour scheme is: Mo, teal; O, red. Highlighted in polyhedral representation is one of the $\{Mo_8\}$ building-block units which make up this structure. The central pentagonal $\{MoO_6(NO)\}$ bipyramid is shown in light blue; the five surrounding, edge-sharing $\{MoO_6\}$ octahedra are shown in dark blue; and the two corner-sharing $\{MoO_6\}$ octahedra, on the periphery of this central pentagonal $\{(Mo)Mo_5\}$ unit, are shown in purple. Right: The $\{Mo_{154}\}$ cluster is shown as a polyhedral representation. The $\{Mo_8\}$ building-blocks are shown in dark blue, the $\{Mo_2\}$ building-blocks are shown in red, and the $\{Mo_1\}$ units in green.

Further work to synthesize analogues of the $\{Mo_{154}\}$ wheel-structure, but without the NO groups, resulted in the isolation of the related mixed-valence, wheel-like $\{Mo_{176}\}$ cluster, i.e. $[(MoO_3)_{176}(H_2O)_{80}H_{32}]$.[166, 167] This structure of this cluster is closely related to that of the $\{Mo_{154}\}$ wheel, being composed of the same building-block units. Indeed the formula for $\{Mo_{176}\}$ can be re-written in the same manner as for $\{Mo_{154}\}$ so revealing this cluster to be a hexadecameric molybdenum blue species, i.e. $[\{Mo_2\}\{Mo_8\}\{Mo_1\}]_n$ or $[\{Mo^{VI}_2O_5(H_2O)_2\}\{Mo^{VI/V}_8XO_{25}(OH)_2(H_2O)_3Mo^{VI/V}\}]_n$ where $n = 16$ and X = O.[16, 168]

These molybdenum blue-type species are of great interest for further study due to their many intriguing properties. For example, they possess a rich electrochemistry due to their mixed-valence molybdenum centres;[162, 166] have nanometer-sized cavities within the centre of their wheel-like structures which can act as hosts for organic and inorganic guest molecules;[16, 169] have a high density of states in the HOMO/LUMO region leading to a small band gap and, therefore, semi-conductor activity;[162] and possess interesting

photochemistry with intervalence charge transfer transitions providing their intense blue colouring.[15, 16]

1.5.2   Keplerate structures

The building-block principles, explained in the previous section, which can be applied in an attempt to understand the self-assembly of the molybdenum blue structures can be further extended when considering the self-assembly of the spherical Keplerate clusters. The key building-block in the formation of these clusters is the pentagonal $\{(Mo)Mo_5\}$ unit described earlier, which allows the assembly of spherical clusters of icosahedral symmetry. Due to the role played by this pentagonal building unit it was decided to name such clusters 'keplerates' after J. Kepler and his study of pentagonal symmetry in 1596, and as illustrated by his model of the cosmos.[170]

Prominent examples of Keplerate structures include the $\{Mo_{132}\}$ cluster anion $[((Mo)Mo_5O_{21}(H_2O)_6)_{12}(Mo^V_2O_4(CH_3COOH))_{30}]^{42-}$,[171] the neutral, mixed-valence $\{Mo_{102}\}$ cluster $[((Mo)Mo_5O_{21}(H_2O)_4(CH_3COO))_{12}(MoO(H_2O))_{30}]$[172] and the mixed-metal analogue of this cluster $\{Mo_{72}Fe_{30}\}$, i.e. $[((Mo)Mo_5O_{21}(H_2O)_6)_{12}(Fe^{III}(OH_2)_2)_{30}]$[173] (see Figure 20). These cluster species are formed in aqueous solution, at the appropriate pH value, through the self-assembly of the pentagonal $\{(Mo)Mo_5\}$ units with smaller linking groups which interconnect these pentagonal building-blocks *via* corner-sharing interactions. For example these linking groups in the $\{Mo_{132}\}$ and $\{Mo_{72}Fe_{30}\}$ clusters are either dinuclear, i.e. $[Mo^V_2O_4(CH_3COO)]^+$, or mono-nuclear linkers, i.e. $[Fe^{III}(OH_2)_2]^{3+}$, respectively. Therefore, the structures of both of these clusters can be described using the analogy: (pentagon)$_{12}$(linker)$_{30}$ and are illustrated in Figure 20.[168]
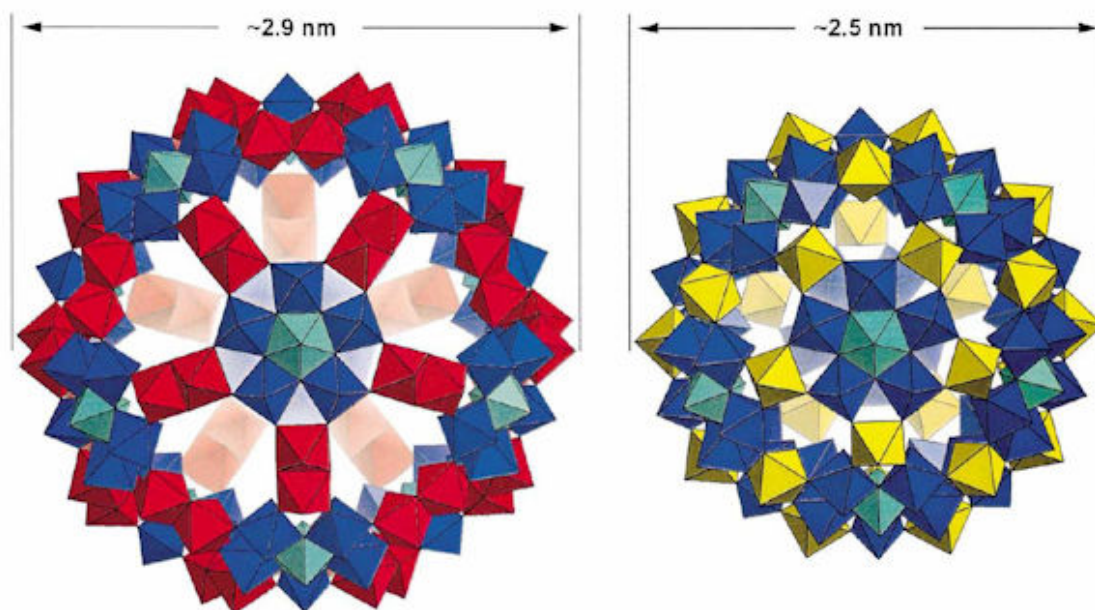
Figure 20: Left: Polyhedral representation of the $\{Mo_{132}\}$ cluster. The pentagonal $\{(Mo)Mo_5\}$ building-block units are shown in blue, with the central pentagonal $\{MoO_7\}$ bipyramid highlighted in light blue. The dinuclear $[Mo^V_2O_4(CH_3COO)]^+$ linkers are shown in red and coordinate through corner-sharing interactions to adjacent $\{(Mo)Mo_5\}$ building-blocks.[168, 171] Right: Polyhedral representation of the $\{Mo_{72}Fe_{30}\}$ cluster. The pentagonal $\{(Mo)Mo_5\}$ building-block units are shown in blue, with the central pentagonal $\{MoO_7\}$ bipyramid highlighted in light blue. The mononuclear $[Fe^{III}(OH_2)_2]^{3+}$ linkers are shown in yellow and coordinate through corner-sharing interactions to adjacent $\{(Mo)Mo_5\}$ building-blocks. The smaller size of these linking groups explains the smaller diameter of the cluster as a whole when compared with the $\{Mo_{132}\}$ cluster. This is illustrated by the dimensions shown above the clusters.[168, 173]

Keplerate clusters of this type are of great interest in the field of polyoxometalate chemistry not only due to properties such as their interesting electrochemistry and their capacity to be linked into extended network structures,[16, 174] but also because their size and therefore, their accessible 'pore' and internal cavity size, can be altered through the choice of linking group (as shown in Figure 20) so allowing the controlled encapsulation of molecules of different sizes.[175-178] Additionally they can be constructed to afford interesting magnetic properties following incorporation of paramagnetic centres, as seen in the $\{Mo_{72}Fe_{30}\}$ cluster;[173] and it has also been reported that, in the presence of surfactants, composites can be produced which are soluble in organic solvents and allow the production of monolayers and Langmuir-Blodgett films.[179]

1.6   Mass spectral studies of polyoxometalates

The use of mass spectrometry in the study of polyoxometalate chemistry has grown steadily over the last two decades. Indeed polyoxometalate compounds are, in some ways, ideal candidates for mass spectral investigations since they have complex isotopic envelopes resulting from the high number of stable isotopes, e.g. tungsten (^{180}W, 0.1%; ^{182}W, 26.5%; ^{183}W, 14.3%; ^{184}W, 30.6%; ^{186}W, 28.4%) and molybdenum (^{92}Mo, 14.8%; ^{94}Mo, 9.3%; ^{95}Mo, 15.9%; ^{96}Mo, 16.7%; ^{97}Mo, 9.6%; ^{98}Mo, 24.1%; ^{100}Mo, 9.6%), and are intrinsically charged.

Initial work using this analytical technique focused on the utilization of the fast atom bombardment (FAB) ionization method. However, although this ionization technique allows accumulation of useful information on the molecular mass and elemental composition of POMs, it also leads to extensive ionization and fragmentation, therefore is not as useful in characterizing the growth processes which control the formation of extended POM frameworks in the solution state.[180]

For these reasons, the 'soft' ionization technique electrospray mass spectrometry (ESI-MS), has increasingly been used as the ionization method of choice in the mass spectral analysis of polyoxoanion solutions within recent years.[180-185] More recently still has been the introduction of an adaptation of this electrospray source, in the form of cryospray (coldspray) ionization (CSI),[186-188] which operates at much lower temperatures than the related electrospray technique (see section 1.6.2). The current application of both of these mass spectral techniques in the area of polyoxometalate research, and their potential future applications within this area of chemistry, will be discussed below.

1.6.1   Electrospray mass spectrometry of polyoxometalates

As explained above, the use of electrospray mass spectrometry (ESI-MS) in the analysis of polyoxoanion solutions has expanded rapidly over the past decade. This ionization technique has been increasingly favoured in this research area because the 'soft' nature of

ESI allows the transfer of even large inorganic POM clusters from solution to the gas phase.[180, 189]

Until very recently the traditional application of the ESI-MS technique in POM chemistry has generally involved the analysis of pre-formed POM compounds dissolved in various solvent systems,[180, 190-192] or investigations into in-source aggregations of POM fragments promoted through the use of high cone voltages.[182, 183, 193] Such studies have been carried out using purely organic solvent systems, e.g. acetonitrile, acetone; mixed aqueous organic systems, e.g. methanol:water (50:50), acetonitrile:water (50:50); and purely aqueous systems. POM compounds characterized to date using these methods have included various species of polyoxovanadates,[193, 194] polyoxoniobates,[195] polyoxotantalates,[195] polyoxochromates,[184] polyoxomolybdates,[182] polyoxotungstates,[180, 183, 191, 196] and polyoxorhenates.[197]

The first group to undertake such studies was that of Howarth et al who investigated aqueous solutions of isopolytungstates, peroxotungstates, and heteropolymolybdates, detecting the $[W_6O_{19}]^{2-}$ and $[W_2O_7]^{2-}$ species in aqueous solution for the first time.[181] Mixed-metal heteropolyanions were also investigated and the $[H_xPW_nMo_{12-n}O_{40}]^{(3-x)-}$ species, where n = 0 to 12, were reported. Indeed this piece of work represents one of only a handful of studies that have applied ESI-MS to directly observe a reacting POM solution.[185, 196] In this case ESI-MS was used to monitor the metal interchange between phopshododecatungstates and molybdate anions over time. Through this work Howarth et al also showed that the ESI-MS-determined concentration of sensitive species (i.e. sensitive to changes in pH or the presence of other species) may differ from that determined in bulk measurements. This is due to the interference in the equilibrium process by the drying agent (e.g. nitrogen gas) in ESI-MS as the desolvation rapidly affects the pH and the concentrations of the solutes in the formation of the analytes.

Colton and Traeger[198] investigated heteropolyoxomolybdates compounds dissolved in acetonitrile and successfully identified intact anionic species e.g. $[S_2Mo_{18}O_{62}]^{2-}$. Le Quan Tuoi and Muller[199] studied mixed metal polyoxomolybates and polyoxotunstates in mixed solvent systems such as methanol:water and acetonitrile:water, and identified mono-, di- and tri- anionic species of $[H_3PMo_{12}O_{40}]$, $[H_4PMo_{11}VO_{40}]$, $[H_3PW_{12}O_{40}]$ and $[H_4SiW_{12}O_{40}]$. The group Lau and Siu et al carried out similar investigations of mixed

metal POM systems before extending their research to various tetrabutylammonium salts of the isopolyoxomolybdates and tungstates in either acetone or mixed methanol:water solvent systems.[200]   Results from this work included detection of the parent anions $[Mo_2O_7]^{2-}$, $[Mo_6O_{19}]^{2-}$ and $[Mo_8O_{26}]^{4-}$, as well as the anionic fragments: $[HMoO_4]^-$ and $[Mo^VO_3]^-$ from fragmentation of the parent $[Mo_2O_7]^{2-}$ ion; and $[Mo_2O_7]^{2-}$, $[Mo_3O_{10}]^{2-}$, $[Mo_4O_{13}]^{2-}$ and $[Mo_5O_{16}]^{2-}$ recorded in the fragmentation of the larger parent $[Mo_6O_{19}]^{2-}$ and $[Mo_8O_{26}]^{4-}$ anions.

Von Nagy-Felsobuki *et al* have investigated ammonium and various alkali metal isopolyoxomolybdates dissolved in aqueous solution by ESI-MS.[182]   Results from the negative ion mode experiments on the ammonium isopolyoxomolybdate systems revealed three main ion series: (i) monoprotonated mono-anionic series; (ii) unprotonated di-anionic series; (iii) unprotonated tetra-anionic series.   Within each of these series an aggregation process of additive polymerisation involving $\{MoO_3\}$ moiety additions was recognised as giving rise to the large range of aggregate POM units observed.   The monoprotonated monomolybdate anion $[HMoO_4]^-$ was the most abundant peak in almost all sample solutions tested.   The proposed condensation reaction (1) of this abundant species provides an explanation of the aggregating $\{MoO_3\}$ moieties.[182]

$$[HMoO_4]^- + \{H^+\} \rightleftharpoons \{MoO_3\} + H_2O \quad (1)$$
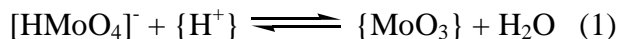
A reaction scheme for the aggregation of the polyoxomolybdate species may then be represented as the general condensation or protonation reaction given below[182] (2).

$$p H^+ + q[MoO_4]^{2-} \rightleftharpoons [H_{p-2r}Mo_qO_{4q-r}]^{(2q-p)-} + r H_2O \quad (2)$$
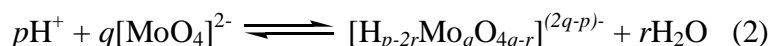
Von Nagy-Felsobuki *et al* investigated aqueous solutions of ammonium and various alkali metal isopolyoxotungstates[183] in a similar way with results showing the same general trends in ion series and aggregation via addition polymerisation processes as seen for the isopolyoxomolybdate systems.

An investigation of aqueous solutions of ammonium and various alkali metal polyoxochromates was also carried out by von Nagy-Felsobuki *et al*.[184] Results from the negative ion mode experiments on the ammonium dichromate systems revealed three main

ion series all of which were mono-anionic: (i) unprotonated series; (ii) monoprotonated series; (iii) triprotonated series. Of particular interest are the unprotonated and monoprotonated anion series which were found to contain mixed oxidation state species where the oxidation state of the chromium varied from +5 to +2, in conjunction with +6. The aggregation process within each mono-anionic series, similarly to the polyoxomolybdates and polyoxotungstates, was recognized as a polymerisation process involving $\{CrO_3\}$ moiety additions to give rise to the larger range of POM aggregate units observed. Condensation reactions of the form of reactions (1) and (2) above were used to explain the aggregation process. Also, again similarly to the polyoxomolybdates and polyoxotungstates, the monoprotonated mono-metalate anion, in this case $[HCrO_4]^-$ was found to be the most abundant peak in all sample solutions tested.

In addition to the detailed studies discussed above, the wide applicability of the ESI-MS technique to complex systems and mixtures has been demonstrated in catalytic studies where the real time transformation of the substrate can be observed, helping the proposal of a mechanistic pathway.[201, 202] Studies into the potential-dependent formation of unknown multinuclear and mixed-valence polyoxomolybdate complexes when using on-line electrochemical flow cell electrospray mass spectrometry (EC-ESI-MS) have also been presented.[203]

An interesting future application of ESI-MS in POM chemistry is concerned with the monitoring of reacting POM solutions in order to gain some insight into the rearrangement of POM species in solution. As stated previously, there have been very few studies of this kind carried out to date. Indeed, aside from the work carried out by Howarth *et al* in 1997,[181] the only other reports of ESI-MS being utilised in this way have been the study of the organosilane functionalization of a Dawson heteropolytungstate,[196] and a study of molybdate and tungstate clusters with arylated cations.[185]

1.6.2   Background to cryospray mass spectrometry

Due to the very recent development of the technique of cryospray (also known as coldspray) mass spectrometry it is useful, at this point, to provide some details regarding its operation and development, then the application of this technique to polyoxometalate systems will be discussed in section 1.6.3.

Initial investigations into cryospray mass spectrometry were first carried out by Shiea *et al*[186, 187] then further developed by Yamaguchi *et al*[188, 204] for the investigation of unstable organometallic complexes. The development of this technique was required to allow analysis of these unstable organometallic complexes as the presence of weak, non-covalent interactions, had previously precluded analysis by other ionization techniques such as FAB, MALDI, and ESI, due to dissociation of the species. The technique is, therefore, of interest for investigations of labile POM systems because previous ESI-MS studies of such systems have been limited by the use of low resolution detectors and the high temperatures utilized in the ESI process.

The cryospray source consists of, essentially, an electrospray source where the N_2 capillary and sprayer gases are maintained at very low temperatures (minimum -100 ºC). The use of low temperature gases promotes ionization of the target molecules, not by desolvation at high temperature as in the conventional ESI process, but by increasing the polarizability of the target molecules at low temperature (i.e. the result of higher dielectric constant at low temperature).[188] This allows the molecular ions of unstable species to be generated and transferred efficiently into the MS detector with minimal fragmentation effects.[188, 205] See Figure 21 for a schematic diagram of the construction of a cryospray source.
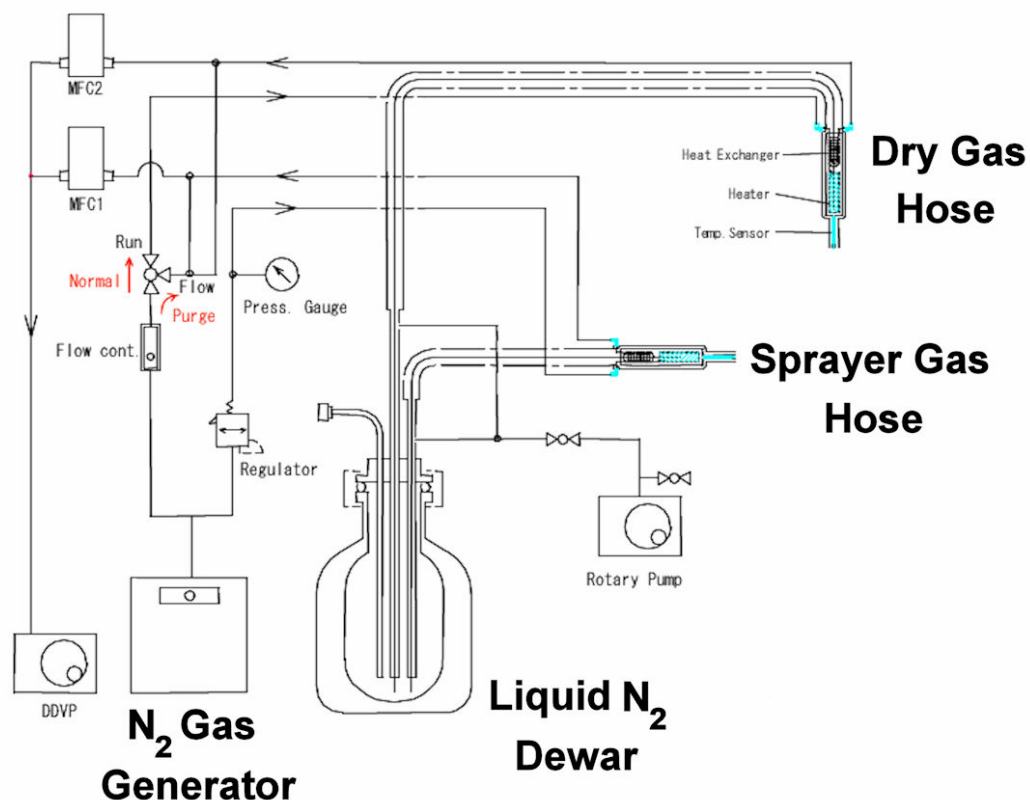
Figure 21: Schematic diagram showing the construction of the Bruker Daltonics Ltd. cryospray source. The dry gas hose and sprayer gas hose which supply low temperature N_2 into the source replace the drying gas and nebulizer gas in the conventional ESI source respectively.

An example of the power of CSI-MS to investigate weakly hydrogen-bonded organic aggregates is the observation of large, hydrogen-bonded, chain structures of amino acids in solution, e.g. L-serine, glycine, L-valine.[206] These observations are consistent with the single crystal X-ray crystallographic data for some of these amino acids in the solid state. In this study CSI-MS analysis also allowed observation of alkali metal ion mediated aggregation of L-proline into cyclic clusters composed of trimeric and tetrameric subunits.

The application of CSI-MS analysis to organometallic systems has not only allowed identification of organometallic complexes in solution,[188] but also clarification of molecular structures previously not possible using other analytical techniques such as NMR and single crystal X-ray diffraction.[188] For example, the study of adamantanoid-type Pt(II) complexes by CSI-MS allowed confirmation of the numbers and structures of encapsulated guest molecules;[188, 204] and the study of interlocking Pt(II) cage complexes composed of tris-(4-pyridyl)-1,3,5-triazine and 2,4,6-tris-(4-pyridin-4-ylmethyl-phenyl)-

[1,3,5]triazine ligands allowed clarification of the interlocking behaviour of the ligand structures in solution.[188] CSI-MS has also been utilised in conjunction with NMR studies to investigate the metal-induced self-assembly in nitromethane of a resorcin[4]arene derivative coordinating Pd or Pt. The coexistence of an interclipped supramolecular capsule and intraclipped bowl in dynamic equilibrium was identified using these techniques.[207]

1.6.3   Application of CSI-MS to polyoxometalate systems

Although ESI-MS studies have been extremely helpful in identifying the composition, extent of protonation, and the existence of other relatively stable POM species in solution, these studies can be limited when we have to deal with labile clusters with complex compositions, or those that adopt large and unstable motifs. Furthermore, given the extent of ionization and the instability of such structures at high temperatures, it is often difficult to establish the presence of some cluster architectures using ESI-MS. This is because the fragmentation of labile POM clusters occurs at the relatively high temperatures (150-200 °C) used to desolvate during the ESI process.

In contrast, the low temperatures accessible (minimum -100 °C) for use with a cryospray source minimize uncontrolled fragmentation and so allow efficient transfer of very high nuclearity, yet labile, ionic species into the detector with minimal interfering effects from the ionization and desolvation processes.[181] By employing this approach it is then possible to transfer many of the labile species present in solution into the mass spectrometer and so allow some correlation between the essentially gas phase measurements with solution and solid state studies.[181, 208]

Therefore, following the successful application of this low temperature mass spectrometry technique to unstable organometallic complexes, this technique is now being utilised in investigations of labile/unstable POM systems. It is hoped that the potential of this technique to transfer unstable, yet intact, POM species into the mass spectrometer, will allow the collection of information important for aiding our understanding of the self-

assembly mechanisms which take place in the synthesis and rearrangements of complex POM systems in solution.

The application of CSI-MS to such POM systems is in its infancy, however, an example of the power of this technique has recently been illustrated by Cronin *et al*.[158] In this work three different tris(alkoxo) derivatives of the $\{P_2V_3W_{15}\}$ Dawson lacuna, described in section 1.4.3.1, were synthesized. These clusters were of the form $[RC(CH_2O)_3P_2V_3W_{15}O_{59}]^{6-}$ where $R = NH_2$, NO_2 and CH_3. The cluster where $R = NH_2$ was successfully crystallized from acetonitrile as the tetrameric, H-bonded nanostructure $([H_2NC(CH_2O)_3P_2V_3W_{15}O_{59}]_4)^{24-}$ shown previously in Figure 18. However, the clusters where $R = NO_2$ or CH_3, could only be crystallized as monomeric cluster units, e.g. $[O_2NC(CH_2O)_3P_2V_3W_{15}O_{59}]^{6-}$.
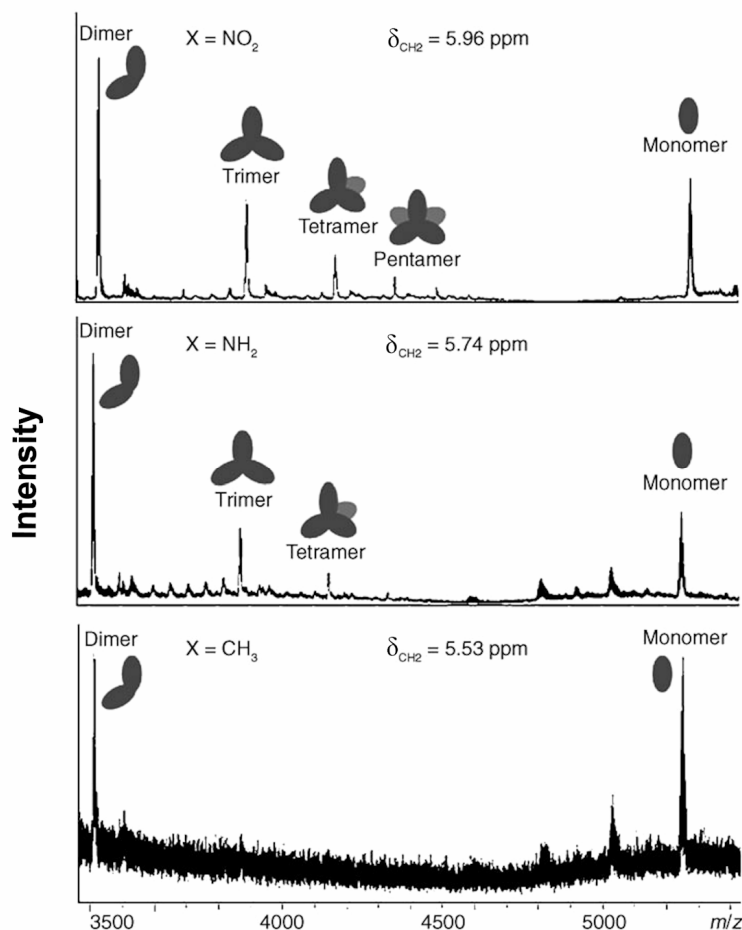
Figure 22: Comparison of the CSI-MS spectra and supramolecular assemblies of the synthesized $[RC(CH_2O)_3P_2V_3W_{15}O_{59}]^{6-}$ cluster compounds dissolved in acetonitrile solution and recorded at -40°C. Top: CSI-MS spectrum where $R = NO_2$. Centre: CSI-MS spectrum where $R = NH_2$. Bottom: CSI-MS spectrum where $R = CH_3$. All spectra shown are on the same m/z scale.

CSI-MS analyses were then carried out on acetonitrile solutions of each of these samples, with the N_2 sprayer and dry gas temperatures set at -40°C (see Figure 22). These analyses allowed the observation, in solution, of the H-bonded tetrameric assembly formed by the cluster where R = NH_2, i.e. $[TBA_{19}(H_2NC(CH_2O)_3P_2V_3W_{15}O_{59})_4]^{5-}$ at 4149.5 m/z, and showed the absence of any such macromolecular cluster aggregates when R = CH_3.

Of particular interest from these results, is the observation (at low temperatures only) of cluster aggregates formed by the cluster where R = NO_2, despite only monomers being isolated for this compound in the solid state. This has been explained by the electron withdrawing NO_2 group increasing the acidity, and therefore the H-bonding ability, of the surrounding CH_2 groups of the tris(alkoxo) cap, as shown by the NMR chemical shift values in Figure 22. The fact that these cluster aggregations are not observed in mass spectral analysis at higher temperatures, and cannot be isolated in the solid state, whereas the tetrameric assembly has been isolated when R = NH_2, is probably due to the greater strength of the N-H⋯O hydrogen-bonding interactions when R = NH_2, than the C-H⋯O interactions established when R = NO_2.

It is also important to note that the use of CSI-MS analysis in this study, not only allowed observation of these weakly bound cluster assemblies when R = NO_2 and NH_2, but also allowed some insight into their formation. For example, when R = NH_2, not only the previously crystallized tetrameric cluster aggregation was observed, but also the smaller building-block units of this structure. i.e. The monomeric unit $[TBA_5(H_2NC(CH_2O)_3P_2V_3W_{15}O_{59})]^-$ was identified at 5247.2 m/z, the dimer $[TBA_9(H_2NC(CH_2O)_3)P_2V_3W_{15}O_{59})_2]^{3-}$ at 3416.7 m/z, and the trimer $[TBA_{14}(H_2NC(CH_2O)_3P_2V_3W_{15}O_{59})_3]^{4-}$ at 3874.5 m/z.

In summary, through the work carried out in this study, CSI-MS has proved to be an extremely powerful analytical tool which is yet to be fully exploited in the field of polyoxometalate chemistry. It has been shown to aid, not only the identification of weakly H-bonded nanoassemblies of clusters in solution, but also to reveal information about the building-blocks, and self-assembly mechanisms governing the formation of these cluster aggregations. Indeed the potential of CSI-MS to aid the design and analysis of novel POM systems is currently being explored in further studies by Cronin *et al*.

2 Aims

In polyoxometalate chemistry the predominant method of synthesizing new architectures involves the use of the 'one-pot' synthetic strategy, where cluster building-blocks self-assemble in solution to form larger, stable cluster aggregates. However, elucidating the key species involved in the self-assembly processes, and so the formation mechanisms, of complex polyoxometalate structures formed in this way, continues to present a huge challenge to the analytical chemist. The application of mass spectrometry techniques to this problem is currently in its infancy, with only a handful of ESI-MS studies having been carried out to directly observe reacting POM solutions.[181, 185, 196] Therefore, in this study cryospray (CSI-) and electrospray mass spectrometry (ESI-MS) techniques will be utilised to investigate the 'in-solution' formation of complex polyoxomolybdate systems from their reaction solutions, and the application of these techniques to monitor the progress of such reactions in real-time will be evaluated.

The second part of this thesis will investigate the incorporation of high oxidation state heteroanion templates into polyoxometalate structures. This research area has been of interest for many years as chemists have strived to synthesize compounds with, for example, improved catalytic activity, or electron-transfer properties. To this end, Cronin *et al* have recently investigated the incorporation of the high oxidation state heteroanion templates $\{I^{VII}O_6\}$ and $\{Te^{VI}O_6\}$ into tungsten-based polyoxometalate clusters, leading to the successful isolation of the periodate- and tellurate-centred Dawson clusters $[H_3W_{18}O_{56}(I^{VII}O_6)]^{6-}$[148] and $[H_3W_{18}O_{56}(Te^{VI}O_6)]^{7-}$.[149] In this current study, the production of the molybdenum analogues of these clusters, and of other new, molybdenum-based polyoxometalate architectures incorporating these high oxidation state templates, will be investigated.

In the third section, the synthesis of new polyoxometalate compounds incorporating large aromatic cations will be explored, in order to develop compounds with interesting architectures and emergent photoactivity. In recent times, research into the introduction into polyoxometalate systems of organic counter-cations with interesting electronic properties or photoactivity, has been of increasing interest. This research has been driven

by the desire to produce new polyoxometalate materials which possess, not only interesting architectures, but which also show emergent properties, i.e. properties not associated with either the lone POM or the organic component of the system. In previous work Cronin *et al* have developed a family of phenanthridinium-based molecules which can vary greatly in structure, size and charge as a feature of the substituent R groups used in these molecules.[209, 210] These Dihydro-Imidazo-Phenanthridinium (DIP) and Imidazo-Phenanthridinium (IP) molecules also possess highly aromatic, electron-rich cores which have led to the observation of some interesting photochemical properties in earlier studies.[211] Therefore, in this current work the incorporation into polyoxometalate systems of DIP and IP cations, of varying size, geometry and charge, will be carried out and the synthesized compounds fully characterized and investigated for emergent photoactivity.

3   Results and Discussion

3.1   Examining the 'in-solution' self-assembly of polyoxometalate systems using mass spectrometry

One of the most interesting aspects of POM chemistry lies with the fact that the clusters can be viewed as transferable building-blocks or synthons.[20] As such, the controlled assembly of polyoxometalate-based building-blocks defines a crucial challenge to engineer these fragments so they can assemble into novel architectures with functionality, such as increased catalytic activity, or photoactivity.[12]   However, despite the increasingly intensive research in this area, understanding of the complex formation mechanisms and self-assembly processes which govern POM structure formation remains limited.[16, 20, 36] In practice, this lack of understanding leads to experimentation where manipulation of reaction parameters in the commonly used 'one-pot' POM syntheses often leads to the formation of new POM structures, all be it *via* a somewhat serendipitous approach.[17, 212]

Although the underlying speciation process behind the formation of low nuclearity molybdates and tungstates is well understood,[17, 20] the process by which larger or polymeric structures is formed is not clear due to the large combinatorial library of cluster types / repeat units potentially available as the number of building-blocks increase.[20] Thus, there is a clear need to develop approaches to bridge the gap[208, 213] between solid state and solution studies so that the key features, of the self-assembly mechanisms of POM cluster formation, can be revealed.

In order to address this challenge we have utilised the techniques of cryospray (CSI-) and electrospray mass spectrometry (ESI-MS) with a high resolution time-of-flight (TOF) dectector, to examine in detail the species present within reaction solutions from which polyoxometalate compounds are crystallized. Additionally we have further developed this approach to allow real-time monitoring of the intensity changes of the detected species, and therefore, their concentrations, over the course of the reaction.

This is a new approach to the use of mass spectrometry when studying the solution state species involved in the self-assembly of POMs, with the general approach adopted to date,

involving the dissolution of pre-formed crystalline POM samples into a suitable solvent[193, 194, 208, 214] (as discussed previously in the Introduction, section 1.6.1). Indeed as yet, the only experiments carried out using ESI-MS to directly observe a reacting POM solution have been the study of the organosilane functionalization of a Dawson heteropolytungstate cluster,[196] the study of metal interchange between phosphododecatungstate and phosphododecamolybdate anions,[181] and a study of molybdate and tungstate clusters with arylated cations.[185]

Therefore, the development of this new approach to the utilisation of the powerful analytical technique of mass spectrometry in the field of polyoxometalate research, opens the door to further exploration and expansion of our understanding of the building-block principles which govern the bottom-up processes in solution and will lead us to future methods for control of these building processes.

3.2 Investigations into the formation of a silver-linked polyoxometalate architecture using mass spectrometry

In order to stabilize particular POM building-blocks in solution, and so allow mechanistic insight into the formation of different POM architectures, Cronin *et al* have previously developed an approach to POM synthesis which uses bulky organic cations to 'direct' the structure growth.[145, 215, 216] This has been illustrated in previous work in which the use of protonated hexamethylenetetramine (HMTAH$^+$) as counter ions, enabled stabilization and isolation of the highly charged polyoxomolybdate anion, $[H_2Mo^V_4Mo^{VI}_{12}O_{52}]^{10-}$,[215, 216] followed by the isolation of a family of sulfite-based Dawson-type mixed-valence polyoxomolybdates $[Mo_{18}O_{54}(SO_3)_2]^{n-}$, using the same synthetic approach.[145]

In particular, this 'encapsulating' organic cation method was utilized to investigate different chain length alkylammonium salts of the well-known molybdenum Lindqvist, $[Mo_6O_{19}]^{2-}$, anion ({Mo$_6$}) in reactions with electrophilic silver(I) ions.[81, 82] This work produced a family of Ag-substituted, polymeric POM architectures consisting of β-octamolybdate, β-$[Mo^{VI}_8O_{26}]^4$, ({Mo$_8$}) building-blocks linked through coordination to electrophilic silver(I) ions (see Figure 23).[80-82]

$[Mo_6O_{19}]^{2-}$

$+ Ag^I$

$(n\text{-}Bu_4N)_{2n}[Ag_2Mo_8O_{26}]_n$

$(n\text{-}Bu_4N)_{2n}[Ag_2Mo_8O_{26}(CH_3CN)_2]_n$

$[Ag_2Mo_8O_{26}]^{2-}$

$((HDMF)_n[Ag_3(Mo_8O_{26})(DMF)_4]_n)$

$((n\text{-}Bu_4N)_{2n}[Ag_2Mo_8O_{26}(DMSO)_2]_n)$
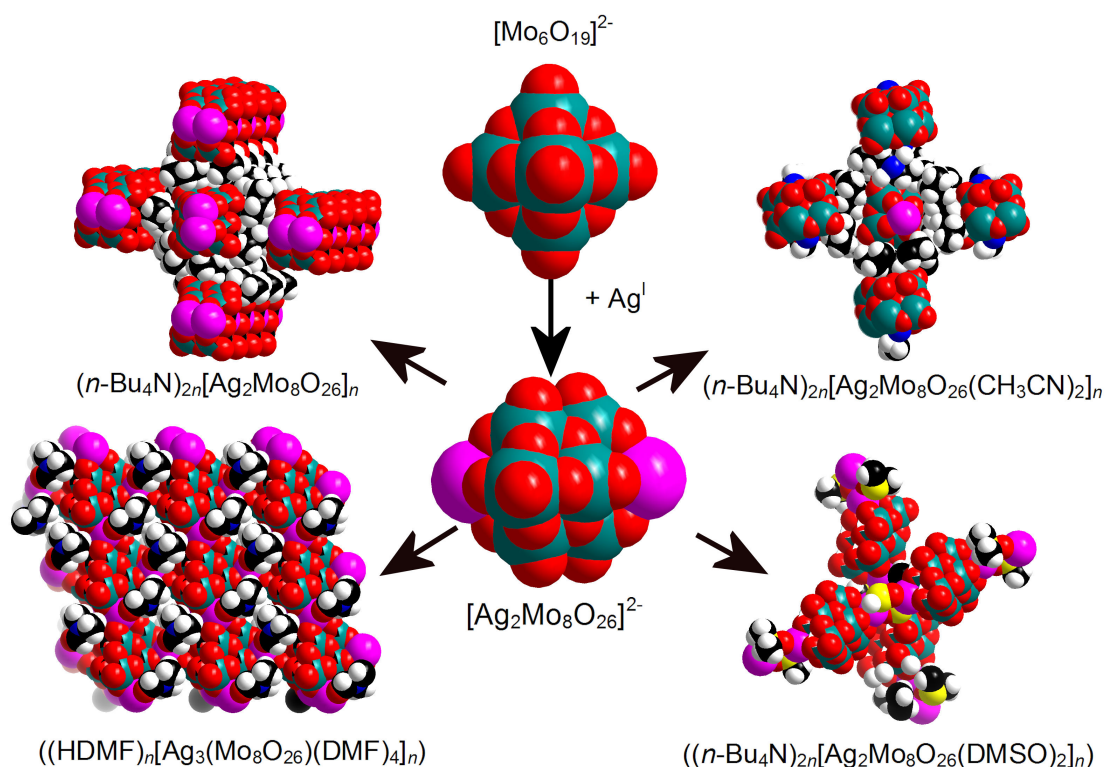
Figure 23: Scheme showing the transformation of the Lindqvist anion, $[Mo_6O_{19}]^{2-}$, into the $[Ag_2Mo_8O_{26}]^{2-}$ building-block (centre) which subsequently forms a variety of POM cluster architectures in the solid state.[17,18] Colour scheme: Mo, teal; Ag, pink; O, red; C, black; H, white; S, yellow.

Therefore, due to the interesting rearrangement of the Lindqvist anion into the silver-linked octamolybdate synthons, which takes place in this POM system and allows the isolation of this family of architectures, it was decided to investigate the formation of this particular reaction system in more detail. To this end, in order to follow the self-assembly processes involved in this polyoxometalate rearrangement, cryospray mass spectrometry (CSI-MS), with a high resolution time-of-flight detector (TOF), and UV/vis spectroscopy were utilised to investigate these cluster rearrangements in the reaction solution.

3.2.1   Utilisation of cryospray mass spectrometry and UV/vis spectroscopy to investigate 'in-solution' polyoxometalate rearrangements

The application of CSI-MS with a high resolution TOF detector to study labile POM systems has recently been under investigation by Cronin *et al.*[208] This is because ESI-MS

studies of such systems have been limited by the use of low resolution detectors and the high desolvation temperatures utilized in the ESI process. As a result, the majority of ionic species observed when studying labile POM structures with this ionisation source have been highly ionised, multiply-charged species.[180, 182, 183, 193, 194] This is indicative that fragmentation of labile POM clusters can occur at the relatively high temperatures (150-200 °C) used to desolvate during the ESI process.

In contrast, the low temperatures accessible (minimum -100 °C) for use with a cryospray source minimize uncontrolled fragmentation and so allow efficient transfer of very high nuclearity, yet labile, ionic species into the detector with minimal interfering effects from the ionisation and desolvation processes.[181] By employing this approach it is then possible to transmit many of the labile species present in solution into the mass spectrometer and so allow a high degree of correlation between the essentially gas phase measurements with solution and solid state studies.[181, 208] However, one must bear in mind when using the technique of CSI-MS, that it is also possible that the CSI-MS determined concentration of sensitive species (i.e. sensitive to changes in pH or the presence of other species) can still differ to some extent from that determined in bulk measurements. This effect was investigated by Howarth *et al.* during ESI-MS studies,[181] and is due to the interference in the equilibrium process by the drying agent (e.g. nitrogen gas) as the desolvation rapidly affects the pH and the concentrations of the solutes in the formation of the analytes.

For this current work, the use of CSI-MS in conjunction with UV/vis spectroscopy was selected, not only to identify species present in the reaction mixture of the chosen POM reaction system, but also to allow real-time monitoring of the Lindqvist rearrangement into the silver-linked octamolybdate species. The combined application of these analytical techniques to monitor real-time, 'in-solution' rearrangements in a POM reactant solution is unprecedented, with previous studies focussing on the isolated use of UV/vis spectroscopic data[217] or electron spin resonance[218] to study the formation of heteropolyoxomolybdates.

3.2.2   The silver-linked polyoxomolybdate system under investigation

The rearrangement of the molybdenum Lindqvist, {Mo_6}, to form the β-octamolybdate anion, {Mo_8}, (as shown in Scheme 1) has previously only been observed indirectly *via* the crystallization of silver-linked β-octamolybdate species such as ((n-$C_4H_9)_4N)_{2n}[Ag_2Mo_8O_{26}]_n$ (**1**) (also referred to as $TBA_{2n}[Ag_2Mo_8O_{26}]_n$).[80, 81]

$$4[Mo_6O_{19}]^{2-} + 2H_2O \rightarrow 3[Mo_8O_{26}]^{4-} + 4H^+$$
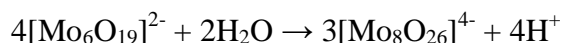
Scheme 1:   A formal reaction scheme showing the rearrangement of the molybdenum Lindqvist anion, $[Mo_6O_{19}]^{2-}$, into the octamolybdate anion, $[Mo_8O_{26}]^{4-}$.

This compound is produced by the reaction of ((n-$C_4H_9)_4N)_2[Mo_6O_{19}]$ (also referred to as $TBA_2[Mo_6O_{19}]$) with silver(I) fluoride in a methanol and acetonitrile mixture. The flexible tetrabutylammonium cations (TBA) wrap around and encapsulate the linear chain of linked $[Ag^I Mo^{VI}_8 O_{26} Ag^I]^{2-}$ units (see Figure 24). X-ray crystallographic studies of **1** have shown that these encapsulating cations are packed into a network of co-linear, organic 'tunnels' along which the polymeric chains of {Ag_2Mo_8}$_n$ anions propagate.[81] The silver(I) centres of these anions form virtually planar O_2AgO_2 bridging groups which result in close Ag–Ag contacts (2.85 Å) that are shorter than metallic Ag···Ag distances (2.89 Å), suggesting significant argentophilic silver(I)–silver(I) interactions.[219]   The presence of these argentophilic interactions was further supported by density functional theory (DFT) calculations which found a significant bonding interaction between the silver centres.[81]
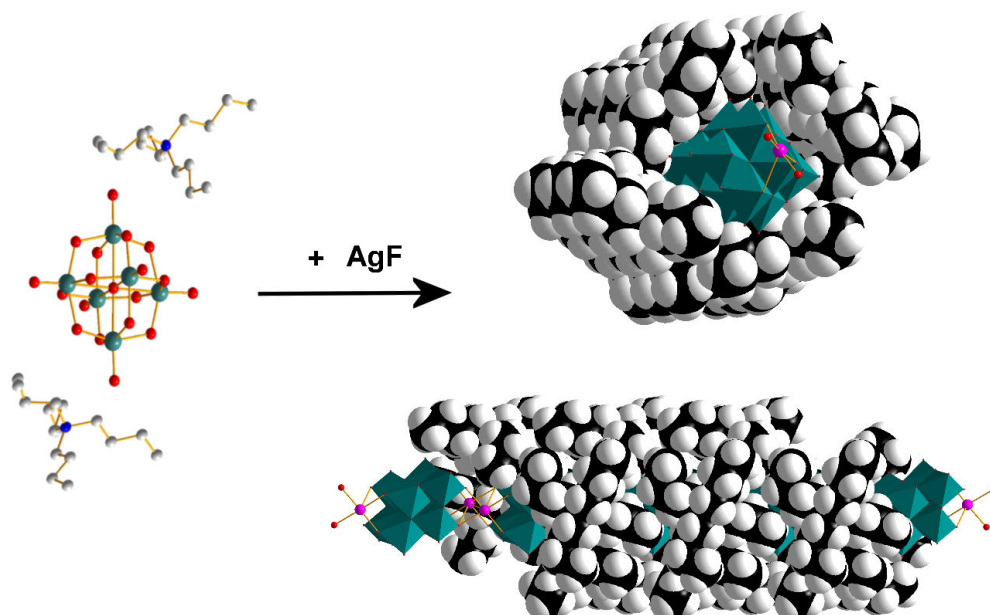
Figure 24: A schematic showing the formation of the polymeric POM architecture $TBA_{2n}[Ag_2Mo_8O_{26}]_n$ (**1**) on the reaction of $TBA_2[Mo_6O_{19}]$ with AgF. Left: $TBA_2[Mo_6O_{19}]$ unit is shown in ball and stick representation. Colour scheme: Mo, teal; O, red; C, light grey; N, blue. Right: Two structural representations of **1** are shown with the silver-linked β-octamolybdate chain (ball and stick, and teal polyhedra) wrapped in the 'encapsulating' TBA cations (space-filling representation). A side view along the $\{Ag_2Mo_8\}_\infty$ chain (bottom right) and end-on view of this chain (top right) is shown. Colour scheme: Mo, teal polyhedra; Ag, pink; O, red; C, black; H, white.

Through this work[81] the nature of the $\{Ag_2\}$ linker groups and the Ag coordination environments, were found to be strongly dependent on the reaction conditions, and it can be suggested that the precursors in the reaction solution were not individual $\{Ag_2\}$ and $\{Mo_8\}$ groups but, most likely, the $(Ag\{Mo_8\}Ag)$-type building-blocks, see Figure 25. Furthermore, the mode of assembly of these synthon units in the solid state is critically dependent on the reaction conditions. This has been illustrated by the use of different chain length organic cations and solvent systems which demonstrated a strategy to control the molecular growth processes from $(Ag\{Mo_8\}Ag)^{2-}$ building-blocks to linear molecular chains and grids.[82]
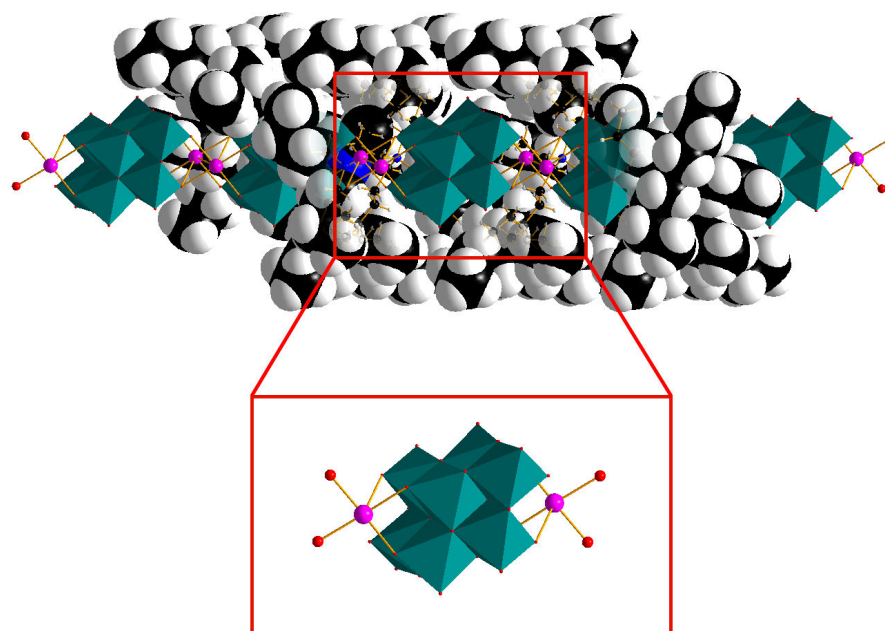
Figure 25: Structural representation of the silver-linked β-octamolybdate chain (ball and stick, and teal polyhedra) wrapped in 'encapsulating' TBA cations (space-filling representation) which makes up the structure of $TBA_{2n}[Ag_2Mo_8O_{26}]_n$ (**1**). The organic cations are partially removed to reveal the encapsulated chain structure (top). The $(Ag\{Mo_8\}Ag)$ synthon unit, the building-block of this chain, is highlighted below. Colour scheme: Mo, teal polyhedra; Ag, pink; O, red; N, blue; C, black; H, white

In this current work the 'in-solution' inter-conversion of Lindqvist into β-octamolybdate anions and subsequent self-assembly into the silver-linked POM structure $((n\text{-}C_4H_9)_4N)_{2n}(Ag_2Mo_8O_{26})_n$ (**1**)[81] has been investigated using CSI-MS and UV/vis spectroscopy. The use of CSI-MS in conjunction with UV/vis spectroscopy was selected, as explained previously, not only to identify the species present in the reaction mixture, but also to allow real-time monitoring of the Lindqvist rearrangement into the silver-linked octamolybdate species. Therefore, this study has examined the rearrangements occurring in the reaction solution from which compound **1** crystallizes, the kinetics of these self-assembly processes, and the effect of organic cation size on the kinetics of these processes.

3.2.2.1 CSI-MS investigations into the $((n\text{-}C_4H_9)_4N)_{2n}(Ag_2Mo_8O_{26})_n$ (**1**) reaction system

This investigation was carried out using CSI-MS analyses on the reaction solution of compound **1** and allowed access to directly observe the rearrangement of Lindqvist anions

into the (Ag{Mo$_8$}Ag) synthon units and the subsequent wrapping of the one-dimensional silver-octamolybdate synthons with organic cations. As discussed previously, this is a new approach to studying the solution state species involved in the self-assembly of POMs with the general approach adopted to date being dissolution of the pre-formed crystalline POM into a suitable solvent. [193, 194, 208, 214]

Thus far, ESI-MS studies on POM systems have been seen to generate only limited mono-anionic series and multiply-charged ion fragments.[182, 183, 191] In contrast, the power of CSI-MS in improving our analytical capabilities in investigating very large, labile POM frameworks is evident immediately on inspection of the following results. Only mono-anionic and di-anionic series are observed in these results, from approximately 285 m/z to as high as approximately 3800 m/z, indicating the efficient transfer of very high nuclearity, yet labile, ionic species into the detector with minimal interfering effects from the ionisation and desolvation processes.

The six mono-anionic series identified within these results are:

(i) $[Mo_mO_{3m}]^-$ where $m = 2, 3$ or 5

(ii) $[HMo_mO_{3m+1}]^-$ where $m = 2$ to 6

(iii) $[H_7Mo_mO_{3m+2}]^-$ where $m = 2$ to 6

(iv) $[H_7Mo_mO_{3m+3}]^-$ where $m = 2$ to 5

(v) $[H_9Mo_mO_{3m+4}]^-$ where $m = 2$ to 6

(vi) $[AgMo_mO_{3m+1}]^-$ where $m = 2$ to 4

From these identified anion series (see Figure 26) only series (ii) has been observed in previous ESI-MS studies on polyoxomolybdate systems[182] which underpins the advance in understanding that can be made with CSI-MS studies for detecting molecular building-blocks.
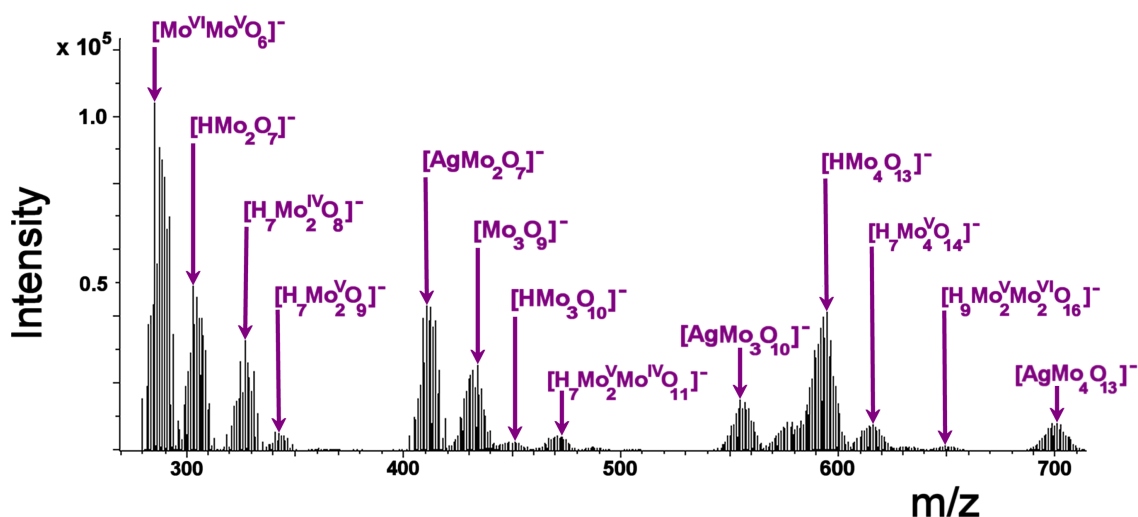
Figure 26: CSI-MS data collected of the reaction solution **1**. The six mono-anionic series identified within these results are highlighted. The steps towards the assembly of the {Ag(Mo$_8$)Ag} synthon units can be observed by examination of anion series (vi) which highlights the role of the Ag$^+$ in the rearrangement process of these clusters. Of particular note from this series are the peaks at 410.7 m/z and 700.5 m/z which are attributed to the species [AgMo$_2$O$_7$]$^-$ and [AgMo$_4$O$_{13}$]$^-$ respectively.

The silver-containing anion series (vi) is of special interest with regards to this POM reaction system. This is because the role of the Ag^I moiety in the assembly of the stable silver-linked octamolybdate species has been observed by mass spectral methods for the first time and is shown to be crucial for the formation of the larger cluster fragments. The detection of fragments of the (Ag{Mo$_8$}Ag) synthon units, especially [AgMo$_2$O$_7$]$^-$ (peak at 410.7 m/z) and [AgMo$_4$O$_{13}$]$^-$ (peak at 700.5 m/z) are particularly important to understanding the formation of compound **1** from this reaction system (see Figure 26). Detection of the [AgMo$_2$O$_7$]$^-$ fragment of the (Ag{Mo$_8$}Ag) synthon from the reaction solution supports the theory of rearrangement of the Lindqvist anion into [AgMo$_2$O$_7$]$^-$ building units, and so indicates that the [AgMo$_2$O$_7$]$^-$ fragment is the smallest stable unit of the silver-linked POM chain. Indeed the stable nature of this fragment of the (Ag{Mo$_8$}Ag) synthon unit allowed the isolation in the solid state of Ag$_2$Mo$_2$O$_7$ clusters by Gatehouse and Leverett in 1976.[220] Detection of the [AgMo$_4$O$_{13}$]$^-$ species (peak at 700.5 m/z), being half the (Ag{Mo$_8$}Ag) synthon unit, represents the next stepping stone in the final rearrangement to the stable silver-linked octamolybdate species. See Figure 27.
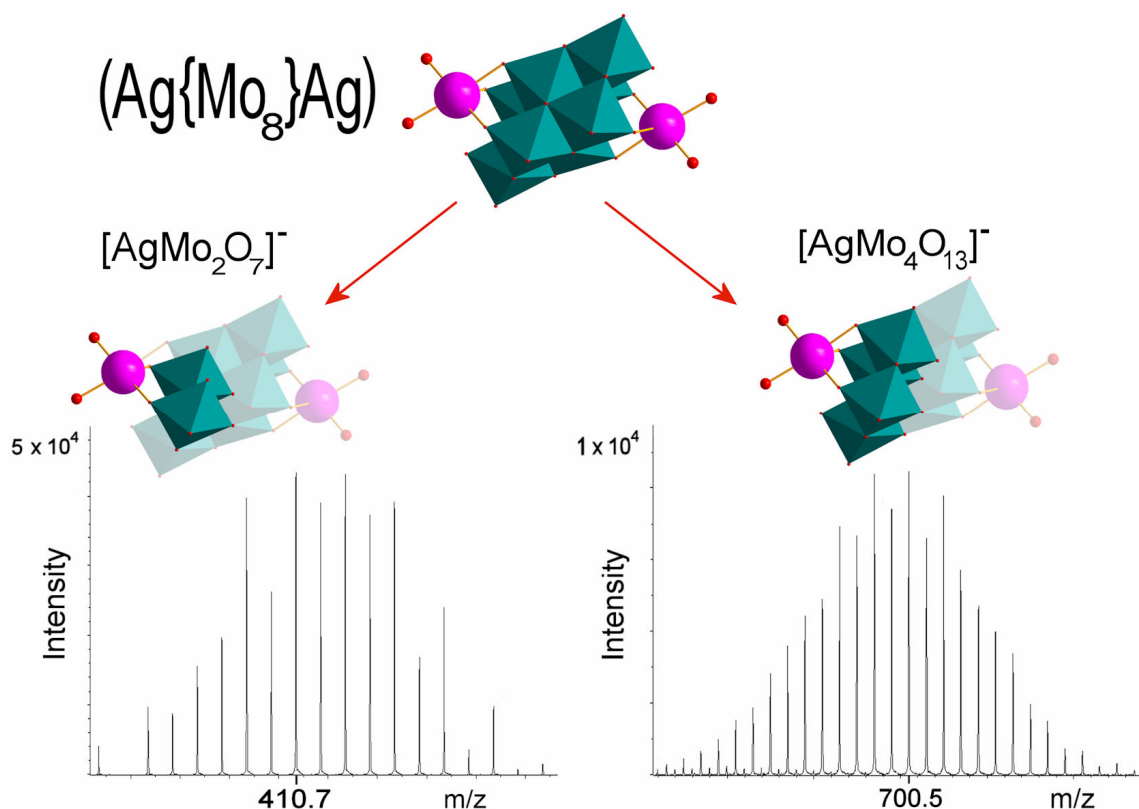
Figure 27: Representation of the $[AgMo_2O_7]^-$ and $[AgMo_4O_{13}]^-$ species identified within the CSI-MS analyses of a reaction solution of **1** (formal representations of structures based on crystallographic data).[81] Top: Representation of the $[AgMo_2O_7]^-$ and $[AgMo_4O_{13}]^-$ species as building-blocks of the $(Ag\{Mo_8\}Ag)$ synthon. Bottom: Mass spectra of the isotopic envelopes for their corresponding mass peaks at 410.7 m/z and 700.5 m/z respectively. Colour scheme: Mo, teal polyhedra; Ag, pink; O, red.

In the higher mass range of the CSI-MS analyses carried out, the structure directing effect of the organic cations, hypothesized by Cronin *et al* in previous work,[81, 82] is illustrated for the first time. Detection of the following species $[(AgMo_8O_{26})TBA_2]^-$ (peak at 1776.6 m/z), $[(Ag_2Mo_8O_{26})(Mo_4O_{13})TBA_3]^-$ (peak at 2718.3 m/z), and $[(Ag_2Mo_8O_{26})(Mo_8O_{26})TBA_5]^-$ (peak at 3796.5 m/z), each with an increasing organic cation contribution, shows the increasing metal nuclearity of the chain of compound **1** concomitant with the associated increase in organic cations present (see Figures 28 to 30). This observation can be interpreted as the start of the self-assembly aggregation process where 'monomeric' units assemble into larger fragments which eventually leads to the formation of crystals of compound **1** (see Figure 30). Also this analysis supports the previously proposed hypothesis[81] that the organic cations used in the synthesis do indeed play an important structural role in promoting the mode of POM structure growth in solution.
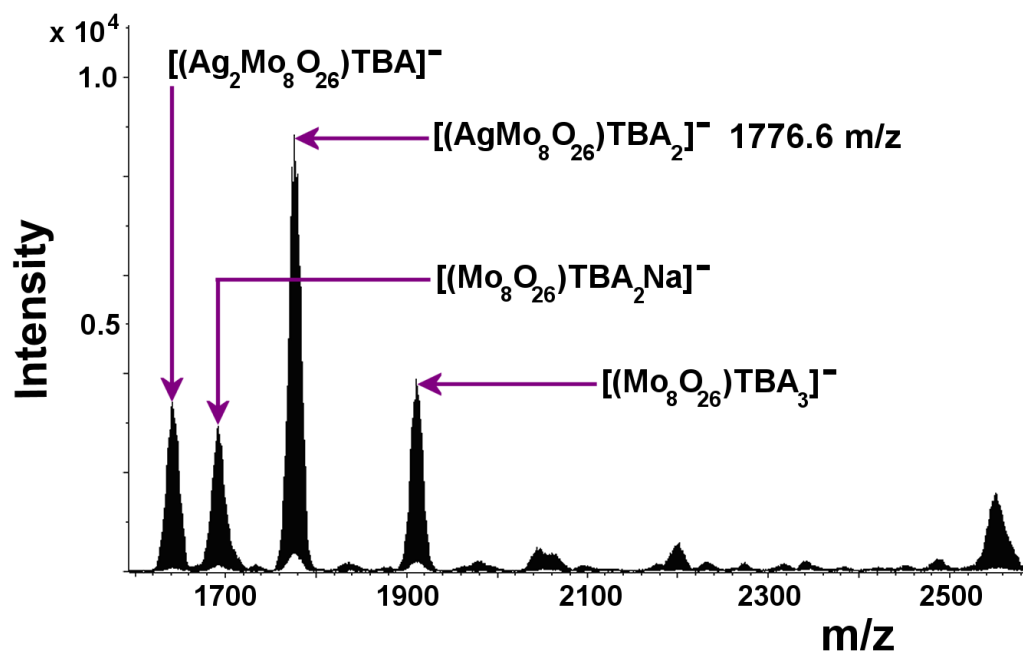
Figure 28: CSI-MS data collected of the reaction solution **1** showing the high nuclearity fragments observed in the 1500 – 2600 m/z range.
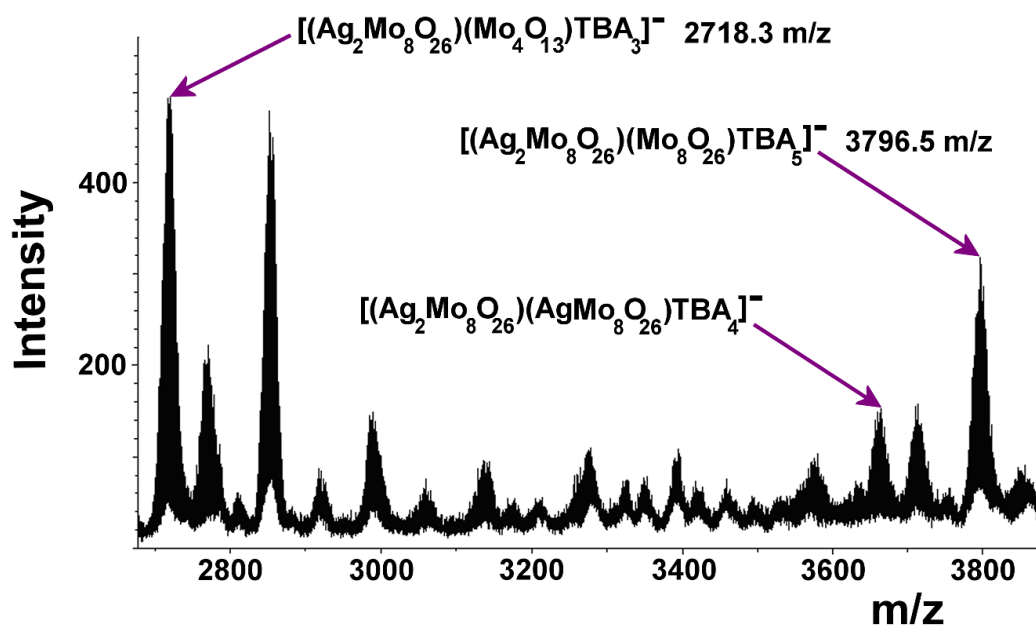
Figure 29: CSI-MS data collected of the reaction solution **1** over the 2500 – 6000 m/z range.

$[(AgMo_8O_{26})TBA_2]^-$

1776.6 m/z

$[(Ag_2Mo_8O_{26})(Mo_4O_{13})TBA_3]^-$

2718.3 m/z

$[(Ag_2Mo_8O_{26})(Mo_8O_{26})TBA_5]^-$

3796.5 m/z

Figure 30: Structural representation of the higher mass fragments (highlighted) identified within the CSI-MS analyses of a reaction solution of **1** (formal representations of structures based on crystallographic data).[81] This diagram illustrates the increasing metal nuclearity of the chain of compound **1** concomitant with the associated increase in organic cations present. Colour scheme: Mo, teal polyhedra; Ag, pink; O, red; C, grey; N, blue.

Another significant observation from these CSI-MS results is the identification of mixed oxidation state species in POM fragments from dimolybdate up to hexamolybdate fragments, where molybdenum is found to exist in oxidation states +4, +5 and +6. This is an important set of observations as although the single reduced molybdate species $[Mo^VO_3]^-$ and the corresponding single reduced tungstate species $[W^VO_6]^-$ have been observed previously,[182, 183] mixed oxidation state fragments, such as the dimolybdate fragment $[Mo^{VI}Mo^VO_6]^-$ (see Figure 31) have only been observed previously when formed under potential-dependent conditions during on-line electrochemical flow-cell ESI-MS (EC-ESI-MS) investigations.[184, 203, 221] The observation of such building units is interesting as similar building-blocks, such as the $\{Mo^V_2O_8\}$ unit,[163, 222, 223] have been seen to act as essential linker units in the formation of mixed-valence POM structures such as $(Me_3NH)_2(Et_4N)Na_4[Na(H_2O)_3H_{15}Mo^V_{36}Mo^{VI}_6O_{109}((OCH_2)_3CCH_2OH)_7]$[224] and $(NH_4)_{12}[Mo_{36}(NO)_4O_{108}(H_2O)_{16}]$.[163] However, in this context it is important to bear in mind that the observation of these reduced POM units could be due to the voltages (e.g. ion

transfer voltages and high collision energy voltage at low mass) used in the technique of mass spectrometry to investigate fragment ion species at low mass.
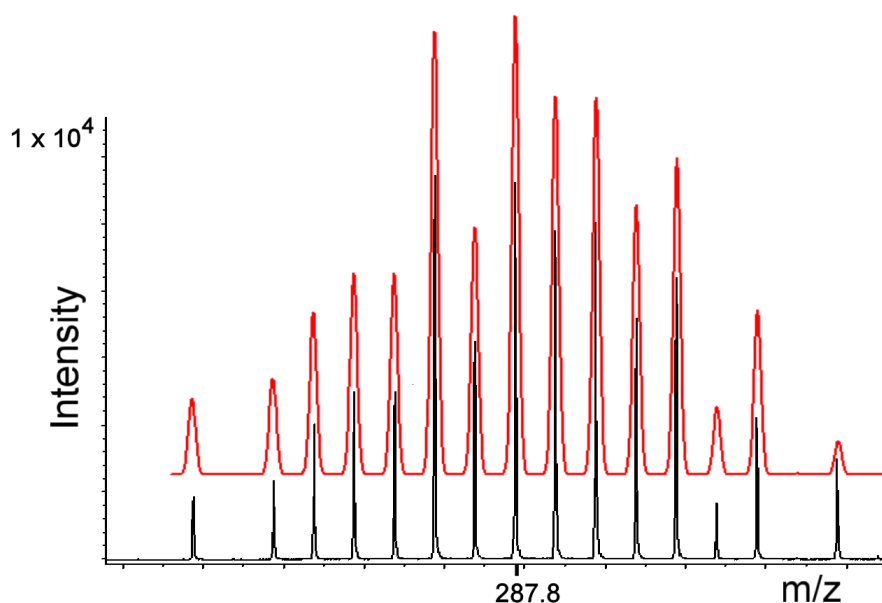
Figure 31: Comparison of the experimental (black spectrum) and simulated (superimposed red spectrum) isotopic envelope for the peak at 287.8 m/z recorded during CSI-MS analyses of a reaction solution of **1**. Through this comparison this peak can be clearly identified as the mixed oxidation state dimolybdate species $[Mo^{VI}Mo^{V}O_6]^-$. Unambiguous identification of small species such as this is accessible in this manner only when the isotopic patterns for the species are very distinct, as for the spectrum shown above.

The CSI-MS analyses described thus far were carried out on the reaction mixture of $TBA_2[Mo_6O_{19}]$ and silver(I) fluoride after stirring overnight, i.e. following the same experimental steps from the reported synthesis of **1**. However, these results then led to further investigations into how rapidly the inter-conversion from the Lindqvist anion into $(Ag\{Mo_8\}Ag)$ synthons actually takes place, and whether the length of organic counter cation used in the reaction system affects the rate of this rearrangement. These further investigations were prompted following the observation that the yellow colour of the $\{Mo_6\}$ solution disappears rapidly following addition of silver(I) fluoride to $((n\text{-}C_4H_9)_4N)_2[Mo_6O_{19}]$ solution, but persists for a much longer period of time when using a longer chain organic cation with the Lindqvist anion., e.g. $((n\text{-}C_7H_{15})_4N)_2[Mo_6O_{19}]$.

3.2.2.2   Combined use of UV/vis spectroscopy and CSI-MS to monitor the real-time
          rearrangements of the Lindqvist cluster in a reaction solution of ((n-
          C$_4$H$_9$)$_4$N)$_{2n}$(Ag$_2$Mo$_8$O$_{26}$)$_n$ (**1**)

In order to investigate the rate of the rearrangement process of Lindqvist anions into
(Ag{Mo$_8$}Ag) synthons, and allow comparison with real-time CSI-MS monitoring of the
reaction solution, UV/vis spectroscopic studies were used to monitor the decrease of the
Lindqvist anion absorption band at $\lambda = 355$ nm over time[37] in a reaction mixture of **1,**
stirred for only 5 min prior to reaction monitoring (see Reaction Mix **A** in Table 1, section
3.2.2.3).

The relationship between decreasing Lindqvist anion concentration as monitored *via*
UV/vis spectroscopy, and concomitant increase in {Mo$_8$} anion concentration, was
supported by monitoring Reaction Mix **A** over time using CSI-MS experiments, hence
providing a real-time profile of the species present in the reaction solution. During these
experiments the CSI-MS method parameters were kept constant throughout. Therefore,
although the lack of a suitable internal standard precludes the quantitative analysis of the
results, a qualitative relationship between the observed species can be elucidated by
monitoring peak intensities over time during the reaction.
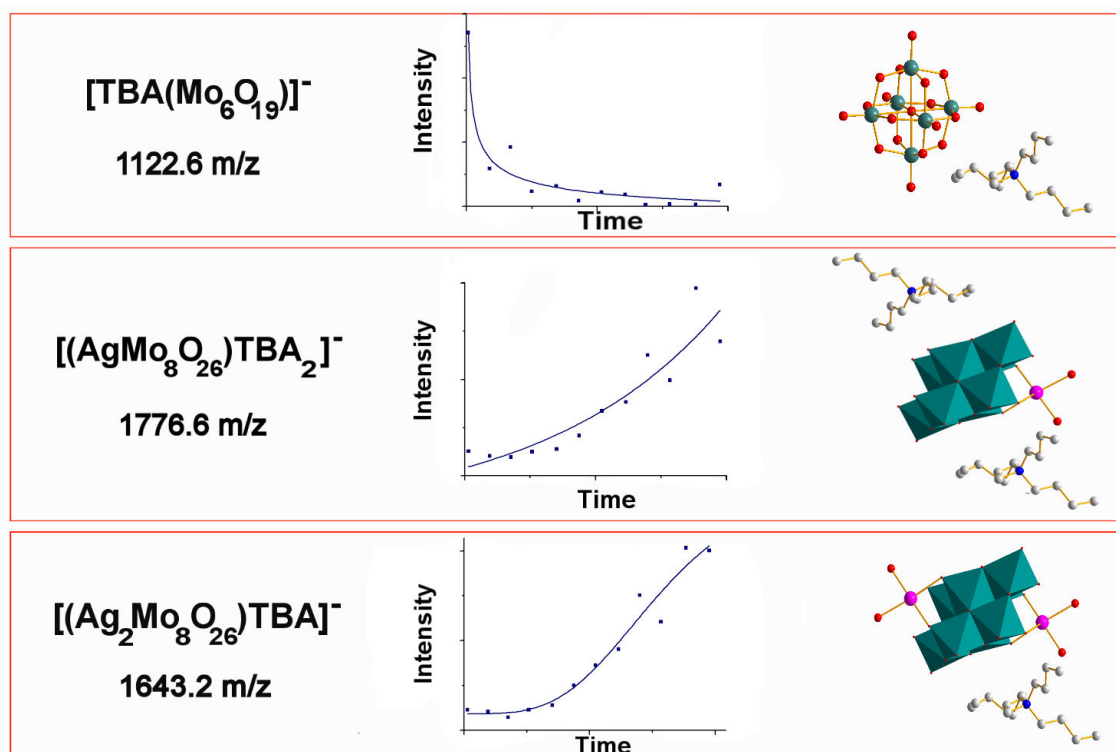
Figure 32: Graphs showing peak intensities plotted against the time of CSI-MS data acquisition during the reaction of $((n\text{-}C_4H_9)_4N)_2[Mo_6O_{19}]$ + AgF, i.e. Reaction Mix **A** (best fits shown). The peak identities and m/z values of the peaks studied are shown (left) along with formal representations of the predicted structures of these species (right). Top: $[TBA(Mo_6O_{19})]^-$ at 1122.6 m/z. Centre: $[(AgMo_8O_{26})TBA_2]^-$ at 1776.6 m/z. Bottom: $[(Ag_2Mo_8O_{26})TBA]^-$ at 1643.2 m/z. Colour scheme: Mo, teal polyhedra; Ag, pink; O, red; C, grey; N, blue.

From these results clear, general trends can be identified in the recorded peak intensities as monitored over the time of reaction for the species $[TBA(Mo_6O_{19})]^-$ (peak at 1122.6 m/z), $[(AgMo_8O_{26})TBA_2]^-$ (peak at 1776.6 m/z), and $[(Ag_2Mo_8O_{26})TBA]^-$ (peak at 1643.2 m/z), see Figure 32. It can be seen from these general trends that the peak intensity of the reagent $[TBA(Mo_6O_{19})]^-$, decreases as the peak intensities recorded for the product species $[(AgMo_8O_{26})TBA_2]^-$ and $[(Ag_2Mo_8O_{26})TBA]^-$ increase. Interestingly, it can also be observed from these CSI-MS results that the recorded peak intensity of species $[AgMo_4O_{13}]^-$ (peak at 700.5 m/z) over reaction time appears to remain almost constant throughout. This suggests that the formation and rearrangement of the $[AgMo_4O_{13}]^-$ species occurs at approximately the same rate.

3.2.2.3   UV/vis spectroscopy investigations into the effect of the length of organic counter
          cation on the rate of Lindqvist anion rearrangement

The effect of the length of organic counter cation used in the reaction system on the rate of Lindqvist to (Ag{Mo$_8$}Ag) synthon rearrangement was then investigated using UV/vis spectroscopic studies on Reaction Mix **A**-**D**, see Table 1. These studies were carried out in the same way as described previously in section 3.2.2.2, i.e. the decrease of the Lindqvist anion absorption band at $\lambda = 355$ nm in each reaction mixture was monitored over time,[37] with each reaction mix being stirred for only 5 min prior to reaction monitoring.

Reaction Mix **A**	$((n\text{-}C_4H_9)_4N)_2[Mo_6O_{19}]$
Reaction Mix **B**	$((n\text{-}C_5H_{11})_4N)_2[Mo_6O_{19}]$
Reaction Mix **C**	$((n\text{-}C_6H_{13})_4N)_2[Mo_6O_{19}]$
Reaction Mix **D**	$((n\text{-}C_7H_{15})_4N)_2[Mo_6O_{19}]$

Table 1:   Hexamolybdate reagents with different chain length alkylammonium cations used in reaction mixtures with AgF, each stirred for only 5 min prior to reaction monitoring.

Comparison of the 'pseudo' first order rate constants (see Experimental, Section 5.3.7 for further information), with respect to [{Mo$_6$}], calculated over the first 75 min of each reaction reveals the general trend that the rate of decrease in the concentration of Lindqvist anions, and as a result the inter-conversion of Lindqvist into β-octamolybdate anions, decreases as the carbon chain length of the alkylammonium cations increases, see Figure 33.[225]
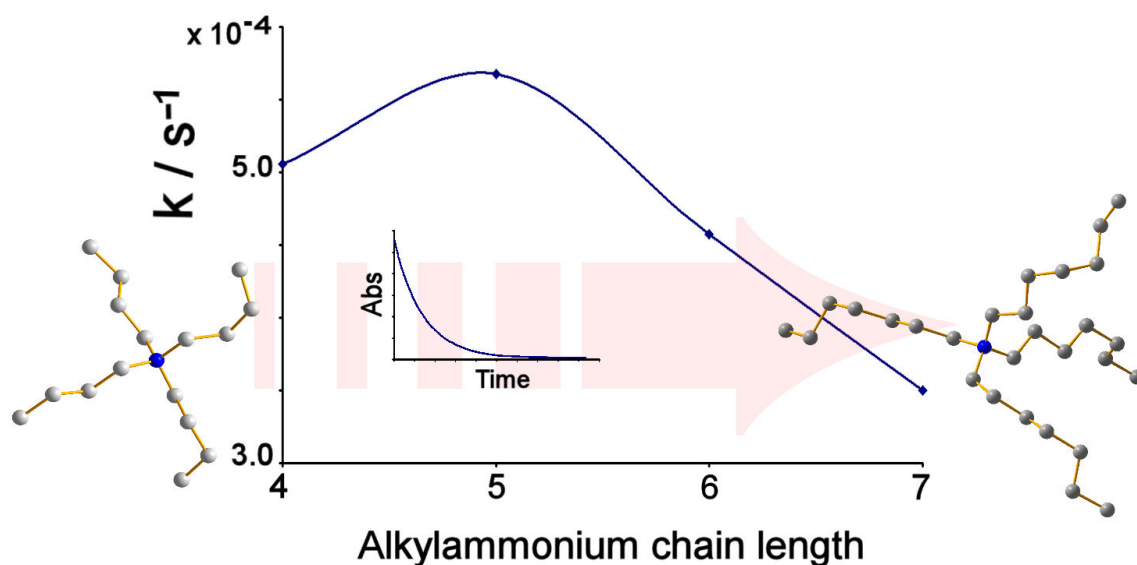
Figure 33: Graph showing the 'pseudo' first order rate constants, calculated using data from UV/vis spectroscopy studies of Reaction Mix **A**-**D**, plotted against the carbon chain length of the alkylammonium cation used. The black line is used as a guide for the eye. Inset: Decrease of the Lindqvist anion absorption band at $\lambda = 355$ nm over time in Reaction Mix **D**. Also shown are ball and stick representations of the tetrabutylammonium cation and the much more sterically hindering tetraheptylammonium cation. Colour scheme: C, grey; N, blue

There is a slight discrepancy in this general trend with the observed rate constant for the tetrapentylammonium cation calculated at approximately 0.6×10^{-4} s^{-1} higher than that for the tetrabutylammonium cation. This may be due to the tetrapentyl side chains representing the maximum cation steric bulk which can be accommodated by the $\{Mo_6\}$ to $\{Mo_8\}$ inter-conversion before the reaction rate is slowed significantly, as per the tetrahexyl- and tetraheptyl side chains.

A possible explanation for the lower rates of inter-conversion of Lindqvist anions into the β-octamolybdate anions observed in Reaction Mix **C** and **D** may be attributed to the long chain, large steric bulk cations hindering the rearrangement of Lindqvist anions by both being too sterically hindering to promote formation of the (Ag$\{Mo_8\}$Ag) synthons *via* wrapping around them as effectively as the smaller chain tetrabutylammonium cations, and also by hindering contact between the silver cations and molybdenum anions. These results also appear to support the previously proposed hypothesis that the steric bulk of the alkylammonium cations present in a reaction system influences the (Ag$\{Mo_8\}$Ag) synthon-containing crystal structures which can be isolated in the solid state from these reaction mixtures.[81, 185]

3.2.3 Summary of the CSI-MS and UV/vis spectroscopic investigations into the 'in-solution' self-assembly of $((n\text{-}C_4H_9)_4N)_{2n}[Ag_2Mo_8O_{26}]_n$ (1)

In summary CSI-MS has been used to elucidate the solution state rearrangement of POM clusters for the first time. Specifically the role of the Ag^I ions in the assembly of the stable, silver-linked β-octamolybdate structure **1** has been revealed using mass spectral investigations. The identification of anion series (vi), i.e. $[AgMo_mO_{3m+1}]^-$ where $m = 2$ to 4, in particular the $[AgMo_2O_7]^-$ and $[AgMo_4O_{13}]^-$ fragments of the $(Ag\{Mo_8\}Ag)$ synthon units, are of significance in understanding the formation of compound **1** from this reaction system. Also mono-anionic series involving mixed oxidation state polyoxomolybdate species, from dimolybdate up to hexamolybdate fragments, have been observed for the first time.[221] Detection, in the CSI-MS analyses, of the species $[(AgMo_8O_{26})TBA_2]^-$, $[(Ag_2Mo_8O_{26})(Mo_4O_{13})TBA_3]^-$, and $[(Ag_2Mo_8O_{26})(Mo_8O_{26})TBA_5]^-$, each with an increasing organic cation contribution, supports the previously proposed hypothesis[81] that the organic cations used in the synthesis do indeed play an important structure-directing role in promoting the mode of POM structure growth in solution.
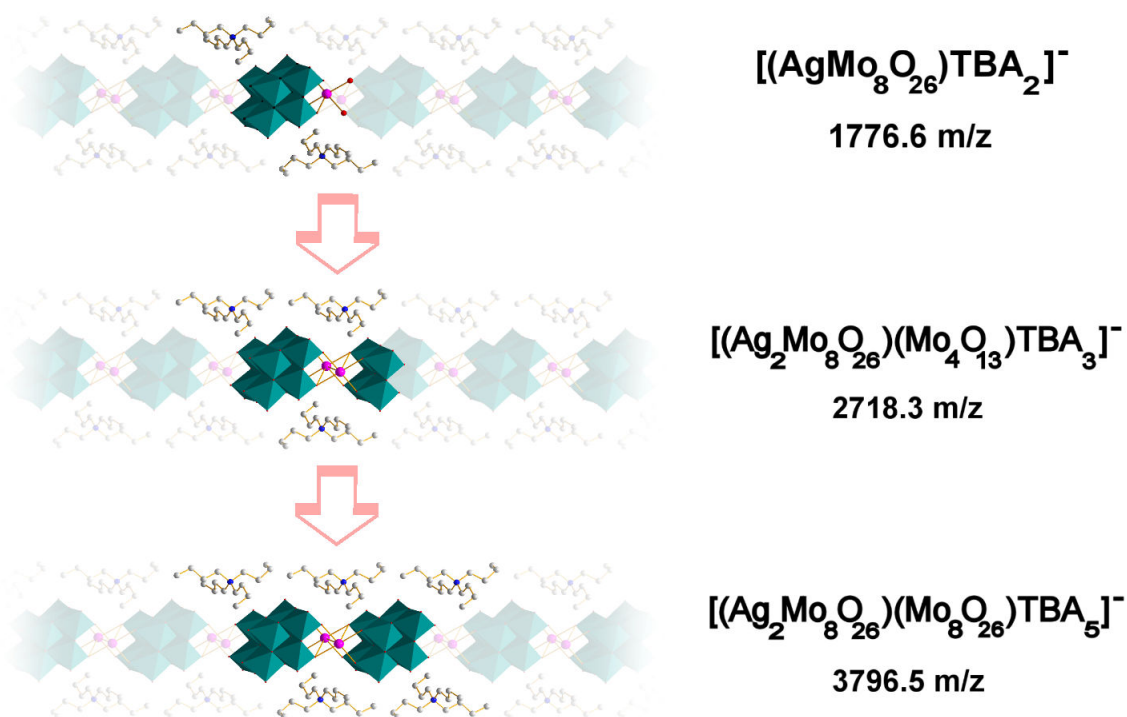
The rate of decrease in Lindqvist anion concentration, and therefore concomitant increase in $\{Mo_8\}$ anion concentration, for Reaction Mixtures **A-D,** were monitored *via* UV/vis spectroscopy. This correlation between decreasing Lindqvist anion and increasing $\{Mo_8\}$ anion concentration was supported by CSI-MS monitoring of Reaction Mix **A**, i.e. $TBA_2[Mo_6O_{19}]$ + AgF, over time. The use of CSI-MS in this way to monitor real-time, 'in-solution' rearrangements in a POM reactant solution is, to our knowledge, unprecedented. This approach can now be extended to investigate the bottom-up, 'in-solution' processes governing the formation of other POM systems so enhancing our understanding and giving us the potential to control the building-block principles involved.

The effect of the length of organic counter cation used in the reaction system on the rate of Lindqvist to $(Ag\{Mo_8\}Ag)$ synthon rearrangement was examined *via* comparison of the 'pseudo' first order rate constants, with respect to $[\{Mo_6\}]$, calculated over the first 75 min in the UV/vis spectroscopy experiment for each reaction mix. The general trend observed from these calculated rate constants was that the rate of decrease in the concentration of Lindqvist anions, and as a result, the inter-conversion of Lindqvist into β-octamolybdate

anions, decreases as the carbon chain length of the alkylammonium cations increases.[225] These lower rates of inter-conversion when using a hexamolybdate reagent with a longer chain cation may be attributed to the steric bulk of these large organic groups hindering the rearrangement of Lindqvist anions, and hindering contact between the silver cations and molybdenum anions. These results therefore, support the previously proposed hypothesis that the steric bulk of the alkylammonium cations present in a reaction system influences the (Ag{Mo_8}Ag) synthon-containing POM structures which can be formed and then isolated in the solid state from these reaction mixtures.[81, 185]

3.3 Examining the formation of an organic-inorganic hybrid polyoxometalate using mass spectrometry

Following the successful use of mass spectrometry techniques to investigate real-time, 'in-solution' rearrangements of the $[Mo_6O_{19}]^{2-}$ Lindqvist in the presence of silver(I) cations into the silver-linked β-octamolybdate structure $((n\text{-}C_4H_9)_4N)_{2n}[Ag_2Mo_8O_{26}]_n$, it was decided to extend this investigative approach to examine a more complex POM system.

Herein, we have applied this approach to elucidate the 'in-solution' formation of a complex organic-inorganic POM-hybrid system involving the rearrangement of $[α\text{-}Mo_8O_{26}]^{4-}$, coordination of Mn^{3+}, and coordination of two tris(hydroxylmethyl)aminomethane molecules (TRIS) to form the symmetrical Mn-Anderson cluster $((n\text{-}C_4H_9)_4N)_3[MnMo_6O_{18}((OCH_2)_3CNH_2)_2]$ (**2**)[92] (see Figure 34).

3.3.1 The manganese Anderson polyoxomolybdate system under investigation

The reaction system selected for investigation in this current work was found, by Hasenknopf *et al*, to produce the symmetrical Mn-Anderson cluster $((n\text{-}C_4H_9)_4N)_3[MnMo_6O_{18}((OCH_2)_3CNH_2)_2]$ (**2**), which was isolated in the solid state and characterized by single crystal X-ray diffraction.[92] It is synthesized by stirring $TBA_4(α\text{-}Mo_8O_{26})$, manganese(III) acetate, and tris(hydroxylmethyl)aminomethane (TRIS) in acetonitrile solution under reflux conditions for approximately 16 hours.
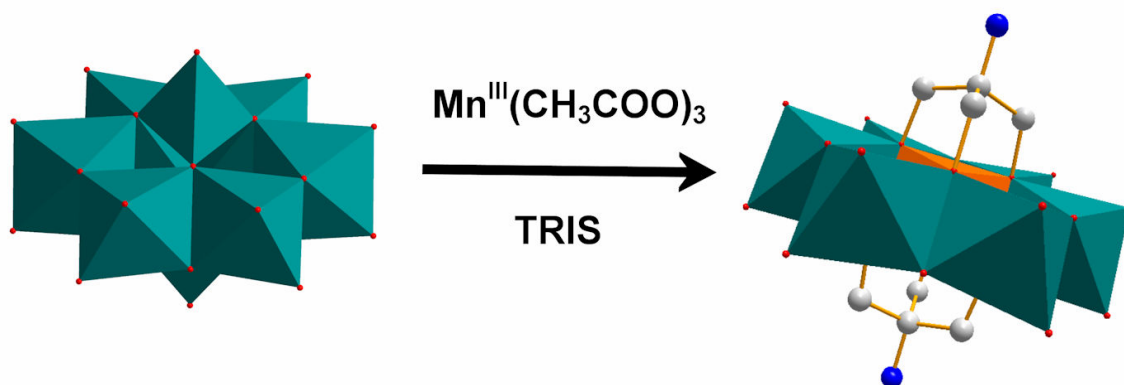
Figure 34: Illustration showing the rearrangement of the $[\alpha\text{-Mo}_8\text{O}_{26}]^{4-}$ anion (shown on the left) in the presence of manganese(III) acetate and TRIS into the symmetrical Mn-Anderson anion $[\text{MnMo}_6\text{O}_{18}((\text{OCH}_2)_3\text{CNH}_2)_2]^{3-}$ of compound **2** (shown on the right).[92] Colour scheme: Mo, teal polyhedra; Mn, orange polyhedron; O, red; N, blue; C, grey. H atoms are omitted for clarity.

Although there have been many solid state investigations using tris(alkoxo) ligands to form novel organic-inorganic hybrid polyoxometalates using, for example , the Anderson,[91-94, 109] Lindqvist,[226-228] and Dawson[151, 158, 229] structural types, along with investigations of other POM architectures,[224, 230-233] there has been very little research into the self-assembly processes which govern the formation of these structures in solution. In particular, the use of the technique of mass spectrometry to aid elucidation of the rearrangements and aggregation processes involved has, so far, been neglected.

This particular reaction system was selected for investigation in this work, not only because it presents a conveniently accessible, more complex, cluster rearrangement than previously studied, but importantly this reaction takes place in acetonitrile solution which is a volatile, moderately polar solvent suitable for use in MS investigations and which usually provides MS data with a good signal:noise ratio. This removes the necessity to adjust the MS dilution with other solvent additives, a technique which is sometimes required to improve the signal:noise ratio when analyzing , for example, samples dissolved in purely aqueous solutions.[189]

3.3.1.1 Mass spectral information on the reaction system which produces ((*n*-C$_4$H$_9$)$_4$N)$_3$[MnMo$_6$O$_{18}$((OCH$_2$)$_3$CNH$_2$)$_2$] (**2**)

The speciation and fragment rearrangements were investigated as follows. Tetrabutylammonium α-octamolybdate, ((*n*-C$_4$H$_9$)$_4$N)$_4$[α-Mo$_8$O$_{26}$], manganese(III) acetate, and TRIS were suspended in acetonitrile solution and stirred at room temperature for approx 15 min, before refluxing at 80 °C for approx 30 h. Aliquots were removed at noted time intervals throughout the reaction, diluted with acetonitrile, and analysed using ESI-MS (the parameters for which were consistent throughout all runs). The first spectrum was recorded after stirring the reaction solution at room temperature for 13 min. This spectrum is dominated by peaks which can be assigned to isopolyoxomolybdate fragments of the rearranging [α-Mo$_8$O$_{26}$]$^{4-}$ anion (Figure 35 and Table 2) and contains the ion series:

    i)   [H$_{m-2}$Mo$_m$O$_{3m}$]$^-$ where *m*= 2 or 3

    ii)   [Mo$_m$O$_{3m+1}$]$^{2-}$ where *m*= 4 or 5

    iii)   [Na$_n$H$_{1-n}$Mo$_m$O$_{3m+1}$]$^-$ where *m*= 3 or 4 and *n* = 0 or 1

    iv)   [H$_2$Mn^{2+}Mo$_m$O$_{3m+1}$]- where *m* = 3 or 4

    v)   [Mo$_m$O$_{3m+1}$TBA$_1$]$^-$ where *m*= 3 to 5

    vi)   [Mo$_8$O$_{26}$TBA$_{3-n}$Na$_n$]$^-$ where *n*= 0 to 2

The dominance of these isopolyoxomolybdate fragments indicates that the [α-Mo$_8$O$_{26}$]$^{4-}$ anion rearranges into these smaller fragment ions prior to further coordination with the Mn cations and TRIS groups. Indeed the first indications of this further coordination are illustrated by the presence of very low intensity peaks containing TRIS groups and manganese cations, e.g. [Mo$_2$O$_5$((OCH$_2$)$_3$CNH$_2$)]$^-$ (387.8 m/z), and [Mn^{III}Mo$_3$O$_8$((OCH$_2$)$_3$CNH$_2$)$_2$]$^-$ (706.7 m/z).
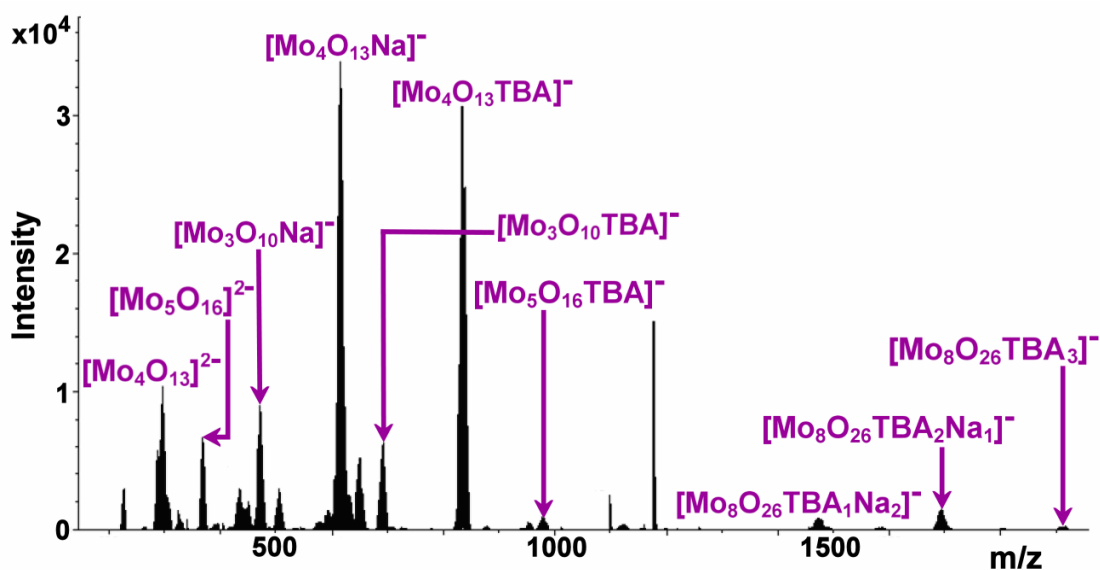
Figure 35: ESI-MS data collected of the reaction solution of **2**, recorded after stirring at room temperature for 13 min. The spectrum is dominated by isopolyoxomolybdate fragment peaks. Of particular note is that the two major peaks in this spectrum, at 614.6 m/z (the base peak) and 833.8 m/z, are attributed to the species $[Mo_4O_{13}Na]^-$ and $[Mo_4O_{13}TBA]^-$ respectively, i.e. half of the parent $(Mo_8O_{26})^{4-}$ cluster anion.

m/z	Peak Assignment
*287.8	$[Mo^{VI}Mo^{V}O_6]^-$
296.8	$[Mo_4O_{13}]^{2-}$
*304.8	$[Mo_2O_7H]^-$
367.7	$[Mo_5O_{16}]^{2-}$
*387.8	$[Mo_2O_5((OCH_2)_3CNH_2)]^-$
432.7	$[Mo^{VI}Mo^{V}_2O_9H]^-$
448.7	$[Mo_3O_{10}H]^-$
470.7	$[Mo_3O_{10}Na_1]^-$
504.7	$[Mn^{II}Mo^{V}_3O_{10}H_2]^-$
*533.7	$[Mo_3O_8((OCH_2)_3CNH_2)]^-$
*594.6	$[Mo_4O_{13}H]^-$
614.6	$[Mo_4O_{13}Na_1]^-$
690.0	$[Mo_3O_{10}TBA]^-$
*706.7	$[Mn^{III}Mo_3O_8((OCH_2)_3CNH_2)_2]^-$
833.8	$[Mo_4O_{13}TBA]^-$
977.8	$[Mo_5O_{16}TBA]^-$
1473.7	$[Mo_8O_{26}TBA_1Na_2]^-$
1690.7	$[Mo_8O_{26}TBA_2Na_1]^-$
1911.0	$[Mo_8O_{26}TBA_3]^-$

Table 2: Full, tabulated details of species assigned to the peaks in the ESI-MS spectrum of the reaction solution of **2**, recorded after stirring at room temperature for 13 min (see spectrum in Figure 35). * Peaks marked with an asterisk are of very low intensity and/or slightly overlaid with other peaks.

The spectrum recorded after refluxing for approx 7 h (Figure 36) can be seen to have increased in complexity. The dominant peaks are now assigned to a wide variety of fragments, i.e. polyoxomolybdate fragments coordinated to Mn cations, e.g. $[Mn^{II}Mo^{VI}Mo^{V}O_7]^-$ (peak at 358.7 m/z); polyoxomolybdate fragments coordinated to TRIS, e.g. $[Mo_2O_5((OCH_2)CNH_2)]^-$ (peak at 389.8 m/z); or fragments of the product cluster **2**, e.g. $[Mn^{III}Mo_3O_8((OCH_2)_3CNH_2)_2]^-$ (peak at 706.7 m/z). The ion series identified at this point in the reaction are:

i) $[H_{m-2}Mo_mO_{3m}]^-$ where m= 2 or 3

ii) $[HMo_mO_{3m+1}]^-$ where m= 2 or 3

iii) $[HMn^{2+}Mo_mO_{3m+2}]^-$ where m = 2 or 3

iv) $[Mo_mO_{3m-1}((OCH_2)_3CNH_2)]^-$ where m = 2 or 3

v) $[Mn^{(n+2)+}Mo_3O_{9+n}((OCH_2)_3CNH_2)H]^-$ where n = 0 or 1

vi) $[Mn^{3+}Mo_mO_{3m-1}((OCH_2)_3CNH_2)_2]^-$ where m = 2 to 5

vii) $[Mn^{3+}Mo_6O_{18}((OCH_2)_3CNH_2)_2TBA_{2-n}H_n]^-$ where n = 0 or 1

viii) $[Mo_mO_{3m+1}TBA_1]^-$ where m= 3 or 4

Figure 36: ESI-MS data collected of the reaction solution of **2**, recorded after refluxing at 80 °C for approximately 7 h.

The complexity and ion series observed in this spectrum remain observable through to the final spectrum recorded after refluxing for approx 30 h (see Figure 37 to 39 and Table 3). Some of the prominent fragment ions, their experimental spectra, and representations of

these fragments as building-block units of the 'parent' octamolybdate or Mn-Anderson-TRIS clusters, are illustrated in Figure 38.
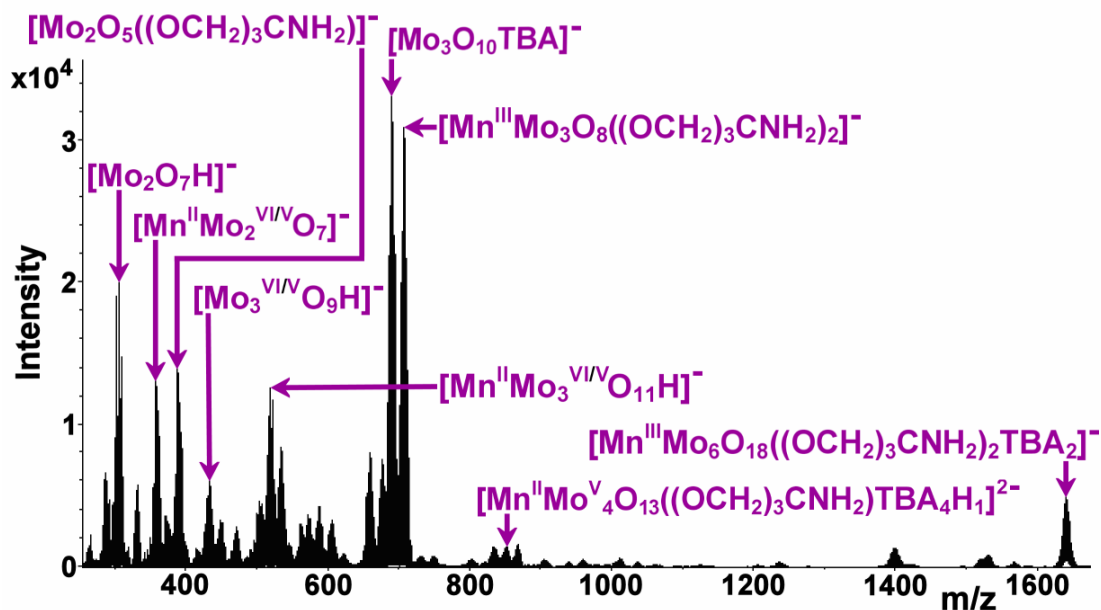
Figure 37: ESI-MS data collected of the reaction solution of **2**, recorded after refluxing at 80 °C for approximately 30 h.
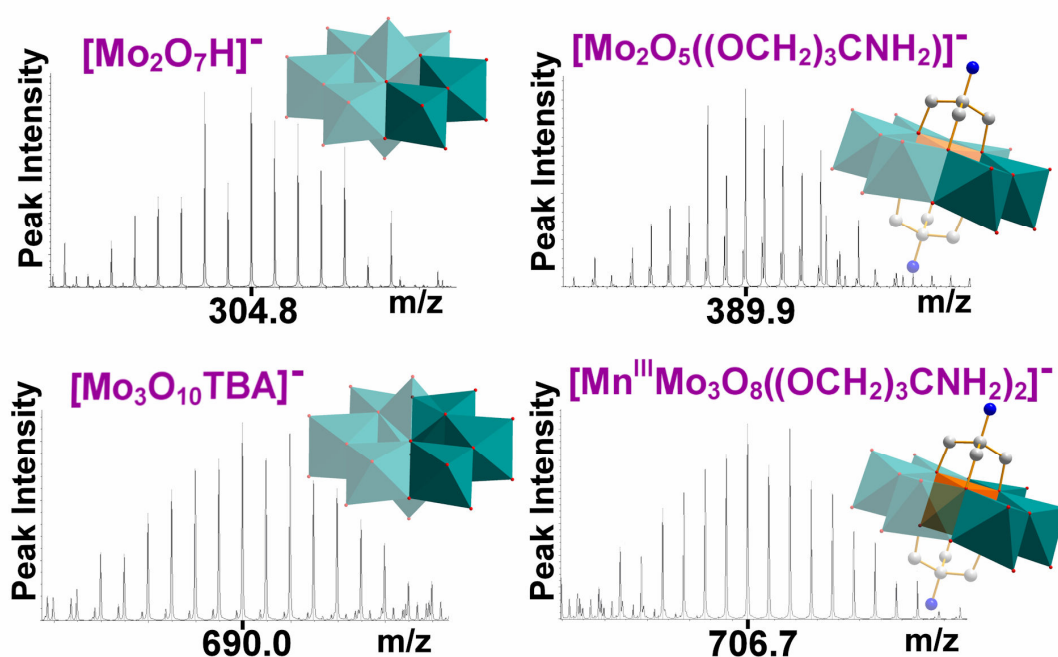
Figure 38: Illustration showing the experimental mass spectra of some prominent small fragment ions observed during ESI-MS monitoring of reaction solution **2**. The structures shown (formal representations based on crystallographic data[92]) are useful to indicate the role of these fragments as building-blocks of the 'parent' octamolybdate and Mn-Anderson-TRIS clusters. Colour scheme: Mo, teal polyhedra; Mn, orange polyhedron; O, red; N, blue; C, grey. H atoms are omitted for clarity.

m/z	Peak Assignment
287.8	$[Mo^{VI}Mo^VO_6]^-$
304.8	$[Mo_2O_7H]^-$
332.2	$[Mn^{II}Mo_4O_{14}]^{2-}$
356.7	$[Mn^{II}Mo^{VI}Mo^VO_7]^-$
*373.8	$[Mn^{II}Mo_2O_8H]^-$
387.8	$[Mo_2O_5((OCH_2)_3CNH_2)]^-$
432.7	$[Mo^{VI}Mo^V_2O_9H]^-$
448.7	$[Mo_3O_{10}H]^-$
470.7	$[Mo_3O_{10}Na_1]^-$
504.7	$[Mn^{II}Mo^V_3O_{10}H_2]^-$
519.6	$[Mn^{II}Mo_3O_{11}H]^-$
533.7	$[Mo_3O_8((OCH_2)_3CNH_2)]^-$
*562.8	$[Mn^{III}Mo_2O_5((OCH_2)_3CNH_2)_2]^-$
*572.6	$[Mn^{II}Mo^V_2Mo^{IV}O_7((OCH_2)_3CNH_2)]^-$
*587.7	$[Mn^{II}Mo^{VI}_2Mo^VO_8((OCH_2)_3CNH)]^-$
*605.7	$[Mn^{II}Mo^{VI}_2Mo^VO_9((OCH_2)_3CNH_2)H]^-$
*621.7	$[Mn^{III}Mo_3O_{10}((OCH_2)_3CNH_2)H]^-$
658.7	$[Mo^VMo^{IV}_2O_8TBA_1H_1]^-$
690.0	$[Mo_3O_{10}TBA]^-$
706.7	$[Mn^{III}Mo_3O_8((OCH_2)_3CNH_2)_2]^-$
833.8	$[Mo_4O_{13}TBA]^-$
852.6	$[Mn^{III}Mo_4O_{11}((OCH_2)_3CNH_2)_2]^-$
868.8	$[Mn^{II}Mo^{VI}Mo^V_3O_{13}((OCH_2)_3CNH_2)TBA_4]^{2-}$
977.8	$[Mo_5O_{16}TBA]^-$
1397.7	$[Mn^{III}Mo_6O_{18}((OCH_2)_3CNH_2)_2TBA_1H]^-$
1639.0	$[Mn^{III}Mo_6O_{18}((OCH_2)_3CNH_2)_2TBA_2]^-$

Table 3: Full, tabulated details of species assigned to the peaks in the ESI-MS spectrum of the reaction solution of **2**, recorded after refluxing at 80 °C for approximately 30 h (see spectrum in Figure 37). * Peaks marked with an asterisk are of very low intensity and/or slightly overlaid with other peaks.

It is interesting to note at this point the presence of Mn^{2+} ions, particularly in the smaller m/z fragment ions; and mixed oxidation state species where molybdenum is found to exist in oxidation states +4, +5, and +6. Observation of molybdenum and manganese centres in reduced oxidation states is not entirely unexpected due to the high voltages utilised in the mass spectrometry ion transfer process.[221] Also single reduced molybdate species $[Mo^VO_3]^-$ and the corresponding single reduced tungstate species $[W^VO_6]^-$ have been observed in previous studies,[180, 182] along with mixed oxidation state fragments of polyoxomolybdate ions.[203, 234] Mixed oxidation state fragments of polyoxochromate systems have also been observed previously when using ESI-MS.[184]
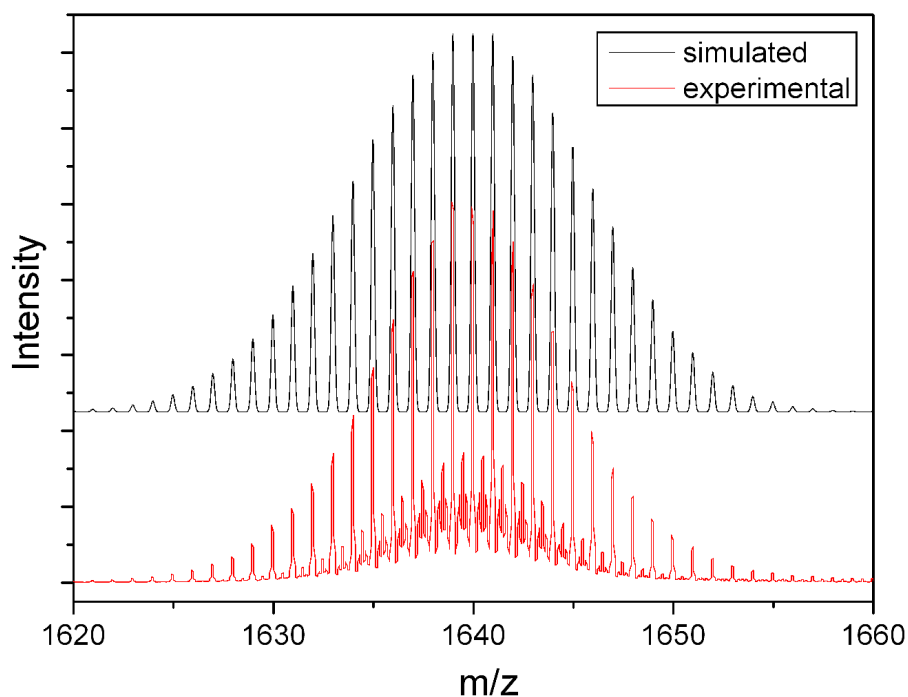
Figure 39: Overlaid ESI-MS spectra for the peak at 1639.0 m/z assigned to $[Mn^{III}Mo_6O_{18}((OCH_2)_3CNH_2)_2TBA_2]^-$. The red line is an expanded section of the experimental spectrum of the reaction solution of **2**, recorded after refluxing at 80 °C for approximately 30 h. The black line is the simulated theoretical spectrum for this peak assignment.

3.3.1.2 Insight into self-assembly through real-time ESI-MS monitoring and examination of fragments

Further information, about the rearrangement processes taking place in solution from $[\alpha-Mo_8O_{26}]^{4-}$ through to the formation of the product cluster anion $[MnMo_6O_{18}((OCH_2)_3CNH_2)_2]^{3-}$, can be extracted from the ESI-MS monitoring of this reaction over time. By plotting the intensities of the peaks assigned, against the time of MS sampling we can build up a qualitative picture of how the concentration of various species in solution varies over the time of reaction.

It is appropriate to mention here that a qualitative rather than a quantitative study has been undertaken because, despite ongoing efforts to find a suitable internal standard for use in such experiments, we have not as yet succeeded in identifying a suitable candidate for use with such reaction systems. This is due to a number of reasons, for example, the large

number of fragment ion present in the mass range under study; interfering aggregations with sample ion fragments; and the lack of a polyoxometalate-based compound with minimal fragmentation in this mass range under these MS conditions.
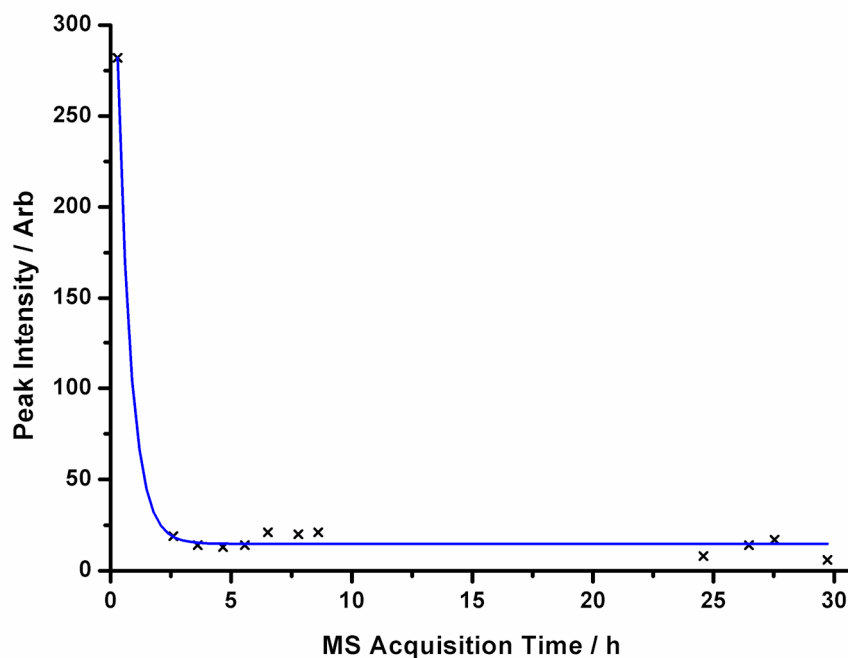
Figure 40: Graph showing the exponential decrease (line of best fit shown) in peak intensity of the species $[Mo_8O_{26}TBA_3]^-$ (1911.0 m/z) within approximately 1 h to a minimum, constant value, when carrying out ESI-MS monitoring of reaction solution **2** over approximately 30 h.

Therefore, through use of a qualitative analysis approach it is observed that the intensity of both the $[Mo_8O_{26}TBA_3]^-$ (peak at 1911.0 m/z) and the $[Mo_4O_{13}TBA]^-$ (peak at 833.8 m/z) decrease exponentially and rapidly (i.e. within approx 1 h, and approx 2 h respectively) to minimum, constant values (Figure 40 and 41), whilst the intensity of the product anion $[Mn^{III}Mo_6O_{18}((OCH_2)_3CNH_2)_2TBA_2]^-$ (peak at 1640.0 m/z) increases at a lower respective rate over the course of the reaction (Figure 42).
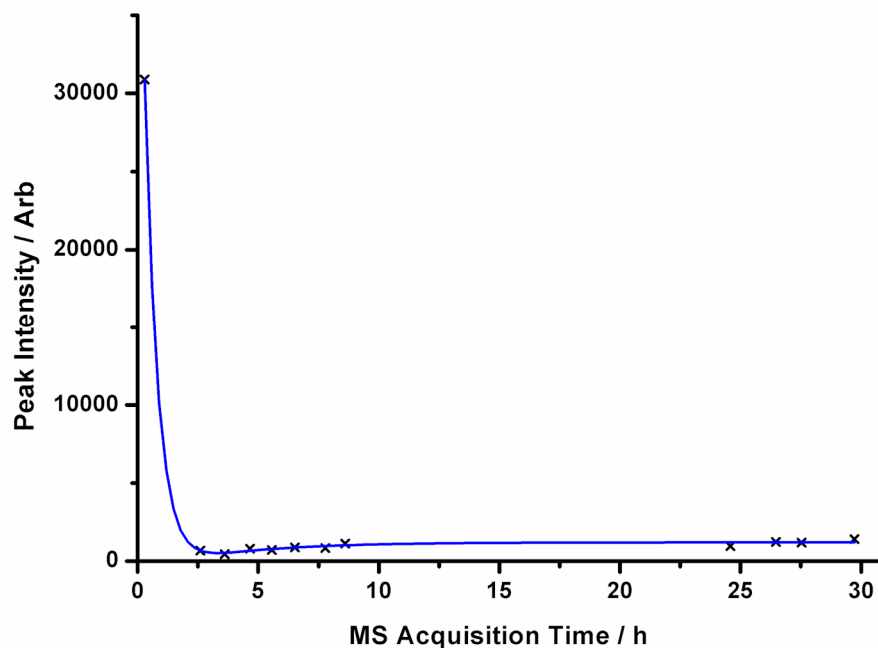
Figure 41: Graph showing the exponential decrease (line of best fit shown) in peak intensity of the species $[Mo_4O_{13}TBA]^-$ (833.8 m/z) within approximately 2 h to a minimum, constant value, when carrying out ESI-MS monitoring of reaction solution **2** over approximately 30 h.
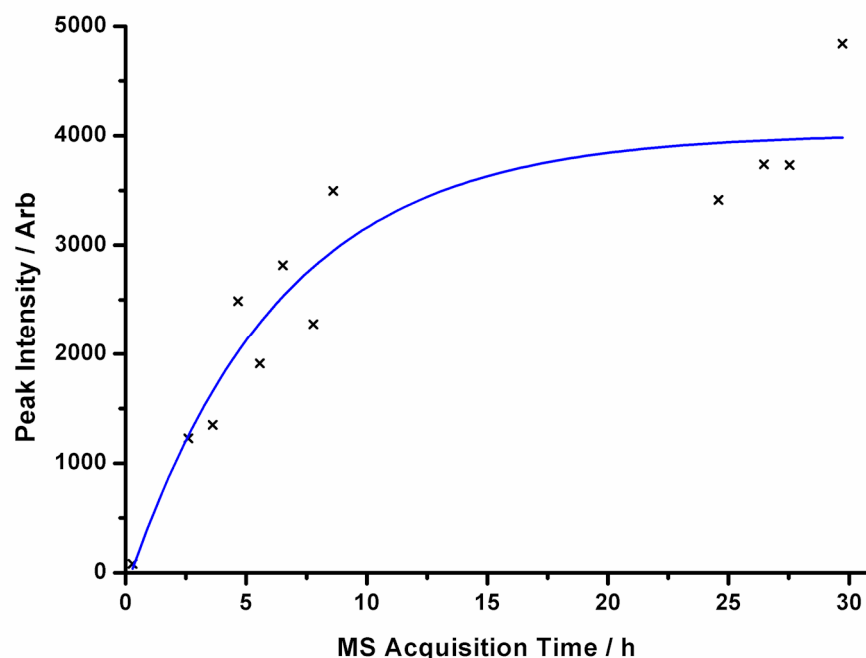
Figure 42: Graph showing the increase in peak intensity of the species $[Mn^{III}Mo_6O_{18}((OCH_2)_3CNH_2)_2TBA_2]^-$ (1640.0 m/z) over time when carrying out ESI-MS monitoring of reaction solution **2** over approximately 30 h. (Line of best fit shown.)

The decrease in reactant ion peak intensity and subsequent increase in product ion peak intensity is not surprising, however, the difference in speed of decomposition of the $[Mo_8O_{26}TBA_3]^-$ ion and formation of the product $[Mn^{III}Mo_6O_{18}((OCH_2)_3CNH_2)_2TBA_2]^-$ ion suggests the mechanism of formation proceeds *via* further intermediate, rate-determining steps which then govern the rate of final product ion formation. It is then interesting to note the changes in intensity of the peaks assigned to the small fragment ions $[Mo_2O_7H]^-$ (304.8 m/z); $[Mo_2O_5((OCH_2)_3CNH_2)]^-$ (389.8 m/z); $[Mo_3O_{10}TBA]^-$ (690.0 m/z); and $[Mn^{III}Mo_3O_8((OCH_2)_3CNH_2)_2]^-$ (706.7 m/z) over the course of the reaction. These peaks are prominent throughout all the spectra taken after reaction time 1 h 20 min, and their intensities are all observed to increase over reaction time (see Figure 38 and 43).
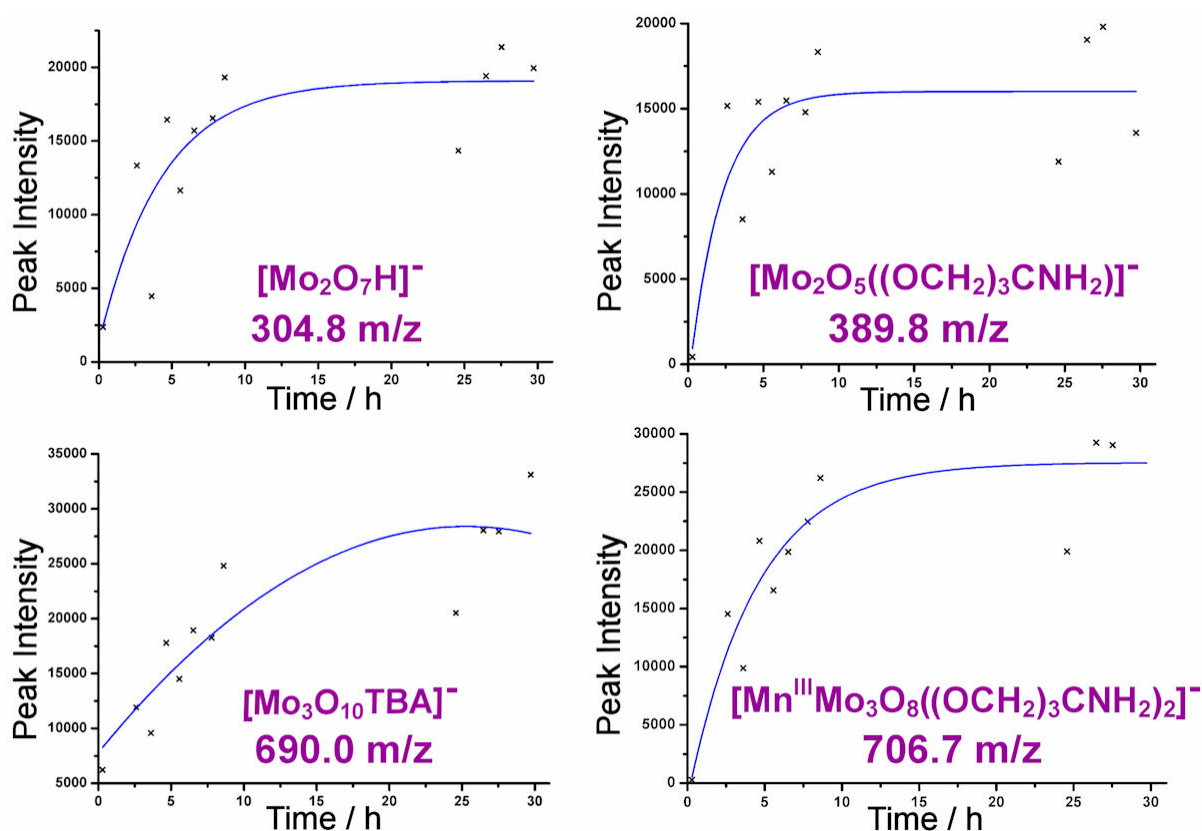
Figure 43: Graphs showing the general trends of increasing peak intensity of $[Mo_2O_7H]^-$ (304.8 m/z); $[Mo_2O_5((OCH_2)_3CNH_2)]^-$ (389.8 m/z); $[Mo_3O_{10}TBA]^-$ (690.0 m/z); and $[Mn^{III}Mo_3O_8((OCH_2)_3CNH_2)_2]^-$ (706.7 m/z) over time, observed when carrying out ESI-MS monitoring of reaction solution **2** over approximately 30 h. (Lines of best fit are shown.)

These observations could suggest that the rapid decomposition and rearrangement of the $[\alpha-Mo_8O_{26}]^{4-}$ anion proceeds initially *via* the formation of $[Mo_4O_{13}]^{2-}$ cluster species (i.e. $[Mo_4O_{13}Na_1]^-$ (614.6 m/z, base peak) and $[Mo_4O_{13}TBA]^-$ (833.8 m/z)) which are half fragments of the {Mo_8} clusters and the most prominent peaks in the first spectrum

recorded (see Figure 35); followed by decomposition to smaller, stable dinuclear, i.e. $[Mo_2O_7H]^-$, and trinuclear, i.e. $[Mo_3O_{10}TBA]^-$, isopolyoxomolybdate fragment ions; which subsequently coordinate with the TRIS and manganese ions, so building-up to the final Mn-Anderson-TRIS product ion.

The peak assignments of these small fragment ions, and the suggestion that they could act as intermediates in the formation of the full Mn-Anderson-TRIS cluster, are further supported by previous solid state studies in which rearrangement of $[\alpha\text{-}Mo_8O_{26}]^{4-}$ clusters has been investigated; and similar bi- and tri-oxomolybdate anions coordinated to trialkoxy ligands have been isolated and characterized using single crystal X-ray diffraction.

The hypothesis of initial, rapid rearrangement of $[\alpha\text{-}Mo_8O_{26}]^{4-}$ clusters, *via* $[Mo_4O_{13}]^{2-}$ clusters, into small, stable fragment ions such as $[Mo_2O_7H]^-$ is supported through the work of Klemperer *et al*,[87, 235] which illustrate the disassembly of $[\alpha\text{-}Mo_8O_{26}]^{4-}$ clusters into $[Mo_2O_7]^{2-}$ anions in basic, acetonitrile solution. Also Peng *et al* found evidence that the $[\alpha\text{-}Mo_8O_{26}]^{4-}$ cluster rearranges in solution into $[Mo_2O_7]^{2-}$ anions prior to functionalization with organoimido ligands and subsequent aggregation with further $[Mo_2O_7]^{2-}$ units into the bifunctionalized hexamolybdate (Lindqvist) cluster.[36]

The proposed formation of tri-molybdate centered fragments, e.g. $[Mo_3O_{10}TBA]^-$ (690.0 m/z) and $[Mn^{III}Mo_3O_8((OCH_2)_3CNH_2)_2]^-$ (706.7 m/z), following the disassembly of the $[\alpha\text{-}Mo_8O_{26}]^{4-}$ clusters into $[Mo_2O_7]^{2-}$ anions, is supported by the work of Zubieta *et al*[231] in which the authors found that reaction of $TBA_4[\alpha\text{-}Mo_8O_{26}]$ with 2-(hydroxymethyl)-2-methyl-1,3-propanediol $(CH_3C(CH_2OH)_3)$ in acetonitrile resulted in the rearrangement of the $\{\alpha\text{-}Mo_8\}$ cluster into the small, tri-nuclear crystal structure $TBA_2[Mo_3O_7(CH_3C(CH_2O)_3)_2]$. (See Figure 44).
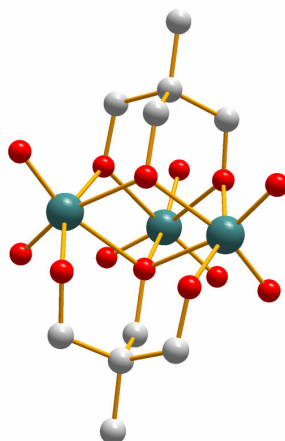
Figure 44: Ball-and-stick representation of the tri-nuclear cluster anion in the crystal structure of $TBA_2[Mo_3O_7(CH_3C(CH_2O)_3)_2]$.[231] This compound was produced by Zubieta *et al* by reaction of $TBA_4[\alpha\text{-}Mo_8O_{26}]$ with 2-(hydroxymethyl)-2-methyl-1,3-propanediol $(CH_3C(CH_2OH)_3)$ in acetonitrile. Colour scheme: Mo, teal; O, red; C, grey. H atoms are omitted for clarity.

It is also interesting to note in subsequent work by Zubieta *et al*[232] that $TBA_2[Mo_2O_4(O_2NC(CH_2O)_3)_2]\cdot2O_2NC(CH_2OH)_3$ was isolated by reaction of $TBA_2[Mo_2O_7]$ with $O_2NC(CH_2OH)_3$ in methanol, followed by diffusion with diethyl ether (see Figure 45). On addition of more $TBA_2[Mo_2O_7]$ further aggregation was observed leading to isolation of both $TBA[Mo_3O_6(OCH_3)(O_2NC(CH_2O)_3)_2]$ and $TBA_2[Mo_3O_7(O_2NC(CH_2O)_3)_2]$, which is an analogue of the previously reported $TBA_2[Mo_3O_7(CH_3C(CH_2O)_3)_2]$ compound.[231]
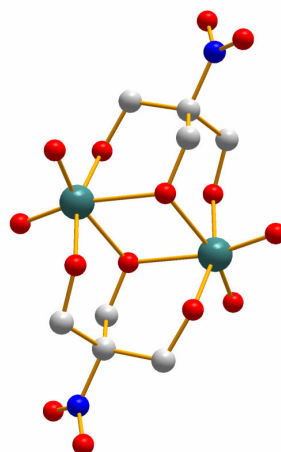
Figure 45: Ball-and-stick representation of the bi-nuclear cluster anion in the crystal structure of $TBA_2[Mo_2O_4(O_2NC(CH_2O)_3)_2]\cdot2O_2NC(CH_2OH)_3$.[232] This compound was produced by Zubieta *et al* on reaction of $TBA_2[Mo_2O_7]$ with $O_2NC(CH_2OH)_3$ in methanol. Colour scheme: Mo, teal; O, red; N, blue; C, grey. H atoms are omitted for clarity.

In this particular set of experiments Zubieta *et al* then found that on addition of more TBA$_2$[Mo$_2$O$_7$] to TBA[Mo$_3$O$_6$(OCH$_3$)(O$_2$NC(CH$_2$O)$_3$)$_2$] they were able to isolate another methoxylated product [Mo$_4$O$_8$(OMe)$_2$(O$_2$NC(CH$_2$O)$_3$)$_2$]. These findings led them to propose the stepwise aggregation scheme of condensation reactions given below (where H$_3$L = CH$_3$C(CH$_2$OH)$_3$) in an attempt to explain the self-assembly processes linking the bi-nuclear, tri-nuclear and tetra-nuclear clusters isolated:

$$[Mo_2O_7]^{2-} + 2H_3L \rightarrow [Mo_2O_4L_2]^{2-} + 3H_2O$$

$$2[Mo_2O_4L_2]^{2-} + [Mo_2O_7]^{2-} + H_3L + MeOH \rightarrow$$
$$[Mo_3O_6(OMe)L_2]^- + [Mo_3O_7L_2]^{2-} + 2H_2O + L^{3-}$$

$$2[Mo_3O_6(OMe)L_2]^- + [Mo_2O_7]^{2-} + 6MeOH \rightarrow$$
$$[Mo_4O_8(OMe)_2L_2] + [Mo_4O_{10}(OMe)_6]^{2-} + H_2O + 2H_2L^-$$
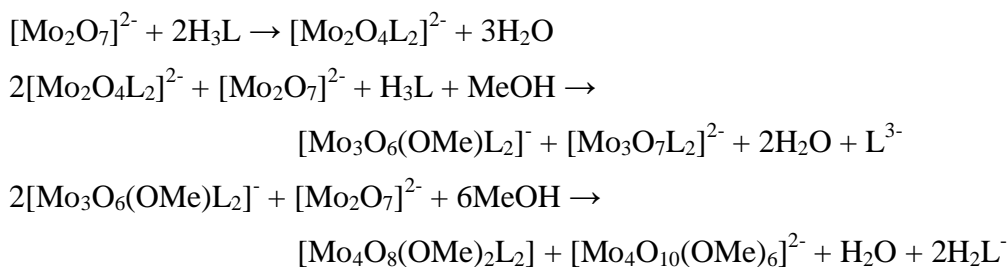
Although these investigations and proposed reaction scheme relate to the formation of complexes in methanolic solution, some of which contain coordinated methoxy-ligands, it is nevertheless, of interest to compare the potential aggregation scheme above, with the bi-, tri- and tetra-molybdate centered cluster fragments observed in the current mass spectral study of the formation of the TBA$_3$[MnMo$_6$O$_{18}$((OCH$_2$)$_3$CNH$_2$)$_2$] (**2**) compound (see Tables 2 and 3).

Another noticeable feature of the mass spectral data of this reaction system is the increasing prominence of the peaks assigned to [Mo$_3$O$_{10}$TBA]$^-$ (690.0 m/z) and [Mn^{III}Mo$_3$O$_8$((OCH$_2$)$_3$CNH$_2$)$_2$]$^-$ (706.7 m/z) as the reaction proceeds. Indeed in the final spectrum, recorded after approximately 30 h reflux, the [Mo$_3$O$_{10}$TBA]$^-$ (690.0m/z) peak is the base peak, with the [Mn^{III}Mo$_3$O$_8$((OCH$_2$)$_3$CNH$_2$)$_2$]$^-$ (706.7 m/z) peak at only slightly lower intensity (see Figure 37). Although the prominence of, particularly the [Mn^{III}Mo$_3$O$_8$((OCH$_2$)$_3$CNH$_2$)$_2$]$^-$ (706.7 m/z) peak at the end of the reaction, might be considered to be due, in part, from fragmentation of the final Mn-Anderson-TRIS product ion, the high intensity of this peak and that of the [Mo$_3$O$_{10}$TBA]$^-$ (690.0m/z) peak, relative to the other fragment ions in the spectrum, could be interpreted as indicative of these fragments having a greater degree of stabilization than the other fragments present. An explanation for this, as suggested in work by Zubieta *et al*[224] and Müller *et al*[233], is that correlation of the tripodal geometry of the TRIS ligand with the {Mo$_3$} anionic units, and the organic ligand's ability to reduce the charge density of this building-block unit, both act to lend greater stability to these tri-molybdate centred fragment ions.

Consideration of all of these results, alongside the conclusions drawn from the previous investigation of the 'in-solution' rearrangement of the molybdenum Lindqvist anion, $[Mo_6O_{19}]^{2-}$, adds further weight to the hypotheses presented above regarding the rearrangement of $[\alpha\text{-}Mo_8O_{26}]^{4-}$, *via* $[Mo_4O_{13}]^{2-}$ clusters, into small, stable anionic units, i.e. $[Mo_2O_7]^{2-}$ anions, which subsequently aggregate further with the coordinating tripodal TRIS ligands, manganese ions, and molybdate anionic units, into the final Mn-Anderson-TRIS product ion.

3.3.2   Summary of the mass spectral investigations into the 'in-solution' formation of $((n\text{-}C_4H_9)_4N)_3[MnMo_6O_{18}((OCH_2)_3CNH_2)_2]$ (2)

In summary, the technique of ESI-MS has been utilised for the first time to monitor the real-time, 'in-solution' formation of a complex organic-inorganic POM-hybrid system. Through assignment of the fragment ions observed in the ESI-MS spectra of the reaction solution of **2,** and by noting the changes in peak intensity of prominent peaks in these spectra over the time of reaction, we have been able to propose that the rearrangement of $[\alpha\text{-}Mo_8O_{26}]^{4-}$, occurs first *via* the formation of $[Mo_4O_{13}]^{2-}$ cluster species (i.e. $[Mo_4O_{13}Na_1]^-$ (614.6 m/z) and $[Mo_4O_{13}TBA]^-$ (833.8 m/z)) which are half-fragments of the {Mo$_8$} clusters and the most prominent peaks in the first spectrum recorded (see Figure 35). It is then proposed that this is followed by decomposition to smaller, stable isopolyoxomolybdate fragment ions containing just two, i.e. $[Mo_2O_7H]^-$, and three molybdenum centres, i.e. $[Mo_3O_{10}TBA]^-$; which subsequently coordinate with the tripodal TRIS ligands, i.e. $[Mo_2O_5((OCH_2)_3CNH_2)]^-$ (389.8 m/z); manganese ions, i.e. $[Mn^{III}Mo_3O_8((OCH_2)_3CNH_2)_2]^-$ (706.7 m/z); and further molybdate anionic units, to form the final Mn-Anderson-TRIS cluster of **2,** i.e. $[Mn^{III}Mo_6O_{18}((OCH_2)_3CNH_2)_2TBA_2]^-$ (1640.0 m/z).

3.4 Encapsulating high oxidation state heteroatoms within polyoxometalate clusters

It has been of interest for many years to incorporate high oxidation state heteroanion templates, such as $\{I^{VII}O_6\}$ and $\{Te^{VI}O_6\}$, within polyoxometalate clusters in order to affect the properties of the synthesized compounds, e.g. to improve their catalytic activity and electron-transfer properties.   Such clusters have included periodate-centred molybdenum[112, 236-238] Anderson clusters; periodate-centered nonanuclear i.e. $[IMo_9O_{32}(OH)(OH_2)_3]^{4-}$, and tetradecanuclear $[(IMo_7O_{26})_2]^{6-}$ molybdenum clusters;[239] tellurate-centred molybdenum[240-242] and tungsten Anderson clusters; [99, 108, 243] tellurate-centred octamolybdate clusters of structural formula $[TeMo_8O_{29}(OH_2)]^{4-}$;[244] and the first example of a vanadotellurate cluster anion, i.e. $[HTeV_9O_{28}]^{4-}$.[245]   Subsequently the catalytic activity of some of these clusters has been investigated, for example, periodate-centred Anderson clusters have been found to catalyse the oxidation of glycols,[246] and tellurate-centred Anderson clusters have been utilised in the synthesis of mixed metal-oxide catalysts.[247, 248]   Recently Cronin *et al* have investigated and successfully synthesized a periodate-centred tungsten Dawson[148] and a tellurate-centred tungsten Dawson cluster,[149] both of which have been shown to possess catalytic activity towards the oxidation of alcohols.

Following this work of Cronin *et al* it was decided to investigate whether the analogous periodate-centred and tellurate-centred molybdenum analogues could also be produced. Although many experiments have been carried out with this aim in mind, for example, by adapting the experimental procedures used to produce the tungsten analogues; making subtle changes to these procedures e.g. changes to the pH, the order of reagent addition; and then altering the counter-cations utilised; we have, so far, been unsuccessful in isolating the molybdenum Dawson analogues. Despite this however, these experiments have led to the isolation and characterization of the new molybdenum Anderson-based polyoxometalate structures described in the following sections.

3.5   Formation of $Cs_{4.67}Na_{0.33}[IMo_6O_{24}] \cdot ca7H_2O$ (3)

Following the previously described success in isolating the periodate-centred tungsten Dawson cluster,[148] it was decided to pursue the isolation of the periodate-centred molybdenum analogue. In the pursuit of this aim a number of experiments were carried out, based initially on the experimental procedure used to produce the tungsten analogue, but substituting the sodium tungstate starting material for sodium molybdate. Subsequently, various changes to the experimental procedure such as, the acid used to adjust the pH of the reaction system, the final pH of the reaction system, the order of reagent addition, and the counter-cations used, were made to this experimental procedure in the hope that this would lead to the isolation of the desired product. However, instead these experiments showed a tendency of the molybdenum system to crystallize out of the reaction solution at approximately pH 1.5, either as analogues of the previously reported $\{Mo_{36}\}$ isopolyoxomolybdate cluster, e.g. as $((CH_2CH_2OH)_3NH)_6\{Na_2[Mo_{36}O_{112}(H_2O)_{14}]\}$[56] when using protonated triethanolamine as a counter-cation; or as various previously reported periodate-centered molybdenum Anderson structures, or low nuclearity isopolyoxomolybdates,[249] when using sodium or potassium as counter-cations.

Despite these setbacks, a new polyoxometalate structure based on a periodate-centred molybdenum Anderson cluster was produced on the introduction of caesium as counter-cations in the reaction system. It was found that addition of periodic acid to an aqueous solution of sodium molybdate, followed by acidification to pH 1.8 using hydrochloric acid and subsequent addition of an aqueous caesium chloride solution, led to the isolation of colourless, block, single crystals suitable for single crystal X-ray diffraction. Structural analysis of the X-ray diffraction data, along with analytical data from other techniques such as TGA, EA and FAAS, revealed the composition of the crystals to be $Cs_{4.67}Na_{0.33}[IMo_6O_{24}] \cdot ca7H_2O$ (3).

The POM cluster anion in compound 3 is, as previously stated, a periodate-centred molybdenum Anderson cluster composed of six planar, edge-sharing $\{MoO_6\}$ octahedra surrounding a central $(IO_6)^{5-}$ heteroanion template, containing iodine in the +7 oxidation state. The charge on this $[IMo_6O_{24}]^{5-}$ Anderson cluster is balanced in the crystal structure of 3 by caesium and sodium ions. Inspection of the bond lengths within this POM cluster

anion reveals all the Mo=O terminal, bridging Mo-O, and I-O bonds to be within the expected range of those values quoted in the literature,[236] see Table 4.

Bond Type	Average Bond Distances in Compound 3 / Å
Mo=O (terminal)	1.71
Mo-O (μ_2-bridging)	1.92
Mo-O (μ_3-bridging)	2.34
I-O	1.89

Table 4: Average bond distances within the $[IMo_6O_{24}]^{5-}$ cluster anions in compound **3.**

Examination of the supramolecular lattice of compound **3** along the crystallographic *b*-axis reveals that the $[IMo_6O_{24}]^{5-}$ cluster anions are arranged into a series of layers within the crystallographic *ac*-plane. One of these layers, assigned layer A, can be considered as a bilayer composed of two co-linear, offset arrays of POM cluster anions running parallel with the crystallographic *a*-axis, where the clusters in each of these layers are separated by three coordinating caesium cations (minimum cluster spacing 5.450 Å) and H-bonding solvent H_2O molecules which reinforce the layer formation. These offset cluster layers are separated by a minimum cluster spacing of 3.181 Å and two coordinating caesium cations are situated between adjacent clusters from these offset layers. See Figure 46.
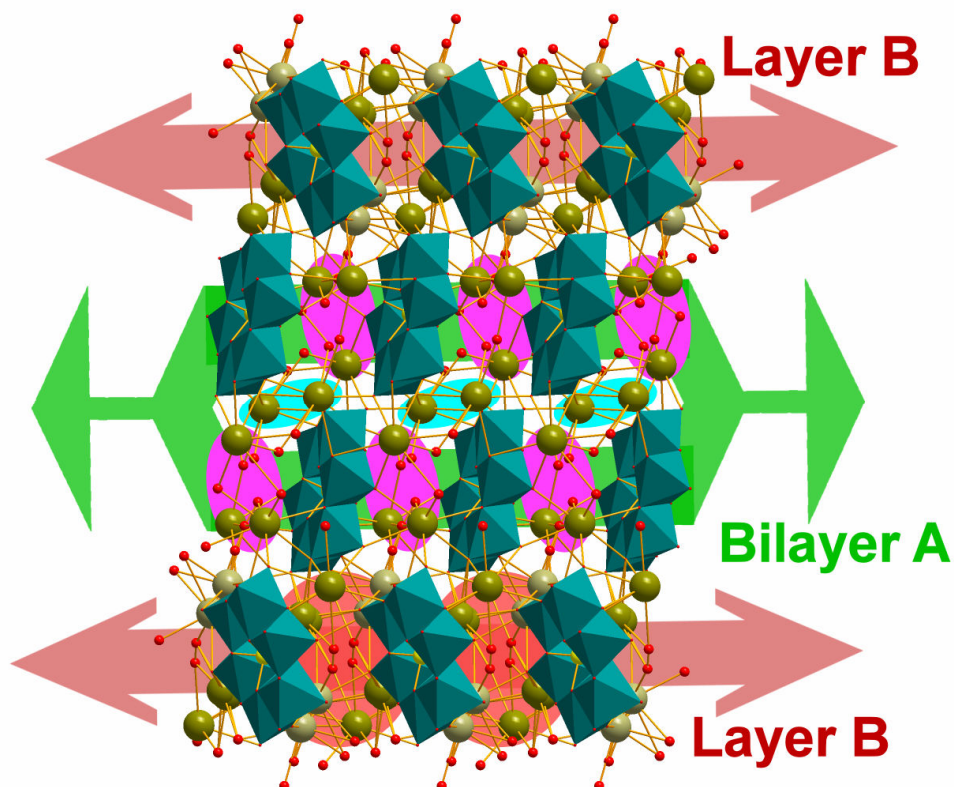
Figure 46: Illustration of compound **3** viewed along the crystallographic *b*-axis. Bilayer A is highlighted with a green arrow showing the offset cluster arrays within this bilayer; the three coordinating caesium cations in the intra-layer voids are highlighted by pink ellipsoids, whilst the two coordinating caesium cations between adjacent offset cluster arrays are highlighted with light blue ellipsoids. Layer B is also shown, with the six coordinating caesium cations and four coordinating, partially-occupied sodium cations (disordered with caesium cations) between the clusters within this layer being highlighted with light red ellipsoids. Colour scheme: Mo, teal polyhedra; I, gold; Cs, green; Na, grey; O, red.

The neighbouring, co-linear POM cluster layer, i.e. layer B, is composed of stacked arrangements of POM clusters running parallel with the crystallographic *a*-axis, with the minimum inter-layer cluster spacing found to be 3.077 Å, which is also the overall minimum cluster spacing within the supramolecular lattice of **3**. However, the clusters within this layer are found to be offset and oriented at an angle of 25.5° with respect to the clusters in bilayer A, when calculating this angle of orientation through the assignment of mean planes through the molybdenum and iodine centres of each Anderson cluster. The clusters in this layer (minimum cluster spacing 5.302 Å) are separated by six coordinating caesium cations; four coordinating, partially-occupied sodium cations (disordered with caesium cations); and H-bonding solvent H_2O molecules which lend further stability to this cluster layer (Figure 46). To complete the cluster framework this layer of POM clusters,

and the neighbouring bilayer A, are arranged into a repeating ABAB pattern within the crystallographic *ac*-plane (see Figure 47).
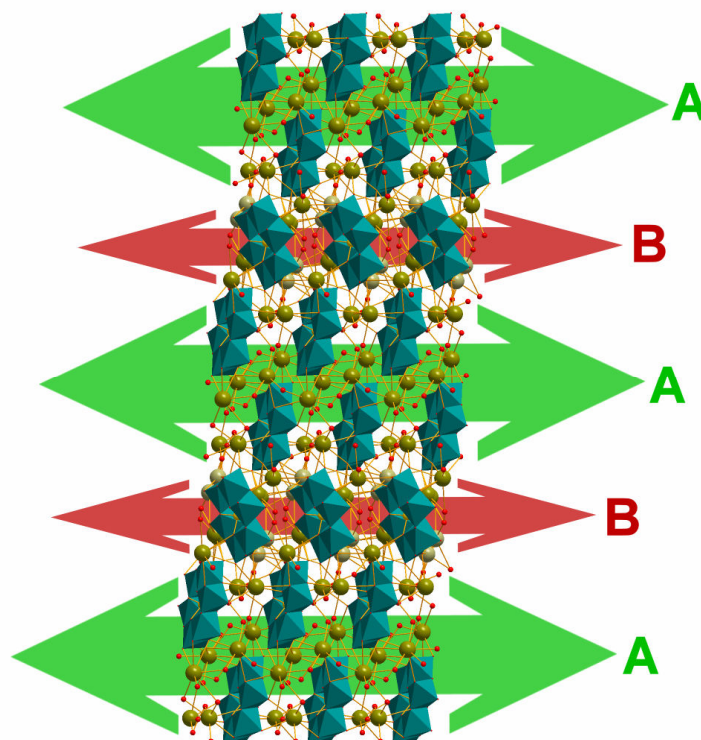
Figure 47: View of compound **3** along the crystallographic *b*-axis highlighting the ABAB layer arrangements of cluster layers running parallel with the crystallographic *a*-axis. Colour scheme: Mo, teal polyhedra; I, gold; Cs, green; Na, grey; O, red.

When viewing the crystal lattice along the crystallographic *a*-axis this repeating ABAB layer pattern of POM cluster layers remains clearly observable. However, when viewing along this axis the two offset, co-linear layers of POM clusters which make up bilayer A are seen to run parallel to the crystallographic *b*-axis. The neighbouring layer B, found previously to be composed of clusters oriented at an angle of 25.5° with respect to those clusters in bilayer A, is also seen to run parallel to the crystallographic *b*-axis; and so the subsequent ABAB cluster layer arrangement is observed to extend within the crystallographic *bc*-plane when viewing the lattice along the crystallographic *a*-axis (see Figure 48).
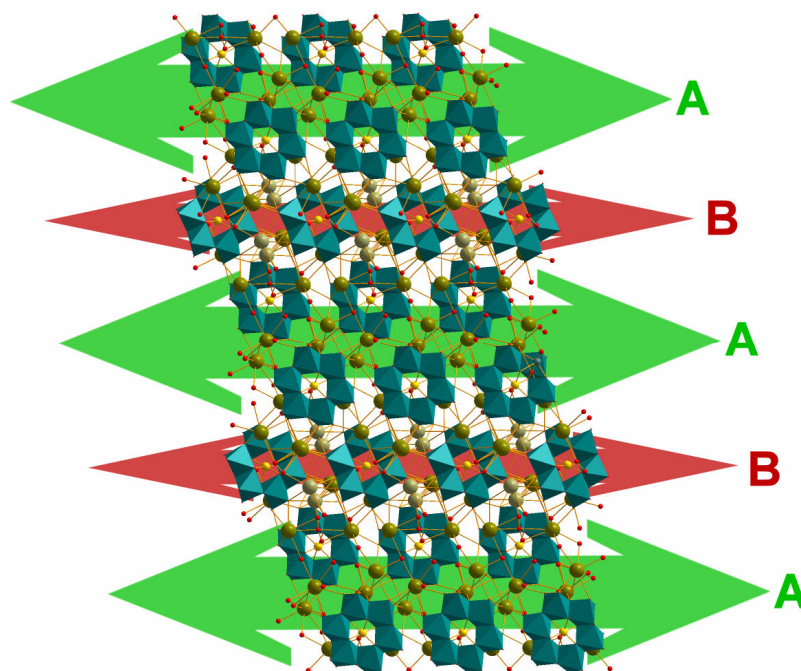
Figure 48: View of compound **3** along the crystallographic *a*-axis. The ABAB layer arrangements of cluster layers running parallel with the crystallographic *b*-axis are highlighted. Colour scheme: Mo, teal polyhedra; I, gold; Cs, green; Na, grey; O, red.

It is important to note, when considering these arrangements of A and B layers along both the crystallographic *a*- and *b*-axes, that the POM clusters in these layers are offset relative to one another. Therefore, when viewing the lattice along the crystallographic *c*-axis, this leads to the interesting observation that these offset arrangements of POM clusters then overlay one another to form co-linear layers within the crystallographic *ab*-plane, oriented at approximately 30° to the crystallographic *b*-axis. Also when viewing the lattice along this axis the H_2O solvent molecules are seen to be positioned in the inter-layer voids, and form H-bonding interactions between the adjacent layers. See Figure 49.
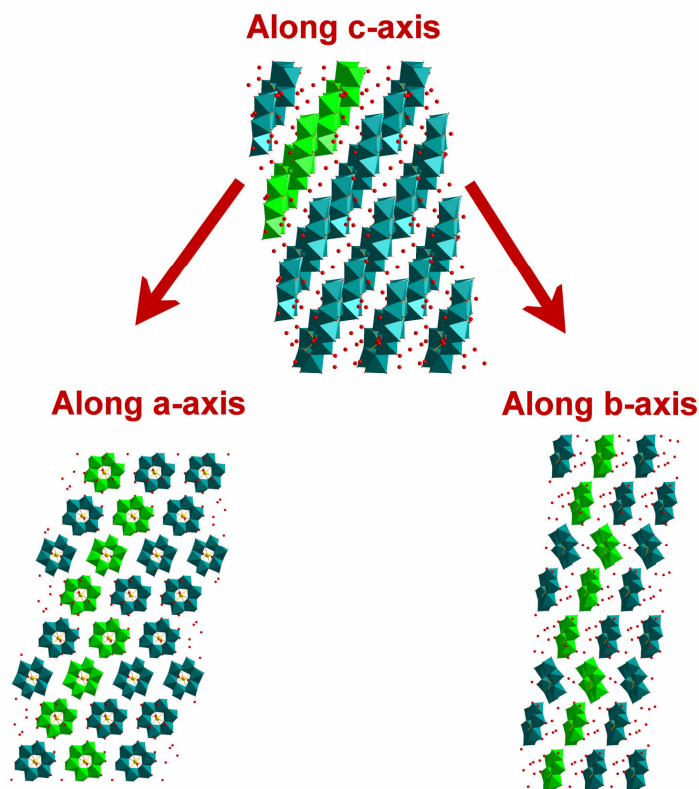
Figure 49: Representation of **3**, when viewed along the crystallographic *c*-axis (top), showing the co-linear layers within the crystallographic *ab*-plane, oriented at approx 30° to the crystallographic *b*-axis. The H_2O solvent molecules which form H-bonding interactions between the adjacent layers can be seen in the inter-layer voids. One of the cluster layers is highlighted in light green to show the position of these clusters when viewing the lattice once again along the crystallographic *a*-axis (bottom left) and along the crystallographic *b*-axis (bottom right). The offset nature of the clusters within each layer is highlighted through these representations. All cations are removed from these figures for ease of viewing the POM cluster layers. Colour scheme: Mo, teal (and light green) polyhedra; I, gold; O, red.

3.6 Formation of $Na_4((HOCH_2CH_2)_3NH)_2[TeMo_6O_{24}]\cdot ca10H_2O$ (4)

The tellurate-centred tungsten Dawson cluster has been successfully isolated and characterized by Cronin *et al* as described in section 1.4.3.[149] Following this discovery it was hoped, as explained previously for the case of the periodate-centred Dawson cluster, that a successful synthetic route to the tellurate-centred molybdenum analogue could also be developed. However, once again these investigations have, so far, allowed only the novel molybdenum Anderson-based compound $Na_4((HOCH_2CH_2)_3NH)_2[TeMo_6O_{24}]$ (**4**) described below, to be isolated and characterized.

It was found that addition of telluric acid, then dropwise addition of an aqueous solution of triethanolamine hydrochloride to an aqueous solution of sodium molybdate, followed by acidification to pH 6.0 using hydrochloric acid, led to the isolation of colourless, rod and block single crystals suitable for single crystal X-ray diffraction. Structural analysis of the X-ray diffraction data revealed the composition of the crystals to be $Na_4((HOCH_2CH_2)_3NH)_2[TeMo_6O_{24}] \cdot ca10H_2O$ (**4**).

The POM cluster anion $[TeMo_6O_{24}]^{6-}$ in compound **4** is, as stated previously, a tellurate-centred Anderson cluster. This cluster comprises six planar, edge sharing $\{MoO_6\}$ octahedra surrounding a central $\{Te^{VI}O_6\}$ heteroanion template, where the tellurium is in the +6 oxidation state. Examination of the unit cell reveals that the charge on this POM cluster is balanced by the four coordinating sodium ions and two singly-charged, protonated triethanolamine (TEAH$^+$) cations, whilst inspection of the cluster bond lengths allows confirmation that all Mo=O terminal, Mo-O bridging, and Te-O bonds are within the expected range of those values quoted in the literature[250] (see Table 5).

Bond Type	Average Bond Distances in Compound **4** / Å
Mo=O (terminal)	1.71
Mo-O (μ_2-bridging)	1.94
Mo-O (μ_3-bridging)	2.28
Te-O	1.92

Table 5: Average bond distances within the $[TeMo_6O_{24}]^{6-}$ cluster anions in compound **4**.

When examining the unit cell of **4** it can be seen that the main building-blocks are the $[TeMo_6O_{24}]^{6-}$ anions and two coordinated cation arrangements, each of which is composed of a $\{Na_2\}$ dimer and a coordinated TEAH$^+$ cation (see Figure 50). In more detail, one of the sodium cations coordinates to the POM cluster through a Mo=O terminal oxo ligand, then coordinates to an adjacent sodium cation through two equatorial, μ_2-bridging oxygen ligands, provided by a water molecule and one of the hydroxyl groups of a TEAH$^+$ cation respectively. The two remaining hydroxyl groups of the TEAH$^+$ cation coordinate in the axial positions of each of these sodium cations, whilst the remaining axial coordination site of these sodium cations coordinates to the POM through a μ_3-bridging oxo ligand on the cluster. This $\{Na_2\}$ dimer and coordinated TEAH$^+$ arrangement is then repeated on the

opposing face of the Anderson cluster anion, and these arrangements of cations are related through a centre of inversion positioned at the tellurium atom in the centre of the Anderson cluster (see Figure 50).
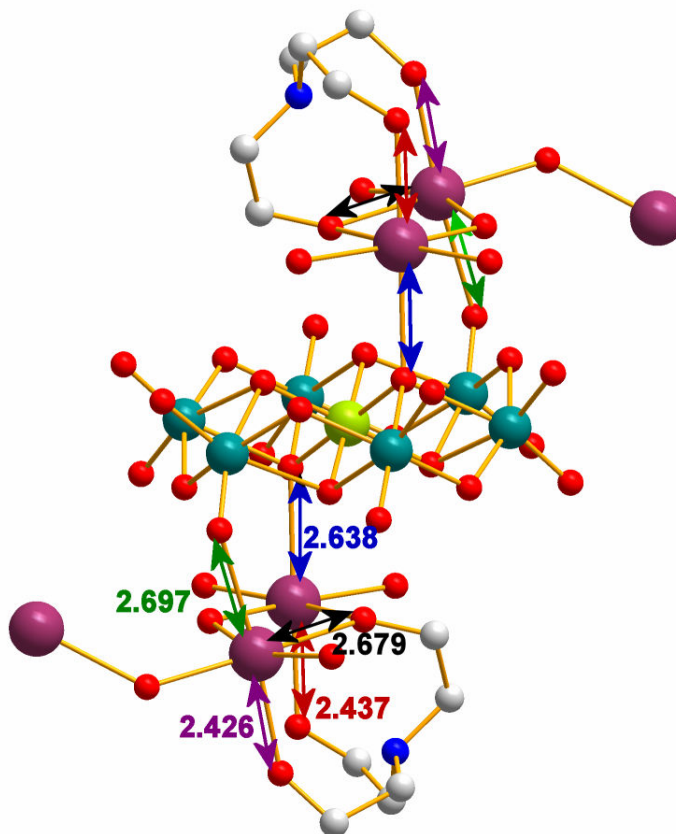
Figure 50: Illustration of the coordinated cation arrangements, each composed of a $\{Na_2\}$ dimer and TEAH$^+$ cation, which are coordinated to opposing faces of the central $[TeMo_6O_{24}]^{6-}$ Anderson cluster. Identical bond lengths in this illustration are shown using arrows of the same colour and all distances shown are measured in Ångströms (Å). Colour scheme for cluster and cation arrangements: Mo, teal; Te, light green; Na, purple; O, red; C, grey; N, blue. H atoms are omitted for clarity.

In each of these coordinated cation arrangements, it can be seen that the other four available coordination sites of the sodium cations are filled with coordinated water molecules, two of which act as μ_2-bridging ligands, each coordinating to the adjacent $\{Na_2\}$ dimer arrangement on a neighbouring POM cluster. This leads to the connection of four adjacent POM clusters to the central cluster shown in Figure 50; where these connected clusters are aligned in an almost parallel fashion, and are tilted at an angle of 71.5° with respect to the central Anderson cluster (see Figure 51).
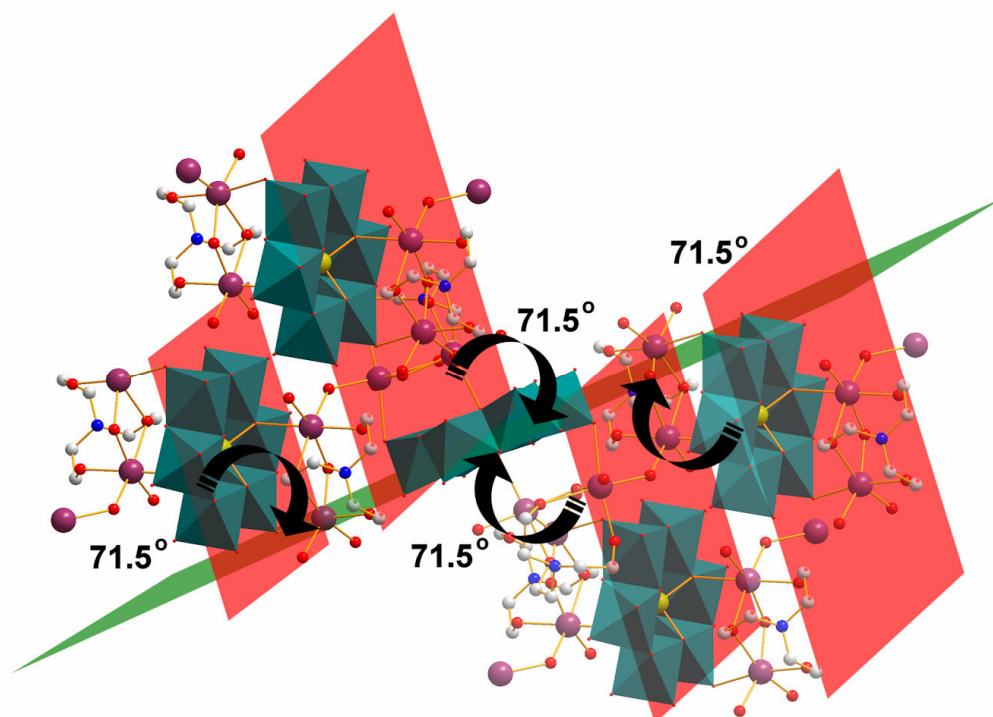
Figure 51: Representation of the central Anderson cluster and its two, coordinated cation arrangements as shown in Figure 50, which then coordinate further through μ_2-bridging H_2O ligands to the {Na_2} dimer units of four neighbouring POM clusters. The almost parallel alignment of these neighbouring POM clusters with one another is highlighted using red planes. Their tilted arrangement at an angle of 71.5° with respect to the green plane through the central Anderson cluster is shown using black arrows. Colour scheme: Mo, teal polyhedra; Te, light green; Na, purple; O, red; C, grey; N, blue. H atoms are omitted for clarity.

It is also interesting to note that while two of these connected adjacent clusters are situated to one side of the central Anderson cluster; due to the effect of the centre of inversion, the two adjacent clusters connected to the opposing face of the central Anderson, are then situated to the opposite side of this cluster (see Figure 52).
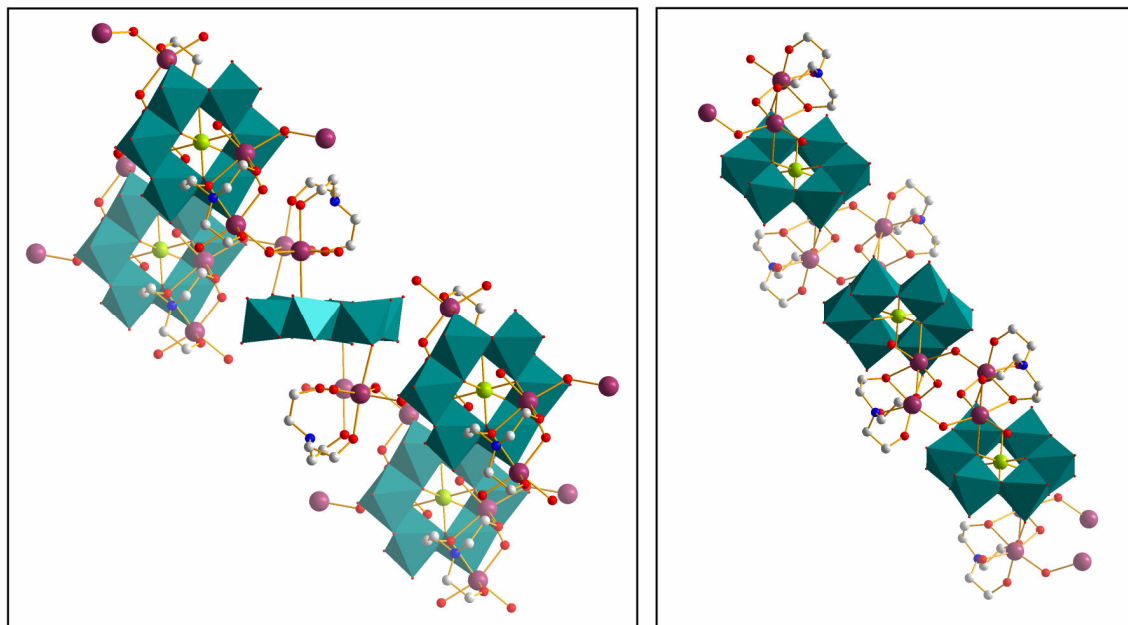
Figure 52: Illustrations of the positioning of the four neighbouring POM clusters which are connected to opposing faces of the central Anderson cluster shown in Figure 50. Due to the effect of the centre of inversion through the central Anderson cluster these neighbouring POM clusters can be seen to be positioned in pairs, one pair on either side of the central Anderson cluster (left). This arrangement of clusters around the central Anderson cluster can also be seen when viewing this structure along the crystallographic *b*-axis (right). Colour scheme: Mo, teal polyhedra; Te, light green; Na, purple; O, red; C, grey; N, blue. H atoms are omitted for clarity.

When extending the packing and viewing the crystal lattice of **4** along the crystallographic *a*-axis, this repeating structural motif of four adjacent POM clusters connected through {Na$_2$} dimers to a central Anderson cluster, reveals an interesting layered structure of inorganic POM building-blocks within the crystallographic *bc*-plane. The POM clusters are seen to be arranged into co-linear layers running parallel with the crystallographic *b*-axis, and the planes of the clusters within each layer lie parallel to one another. However, due to the tilted arrangement of the clusters surrounding the central Anderson cluster of the structural motif, as described previously (see Figure 51), this leads to the observation of a repeating ABAB pattern of POM cluster layers within the crystallographic *bc*-plane (see Figure 53).
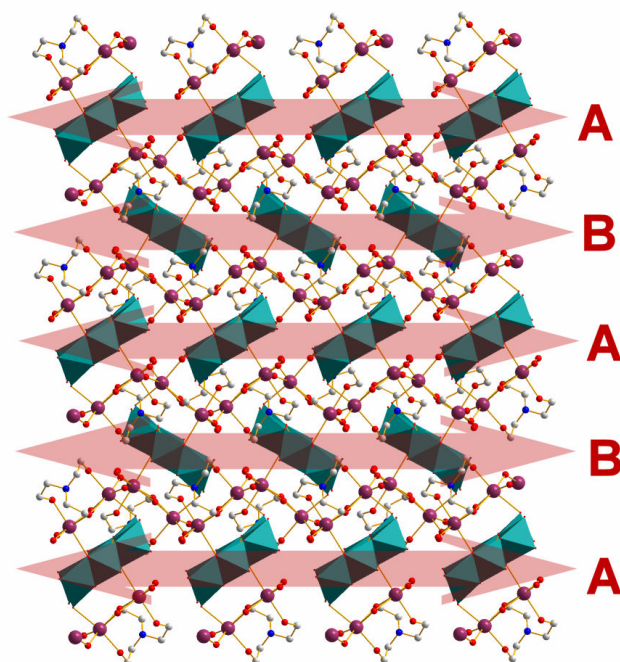
Figure 53: View of compound **4** along the crystallographic *a*-axis showing the co-linear layers of POM clusters running parallel to the crystallographic *b*-axis. Due to the tilted arrangement of the clusters surrounding the central Anderson cluster of the structural motif (as described in Figure 51), this leads to the observation of a repeating ABAB pattern of these POM cluster layers within the crystallographic *bc*-plane. Colour scheme: Mo, teal polyhedra; Te, light green; Na, purple; O, red; C, grey; N, blue. H atoms are omitted for clarity.

This packing arrangement is further reinforced by a vast network of H-bonding interactions formed between the H_2O molecules coordinated to the $\{Na_2\}$ dimer units, the bridging and terminal oxo ligands of the surrounding POM clusters, and the H_2O solvent molecules which fill the intra-layer voids between the clusters.

The minimum intra-layer cluster spacing is found to be 3.493 Å, i.e. between terminal oxo ligands from adjacent POM clusters (also the overall minimum cluster spacing within the lattice of **4**); whilst the minimum inter-layer spacing is found to be 4.353 Å, i.e. between the terminal oxo ligand of a POM cluster which coordinates to a $\{Na_2\}$ dimer, and a terminal oxo ligand of the POM cluster in the adjacent layer which is coordinated to the same $\{Na_2\}$ dimer (see Figure 54).
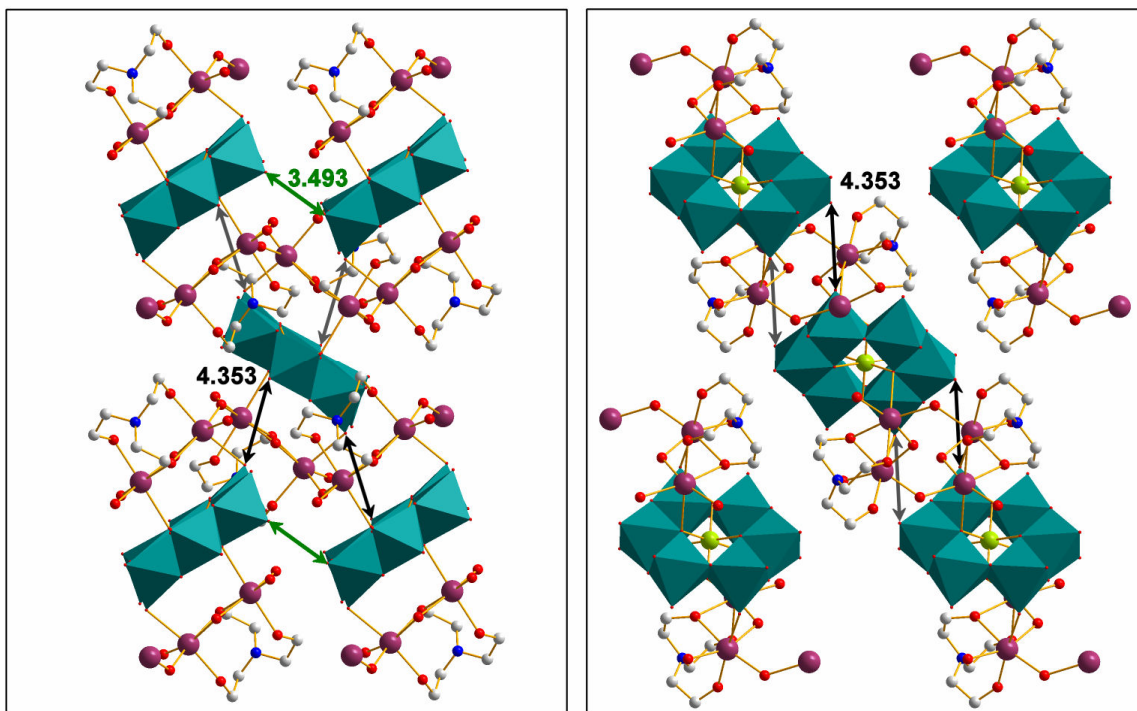
Figure 54: Illustration of the minimum intra- and inter-cluster layer distances when viewing the lattice of compound **4** along the crystallographic *a*-axis (left). The minimum intra-cluster layer distances of 3.493 Å are shown using green arrows, whilst the minimum inter-cluster layer distances of 4.353 Å are shown using black arrows. These inter-cluster layer distances can be illustrated more clearly when viewing along the crystallographic *b*-axis (right). Colour scheme: Mo, teal polyhedra; Te, light green; Na, purple; O, red; C, grey; N, blue. H atoms are omitted for clarity.

It is interesting to note that, situated between these layers of POM clusters, are inorganic-organic cation layers composed of the {Na$_2$} dimer and coordinated TEAH$^+$ cation motifs, described previously and illustrated in Figure 50. These cation layers also run parallel with the crystallographic *b*-axis and, due to the tilted arrangement of the POM cluster layers, this leads to the observation of a wave-like arrangement of sodium cations within each layer (see Figure 55). Further detailed examination of these inorganic-organic cation layers reveals that, once again as a result of the angle between the POM cluster layers, the foremost section of the cationic structural motif within each layer alternates between neighbouring layers. i.e. When the TEAH$^+$ cation is the foremost section of the repeating cationic structural motif within one cation layer, then it is the {Na$_2$} dimer of this repeating motif within the adjacent cation layer which is to the forefront of the layer (see Figure 55). These inorganic-organic cation layers then follow a repeating ABAB arrangement within the crystallographic *bc*-plane (see Figure 55).
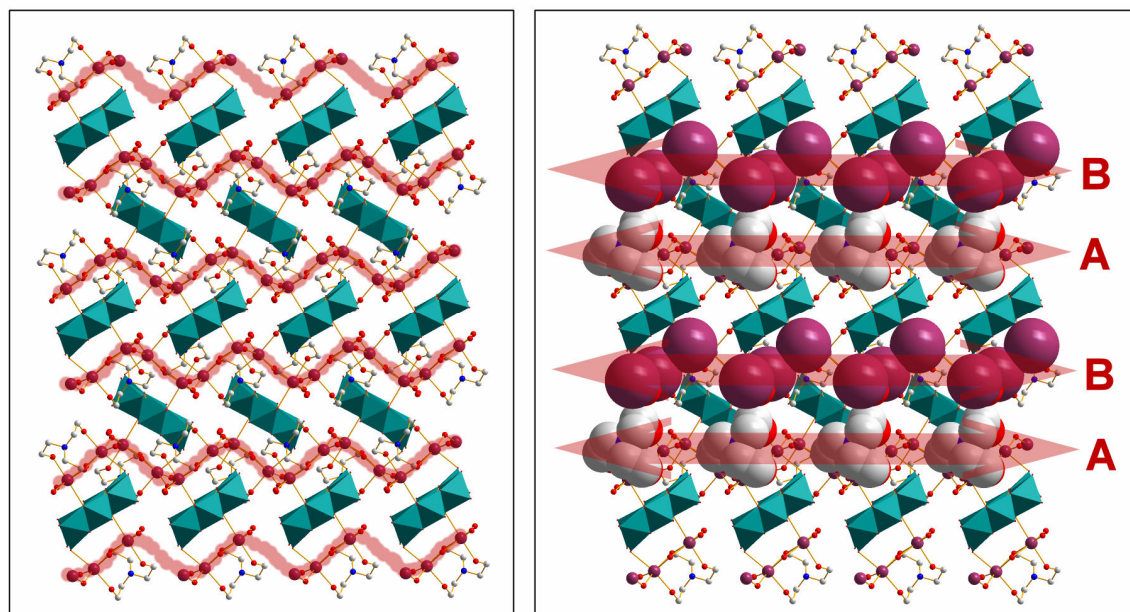
Figure 55: Left: View of compound **4** along the crystallographic *a*-axis with the wave-like arrangement of sodium cations between the POM cluster layers highlighted with red shading. Right: View of **4** along the crystallographic *a*-axis highlighting the inorganic-organic cation layers running between the POM cluster layers. Space-filling representations are used to illustrate how the foremost section of these inorganic-organic cation layers alternates between neighbouring layers, i.e. the TEAH$^+$ cations are positioned to the forefront of layer A, whilst the {Na$_2$} dimer units are positioned to the forefront of layer B. These cation layers are then arranged into a repeating ABAB pattern within the crystallographic *bc*-plane. Colour scheme: Mo, teal polyhedra; Te, light green; Na, purple; O, red; C, grey; N, blue. H atoms are omitted for clarity.

Close inspection of these inorganic-organic cation layers reveals that the minimum intra-layer spacing of sodium cations is 3.925 Å, and the minimum intra-layer carbon-carbon distance between adjacent TEAH$^+$ cations is 4.723 Å (see black arrows in Figure 56). The minimum inter-layer distance between sodium cations is found to be 7.360 Å, whilst the minimum inter-layer spacing between carbon atoms on adjacent TEAH$^+$ cations is 3.787 Å (see green arrows in Figure 56).
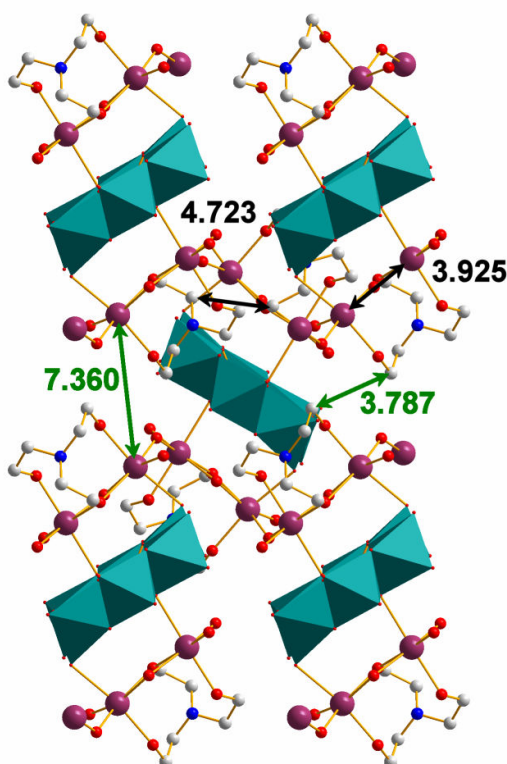
Figure 56: Illustration of a section of compound **4** when viewed along the crystallographic *a*-axis, highlighting the inorganic-organic cation layers. The black arrows show the minimum intra-layer spacing of sodium cations (3.925 Å), and the minimum intra-layer carbon-carbon distance between adjacent TEAH$^+$ cations (4.723 Å). The green arrows show the minimum inter-layer distance between sodium cations (7.360 Å), and the minimum inter-layer spacing between carbon atoms on adjacent TEAH$^+$ cations (3.787 Å). Colour scheme: Mo, teal polyhedra; Te, light green; Na, purple; O, red; C, grey; N, blue. H atoms are omitted for clarity.

When viewing the crystal lattice of compound **4** along the crystallographic *b*-axis the POM clusters can, once again, be seen to be arranged into layers due to the repeating structural motif of four adjacent POM clusters connected through {Na$_2$} dimers to a central Anderson cluster, as illustrated in Figure 51 and 52. However, when studying the lattice along this crystallographic axis it is evident that these layers of clusters can be viewed in two different ways.

The first interpretation (Interpretation (a)) of the arrangement of POM clusters is that they are arranged into co-linear layers running parallel with the crystallographic *c*-axis and extending within the *bc*-plane. Each of these layers is composed of processional arrangements of the central Anderson cluster with its two, coordinated {Na$_2$} dimer and TEAH$^+$ cationic motifs (described in Figure 50), into a columnar sub-structure running parallel with the crystallographic *c*-axis. The planes of the clusters within each layer lie

parallel to one another, however, they are tilted with respect to those in neighbouring layers (see Figure 51), leading to the observation that these integrated POM-cation layers then follow a repeating ABAB pattern within the crystallographic *ab*-plane (see Figure 57).
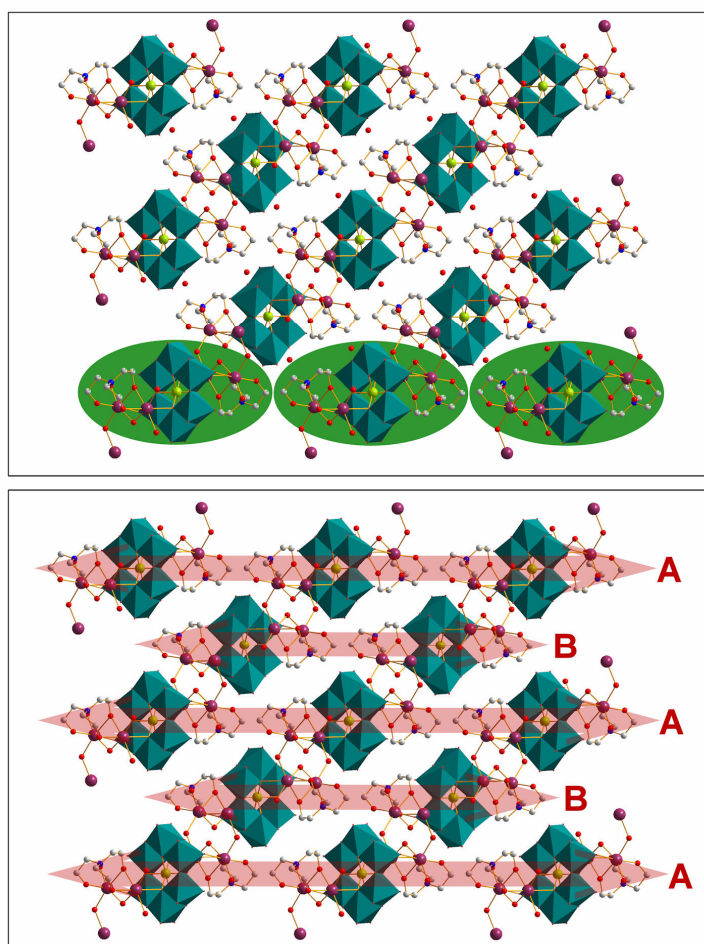
Figure 57: View of compound **4** along the crystallographic *b*-axis. Top: The processional arrangement of coordinated cluster-$\{Na_2\}$ dimer units (described in Figure 50), into a columnar sub-structure running parallel with the crystallographic *c*-axis, is highlighted within one of the POM-cation layers using green ellipsoids round each cluster-$\{Na_2\}$ dimer unit. The H-bonding H_2O solvent molecules lying in the inter-layer voids are also shown. Bottom: The planes of the clusters within each layer lie parallel with one another, however, they are tilted with respect to those of the adjacent layers. This leads to the observation that these layers are arranged into a repeating ABAB pattern within the crystallographic *ab*-plane. Solvent molecules are removed from this illustration for clarity. Colour scheme: Mo, teal polyhedra; Te, light green; Na, purple; O, red; C, grey; N, blue. H atoms are omitted from both illustrations for clarity.

When considering the layers of POM clusters in this way, the inter-layer voids are seen to be filled with H-bonding solvent H_2O molecules (see Figure 57, top illustration), which reinforce the crystal lattice by forming H-bonds between terminal oxo ligands of adjacent clusters within each layer (*ca* 2.9 Å), and with water molecules coordinated to the $\{Na_2\}$

dimers within the next POM-cation layer (*ca* 2.8 Å). Also noticeable when studying the inter-layer spaces is that, on either side of the voids filled with the H-bonding H_2O molecules, the offset clusters from neighbouring layers are actually connected together through the {Na_2} dimer motifs, so forming part of the repeating sub-structure of four adjacent POM clusters connected through {Na_2} dimers to a central Anderson cluster, discussed previously and illustrated in Figures 51 and 52.

Observation of this inter-layer connection between clusters then leads to an alternative interpretation (Interpretation (b)) of the POM cluster arrangement when viewing the lattice of **4** along the crystallographic *b*-axis. This alternative interpretation is centred around the arrangement of the POM clusters into chains which run at an angle of approximately 45° to the crystallographic *a*-axis, and which then connect further through the {Na_2} dimer cation motifs to produce an inter-connected layer of these cluster chains extending along the crystallographic *b*-axis (see Figure 58). This layer is then repeated to form a parallel arrangement of layers within the crystallographic *ac*-plane (see Figure 59, bottom illustration).
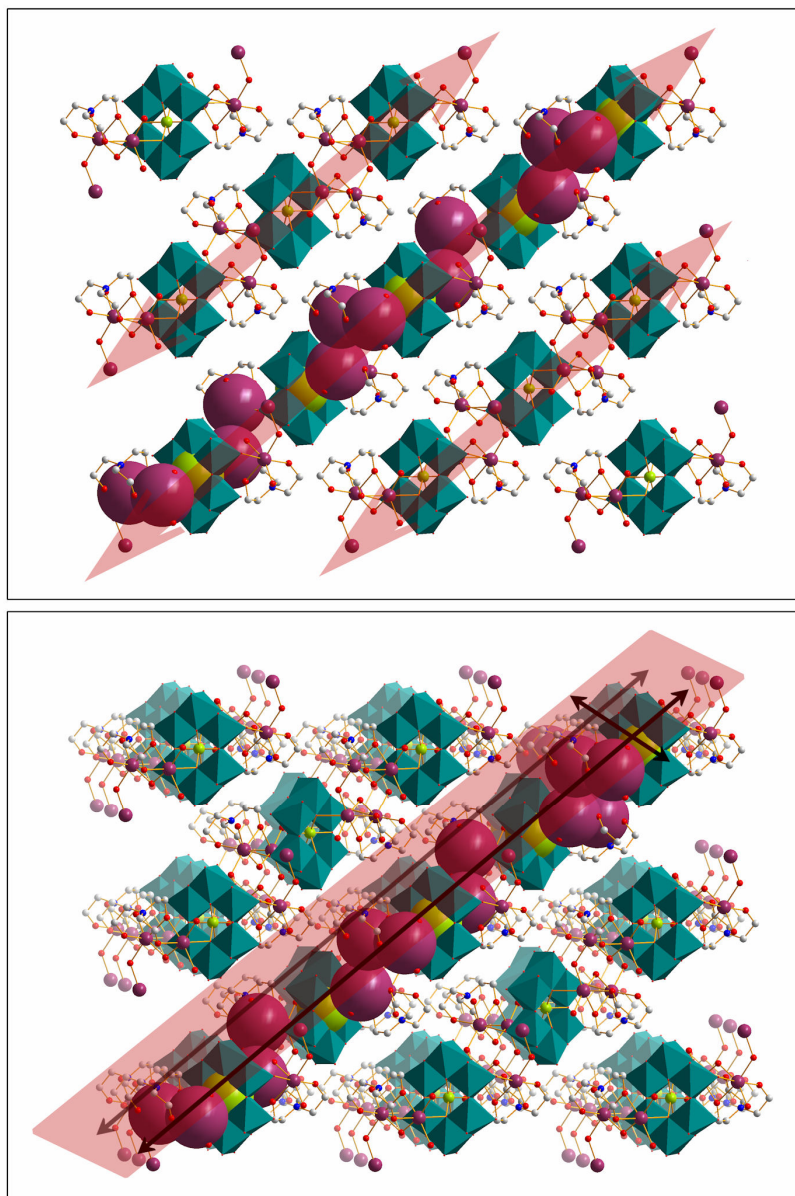
Figure 58: Top: Illustration of compound **4** showing Interpretation (b) of the POM cluster arrangement when viewing along the crystallographic *b*-axis. Space-filling representations are used to show the connection of the POM clusters into chains running at an angle of approximately 45° to the crystallographic *a*-axis. Bottom: Illustration of compound **4** when viewed slightly offset from the crystallographic *b*-axis. This illustration uses a space-filling representation to show the connection of these chains, *via* the {Na$_2$} dimer cation motifs, into layers of cluster chains extending along the crystallographic *b*-axis (as indicated by the black arrows and red plane). Colour scheme: Mo, teal polyhedra; Te, light green; Na, purple; O, red; C, grey; N, blue. Solvent molecules and H atoms are omitted from both illustrations for clarity.

This interpretation of the chain-like arrangement of POM clusters leads to the further observation that the inter-layer spaces between the POM clusters actually form organic cation layers composed of TEAH$^+$ cations, with H-bonding H$_2$O molecules positioned

within the intra-layer voids. It is the protonated amine face of each TEAH$^+$ cation which points into the space between each POM cluster layer, whilst the hydroxyl groups on the opposing face of each cation are coordinated to the {Na$_2$} dimers within the POM cluster layers. In a similar fashion to the layers of POM clusters, these layers of TEAH$^+$ cations follow a repeating pattern within the crystallographic *ac*-plane, each layer lying at approximately 45° to the crystallographic *a*-axis (see Figure 59).
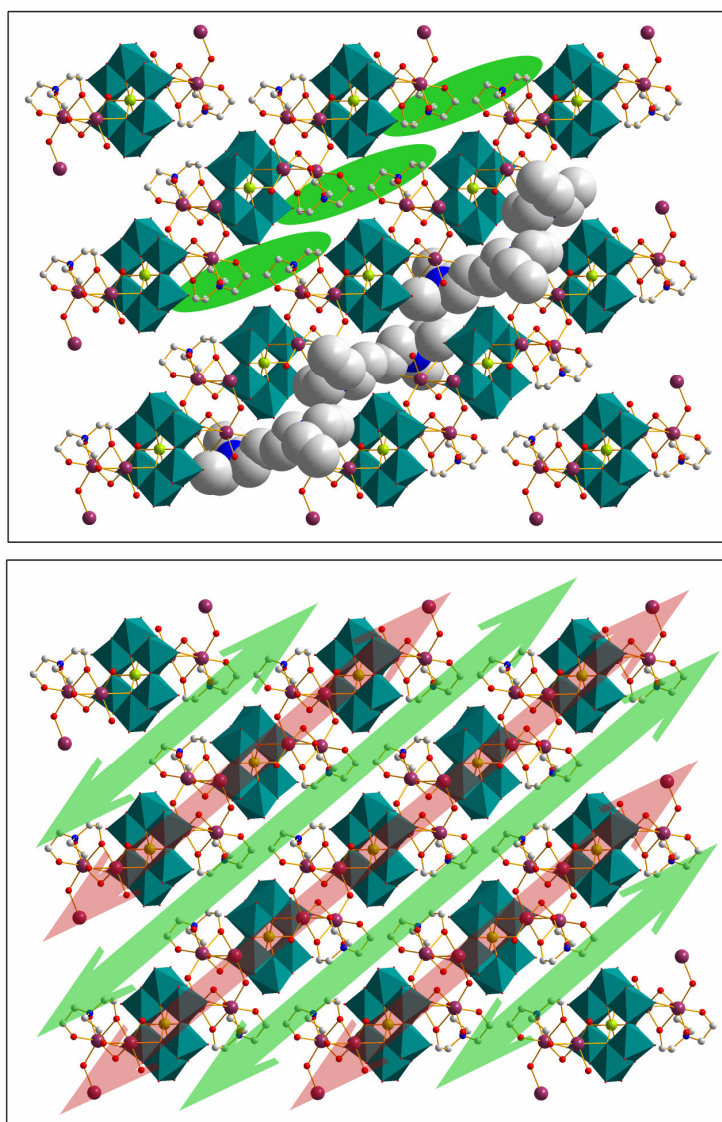
Figure 59: View of compound **4** along the crystallographic *b*-axis. Top: Green ellipsoids are used to highlight the manner in which the protonated amine face of each TEAH$^+$ cation points into the space between the POM cluster layers. Also a space-filling representation of these TEAH$^+$ cation-arms illustrates how these cations form organic cation layers between the POM cluster layers. Bottom: Green and red arrows highlight the repeating pattern of both POM cluster layers and the organic cation layers within the crystallographic *ac*-plane, with both layers lying at an angle of approximately 45° to the crystallographic *a*-axis. Colour scheme: Mo, teal polyhedra; Te, light green; Na, purple; O, red; C, grey; N, blue. Solvent molecules and H atoms are omitted from both illustrations for clarity.

After describing both interpretations of the packing which can be made when viewing the lattice of **4** along the crystallographic *b*-axis, it is now useful to look back to Interpretation (a) and Figure 57 before examining the lattice further along the crystallographic *c*-axis. When studying the lattice along the crystallographic *c*-axis the A and B layers described in Interpretation (a), which are constructed of columns of processional cluster-{Na$_2$} dimer units and run parallel with the crystallographic *c*-axis, are still evident. However, along this axis an end-on view of the columnar sub-structure is observed; where each of the layers runs parallel with the crystallographic *a*-axis; and the layers then follow a repeating co-linear, yet offset, ABAB arrangement within the crystallographic *ab*-plane (see Figure 60).
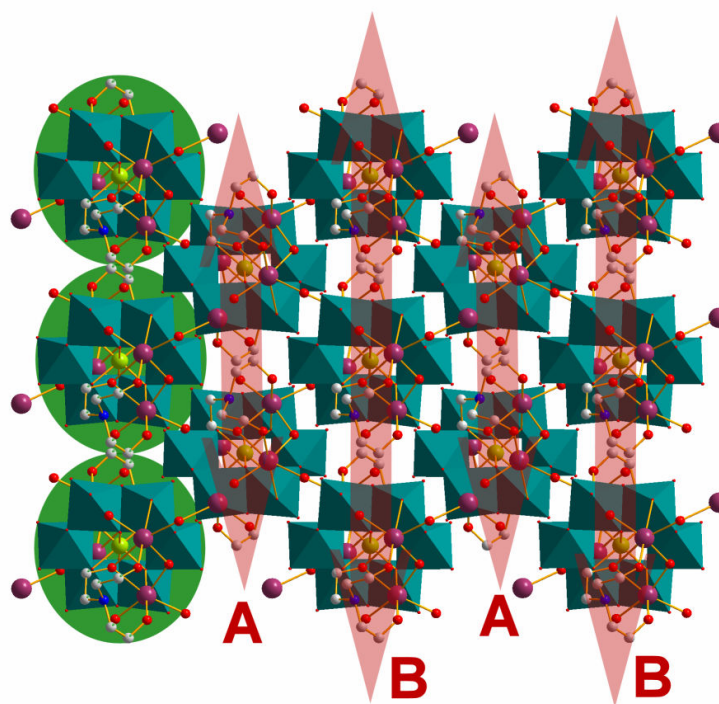
Figure 60: Representation of compound **4** when viewed along the crystallographic *c*-axis. The end-on view of the columnar sub-structures which make up each layer, and which are composed of processional cluster-{Na$_2$} dimer units, are highlighted in one of these layers using green circles. The offset arrangement of these layers, which run parallel to the crystallographic *a*-axis, leads to the observation of a repeating ABAB pattern of layers within the crystallographic *ab*-plane. Colour scheme: Mo, teal polyhedra; Te, light green; Na, purple; O, red; C, grey; N, blue. Solvent molecules and H atoms are omitted for clarity.

3.6.1 Summary of investigations into the encapsulation of periodate and tellurate heteroanion templates within polyoxomolybdate clusters

In summary, through investigations into the synthesis of periodate and tellurate-centered molybdenum Dawson clusters, two novel molybdenum Anderson-based polyoxometalate structures have been isolated and characterized.

Detailed analysis of the first structure $Cs_{4.67}Na_{0.33}[IMo_6O_{24}]\cdot ca7H_2O$ (**3**) has revealed a closely-packed arrangement of periodate-centred molybdenum Anderson clusters (minimum cluster spacing 3.077 Å) which can be seen to form an ABAB layered cluster arrangement, when viewing along both the crystallographic *a*- and *b*-axes. Layer A is composed of a bilayer of offset POM cluster arrays, where three coordinating caesium cations and H-bonding water molecules separate the clusters and reinforce each of these 'sub-layers'; then two further caesium cations reinforce the bilayer arrangement by coordinating between adjacent clusters from each 'sub-layer' (see Figure 46). Layer B is formed by an array of POM clusters which are offset and oriented at an angle of 25.5° with respect to the clusters which make up bilayer A. The structure of this layer is again found to be reinforced by cation coordination and H-bonding interactions, i.e. coordinating caesium cations; partially-occupied sodium cations (disordered with caesium cations); and H-bonding solvent H_2O molecules are found to occupy the spaces between the clusters and so lend further stability to this cluster layer (see Figure 47).

Examination of the tellurate-centred molybdenum Anderson structure $Na_4((HOCH_2CH_2)_3NH)_2[TeMo_6O_{24}]\cdot ca10H_2O$ (**4**) has revealed some interesting packing arrangements which occur as a result of the $\{Na_2\}$ dimer and $TEAH^+$ cation motifs coordinated to the $[TeMo_6O_{24}]^{6-}$ Anderson clusters. Within the unit cell, two of these $\{Na_2\}$ dimer and $TEAH^+$ cation motifs can be seen coordinated to a central Anderson cluster, one situated on each face, and which are related by a centre of inversion positioned at the tellurium atom in the centre of the POM cluster (see Figure 50). Two of the μ_2-bridging H_2O ligands, from each of these $\{Na_2\}$ dimer units, then coordinate to the $\{Na_2\}$ dimers on neighbouring POM clusters, resulting in the connection of four adjacent POM clusters to the central Anderson cluster. These inter-connected clusters are aligned in an

almost parallel fashion, and are tilted at an angle of 71.5° with respect to the central Anderson cluster (see Figure 51).

The presence of this sub-structural, cluster-packing motif, results in a particularly interesting, layered arrangement of inter-connected chains of POM clusters when viewing the lattice along the crystallographic b-axis. These chains of POM clusters are observed to be formed *via* connection through the {Na$_2$} dimer units, and lie at approximately 45° to the crystallographic a-axis. Further inter-connection between these cluster chains results in the formation of layers which extend along the crystallographic b-axis, then repeat in a co-linear fashion within the crystallographic *ac*-plane (see Figure 59).

3.7 Introduction of large, photoactive organic cations into polyoxometalate cluster compounds

Polyoxometalate clusters, as discussed previously in the Introduction, section 1.2.1, possess a wide range of interesting properties such as redox and photochemical activity,[15] ionic charge, and conductivity.[12] Subsequently these compounds have a diverse range of applications, e.g. from catalysis through to medicinal uses.[12-15] In recent times there has been increasing interest in combining these properties with those of coordinated, or electrostatically associated, organic counter-cations which also present some interesting electronic properties or photoactivity. Such research is carried out in order to produce materials that are not only of structural interest, but also possess emergent electronic properties or photoactivity, i.e. properties not associated with the lone polyoxometalate structure or the lone organic component of the system.

Some examples of such research include the introduction of electron-rich molecules derived from tetrathiafulvalene (TTF),[12, 251-254] substituted amide organic cations,[255-258] aromatic amine cations,[259-264] and large electron-rich porphyrins[169, 265-270], into polyoxometalate systems. The works cited using organic molecules derived from tetrathiafulvalene with POM clusters have focused on the emergent electronic and magnetic properties of the synthesized hybrid structures, whilst the studies using substituted amide, aromatic amine, and porphyrin molecules in POM systems have

investigated the synthesized structures with respect to their interesting framework formations, their photoactivities, and their intermolecular charge transfer interactions with the POM clusters.

In this current work it was, therefore, decided to investigate the synthesis of novel POM-organic compounds with interesting structural compositions, emergent electronic properties, and photoactivities. This was pursued through the introduction, into polyoxometalate systems, of aromatic organic molecules from a family of phenanthridinium-based molecules developed by Cronin *et al*.[209] This family of phenanthridinium-based molecules was chosen for use in this research due to the capacity of these molecules for large variation in structure, size and charge by altering the substituent R groups[209, 210] (as described in section 3.7.1); and their highly aromatic, electron-rich cores, which have led to observation of some interesting photochemical properties in previous work.[211]

As an introduction to this work, this family of phenanthridinium-based molecules (section 3.7.1), and the specific organic molecules chosen from this family for further investigation with POM systems (section 3.7.2), are described in more detail below. The subsequent use of these molecules in the successful isolation and characterization of three novel POM-organic compounds with emergent properties is then described (section 3.8).

3.7.1 2,3-dihydro-1*H*-imidazo[1,2-*f*]phenanthridinium (DIP) and imidazo-phenanthridinium (IP) as organic cations

A family of Dihydro-Imidazo-Phenanthridinium (DIP) molecules, which can be synthesized in facile 'one-pot' synthetic reactions, has been developed by Cronin *et al*.[209] The presence of the phenanthridinium core leads these molecules to exhibit DNA affinity and high cytotoxic activity[271] as well as photoactivity due to the aromaticity of the core. See Figure 61.
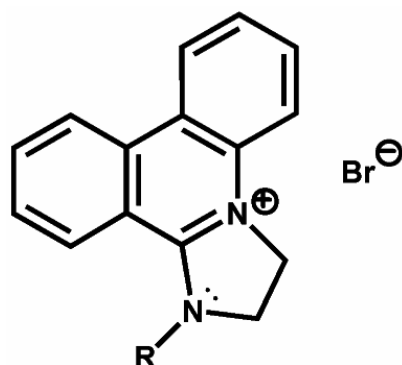
Figure 61: Representation of the DIP framework. The R group is determined by the primary amine chosen for reaction with the 2-bromoethyl-phenanthridinium bromide starting material.

The reaction mechanism for the formation of these molecules is shown in Figure 62 and involves nucleophilic addition of a primary amine to the α position of the highly reactive iminium moiety of the starting material 2-bromoethyl-phenanthridinium bromide (step A), followed by a 5-*exo-tet*-cyclization (step B), and an oxidative hydride loss.[209, 272]
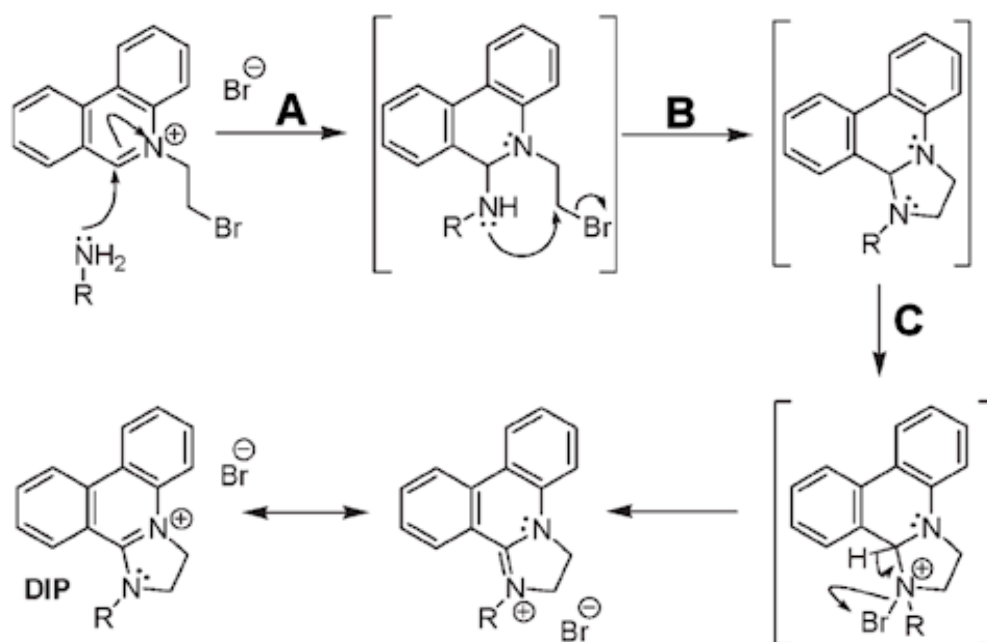
Figure 62: Reaction mechanism for the formation of DIP derivatives. Reaction conditions are as follows. Step A: H_2O/EtOAc, $NaHCO_3$, 0 °C to room temperature, N_2, 2 h; Step C: Aqueous wash, *N*-bromosuccinimide (NBS), 0 °C to room temperature, 2 h.[209]

Following development of this family of DIP compounds, further work was carried out by Cronin *et al* to produce a more planar, fully aromatic Imidazo-Phenanthridinium (IP) molecular framework.[210] The aim was to produce, not only a new subset of imidazole-containing molecules, but also a family of molecules with an even greater DNA binding

affinity, maximised by the more favourable π-π interactions in these higher planarity structures. Additionally, by introducing an imidazole moiety into the structure framework, this would allow the planar, DNA-binding core of the molecule to be modified by substitution at C1 and C2 (see Figure 63). In contrast, substitution at these sites in the DIP molecule is harder to achieve, due to the lower reactivity of the alkane bond.
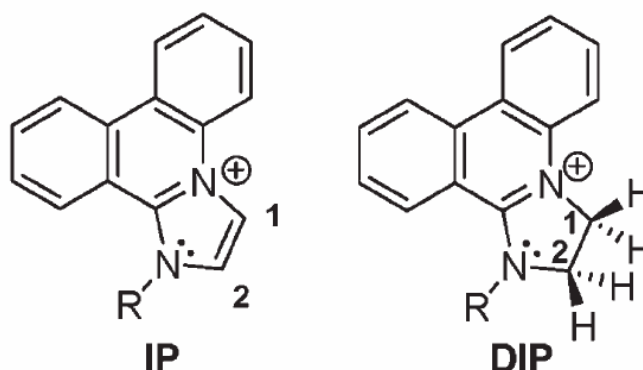
Figure 63: Representations of the IP (left) and DIP (right) frameworks. The R group in the IP framework is determined by the electrophilic reagent chosen for use in the final step of the synthesis. C1 and C2, i.e. the sites for substitution in the IP molecule, and the corresponding carbon positions in the DIP framework are marked.

The reaction mechanism for the formation of the IP molecule is shown in Figure 64. The starting material 2-bromoethyl-phenanthridinium bromide is reacted with liquid ammonia to form an alpha adduct **1** (Step A), which then undergoes an intramolecular cyclisation. Addition of an excess of manganese dioxide under basic reaction conditions (Step B) gives rise to the two oxidation steps required to obtain the imidazo-phenanthridine intermediate **2**. This intermediate subsequently carries out nucleophilic substitution of an electrophile R-X (Step C) giving the final IP product.[210]
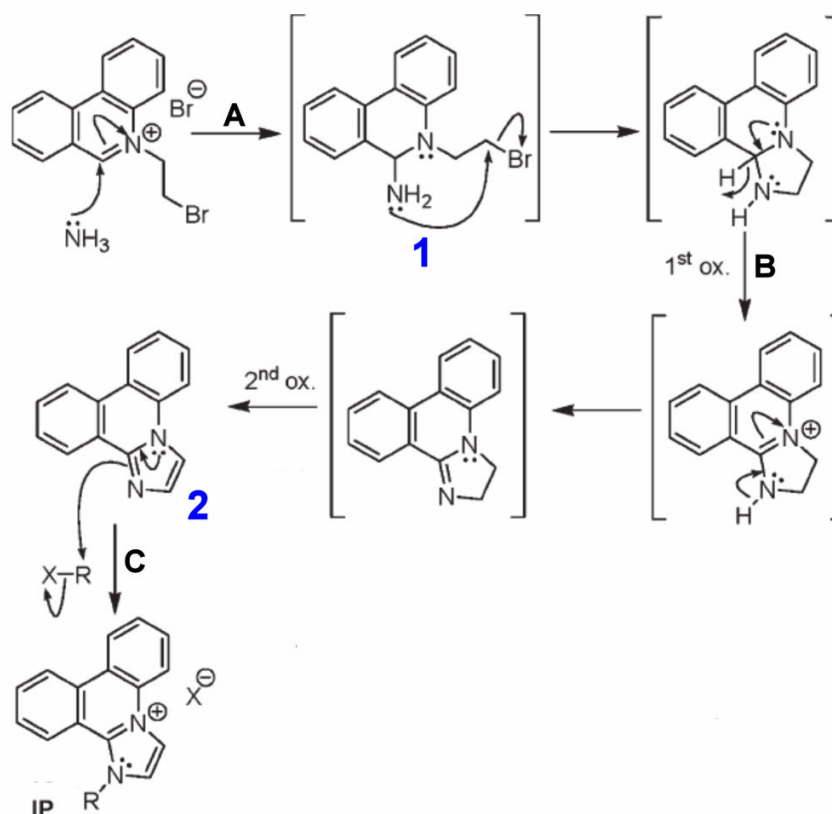
Figure 64: Reaction mechanism for the formation of IP derivatives. Reaction conditions are as follows. Step A: liquid ammonia, -78 °C, 1 h; Step B: Na_2CO_3, MnO_2, -78 °C to reflux in toluene, 3 h; Step C: electrophile R-X, toluene, overnight reflux.[210]

On development of the synthetic route to the IP structures reported[210] it was observed that a chloroform solution of the phenanthridine intermediate **2** in Figure 64 showed an unusual degree of photochromic behaviour, turning to blue within a few hours in daylight. Further investigations by Cronin *et al*[211] with other imidazo-pyridine-like derivatives were carried out which showed that molecules containing unsubstituted imidazole moieties displayed similar photochromic behaviour, whereas molecules where the imidazole moieties carried substituent R groups in the C1 and C2 positions (see Figure 63) remained colourless even when irradiated with UV light.

In this current work, given the interesting properties of these DIP and IP compounds discussed above; their capacity for variation in structure size by altering the substituent R groups; and highly aromatic, electron-rich cores; it was decided to explore the possibility of utilising these properties within a rigid inorganic framework by incorporation of DIP and IP molecules into POM synthetic systems.

3.7.2   DIP and IP compounds selected for use in POM reaction systems

3.7.2.1   1-[2-(2-amino-ethylamino)-ethyl]-2,3-dihydro-1*H*-imidazo[1,2-*f*]phenanthridinium tribromide

The first DIP compound chosen for investigation in POM systems was 1-[2-(2-amino-ethylamino)-ethyl]-2,3-dihyro-1*H*-imidazo[1,2-*f*]phenanthridinium tribromide (also written as (DIP-1)Br$_3$). This was produced *via* the previously reported annulation reaction[209] in which a primary amine, diethylenetriamine, synthesized according to a method by Reineke *et al*,[273] reacts with 2-bromoethyl-phenanthridinium bromide resulting in a ring-extended phenanthridinium system with a pendant amine moiety.[274] The triply-charged DIP-1 cation could then be made readily available for reaction with a highly anionic POM by dissolution in aqueous solution. See Figure 65.
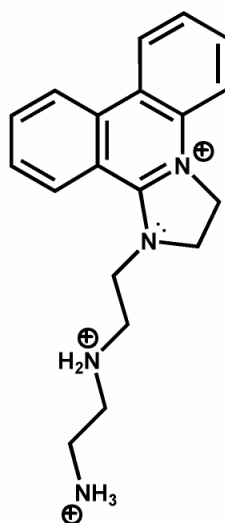
Figure 65: Structural representation of the triply-charged DIP-1 cation, i.e. 1-[2-(2-amino-ethylamino)-ethyl)-2,3-dihyro-1*H*-imidazo[1,2-*f*]phenanthridinium.[274]

3.7.2.2   *cis*-1,3,5-tri(2,3-dihydro-1*H*-imidazo[1,2-*f*]phenanthridinium)cyclohexane tribromide

The second DIP compound chosen for investigation within POM synthetic systems was *cis*-1,3,5-tri(2,3-dihydro-1*H*-imidazo[1,2-*f*]phenanthridinium)cyclohexane tribromide (also written as (DIP-2)Br$_3$). This compound was synthesized as previously reported using a

similar method to that for the DIP-1 compound,[209] but using the synthesized molecule *cis*-1,3,5-triaminocyclohexane[275-277] as the primary amine. Although at the time of synthesis the identity of this molecule was confirmed by ^{1}H NMR, ^{13}C NMR, IR, FAB-MS, and EA, no single crystal structures of this molecule could be isolated. It was for this reason, along with the interesting photoactivity, and stereo-chemistry of this large organic molecule, that it was decided to investigate the introduction of this triply-charged cation, *cis*-1,3,5-dihydro-1*H*-imidazo[1,2-*f*]phenanthridinium)cyclohexane (DIP-2), into POM systems. See Figure 66.
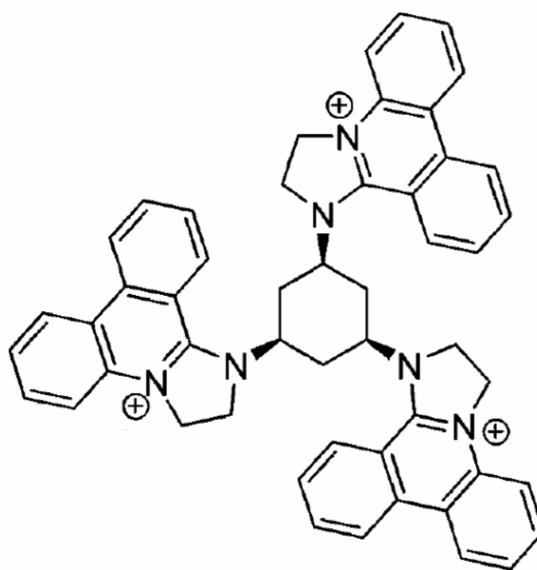
Figure 66: Structural representation of the triply-charged DIP-2 cation, i.e. *cis*-1,3,5-tri(2,3-dihydro-1*H*-imidazo[1,2-*f*]phenanthridinium)cyclohexane.[209]

3.7.2.3   1*H*-Imidazo[1,2-*f*]phenanthridinium chloride

The IP compound chosen for investigation in POM synthetic systems was 1*H*-imidazo[1,2-*f*]phenanthridinium chloride (also written as (IPblue)Cl). This compound was synthesized following the IP synthesis procedure described previously and illustrated in Figure 64.[210, 278] In order to form this unsubstituted IP, the final nucleophilic substitution step (Step C in Figure 64) was carried out using HCl (37%) as the electrophile, so precipitating the final product from the solution as a chloride salt. It was hoped that the use of this singly-charged IP cation (IPblue), see Figure 67, in reactions with POM anions would lead to interesting structures, as well as photoactivity in the products, due to the potential for π-π

stacking interactions between the IP cations when the structure requires multiple cations for charge balance.
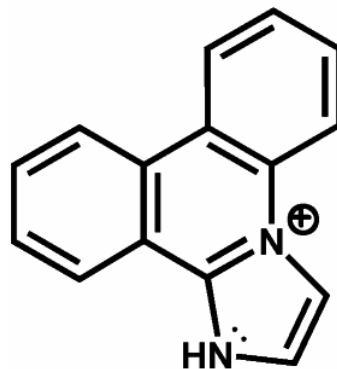
Figure 67: Structural representation of the singly-charged IPblue cation, i.e. 1*H*-imidazo[1,2-*f*]phenanthridinium.[278]

3.8 Introduction of 2,3-dihydro-1*H*-imidazo[1,2-*f*]phenanthridinium (DIP) and imidazo-phenanthridinium (IP) cations into POM systems

In this current work the aforementioned DIP and IP compounds were used in many reactions using a variety of POM anions, for example, various heteroatom-centered Keggin clusters e.g. $[SiW_{12}O_{40}]^{4-}$, $[AlW_{12}O_{40}]^{5-}$, $[CoW_{12}O_{40}]^{6-}$; Dawson clusters e.g. $[P_2W_{18}O_{62}]^{6-}$, $[W_{18}O_{56}(SO_3)_2(H_2O)_2]^{8-}$; lacunary clusters e.g. $[\gamma\text{-}SiW_{10}O_{36}]^{8-}$, and larger POM structures e.g. $[H_{12}W_{36}O_{120}]^{12-}$, were tested. However, due to difficulties during the introduction of these large organic molecules to the POM systems, the majority of these reactions did not lead to the isolation of single crystals suitable for single crystal X-ray diffraction. The two major difficulties experienced in these experiments were:

- insolubility of the DIP-POM or IP-POM precipitates formed during the introduction of these large organic molecules to the POM systems, therefore precluding recrystallization and subsequent successful analyses;
- upon recrystallization, only very poor quality, very small crystals or no crystalline products whatsoever could be recovered from the DMSO or DMF solvents which were required for dissolution of the precipitated product.

However, despite the problems described above, it was found that reaction of the DIP and IP compounds with triply protonated phosphotungstic acid, $H_3[PW_{12}O_{40}]$, allowed the isolation and characterization of the polyoxometalate compounds described in the following sections.

3.8.1 Formation of (DIP-1)[PW$_{12}$O$_{40}$]·5DMSO·*ca*1H$_2$O (5)

Addition of an aqueous solution containing (DIP-1)Br$_3$ in excess, to an aqueous solution of H$_3$[PW$_{12}$O$_{40}$], resulted in the formation of an orange precipitate. Recrystallization of this precipitate from hot DMSO led to the formation of yellow, needle-like, single crystals suitable for single crystal X-ray diffraction. Structural analysis of the X-ray diffraction data revealed the composition of the crystals to be (DIP-1)[PW$_{12}$O$_{40}$]·5DMSO·*ca*1H$_2$O (**5**).

Before investigating the packing arrangements within the lattice of compound **5** the [PW$_{12}$O$_{40}$]$^{3-}$ anion itself, which forms a 1:1 electrostatic relationship with the triply-charged DIP-1 cation, is inspected in more detail. This POM cluster is introduced into the reaction system as a pre-formed cluster building-block which is composed, as discussed previously (see Introduction, section 1.4.2), of four {W$_3$O$_{13}$} sub-units assembled around a central (PO$_4$)$^{3-}$ heteroanion template. Inspection of the bond lengths within this cluster anion in the crystal structure of compound **5** reveals all the W=O terminal bonds, bridging W-O bonds, and P-O bonds to be within the expected range of those values quoted in the literature,[259] see Table 6.

Bond Type	Average Bond Distances in Compound **5** / Å
W=O (terminal)	1.69
W-O (μ_2-bridging)	1.91
W-O (μ_4-bridging)	2.45
P-O	1.53

Table 6: Average bond distances within the [PW$_{12}$O$_{40}$]$^{3-}$ cluster anion in compound **5**.

Examination of the unit cell of compound **5** reveals that the shortest contact distance between the cation and anion is 2.918 Å. Specifically this contact distance is found between a terminal oxo of the cluster and the aromatic ring nitrogen of the DIP cation. Looking at the protonated diethylenetriamine chain of the DIP, the closest contact between this moiety and the cluster is 3.050 Å, i.e. between the carbon atom adjacent to the terminal ammonium group of the DIP-1 cation, and a terminal oxo ligand on the cluster. This close contact could indicate the presence of a H-bonding interaction between the methylene

hydrogens of the DIP cation and the terminal oxo ligand of the POM cluster. This could be induced by the close proximity of the protonated ammonium groups to the methylene hydrogens in the DIP which exert a negative inductive effect upon the methylene group, and so induce a degree of polarity in the C-H bonds. See Figure 68.
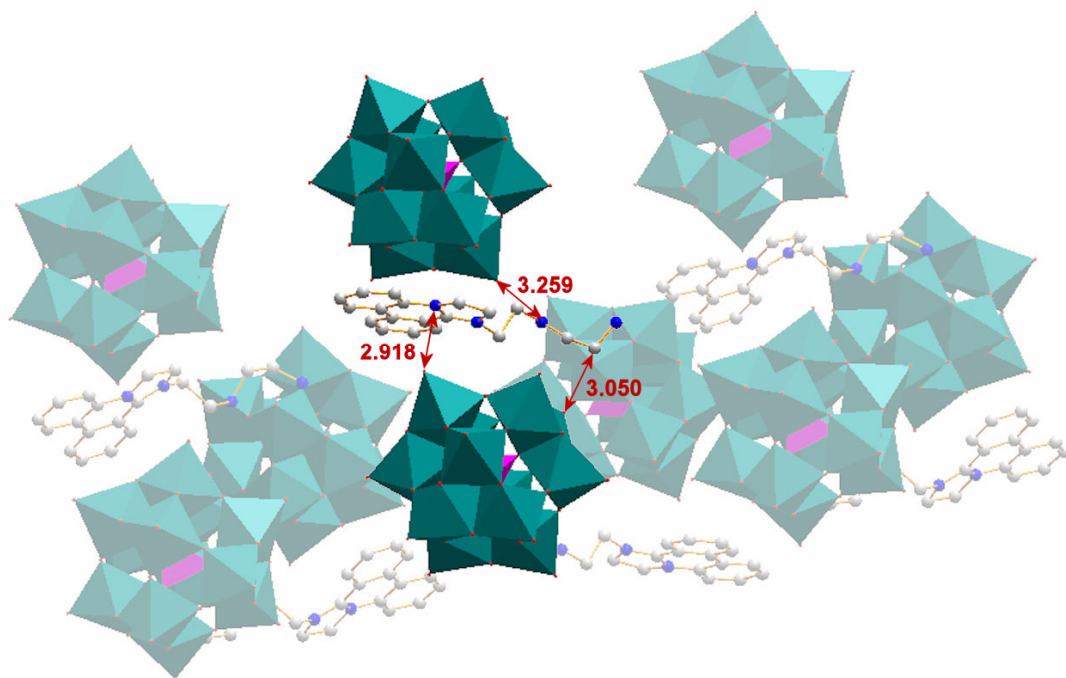
Figure 68: Illustration of the shortest contact distances between the DIP-1 cation and POM anion of compound **5**. All distances shown are measured in Ångströms (Å). Colour scheme: W, teal polyhedra; P, pink polyhedra; O, red; C, grey; N, blue. Solvent molecules and H atoms are omitted for clarity.

When extending the packing and viewing the crystal lattice along the crystallographic a-axis, the $[PW_{12}O_{40}]^{3-}$ clusters can be seen to form the inorganic structure framework of compound **5** through their anti-parallel arrangement in two layers, which run parallel to the crystallographic b-axis. The minimum cluster spacing between these layers is 3.152 Å, i.e. between terminal oxo ligands from adjacent clusters; and this is also the overall, minimum distance between two clusters within the supramolecular lattice of **5**. The anti-parallel layers then follow a repeating ABAB pattern within the crystallographic bc-plane to complete the inorganic framework (see Figure 69).
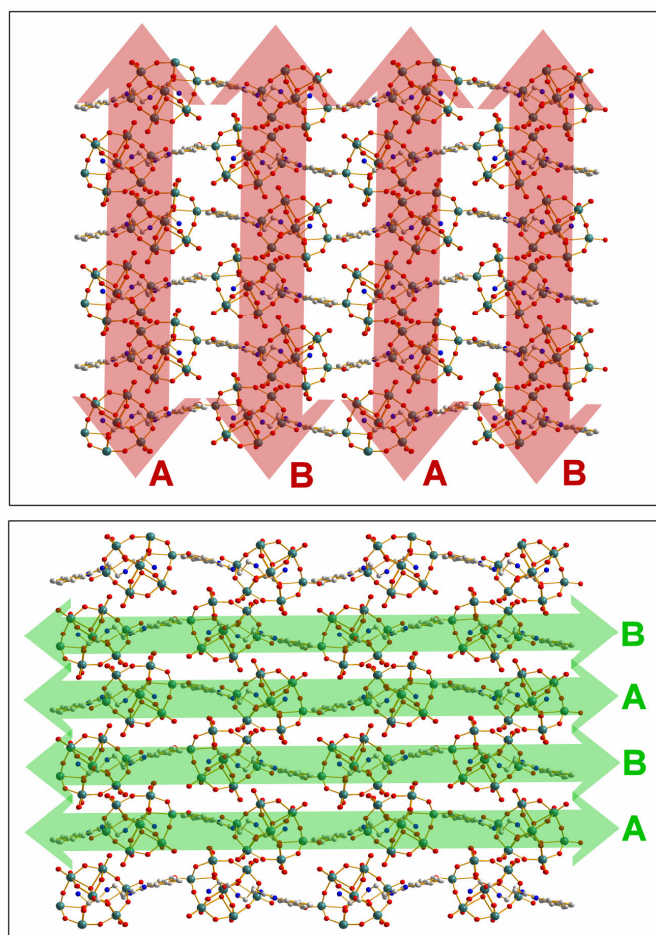
Figure 69: View of compound **5** along the crystallographic *a*-axis. Top: The anti-parallel arrangement of POM clusters in two layers, which run parallel to the crystallographic *b*-axis; and the subsequent repeating ABAB pattern of these layers within the crystallographic *bc*-plane, are highlighted using red arrows. Bottom: The wave-like layers of DIP-1 cations which run parallel to the crystallographic *c*-axis, and which are arranged in a repeating ABAB pattern within the crystallographic *bc*-plane, are highlighted using green arrows. Colour scheme: W, teal; P, pink; O, red; C, grey; N, blue. Solvent molecules and H atoms are omitted from both illustrations for clarity.

It is interesting to look in more detail at the inter-layer voids (minimum cluster spacing 3.655 Å) between the A and B inorganic cluster layers, as they are filled with H-bonding DIP cations, DMSO and H_2O solvent molecules, as well as disordered DMSO solvent molecules. This extended H-bonding network is formed between the protonated diethylenetriamine chain of the DIP and the surrounding DMSO and H_2O solvent molecules, i.e. the shortest H-bond between the DIP cation and a DMSO molecule is 2.653 Å, whilst the H-bond between the DIP cation and a H_2O molecule is 3.020 Å. This H_2O molecule then forms a corresponding H-bond of 3.023 Å with a bridging oxo ligand of an adjacent POM cluster. These interactions all further reinforce the supramolecular lattice of **5**.

Another noticeable feature of the crystal lattice when viewed along the crystallographic a-axis is the wave-like layers of DIP-1 cations which run parallel to the crystallographic c-axis, and which are arranged in a repeating ABAB pattern within the crystallographic bc-plane (see Figure 69). This ABAB arrangement is created by the DIP cations within each layer being arranged in a head-to-tail fashion, whilst the DIP cations of neighbouring layers are formed into anti-parallel arrangements (see Figure 68 and Figure 70). Indeed the closest distance between adjacent DIP-1 cations in **5** is 4.140Å, which is an intra-layer distance between the head unit of one DIP and the tail unit of the adjacent DIP cation. In detail, this distance is between a carbon on the aromatic rings of one DIP, and the terminal ammonium group of the adjacent DIP.
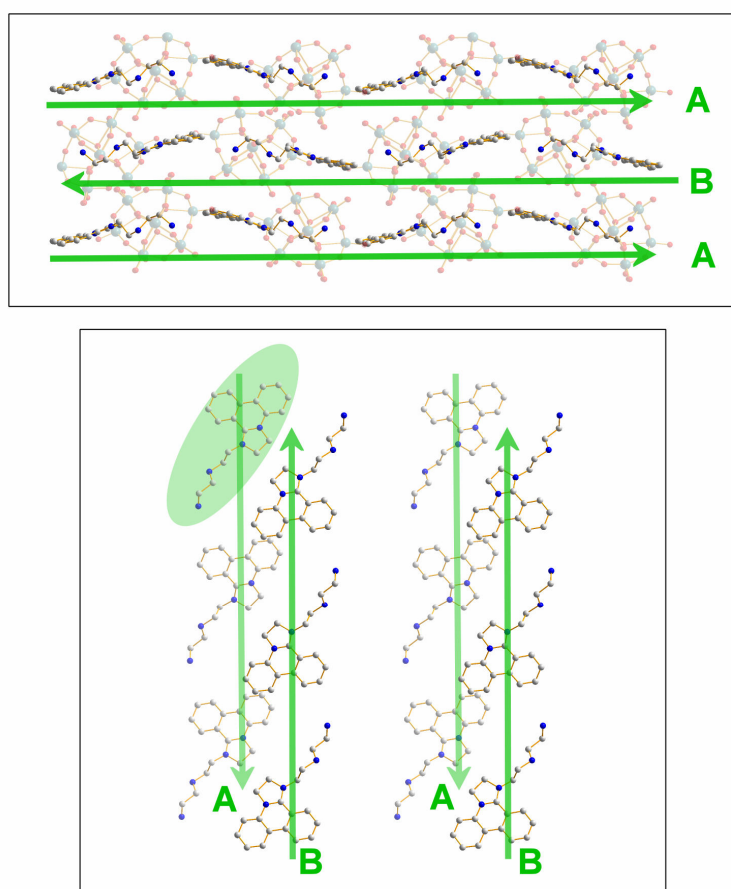
Figure 70: Top: View of compound **5** along the crystallographic a-axis. The head-to-tail orientation of the DIP-1 cations within each wave-like layer of the ABAB pattern is highlighted by the direction of each green arrow. Solvent molecules and H atoms are removed for clarity. Bottom: View of compound **5** along the crystallographic b-axis, showing only the DIP-1 cation layers. This view of the cations provides a clear illustration of the head-to-tail alignments of DIP cations within each layer, and the anti-parallel arrangements of the DIP cations of neighbouring layers. Once again the head-to-tail orientation of the DIP-1 cations within each layer is highlighted by the direction of each green arrow. H atoms are omitted from this illustration for clarity. Colour scheme: W, teal; P, pink; O, red; C, grey; N, blue.

When viewing the lattice of **5** along the crystallographic *c*-axis, further interesting packing details become apparent. The inorganic clusters and DIP cations are aligned together into layers running parallel with the crystallographic *b*-axis, alternating between inorganic and organic components as you move along the length of the layer (see Figure 71). These layers are then arranged into a repeating ABAB pattern within the crystallographic *ab*-plane. It is noticeable, within each of these inorganic-organic layers, that each DIP is positioned so that the aromatic head group is enclosed within the layer, whilst the tail group is directed outwards towards the H-bonding DMSO and H_2O molecules lying within the inter-layer voids. Due to these H-bonding interactions a wave-like layer of DMSO molecules can be seen within each inter-layer void, running parallel to the crystallographic *b*-axis. The wave-like pattern of each layer is introduced by the anti-parallel arrangement the DMSO molecules in order to maximise the H-bonding interactions with the tail groups of the DIP cations (see Figure 71).
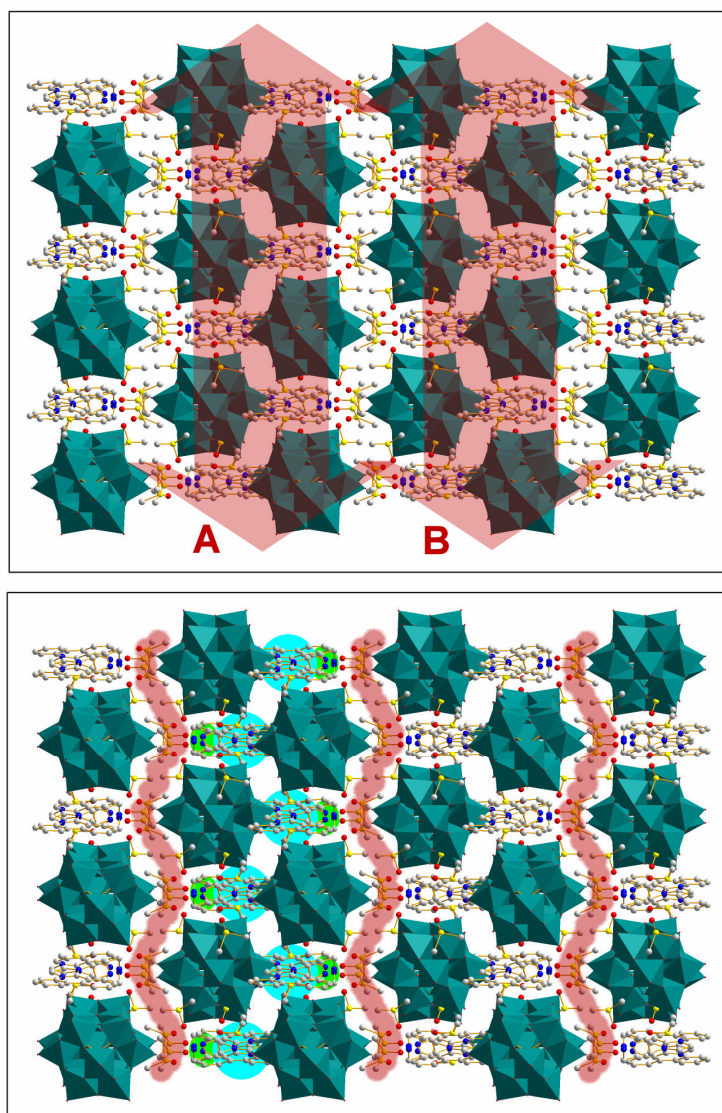
Figure 71: Illustrations of compound **5** when viewed along the crystallographic *c*-axis. Top: The inorganic clusters and DIP cations are aligned together into layers running parallel with the crystallographic *b*-axis, alternating between inorganic and organic components as you move along the length of the layer. The red arrows highlight the repeating ABAB pattern of these layers within the crystallographic *ab*-plane. Bottom: The positioning of the DIP cations within each inorganic-organic layer is highlighted within one these layers, i.e. the enclosed aromatic head groups of the DIP cations are highlighted using blue circles, whilst the tail groups directed outwards from the layer are highlighted using green ellipsoids. Red shading highlights the wave-like layers of DMSO molecules which can be seen within each inter-layer void, running parallel to the crystallographic *b*-axis. Colour scheme: W, teal polyhedra; P, pink; O, red; C, grey; N, blue; S, yellow. Solvent H_2O molecules and H atoms are omitted from both illustrations for clarity.

Indeed it should be noted that consideration of these H-bonding interactions when viewed along the crystallographic *c*-axis could allow the packing to be interpreted equally well in another representative way. One could explain the packing by assigning a layer structure

running parallel with the crystallographic *a*-axis, composed of a repeating sequence of the following units: POM–(head)DIP(tail)-DMSO. These layers are then seen to form an anti-parallel ABAB pattern within the crystallographic *ab*-plane (see Figure 72). When interpreting the packing in this manner it is also to interesting to note that the DIP cations within each layer are all aligned in a parallel, head-to-tail fashion along the crystallographic *c*-axis, whilst the DIP cations within neighbouring layers adopt an anti-parallel head-to-tail arrangement along the *c*-axis (see Figure 72).
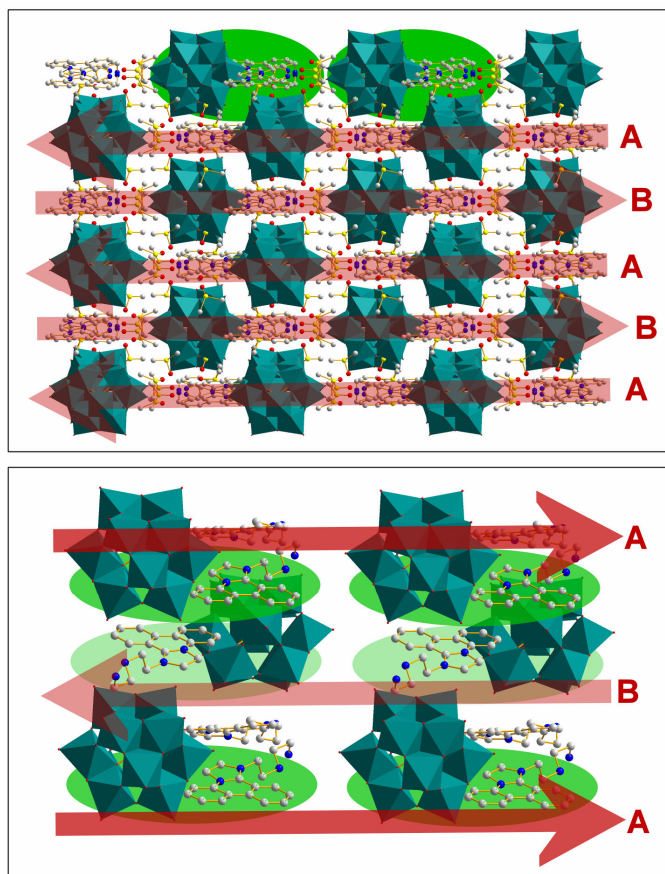
Figure 72: Top: View of compound **5** along the crystallographic *c*-axis. Each layer structure, which runs parallel with the crystallographic *a*-axis, can be considered to be composed of a repeating sequence of the following units: POM–(head)DIP(tail)-DMSO. Two of these repeating structural motifs are highlighted using green ellipsoids. The anti-parallel alignment of these motifs within adjacent layers, and the subsequent ABAB pattern of these layers within the crystallographic *ab*-plane, is then highlighted using red arrows. Solvent H_2O molecules and H atoms are omitted for clarity. Bottom: Illustration of compound **5** showing how the DIP cations within each layer, when viewing the lattice along the crystallographic *c*-axis, are all aligned in a parallel, head-to-tail fashion along the crystallographic *c*-axis (highlighted with dark green ellipsoids), whilst the DIP cations within neighbouring layers adopt an anti-parallel head-to-tail arrangement along the *c*-axis (highlighted with light green ellipsoids). Solvent molecules and H-atoms are omitted for clarity. Colour scheme: W, teal polyhedra; P, pink; O, red; C, grey; N, blue.

3.8.1.1 Solution and solid state UV/vis spectroscopic analysis of (DIP-1)[PW$_{12}$O$_{40}$]·5DMSO ca1H$_2$O (**5**)

Following the successful isolation and characterization of compound **5** it was decided that it would be interesting to investigate the spectroscopic response of this compound to determine whether any intermolecular charge transfer bands would be established between the aromatic DIP cation and POM anion. To this end, some preliminary solid state and solution state UV/vis spectroscopic analyses have been carried out as described below.

When carrying out the solution state measurements all compounds for analysis were dissolved in DMSO (as this solvent was used to recrystallize compound **5**) and each measurement was taken from 900 to 200 nm (although bearing in mind that DMSO begins absorbing at approximately 255 nm, see Experimental, Section 5.6.2.1 for baseline spectrum). Individual spectra over this wavelength range were taken for each of the starting materials, i.e. phosphotungstic acid, and (DIP-1)Br$_3$; so that any emergent intermolecular charge transfer bands in the spectrum of compound **5** could be readily identified. See Figure 73 and Table 7.
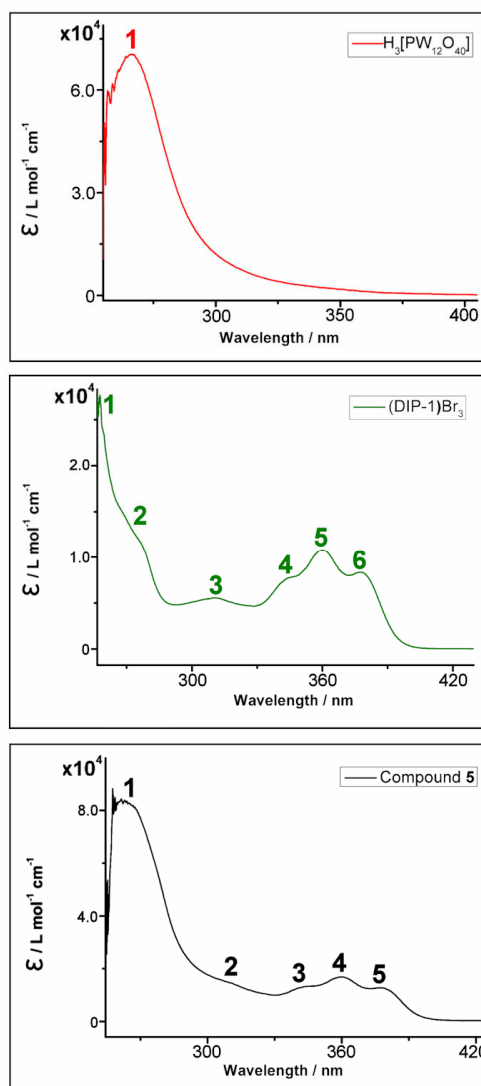
Figure 73: Solution state UV/vis spectra of phosphotungstic acid (1.6 x 10^{-5} mol L^{-1}) (top), (DIP-1)Br_3 (3.8 x 10^{-5} mol L^{-1}) (centre), and compound **5** (1.7 x 10^{-5} mol L^{-1}) (bottom). All compounds are dissolved in DMSO and the spectra recorded over the 900-200 nm wavelength range. Peak maxima are highlighted with numbers which relate to Table 7.

From these results it can be seen that the three absorbance bands at approximately 343, 360 and 378 nm (peaks 3, 4 and 5, bottom spectrum, Figure 73), which are attributed to electronic transitions within the DIP-1 cation, remain observable within the spectrum of compound **5**. The remaining major absorbance is located at approximately 265 nm (peak 1, bottom spectrum, Figure 73), which can be attributed to the oxygen ligand-to-metal charge transfer within the POM anion (found at 266 nm in the individual spectrum of phosphotungtic acid). This strong UV response from the POM anion in compound **5** overlays the same wavelength range where the remaining intra-DIP electronic transitions are located, i.e. at 258, 272, and 308 nm in the individual spectrum of (DIP-1)Br_3 (peaks

1,2 and 3, centre spectrum, Figure 73). Hence this overlaying effect may explain why two of these DIP-centred transitions (258 nm and 272 nm) appear absent from the spectrum of compound **5**, whilst the remaining transition can only be seen as a small, shouldered band at approximately 310 nm (peak 2, bottom spectrum, Figure 73).

It is also noted from these results that no other charge transfer bands are present in the spectrum of compound **5**, indicating no intermolecular charge transfer transitions are observable in the solution state. This is likely to be due to the spatial separation and solvation of the DIP cation and POM anion in solution.

Compound	Peak Maxima Numbering	Wavelength of Absorption / nm	Associated Electronic Transition
$H_3[PW_{12}O_{40}]$	1	266	Oxygen ligand → Metal charge transfer
$(DIP-1)Br_3$	1	258	Electronic transitions centred on DIP-1 cation
	2	272	
	3	308	
	4	343	
	5	359	
	6	377	
Compound **5**	1	265	Oxygen ligand → Metal charge transfer (centred on POM cluster)
	2	310	Electronic transitions centred on DIP-1 cation
	3	343	
	4	360	
	5	378	

Table 7: Summary of absorbance peaks observed in the solution state UV/vis spectroscopy measurements of compounds $H_3PW_{12}O_{40}$, $(DIP-1)Br_3$, and compound **5**.

Despite there being no observable intermolecular charge transfer bands found in the solution state measurements of **5** it was decided to continue these investigations and check the solid state spectroscopic response of **5,** using the technique of diffuse reflectance UV/vis spectroscopy. This was carried out in the hope that, not only would the closer proximity of the DIP cation and POM anion in the solid state lead to a detectable

intermolecular charge transfer transition; but that the presence of even a weak band would be more readily detected using this solid-state measurement, as such measurements lead to the promotion of weak bands and suppression of stronger bands.[279]

When carrying out these solid state measurements each individual starting material was again monitored over the same wavelength range as compound **5**, i.e. 1300 to 190 nm, in order to allow ready identification of any emergent intermolecular charge transfer bands in the spectrum of **5**.
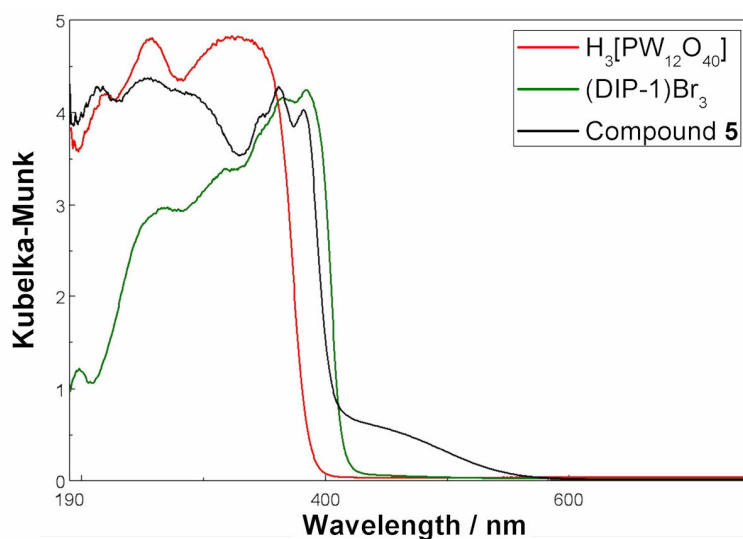
Figure 74 Overlaid diffuse reflectance UV/vis spectra of starting materials and compound **5**. Of particular note is the intermolecular charge transfer band at approximately 460 nm in the spectrum of compound **5** (black line). Colour code as shown in figure.

These results show, as expected, suppression of the stronger absorbance bands between approximately 190 and 400 nm due to the intra-DIP and intra-POM electronic transitions (which were observed in the solution state); and confirm the presence of an intermolecular charge transfer band at approximately 460 nm between the DIP cation and POM anion in the solid state (see Figure 74). The presence of this intermolecular charge transfer band in the solid state, but its absence from the solution state measurement is, therefore, indicative that either: a) the cation and anion are too far apart in solution to allow intermolecular charge transfer transitions; or b) intermolecular charge transfer transitions might take place in the solution state as well, but are just too weak to be observable. Although we cannot say with certainty which of these two factors is responsible for this phenomenon, we are able to deduce that the intermolecular charge transfer observed in the solid state is likely to take place from the aromatic DIP-1 cation to the fully oxidised POM anion.

In addition to these spectroscopic analyses it should be noted that preliminary cyclic voltammetry studies have also been carried out in order to examine the redox processes of compound **5** in solution. These preliminary results for compound **5** have indicated the presence of three redox processes which are attributed to electron processes on the tungsten centres of the POM anion. Also, due to the presence of the DIP-1 cation, these redox processes are shifted to more negative electrode potentials when compared with the lone $H_3PW_{12}O_{40}$ starting material. As these investigations are on-going, these results will be discussed further in the Experimental, section 5.6.2.1.

3.8.2   Formation of (DIP-2)[PW$_{12}$O$_{40}$]·5DMSO·*ca*4H$_2$O (6)

Given the success described above in crystallizing DIP-1 with triply-charged phosphotungstic acid, a similar reaction strategy was carried out with DIP-2 in the hope that such a sterically demanding organic molecule could: a) be crystallized for analysis by single crystal X-ray diffraction for the first time; b) the steric bulk and geometry of the organic molecule could lead to interesting structure formation on reaction with the POM; and c) the aromatic core of the DIP moieties extending from the arms of the central cis-TACH structure would lead to interesting photoactivity in the final DIP-2-POM structure produced.

The addition of an excess of (DIP-2)Br$_3$ in DMSO to an aqueous solution of phosphotungstic acid led to the rapid precipitation of a brown solid. Dissolution and recrystallization of this precipitate from hot DMSO led to isolation of orange, needle-like, single crystals suitable for single crystal X-ray diffraction. Structural analysis of this diffraction data allowed the composition of the crystals to be assigned as (DIP-2)[PW$_{12}$O$_{40}$] 5DMSO·*ca*4H$_2$O (**6**).

The isolation of compound **6** allowed the first crystallographic confirmation of the structure of the DIP cation *cis*-1,3,5-tri(2,3-dihydro-1*H*-imidazo[1,2-*f*]phenanthridinium)cyclohexane. Hence it is of interest to examine, in more detail, its

structure in the solid state. Studying the unit cell of compound **6** it can be seen, as discussed previously, that the DIP rings do not maintain an entirely planar structure in the solid state, a result of its inability to stabilise all four rings effectively through electron delocalisation, due to the presence of the alkane bond between the C1 and C2 atoms (see Figure 63). Further examination reveals that the three pendent DIP arms of DIP-2 do not lie in planes at 120° to one another. Instead, by assigning centroids to the central aromatic rings of each DIP pendent and another inside the ring of the central cis-TACH ring, it is found that the two pendent DIPs closest to the cluster (arms A and B) have 121.0° between their centroids, whereas the angles between these centroids and that of the remaining DIP arms are 127.4° (between arms A and C) and 102.5° (between arms B and C) respectively (see Figure 75).
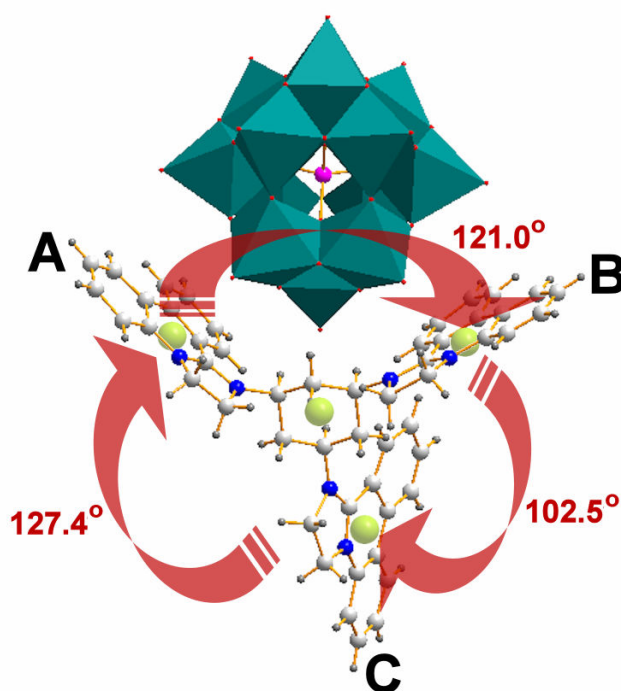
Figure 75: Representation showing the angles between the three DIP arms of the DIP-2 cation in compound **6**. The green spheres show the position of centroids used to calculate these angles. Colour scheme: W, teal polyhedra; P, pink; O, red; C, light grey; N, blue; H, dark grey. Solvent molecules are omitted for clarity.

Given the interesting geometry of the DIP-2 cation, and the lack of any previous single crystal X-ray diffraction information about its structure, the orientation of the three pendent DIP arms and their spatial arrangement with respect to one another is discussed as follows. Within the DIP-2 cation all three pendent DIP arms are directed along the same axis with the shortest C···C distance between carbons on neighbouring DIP moieties being

found between DIP-arm B and DIP-arm C at 4.011 Å. Looking at the remaining shortest C⋯C distances between carbons on neighbouring DIP moieties within the more sterically crowded face of DIP-2, the next shortest distance is 6.270 Å found between DIP-arm A and C, followed by a distance of 6.459 Å between DIP-arm A and B (see Figure 76, figure on left). Consideration of the more open and less sterically crowded face of the DIP-2 cation reveals the shortest inter-DIP moiety C⋯C distance to be 5.262 Å, found between DIP-arm A and B; followed by 5.366 Å between DIP-arm A and C; and 5.866 Å between DIP-arm B and C. See Figure 76, figure on right.
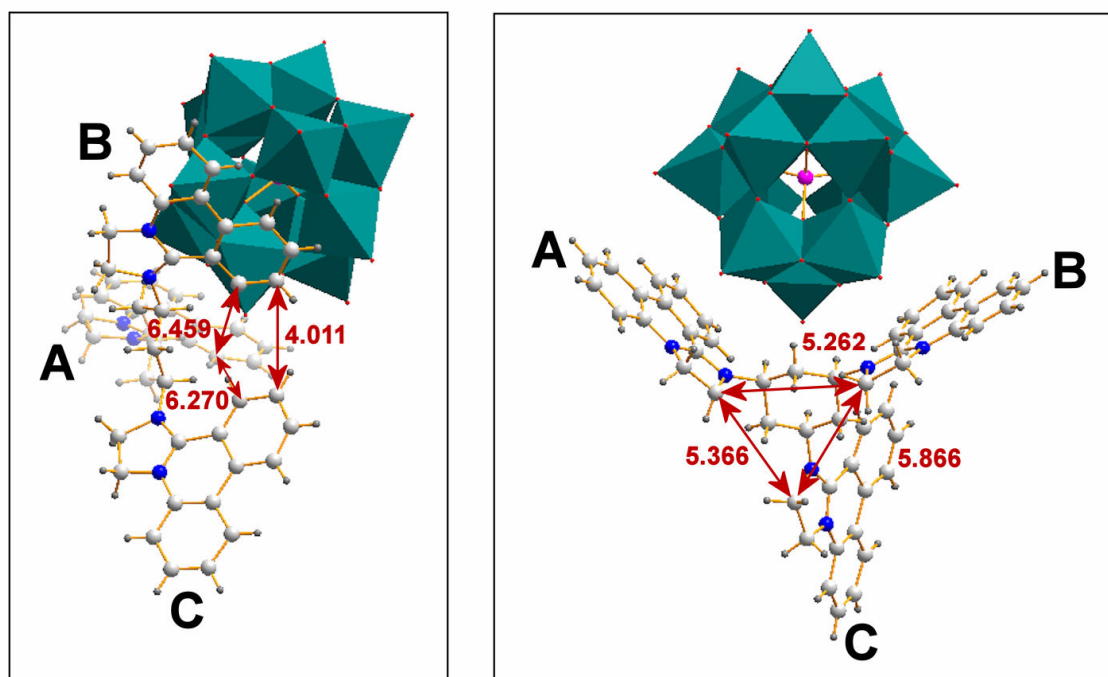
Figure 76: Left: Representation illustrating the position of the shortest C⋯C distances between carbons on neighbouring DIP-arms within the more sterically crowded face of the DIP-2 cation in compound **6**. Right: Representation illustrating the shortest C⋯C distances between carbons on neighbouring DIP-arms within the more open and less sterically crowded face of the DIP-2 cation in compound **6**. All distances shown are measured in Ångströms (Å). Colour scheme: W, teal polyhedra; P, pink; O, red; C, light grey; N, blue; H, dark grey. Solvent molecules are omitted for clarity.

It is evident through this analysis of the various C⋯C distances between the DIP pendent arms that there is a degree of torsion of the plane of these DIP moieties with respect to one another. Through the examination of the torsion between a selected bond in the aromatic region of each DIP arm these torsion angles can be studied more closely (see Figure 77, illustration on left). It is interesting to note that while the mean torsion angles between DIP-arms A and B, and between B and C, are only 1.2° and 6.4° respectively; the mean torsion angle between arms A and C is found to be 34.3°. See Figure 77.
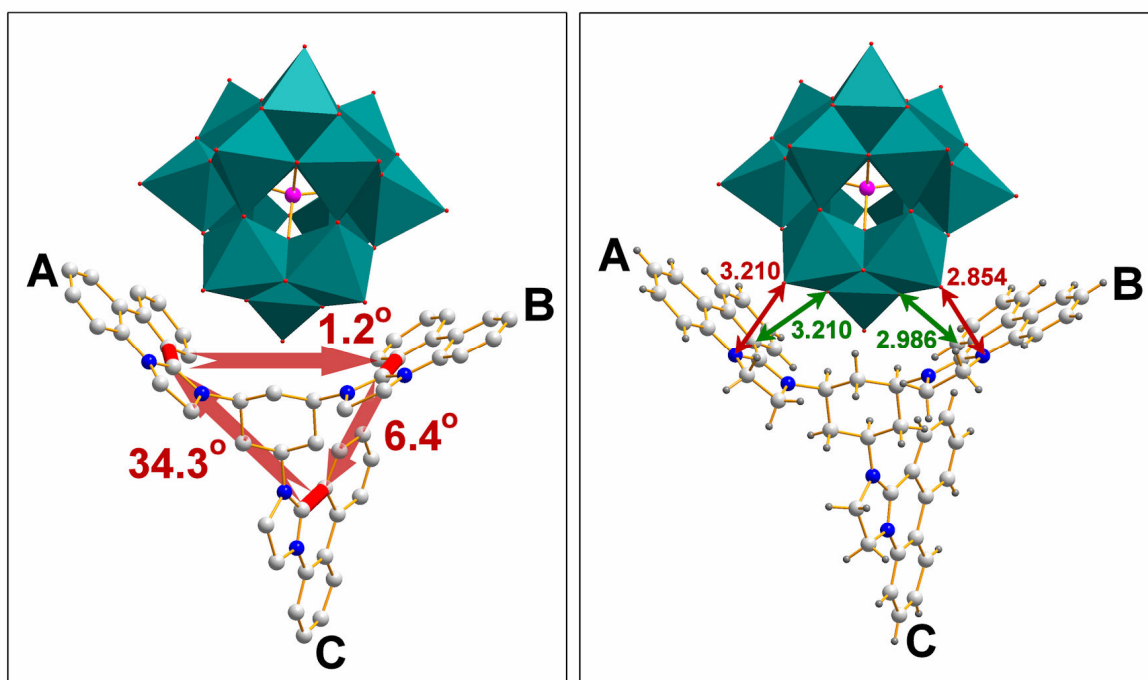
Figure 77: Representations of one DIP-2 cation and closest POM cluster anion in compound **6**. Left: The bonds, one in each DIP-arm of the DIP-2 cation, used to calculate the torsions between each these DIP arms are highlighted in red. The torsion angles are also shown. Solvent molecules and H atoms are omitted for clarity. Right: The minimum distances between the DIP-arms in closest contact with the cluster anion, are shown. Red arrows show the minimum distances between cluster terminal oxo ligands and the aromatic ring nitrogens in the DIP-arms of DIP-2. Green arrows show the minimum distances between cluster μ_2-bridging oxo ligands and carbons atoms in the DIP-arms of DIP-2. All distances shown are measured in Ångströms (Å). Solvent molecules are omitted for clarity. Colour scheme: W, teal polyhedra; P, pink; O, red; C, light grey; N, blue; H, dark grey.

We have so far discussed the structural features of the DIP-2 cation, however, we must now consider its relationship with the the $[PW_{12}O_{40}]^{3-}$ anion with which it forms a 1:1 electrostatic relationship, and directs the development of an intriguing packing structure in the solid state, so allowing the recrystallization of compound **6**.

The $[PW_{12}O_{40}]^{3-}$ anion itself is introduced into the reaction system as a pre-formed cluster building-block. It is composed, as discussed previously (see Introduction, section 1.4.2), of four $\{W_3O_{13}\}$ sub-units assembled around the central $(PO_4)^{3-}$ heteroanion template. Examination of this cluster anion in the crystal structure of compound **6** reveals all the W=O terminal bonds, bridging W-O bonds, and P-O bonds to be within the expected range of those values quoted in the literature,[259] see Table 8.

Bond Type	Average Bond Distances in Compound **6** / Å
W=O (terminal)	1.69
W-O (μ_2-bridging)	1.91
W-O (μ_4-bridging)	2.43
P-O	1.55

Table 8: Average bond distances within the $[PW_{12}O_{40}]^{3-}$ cluster anion in compound **6.**

In the unit cell the $[PW_{12}O_{40}]^{3-}$ anion can be seen to be cupped, within the more sterically crowded face of the DIP-2 cation, by the two DIP arms A and B. The shortest contact distance between the cation and anion is 2.854 Å, i.e. between a terminal oxo ligand of the cluster and the aromatic ring nitrogen of DIP-arm B of the DIP-2 cation. Indeed further consideration of these short contact distances reveals that the cluster is positioned in the matrix in such a way as to have a slightly greater interaction with DIP-arm B than DIP-arm A. This is shown by studying the shortest distances between the terminal oxo and bridging oxo ligands of the cluster anion, and the ring atoms of the two DIP-arms A and B. In this way the shortest distance between a terminal oxo on the cluster anion and a nitrogen atom in DIP-arm A is found to be 3.210 Å, and the shortest distance between a μ_2-bridging oxo on the cluster anion and a carbon atom in DIP-arm A is also found to be 3.210 Å. In contrast, looking at the interactions between the cluster and the other cupping DIP-arm B, the shortest distance between a terminal oxo on the cluster anion and a nitrogen atom in DIP-arm B is 2.854 Å, whereas the shortest distance between a μ_2-bridging oxo and a carbon atom in DIP-arm B is 2.986 Å. See Figure 77, illustration on right.

When extending the packing, to view the extended supramolecular lattice of compound **6**, further interesting structural features can be observed. When viewing the crystal lattice along the crystallographic *a*-axis, the $[PW_{12}O_{40}]^{3-}$ cluster anions, which act as the inorganic building-blocks of the structure, can be seen to be arranged into layers composed of two anti-parallel arrays of clusters (minimum cluster spacing 3.126 Å). These layers then follow a repeating ABAB pattern within the crystallographic *bc*-plane. The co-linear alignment of the clusters within these layers runs parallel with the crystallographic *c*-axis, the inter-layer voids (minimum cluster spacing 4.604 Å) being filled with interacting pendent DIP arms of the DIP-2 cations, and H-bonding solvent DMSO and H_2O molecules. See Figure 78.
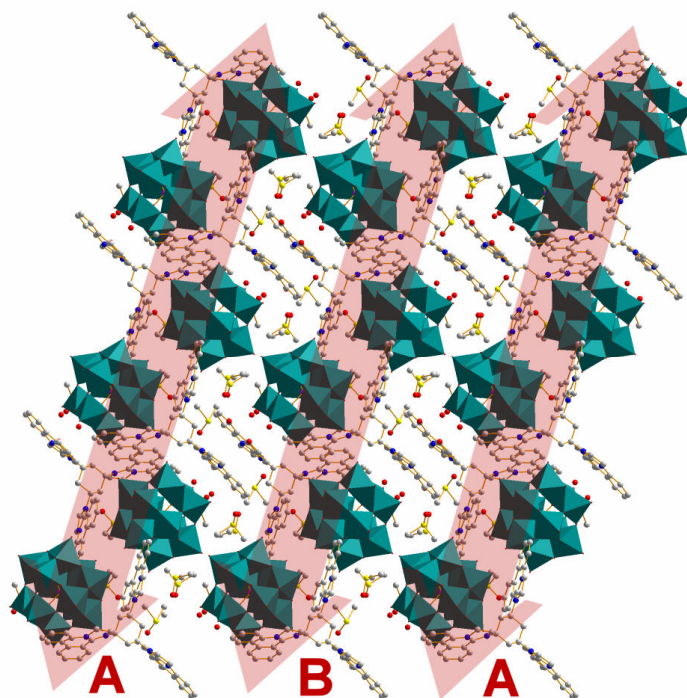
Figure 78: View of compound **6** along the crystallographic *a*-axis. Each cluster layer is highlighted by a red arrow and is composed of two anti-parallel arrays of clusters running parallel with the crystallographic *c*-axis. The repeating ABAB pattern of these cluster layers within the crystallographic *bc*-plane is also indicated. ππ-stacking DIP-arm C moieties of adjacent DIP-2 cations, and H-bonding DMSO and H_2O molecules are also noticeable in the inter-layer voids. Colour scheme: W, teal polyhedra; P, pink; O, red; C, light grey; N, blue; S, yellow. H atoms are omitted for clarity.

It is particularly interesting that, on viewing the lattice along the crystallographic *a*-axis, it is noticeable that the DIP-2 cations form another organic-supramolecular lattice within the greater lattice structure. This organic 'sub-lattice' is comprised of two layers of DIP-2 cations arranged in an anti-parallel fashion, which then follow a repeating ABAB pattern within the crystallographic *bc*-plane, and which runs parallel with the crystallographic *b*-axis. This repeating ABAB pattern of organic sub-structure both intersects the anti-parallel layers of the inorganic clusters, and plays a role in separating these layers into their inorganic ABAB pattern parallel to the crystallographic *c*-axis, by occupying part of the void space between these layers (see Figure 79).
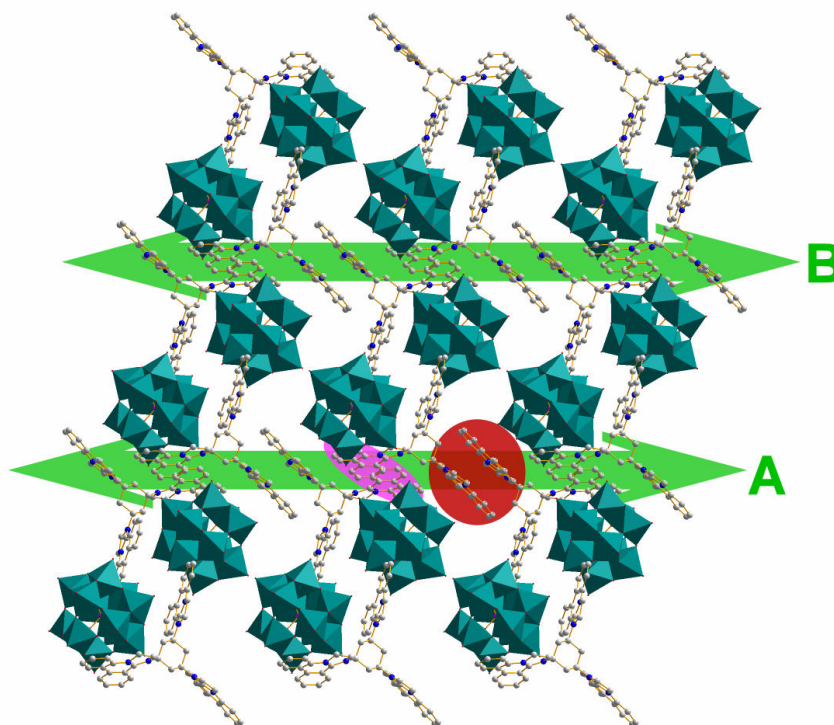
Figure 79: View of compound **6** along the crystallographic *a*-axis. The green arrows highlight the anti-parallel arrangements of DIP-2 cations into organic layers within the lattice of **6.** These layers follow a repeating ABAB pattern within the crystallographic *bc*-plane, and run parallel to the crystallographic *b*-axis. One of the a)-type ππ-stacking interactions (between DIP-arm C moieties) is highlighted with a red circle; and one of the b)-type ππ-stacking interactions (between DIP-arm A moieties) is highlighted with a purple ellipsoid. Colour scheme: W, teal polyhedra; P, pink; O, red; C, light grey; N, blue. Solvent molecules and H atoms are omitted for clarity.

The organic 'sub-lattice' of DIP-2 cations is held together through two different sets of ππ-stacking interactions: a) between the DIP pendent moieties pointing into the void spaces between the inorganic layers; and b) between the DIP pendent moieties intersecting the anti-parallel layers of inorganic clusters. See Figure 79.

In the a)-type ππ-stacking interactions these are found to be established between DIP-arm C pendent moieties of DIP-2 cations from each alternating inorganic ABAB cluster layer. This is confirmed by measuring the distance between the plane of the aromatic region of one of the interacting DIP arms, with the centroid of the aromatic region of the other DIP arm. This minimum inter-planar distance was found to be 3.513 Å, which is within the expected range for a ππ-stacking interaction distance as quoted in the literature.[280-282] However, it is pertinent to mention at this point that, due to the torsion in the DIP-2 cation

arms, the actual shortest C···C distance between the two ππ-stacking DIP arms is slightly lower than this value, at 3.442 Å.

Another important point of note when considering these ππ-stacking interactions is that they are seen to be established between only two of the three aromatic rings of each DIP arm. The application of a space-filling representation to the ππ-stacking DIP-arm C moieties and one of the adjacent DIP-arm B moieties, illustrates clearly that this packing arrangement is dictated by the steric bulk of the interacting DIP-2 cations, the observed structure representing the closest contact which can be formed between two adjacent DIP-2 cations in this orientation. More specifically, the shortest C···C distance between DIP-arm B and DIP-arm C on the adjacent DIP-2 cation is found to be 3.680 Å, whilst the shortest C···C distance between the central cis-TACH ring and DIP-arm C of the adjacent DIP-2 cation is 3.939 Å. See Figure 80.
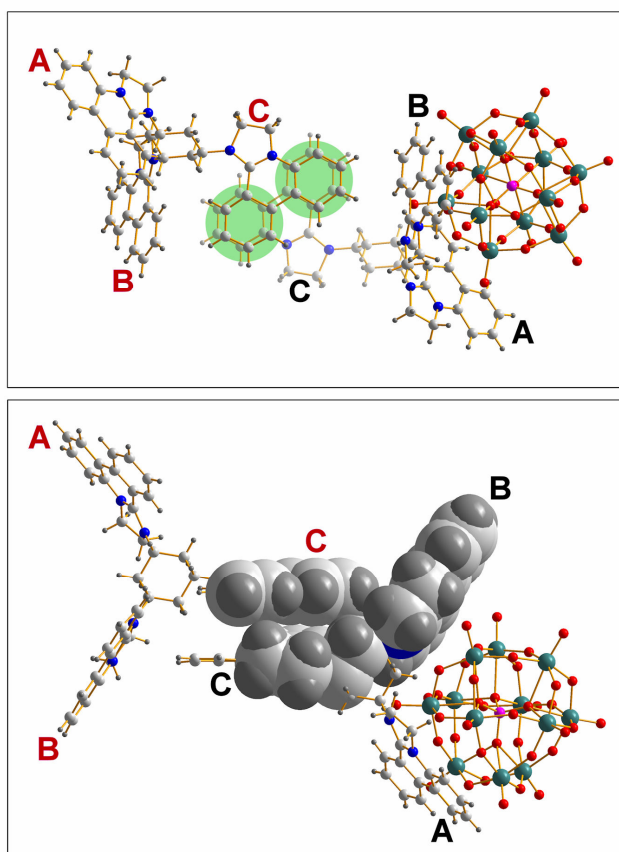
Figure 80: Illustrations showing the a)-type ππ-stacking interactions within compound **6**. Top: The two ππ-stacking aromatic rings of DIP-arm C moieties from adjacent DIP-2 cations are highlighted by green circles. Bottom: A space-filling representation shows the steric clash between adjacent DIP-2 cations, so illustrating that this packing arrangement represents the closest contact which can be formed between two adjacent DIP-2 cations in this orientation. Colour scheme: W, teal; P, pink; O, red; C, light grey; N, blue; H, dark grey. Solvent molecules are omitted for clarity.

In the b)-type ππ-stacking interactions, these are found to be established between DIP-arm A moieties from adjacent DIP-2 cations (see Figure 79). This is confirmed by measuring the distance between the plane of the aromatic region of one of the interacting DIP arms, with the centroid of a selected bond in the aromatic region of the other DIP arm. This minimum inter-planar distance was found to be 3.471 Å. However, due to the torsion in the DIP-2 cation arms, and the manner of overlap of these two DIP arms, the actual shortest C···N distance (both atoms within the central aromatic ring of the DIP moieties) between the two ππ-stacking DIP arms is slightly higher than this value at 3.495 Å, whilst the shortest C···C distance is also slightly higher at 3.584 Å.

The manner of overlap of the DIP arms in the b)-type ππ-stacking interactions can be seen to be quite different from that for the a)-type interactions as only a small portion of the delocalised aromatic ring system of the DIP arms are overlaid in establishing the b)-type form, so indicating this is weaker than the a)-type ππ-stacking interaction (see Figure 81). The finding that the shortest C···C distance in the b)-type interaction (3.584 Å), is slightly higher than that in the a)-type interaction (3.442 Å), reaffirms this analysis of the interaction strength.
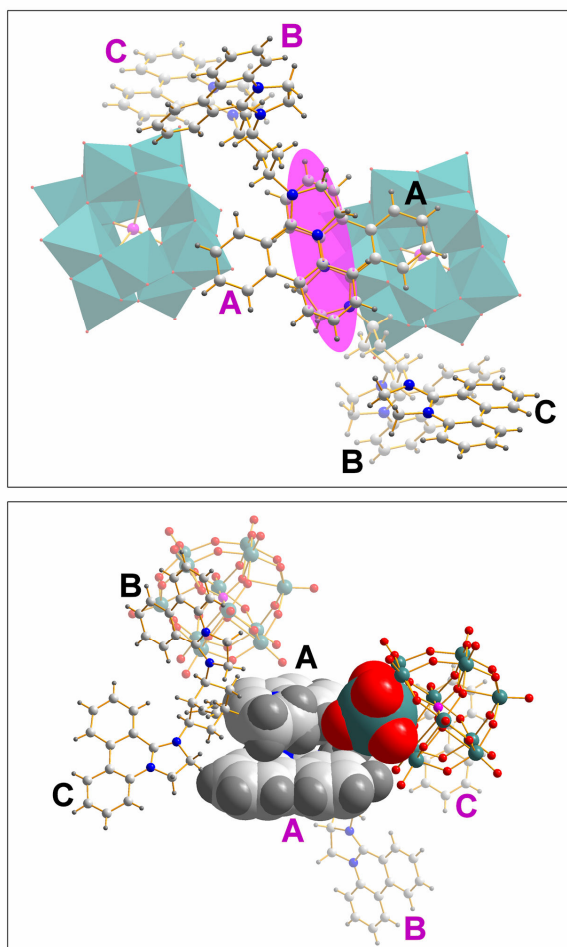
Figure 81: Illustrations showing the b)-type ππ-stacking interactions within compound **6**. Top: The overlaid region of DIP-arm A moieties from adjacent DIP-2 cations, which forms the b)-type ππ-stacking interaction, is highlighted by a purple ellipsoid. Bottom: A space-filling representation shows the steric clash between the ππ-stacking DIP-2 cations and the adjacent inorganic cluster. This illustrates that the weaker overlap in this ππ-stacking interaction is dictated by the closest packing arrangement of the sterically bulky DIP-2 cation with the surrounding inorganic cluster framework. Colour scheme: W, teal; P, pink; O, red; C, light grey; N, blue; H, dark grey. Solvent molecules are omitted for clarity.

Through the application of a space-filling representation to the ππ-stacking DIP-arm A moieties and the inorganic cluster anion of an adjacent unit cell, this illustrates clearly that this weaker overlap is dictated by the closest packing arrangement of the sterically bulky DIP-2 cation with the surrounding inorganic cluster framework. In detail, the shortest C⋯O distance between DIP-arm A and a terminal oxo ligand on the adjacent cluster anion is found to be 3.266 Å, whilst the shortest C⋯C distance between DIP-arm A and the central cis-TACH ring of the other ππ-stacking DIP-2 cation is 4.004 Å. See Figure 81.

Although it has been found that both DIP-arms C and A establish ππ-stacking interactions, the remaining DIP pendent arm of the DIP-2 cation, i.e. DIP-arm B, is not found to establish any such interaction. Specifically the shortest C···C distance between the DIP-arm B on one DIP-2 cation, and that on the nearest adjacent cation, when looking along the crystallographic *c*-axis, is 6.252 Å. This is not only too long a distance to form a ππ-stacking interaction, but more importantly, as can be seen by viewing the lattice along the crystallographic *b*-axis, no part of these two DIP-2 cations are overlaid with one another (see Figure 82).
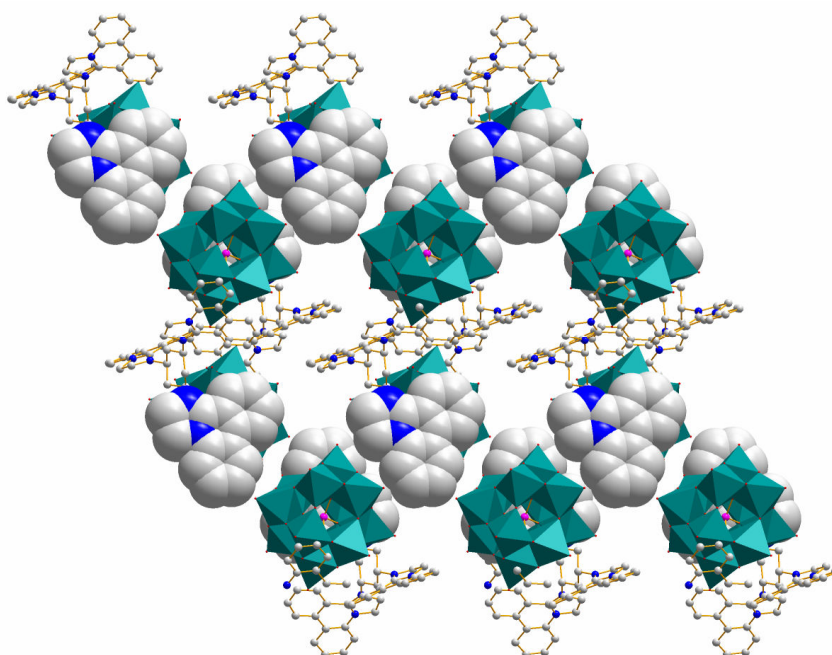
Figure 82: Representation of compound **6** viewed along the crystallographic *b*-axis. The DIP-arm B moieties of each DIP-2 cation are shown as space-filling models, and using this representation it can be seen that these DIP arms do not overlay one another, and so do not form any ππ-stacking interactions. Colour scheme: W, teal polyhedra; P, pink; O, red; C, light grey; N, blue. Solvent molecules and H atoms are omitted for clarity.

3.8.2.1 Solution and solid state UV/vis spectroscopic analysis of (DIP-2)[PW$_{12}$O$_{40}$]·5DMSO *ca*3H$_2$O (**6**)

Following the successful isolation and characterization of compound **6** it was decided that examination of the spectroscopic response of this compound should be undertaken. This was to allow investigation into the presence of any charge transfer interactions between the

aromatic cation and POM anion. To this end, some preliminary solution and solid state UV/vis spectroscopy measurements were carried out.

For the solution state measurements all compounds were dissolved in DMSO (the solvent used to recrystallize compound **6**) and each measurement was carried out from 900 to 200 nm (although bearing in mind that DMSO begins absorbing at approx 255nm, see Experimental, Section 5.6.2.2 for baseline spectrum). To allow identification of emergent electronic absorption bands in compound **6,** spectra were recorded for both lone starting materials, i.e. for phosphotungstic acid, and (DIP-2)Br$_3$. See Figure 83 and Table 9.
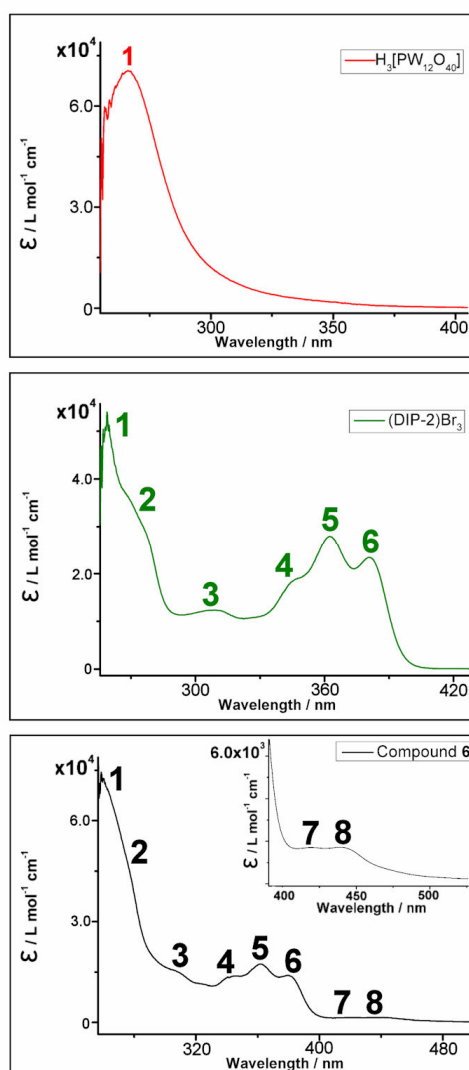
Figure 83: Solution state UV/vis spectra of phosphotungstic acid (1.6 x 10^{-5} mol L^{-1}) (top), (DIP-2)Br$_3$ (2.6 x 10^{-5} mol L^{-1}) (centre), and compound **6** (1.5 x 10^{-5} mol L^{-1}) (bottom). Inset graph for compound **6** (bottom spectrum) is at higher concentration (1.7 x 10^{-4} mol L^{-1}) to show peak maxima 7 and 8. All compounds are dissolved in DMSO and the spectra recorded over the 900-200 nm wavelength range. Peak maxima are highlighted with numbers which relate to Table 9.

From these results it can be clearly seen that the six absorbance peaks attributed to the electronic transitions within the DIP-2 cation can still be seen in the spectrum of compound **6** (peaks 1-6, bottom spectrum, Figure 83). The electronic transition at 266 nm due to the oxygen ligand-to-metal charge transfer band within the POM anion (peak 1, top spectrum, Figure 83) cannot be seen in the spectrum of compound **6**, however, this may be due to the strong UV response of the DIP cation in this area overlaying the signal. However, the result of most interest from these measurements is the presence of two extra absorption bands (i.e. emergent electronic transitions) in the spectrum of compound **6** which are absent from either the POM or (DIP-2)Br$_3$ spectra. These bands are positioned at approximately 421 and 440 nm (peaks 7 and 8, bottom spectrum, Figure 83 and although they are obviously weak, they nevertheless indicate the presence of intermolecular charge transfer bands between the DIP cation and POM anion in solution. The fact that this is a solution state measurement may account for the weak nature of these bands, as the cation-anion interaction will be weaker in the solution state, where they are not held as closely together as when in the solid state. We can also deduce that, as the POM anion is fully oxidised, then the electronic transition is likely to involve an intermolecular electron transfer from the aromatic DIP-2 cation to the POM anion.

Compound	Peak Maxima Numbering	Wavelength of Absorption / nm	Associated Electronic Transition
$H_3[PW_{12}O_{40}]$	1	266	Oxygen ligand → Metal charge transfer
$(DIP-2)Br_3$	1	258	Electronic transitions centred on DIP-2 cation
	2	273	
	3	310	
	4	345	
	5	362	
	6	381	
Compound **6**	1	257	Electronic transitions centred on DIP-2 cation, (possibly overlaying POM-centred oxygen ligand → metal charge transfer)
	2	275	
	3	306	Electronic transitions centred on DIP-2 cation
	4	345	
	5	362	
	6	381	
	7	421	DIP-2 → POM cluster (Intermolecular charge transfer)
	8	440	DIP-2 → POM cluster (Intermolecular charge transfer)

Table 9: Summary of absorbance peaks observed in the solution state UV/vis spectroscopy measurements of compounds $H_3PW_{12}O_{40}$, (DIP-2)Br$_3$, and compound **6**.

Following the successful identification of intermolecular charge transfer bands in the solution state measurement of compound **6**, it was decided to investigate the solid state response of this compound, and its starting materials, using the technique of diffuse reflectance UV/vis spectroscopy. Once again, comparison of the spectrum of compound **6**, with those of its lone starting materials, allows the identification of emergent electronic transition bands.

A typical feature of solid state UV/vis spectroscopy is that strong electronic transition bands are suppressed, whilst weak bands are promoted.[279] This feature is illustrated in these experiments because those strong bands between approximately 190 and 450 nm, due

to electronic transitions within the DIP-2 cation and within the POM anion, are somewhat suppressed, whilst the intermolecular charge transfer band at approximately 448 nm is promoted (see Figure 84). Another reason that this intermolecular charge transfer band is more prominent in the solid state than in the solution state measurement could be, as described previously, due to the closer contact and therefore, stronger intermolecular interaction between the cation and anion in the solid state.
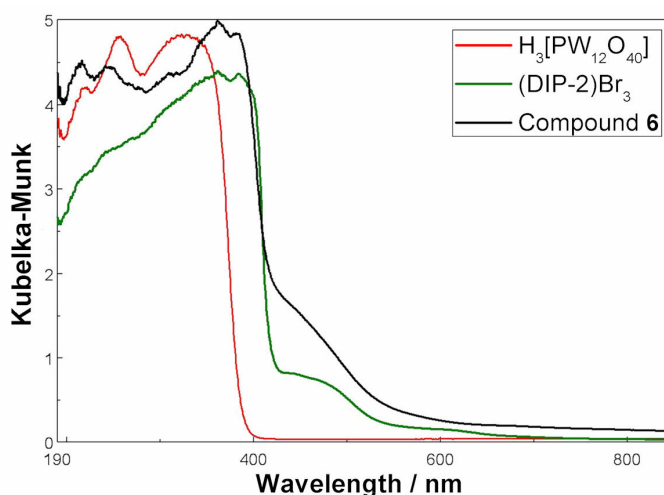
Figure 84: Overlaid diffuse reflectance UV/vis spectra for compounds $H_3PW_{12}O_{40}$, (DIP-2)Br_3, and compound **6**. Of particular note is the intermolecular charge transfer band at approximately 448 nm in the spectrum of compound **6** (black line). Colour code as shown in figure.

In addition to these spectroscopic analyses, preliminary cyclic voltammetry studies have also been carried out in order to examine the redox processes of compound **6** in solution. In a similar manner to compound **5**, the preliminary results for compound **6** have indicated the presence of three redox processes attributed to electron processes on the tungsten centres of the POM anion. Due to the presence of the DIP-2 cation, two of these redox processes are shifted to more negative electrode potentials when compared with the lone $H_3PW_{12}O_{40}$ starting material. As these investigations are on-going these results will be discussed further in the Experimental, section 5.6.2.2.

3.8.2.2 SEM and EDX analysis of (DIP-2)[PW$_{12}$O$_{40}$]·5DMSO ca3H$_2$O (**6**)

Due to the use of the sterically bulky and geometrically interesting DIP-2 cation in producing compound **6**, it was decided to investigate the structure of the remaining inorganic framework using SEM and EDX analysis after heating the compound to high temperatures in an air atmosphere. In detail, samples of compound **6** were heated at 5 °C min^{-1} from room temperature to 1000 °C, under an air atmosphere, removing first the solvent through evaporation, then the organic cations through oxidation. These samples were then ground up with a pestle and mortar, transferred to carbon SEM sample holders, and sputter-coated with gold prior to SEM and EDX analysis.
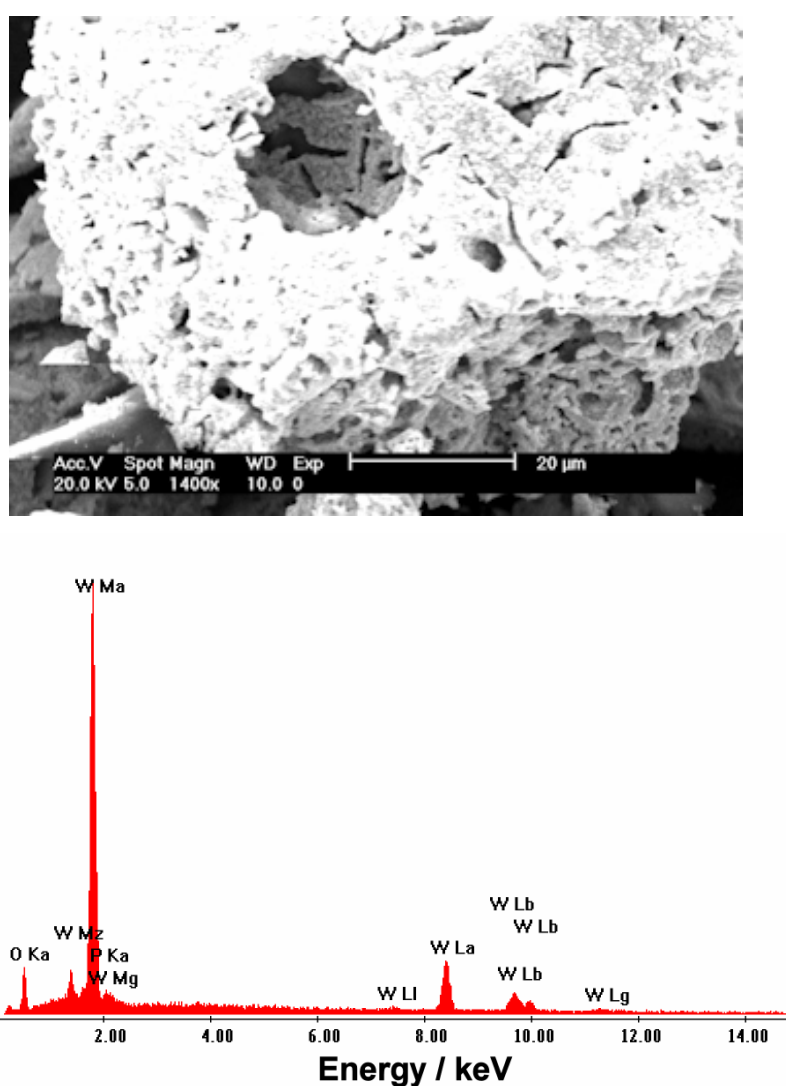
Figure 85: Top: SEM image of the area of the prepared compound **6** sample used for EDX analysis. Bottom: EDX data acquired from this area of the sample confirming the composition as WO$_3$.

Initial SEM and EDX analysis of these samples revealed some interesting results. Firstly EDX analysis (and also powder XRD analysis, see Experimental, section 5.6.2.2) of the samples revealed their composition to be WO_3 as expected (see Figure 85); and secondly these WO_3 structures appeared to possess a degree of porosity (see Figure 86).
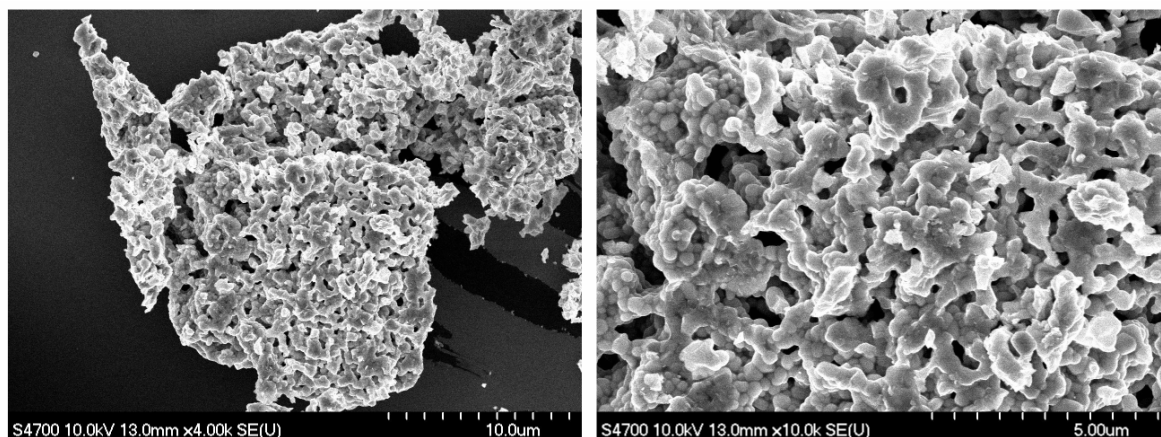
Figure 86: Left: SEM image of the apparently porous structure of the prepared compound **6** sample. Right: A close-up SEM image of this porous structure.

Further SEM analysis revealed this inorganic framework to be composed of disc-like, and in some cases, multi-faceted units packed together (see Figure 87). These units were found to vary within the range of tenths of microns to microns in diameter (see Figure 88).
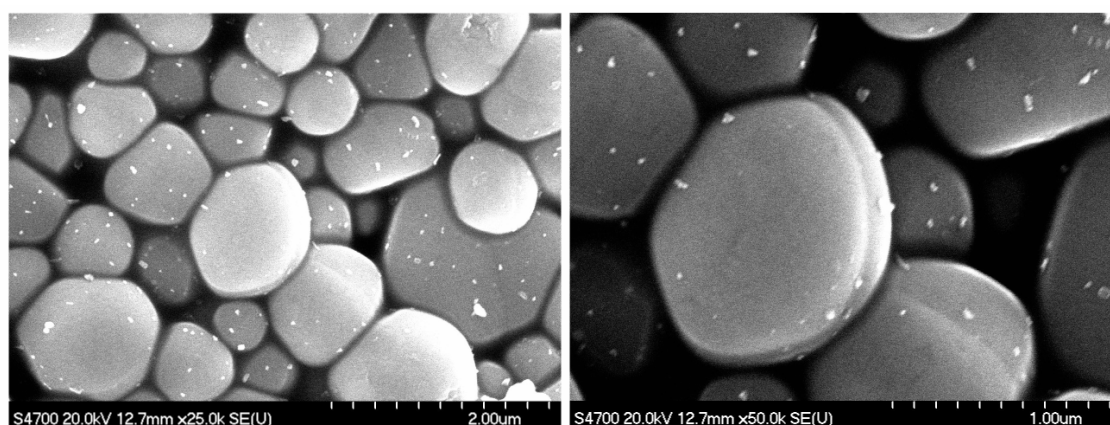
Figure 87: Left: SEM image of the WO_3 framework of the prepared compound **6** sample. The disc-like and multi-faceted units composing this framework are clearly observed. Right: A close-up SEM image of the disc-like unit positioned in the centre of the image on the left.
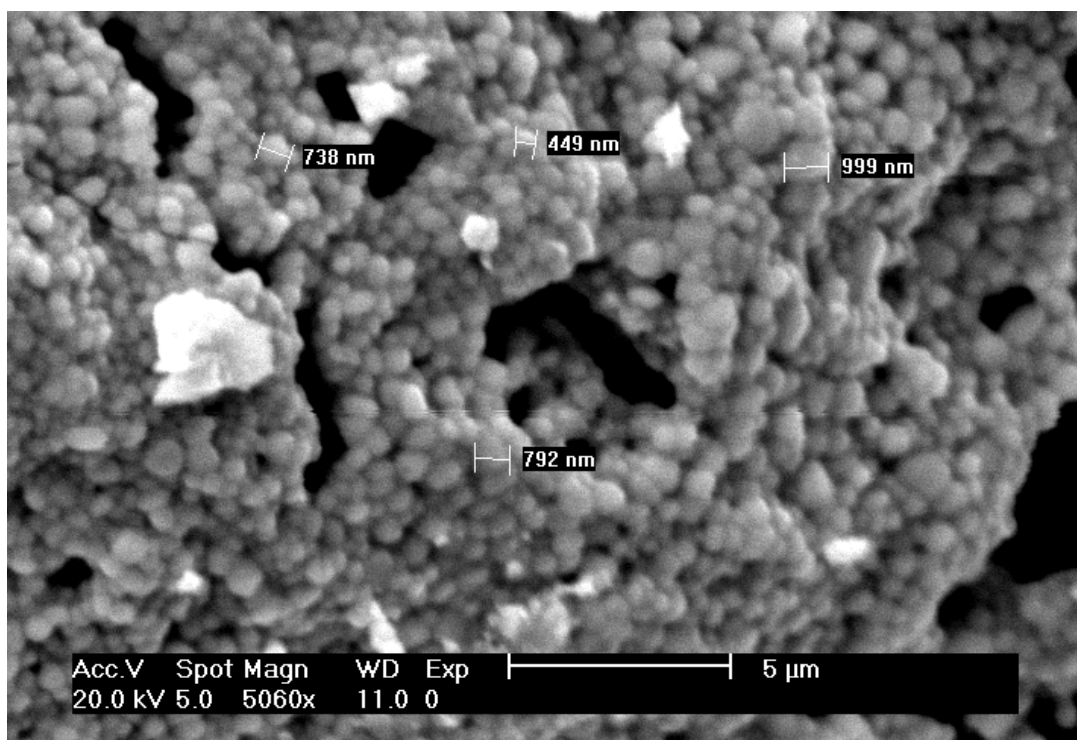
Figure 88: SEM image of the prepared compound **6** sample, where the WO_3 framework units have been measured and been found to vary within the range of tenths of microns to microns in diameter.

More detailed SEM analysis to examine the porous nature of the sample (see Figure 86) was also carried out. However, although this analysis allowed measurement of some of the widely varying pore sizes observed (see top image, Figure 89), it also revealed that the apparent porosity is not consistent throughout the sample. This is illustrated in the bottom images of Figure 89 where the 'porous' WO_3 structure can be seen at the broken edge of a more closely packed WO_3 structure.
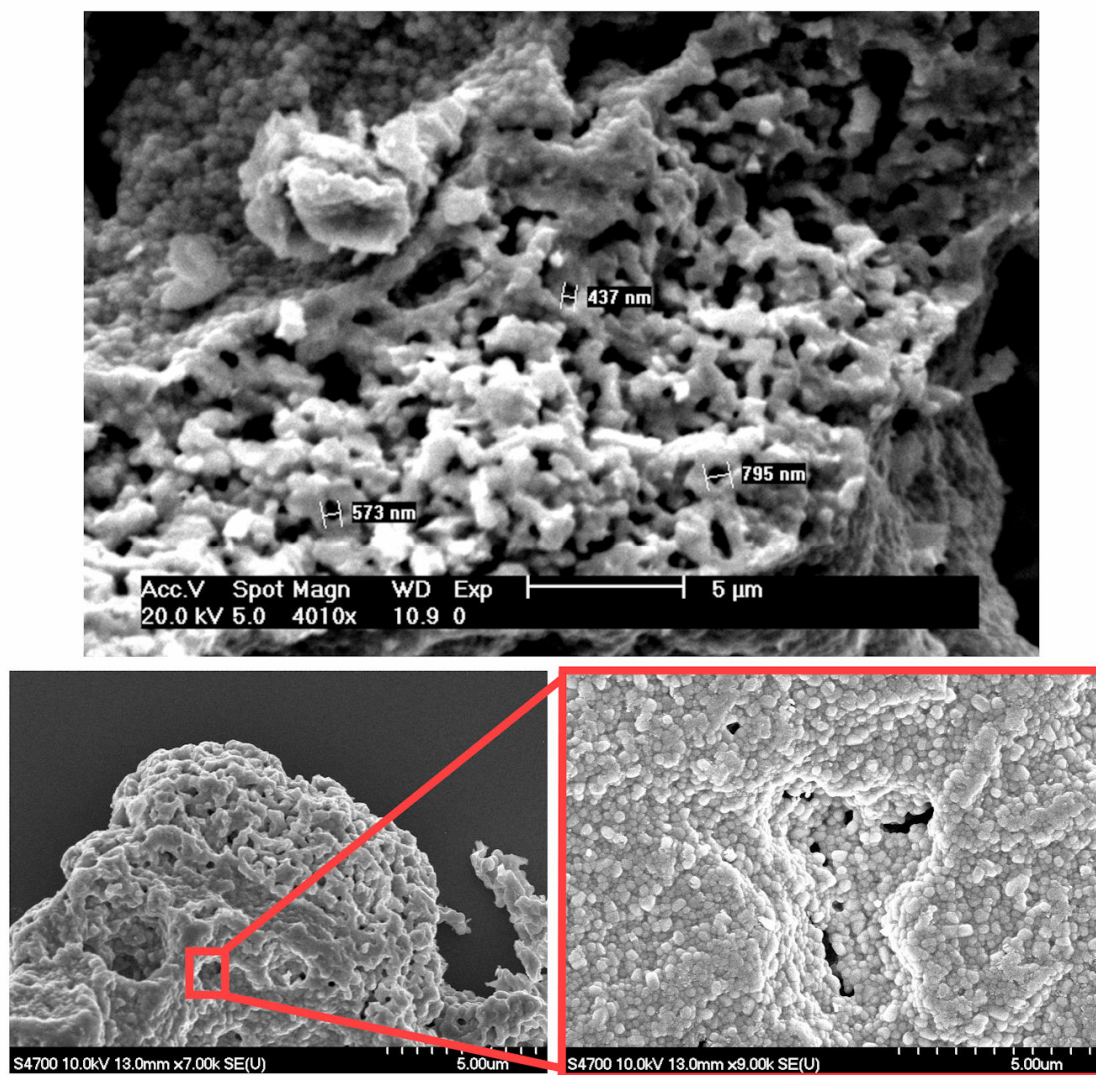
Figure 89: Top: SEM image of the apparently porous structure of the heated compound **6** sample, where the 'pores' have been measured and are typically between 0.5 to 1.0 μm in diameter. Bottom Left: SEM image showing that the apparent porosity of the prepared compound **6** sample is not consistent throughout the sample. i.e. The area of the sample towards the top of the image appears to possess some degree of porosity, whilst the area towards the bottom of the image presents a more close-packed WO_3 framework. Bottom Right: This more closely packed WO_3 framework is shown in more detail as a close-up SEM image.

Despite this it was decided to submit some of the sample for a BET analysis to confirm if any degree of porosity would be displayed by the bulk sample. However, the almost negligible BET reading confirmed the bulk structure to be non-porous. This may be due in part to the non-consistency of the apparently porous WO_3 structure throughout the sample, but another contributing factor may be the wide variation in depth of the 'pores', as can be seen in Figure 86.

3.8.3   Formation of (IPblue)$_3$[PW$_{12}$O$_{40}$]·4DMSO (7)

Following the previously described investigations using triply-charged DIP cations in reactions with phosphotungstic acid, it was decided to pursue this reaction strategy further using a more planar, singly-charged imidazo-phenanthridinium cation.   Hence, the IP compound selected for use in this reaction was 1H-imidazo[1,2-f]phenanthridinium chloride ((IPblue)Cl)(as described previously in section 3.7.2.3).

The synthesis of compound **7** was carried out as follows.   Initially an aqueous solution containing an excess of (IPblue)Cl was added to an aqueous solution of phosphotungstic acid, leading to the formation of an orange precipitate.   Subsequent redissolution of this precipitate in hot DMSO led to the recrystallization of yellow, needle-like single crystals suitable for single crystal X-ray diffraction.   Structural analysis of the X-ray diffraction data revealed the composition of the crystals to be (IPblue)$_3$[PW$_{12}$O$_{40}$]·4DMSO (**7**).

Examination of the unit cell of compound **7** shows that each triply-charged POM anion forms an electrostatic relationship with a columnar arrangement of three, singly-charged, ππ-stacked IPblue cations.   More detailed study of the unit cell reveals that the closest contact distance between the IPblue cation and POM anion in the supramolecular lattice of **7** is 2.992 Å.   Specifically, this contact distance is found between a terminal oxo ligand of the POM cluster, and the phenanthridinium ring nitrogen atom of an adjacent IPblue cation (see Figure 90).   Also a H-bonding interaction of 2.995 Å can be observed between the cluster and this IPblue cation, i.e. between a bridging oxo-ligand of the cluster and the protonated nitrogen atom of the IPblue cation.

When viewing the unit cell along the crystallographic b-axis it can then be seen that this IPblue cation forms part of a ππ-stacking arrangement of three cations running parallel to the crystallographic c-axis.   This is confirmed by measuring the distance between the plane of one IP cation with the centroid of the adjacent IP cation.   The minimum inter-planar distances found, using this method, between the three IP cations were 3.361 Å and 3.289 Å respectively (see Figure 90).   The actual shortest contact distances between the three IP cations vary slightly from these values, i.e. at 3.298 Å (carbon-carbon distance) and 3.350 Å (carbon-nitrogen distance) respectively.   Additionally the carbon-carbon distance of

3.298 Å found between neighbouring IP cations is also the overall, shortest contact distance between IP cations within the crystal lattice of compound **7**.
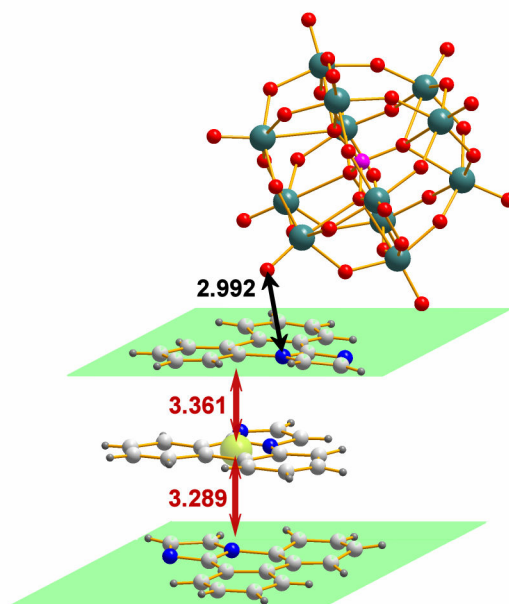
Figure 90: Illustration of part of the unit cell of compound **7**. This representation shows one of the POM clusters and the closest contact distance (i.e. 2.992 Å, shown in black) it makes with the IPblue cation positioned at the top of a ππ-stacking arrangement of three IPblue cations. The distances shown using red arrows represent the minimum inter-planar distances between the three ππ-stacking IPblue cations. These distances are calculated between the planes of the outer IPblue cations (shown using green planes) and the centroid (shown by a green sphere) within the central IPblue cation of the stack. All distances shown are measured in Ångströms (Å). Colour scheme: W, teal; P, pink; O, red; C, light grey; N, blue; H, dark grey. Solvent molecules are omitted for clarity.

However, although these coplanar IP cations are formed into a ππ-stacking arrangement, they do not overlay one another completely. This can be illustrated by checking the torsion angle between each cation *via* the examination of the torsion between a selected bond in each cation. Using this approach it can be found that the torsion angle between the IP cation in closest contact with the POM cluster and the next IP cation in the stack is 111.4°, then the torsion angle between this cation and the last cation in the stack is 70.3° (see Figure 91). Overall this can be seen to create a torsion angle of approximately 180° between the IP cation in closest contact with the POM cluster and the last cation in this three-cation stack (see Figure 91).
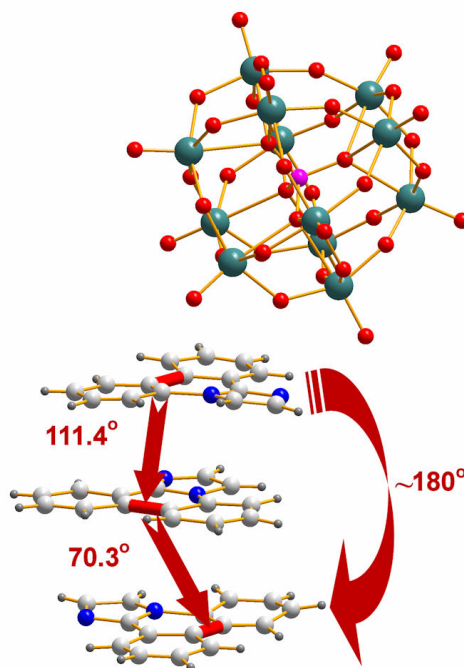
Figure 91: Illustration of part of the unit cell of compound **7**. This representation shows one of the POM clusters and the closest ππ-stacking arrangement of three IPblue cations. The bond highlighted in red within each IPblue cation is used to calculate the torsion angles between each cation in the stack. These torsion angles are shown using red arrows. Also highlighted is the torsion angle of approximately 180° between the top and bottom IPblue cations in the stack. Colour scheme: W, teal; P, pink; O, red; C, light grey; N, blue; H, dark grey. Solvent molecules are omitted for clarity.

Before considering the packing in the crystal lattice in more detail, the $[PW_{12}O_{40}]^{3-}$ cluster anions in the structure, which each form an electrostatic relationship with the three singly-charged IP cations, are examined more closely. As in the previous studies of compounds **5** and **6**, once again the $[PW_{12}O_{40}]^{3-}$ anions are introduced into the reaction system as pre-formed clusters, and as such the lengths of all the W=O terminal bonds, bridging W-O bonds, and P-O bonds are checked to ensure they fall within the expected range of those values quoted in the literature[259] (see Table 10).

Bond Type	Average Bond Distances in Compound **7** / Å
W=O (terminal)	1.70
W-O (μ_2-bridging)	1.91
W-O (μ_4-bridging)	2.46
P-O	1.52

Table 10: Average bond distances within the $[PW_{12}O_{40}]^{3-}$ cluster anion in compound **7**.

Another particularly striking feature when examining the unit cell of compound **7** is the arrangement of the eight POM clusters within the unit cell into two tetrahedral motifs, each of which is centred around a DMSO solvent molecule. When viewing the unit cell along the crystallographic *b*-axis these idealised tetrahedra are seen to be positioned in a co-linear fashion parallel to the crystallographic *c*-axis. However, one of the tetrahedra is rotated, with respect to the neighbouring tetrahedron, through 90° along its C_2 axis which runs parallel to the crystallographic *b*-axis (see Figure 92). It is important to note here that these decriptions of the tetrahedral arrangements of the clusters are based on idealised tetrahedra for ease of description, although on examination of the distances between the central phosphate heteroanion groups of the clusters it can be seen that the tetrahedra are actually distorted. In detail, one of the edges of the tetrahedron is significantly longer, i.e. 16.172 Å, than the neighbouring edges which have an average length of approximately 14.03 Å, whilst the opposite edge is rather shorter at 12.139 Å (see Figure 93).
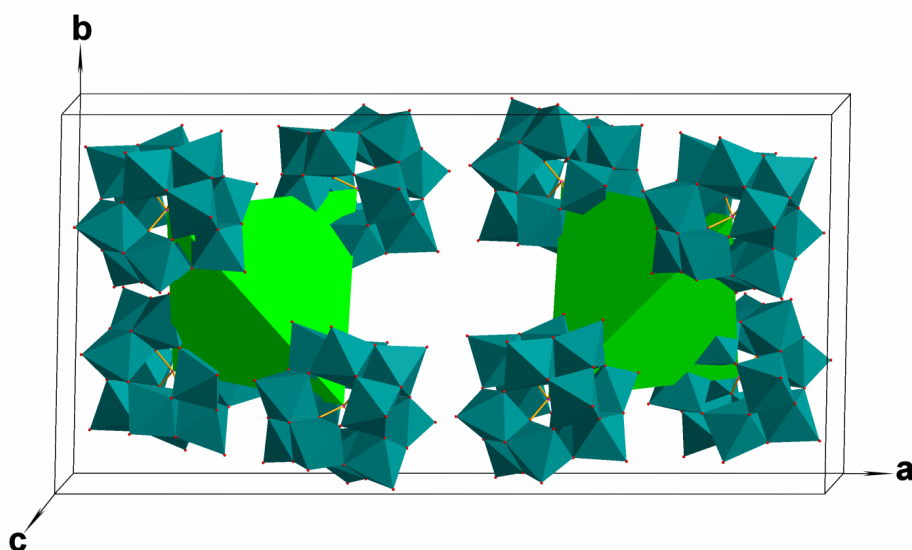
Figure 92: Illustration of the unit cell of compound **7** showing the arrangement of the eight POM clusters within the unit cell into two tetrahedral motifs (highlighted in green), each of which is centred around a DMSO solvent molecule. One of these idealised tetrahedra is rotated, with respect to its neighbour, through 90° along its C_2 axis which runs parallel to the crystallographic *b*-axis. Colour scheme: W, teal polyhedra; P, pink; O, red. Cations and solvent molecules are omitted for clarity.
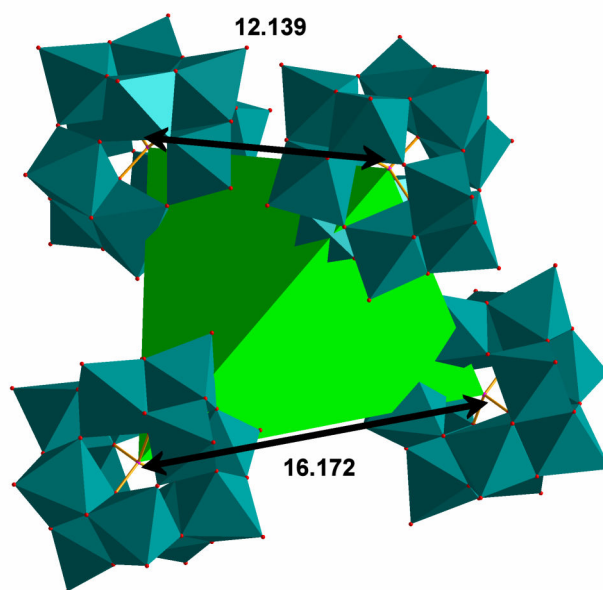
Figure 93: Representation of one of the idealised tetrahedra (highlighted in green) from the unit cell of compound **7**. Although these tetrahedral representations are based on idealised tetrahedra for ease of description, examination of the distances between the central phosphate heteroanion groups of the clusters reveals that these tetrahedra are actually distorted with one of the edges of the tetrahedron being significantly longer than the opposite edge. These distances are indicated in the figure with black arrows and are measured in Ångströms (Å). Colour scheme: W, teal polyhedra; P, pink; O, red.

When extending the packing and viewing the crystal lattice along the crystallographic *b*-axis, these alternating tetrahedral arrangements of POM clusters can be seen to form layers running parallel with the crystallographic *c*-axis. These co-linear layers are then arranged into a repeating ABAB pattern within the crystallographic *ac*-plane, whilst the inter-layer voids (minimum cluster spacing 4.887 Å) are filled with disordered DMSO solvent molecules (see Figure 94).
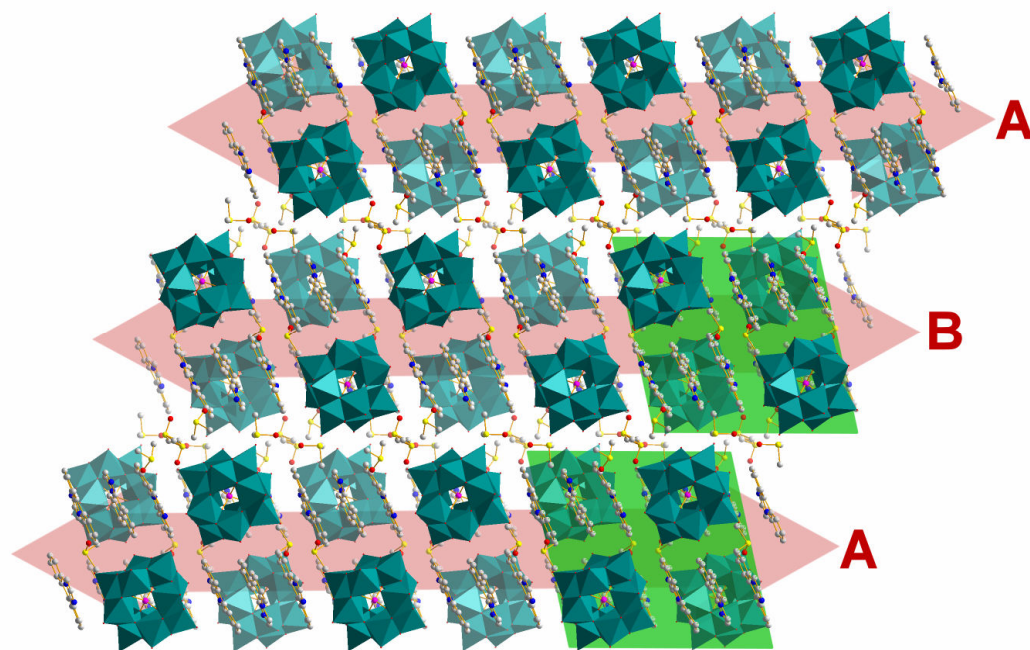
Figure 94: View of compound **7** along the crystallographic *b*-axis. The two idealised tetrahedral arrangements of clusters within the unit cell of **7** (shown in Figure 92) are highlighted using green parallelograms. These green parallelograms also enclose the corresponding organic tetrahedra of IP cation stacks (as shown in Figure 95). The red arrows highlight the layers of these alternating tetrahedral arrangements, which run parallel with the crystallographic *c*-axis. Further the red arrows illustrate the arrangement of these layers into a repeating ABAB pattern within the crystallographic *ac*-plane. The inter-layer voids are seen to be filled with disordered DMSO solvent molecules. Colour scheme: W, teal polyhedra; P, pink; O, red; C, grey; N, blue; S, yellow. H atoms are omitted for clarity.

Examination of the crystal lattice when viewed along the crystallographic *b*-axis reveals, not only the tetrahedral packing arrangements of the inorganic POM building-blocks, but also a corresponding tetrahedron-based organic sub-structure as well. These organic tetrahedral sub-structures are seen to be interlocked with those composed from the inorganic POM clusters and are centred around the same DMSO solvent molecule (see Figure 95 and Figure 96).
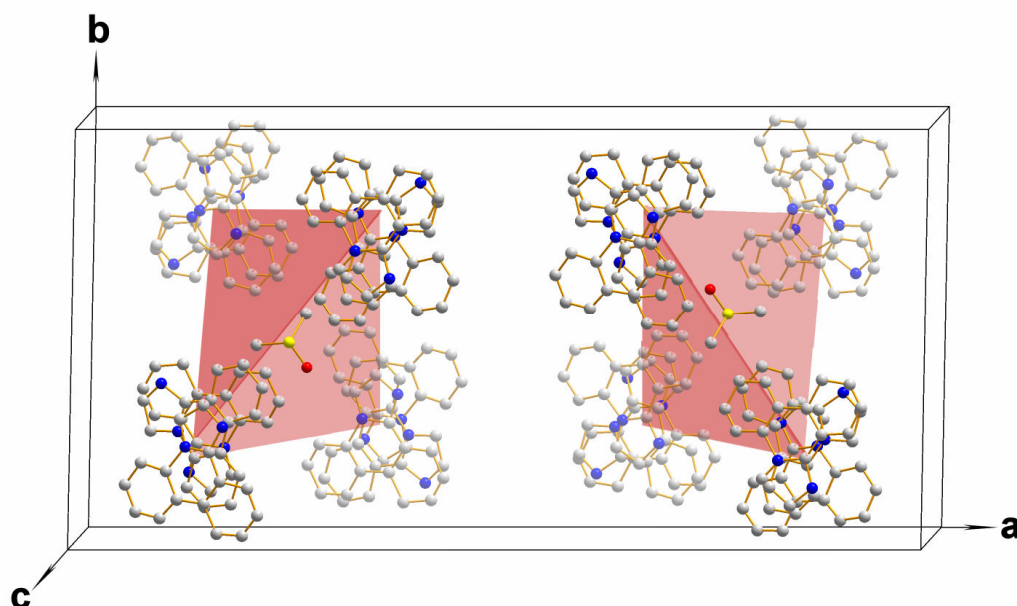
Figure 95: Illustration of the unit cell of compound **7** showing the arrangement of eight, three-cation π-stacks into two tetrahedral motifs (highlighted in red), each of which is centred around a DMSO solvent molecule. One of these idealised tetrahedra is rotated, with respect to its neighbour, through 90° along its C_2 axis which runs parallel to the crystallographic *b*-axis. Colour scheme: C, grey; N, blue; O, red; S, yellow. POM clusters, solvent molecules (aside from the DMSO molecules positioned in the centre of each tetrahedron), and H atoms are omitted for clarity.

Subsequently, these idealised organic tetrahedra are seen to be positioned in a co-linear fashion with each adjacent organic tetrahedron within the crystallographic *ac*-plane, and they are aligned parallel to the crystallographic *c*-axis. However, in a similar fashion to the inorganic tetrahedra, one of these organic tetrahedra is rotated, with respect to its neighbour, through 90° along its C_2 axis which runs parallel to the crystallographic *b*-axis (see Figure 95). Once again, these descriptions of the tetrahedral arrangements of organic cations are based on idealised tetrahedra for ease of description. However, examination of the distances between each of the three-cation stacks, which form the vertices of the tetrahedra, reveals that these organic tetrahedra are actually distorted. This distortion is shown in Figure 97 and the distances have been calculated between centroids positioned within the central ring of the middle cation in each three-cation stack.
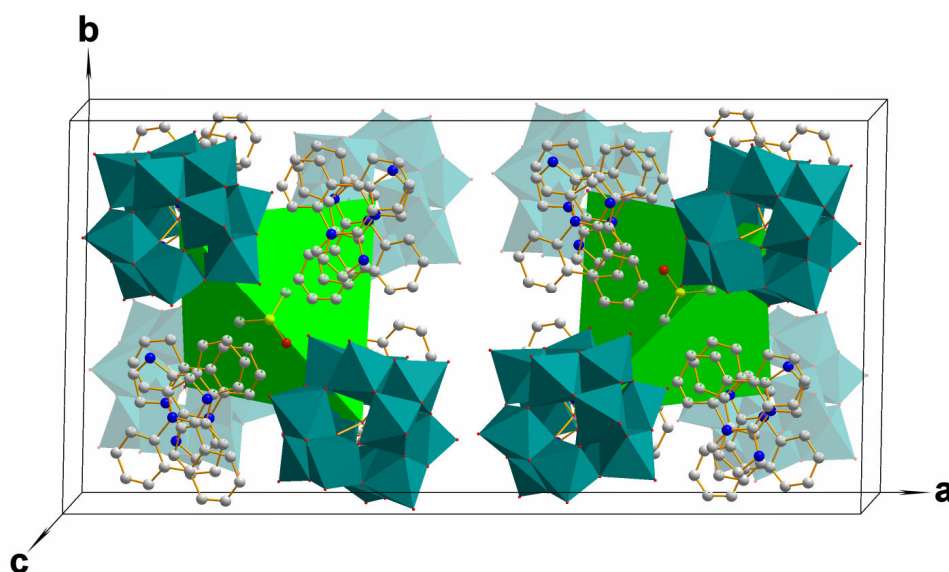
Figure 96: Illustration of the unit cell of compound **7** showing the vertex positions of the interlocked inorganic (POM clusters) and organic (three-cation stacks) tetrahedra, both of which are centred around the same DMSO solvent molecule. For clarity, only the inorganic tetrahedra are shown (highlighted in green). Colour scheme: W, teal polyhedra; O, red; C, grey; N, blue; S, yellow. H atoms and solvent molecules (aside from the DMSO molecules positioned in the centre of each tetrahedron) are omitted for clarity.
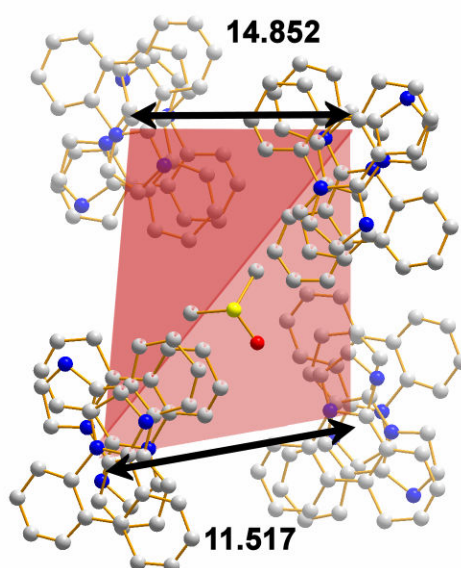
Figure 97: Representation of one of the idealised organic tetrahedra (highlighted in red) from the unit cell of compound **7**. Although these tetrahedral representations are based on idealised tetrahedra for ease of description, examination of the distances between each of the three-cation stacks, which form the vertices of the tetrahedra, reveals that these organic tetrahedra are actually distorted. I.e. One of the edges of the tetrahedron is significantly longer than the opposite edge. These distances are indicated in the figure with black arrows and are measured in Ångströms (Å). Colour scheme: C, grey; N, blue; O, red; S, yellow. POM clusters, solvent molecules (aside from the DMSO molecule positioned in the centre of the tetrahedron), and H atoms are omitted for clarity.

Also, as a result of the interlocking nature of these organic and inorganic tetrahedra, when viewing the crystal lattice along the crystallographic *b*-axis, these alternating, interlocked tetrahedral arrangements can be seen to form layers running parallel with the crystallographic *c*-axis. As described previously, these co-linear layers are then arranged into a repeating ABAB pattern within the crystallographic *ac*-plane, as illustrated in Figure 94.

When viewing the crystal lattice of compound **7** along the crystallographic *c*-axis these alternating, interlocked tetrahedral arrangements which run parallel to the crystallographic *c*-axis are even more clearly displayed and can be seen to extend into layers running parallel to the crystallographic *b*-axis. Each of these co-linear layers is then arranged into the repeating ABAB pattern within the crystallographic *ab*-plane, as described previously when viewing the lattice along the crystallographic *b*-axis. Another feature of viewing the lattice along the crystallographic *c*-axis is that the interlocked nature of the IP cations and POM anions is made more evident by the obvious absence of any organic cations from the inter-layer voids (minimum cluster spacing 4.887 Å). Instead, it is very clear from this view of the lattice that the inter-layer voids are filled only with disordered DMSO solvent molecules. See Figure 98.
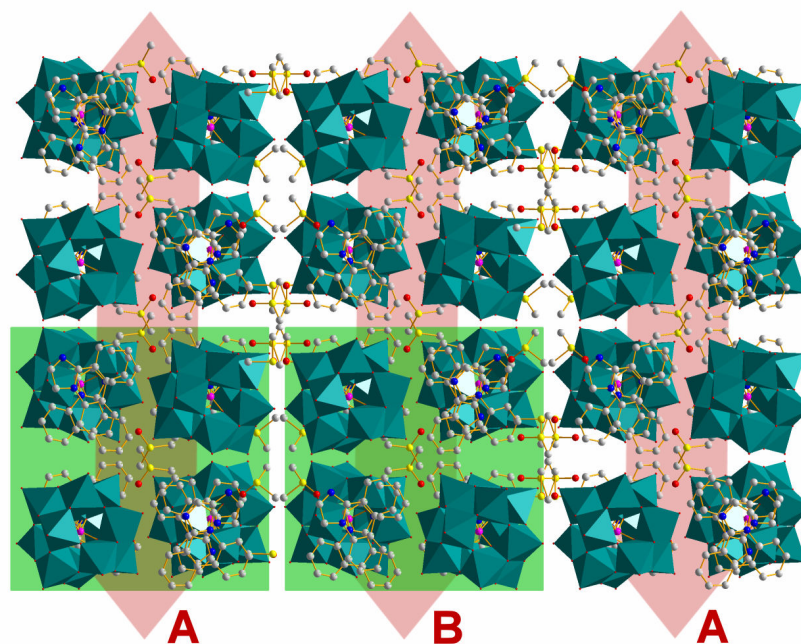
Figure 98: View of compound **7** along the crystallographic *c*-axis. The two interlocked inorganic (POM clusters) and organic (three-cation stacks) tetrahedra within the unit cell of **7** (shown in Figure 96) are highlighted using green squares. The red arrows highlight the layers of these alternating tetrahedral arrangements, which run parallel with the crystallographic *b*-axis; and illustrate the arrangement of these layers into a repeating ABAB pattern within the crystallographic *ab*-plane. The inter-layer voids are filled with DMSO solvent molecules. Colour scheme: W, teal polyhedra; P, pink; O, red; C, grey; N, blue; S, yellow. H atoms are omitted for clarity.

It is also interesting to note that, when viewing the crystal lattice along the crystallographic *b*-axis, an alternative informative interpretation of the packing can be made. This alternative interpretation involves consideration of the inorganic and organic components as forming integrated layers, consisting of a repeating unit composed of a POM cluster and the closest adjacent stack of three IP cations, as represented in Figure 90, i.e. where the closest distance between the POM and IP cation is found to be 2.992 Å. This 'POM-IPstack' unit repeats in a processional, columnar manner parallel with the crystallographic *c*-axis. These columns of 'POM-IPstack' units are then arranged in an offset, yet parallel fashion, into a layer of 'POM-IPstack' columns within the crystallographic *bc*-plane (see Figure 99).
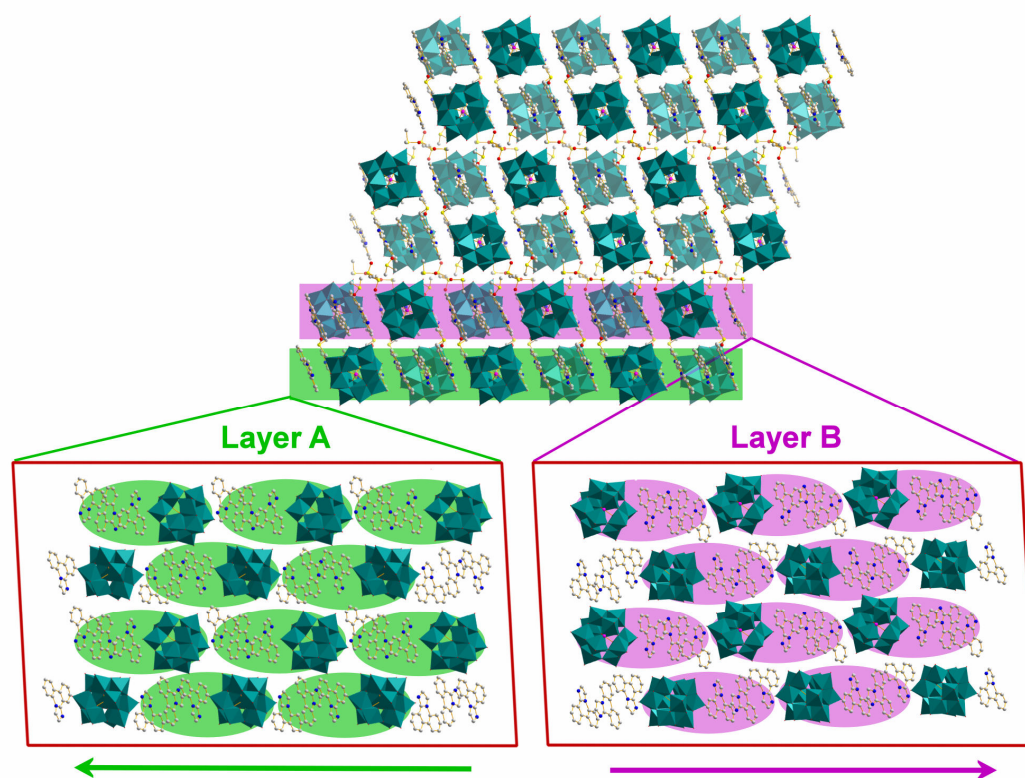
Figure 99: Top: View of compound **7** along the crystallographic *b*-axis where the green rectangle and purple rectangle highlight adjacent, integrated inorganic-organic layers. Bottom left: This figure illustrates layer A when viewed from above. Each 'POM-IPstack' unit is highlighted using a green ellipsoid. These units repeat in a processional, columnar manner parallel with the crystallographic *c*-axis and each, of the four columns shown, follows the direction of the green arrow below the figure. These four columns are then arranged in an offset, yet parallel fashion, so forming a layer of 'POM-IPstack' columns within the crystallographic *bc*-plane. Bottom right: This figure illustrates layer B when viewed from above. Each 'POM-IPstack' unit in this layer is highlighted using a purple ellipsoid. This layer is composed of columns of these units arranged in a similar fashion to those in layer A, however, these repeating units in layer B are positioned in an anti-parallel fashion to those from layer A, as indicated by the direction of the purple arrow below the figure. Colour scheme: W, teal polyhedra; P, pink; O, red; C, grey; N, blue; S, yellow. H atoms are omitted from all figures, and solvent molecules are also omitted from the bottom two figures for clarity.

A similarly composed layer, but with the repeating 'POM-IPstack' units positioned in an anti-parallel fashion, is arranged parallel to the neighbouring layer. The minimum cluster spacing between these two layers is found to be 3.447 Å, which is also the overall minimum cluster spacing within the lattice of compound **7**. These two anti-parallel layers then follow a repeating ABAB pattern within the crystallographic *ac*-plane (see Figure 100). Also every alternate inter-layer void (minimum cluster spacing 4.887 Å), as described previously, is filled with disordered DMSO solvent molecules.
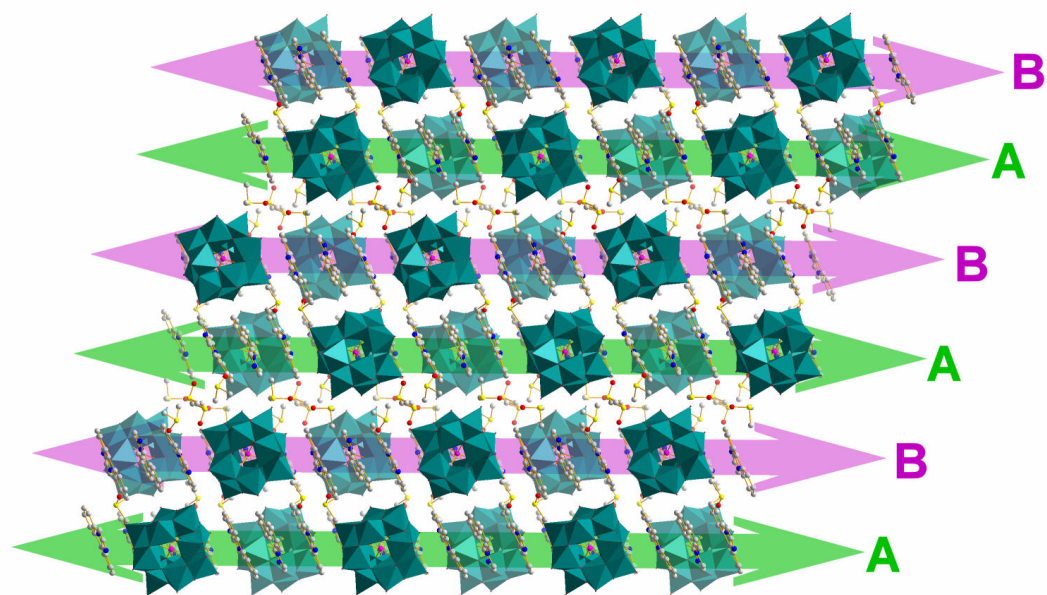
Figure 100: View of compound **7** along the crystallographic *b*-axis showing the anti-parallel, integrated inorganic-organic layers described in Figure 99, following a repeating ABAB pattern within the crystallographic *ac*-plane. Colour scheme: W, teal polyhedra; P, pink; O, red; C, grey; N, blue; S, yellow. H atoms are omitted for clarity.

This alternative interpretation of the lattice, as viewed along the crystallographic *b*-axis, is also helpful when studying the lattice along the crystallographic *a*-axis. To apply this interpretation to the lattice when viewed along the crystallographic *a*-axis, we must consider once again the repeating 'POM-IPstack' units which are arranged in processional, columns running parallel to the crystallographic *c*-axis. When viewed along the *a*-axis each of these 'POM-IPstack' columns is seen to be overlaid with the adjacent, co-linear, yet anti-parallel 'POM-IPstack' column along the *a*-axis (see Figure 101).
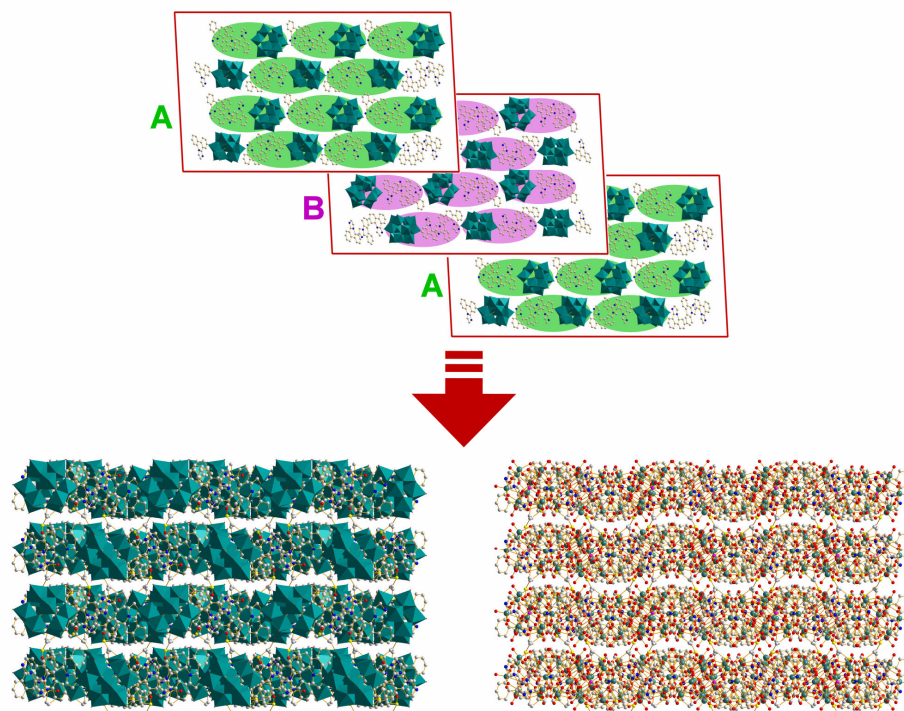
Figure 101: Top: Illustration showing the anti-parallel 'POM-IPstack' columns from each layer of the lattice of **7** (refer to Figure 99), which are overlaid when viewed along the crystallographic *a*-axis. Solvent molecules and H atoms are omitted for clarity. Bottom: When viewing the lattice of **7** along the crystallographic *a*-axis, these overlaid layers give the appearance of wave-like stacked layers, repeating within the crystallographic *bc*-plane. This wave-like arrangement is particularly noticeable when viewing the lattice without the use of polyhedral representations of the cluster anions (right). Colour scheme: W, teal (polyhedra); P, pink; O, red; C, grey; N, blue. H atoms are omitted for clarity.

This presents a wave-like, stacked layer of anti-parallel 'POM-IPstack' columns which runs parallel to the crystallographic *c*-axis. This layer formation of anti-parallel columnar stacks is then repeated within the crystallographic *bc*-plane, but with each 'POM-IPstack' column making up the layer being offset with respect to the 'POM-IPstack' column in the adjacent layer (see Figure 101).

3.8.3.1 Solution and solid state UV/vis spectroscopic analysis of (IPblue)$_3$[PW$_{12}$O$_{40}$]·4DMSO (**7**)

Following the successful isolation and characterization of compound **7** it was decided that, as carried out previously for compounds **5** and **6**, some preliminary spectroscopic analyses of this IP-containing compound should also be undertaken to investigate the presence of any charge transfer interactions between the aromatic cation and POM anion, when both in solution and in the solid state.

For the solution state measurements all compounds were once again dissolved in DMSO, as this solvent was used to recrystallize compound **7**, and each measurement was carried out over the 900 to 200 nm wavelength range (see Experimental, Section 5.6.2.3 for baseline spectrum of DMSO). Recording the spectra of the lone starting materials, i.e. phosphotungstic acid, and (IPblue)Cl; allows clear determination of emergent charge transfer bands in the spectrum of compound **7**, as can be seen from Figures 102 and Table 11.
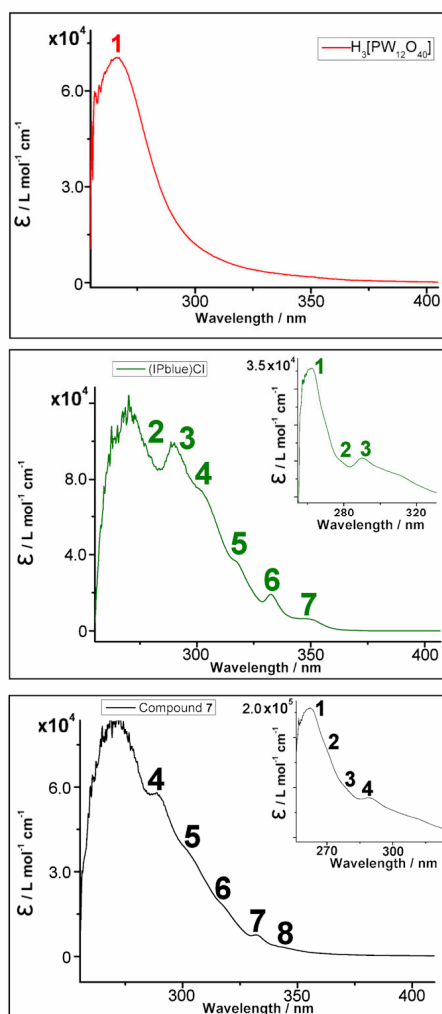
Figure 102: Solution state UV/vis spectra of phosphotungstic acid (1.6 x 10^{-5} mol L^{-1}) (top), (IPblue)Cl (2.6 x 10^{-4} mol L^{-1}) (centre), and compound **7** (3.8 x 10^{-5} mol L^{-1}) (bottom). Inset graph for (IPblue)Cl (centre spectrum) is at lower concentration (2.6 x 10^{-5} mol L^{-1}) to show peak maxima 1, 2 and 3 clearly. Inset graph for compound **7** (bottom spectrum) is at lower concentration (3.7 x 10^{-6} mol L^{-1}) to show peak maxima 1-4 clearly. All compounds are dissolved in DMSO and the spectra recorded over the 900-200 nm wavelength range. Peak maxima are highlighted with numbers which relate to Table 11.

From these results it can be clearly seen that the seven absorbance peaks due to electronic transitions within the IPblue cation are still observable within the spectrum of compound **7** (peak 1 and peaks 3-8, bottom spectrum, Figure 102). It is also possible that the shouldered peak at approximately 270 nm in the spectra of compound **7** (peak 2, bottom spectrum, Figure 102) might be attributed to the overlaid, POM-centred, oxygen ligand-to-metal charge transfer signal found at approximately 266 nm in the spectrum of phosphotungstic acid alone (peak 1, top spectrum, Figure 102). However, although these IP cation-centred and POM-centred transitions can still be observed in the spectrum of compound **7**, no further emergent intermolecular charge transfer bands are detected.

Compound	Peak Maxima Numbering	Wavelength of Absorption / nm	Associated Electronic Transition
$H_3[PW_{12}O_{40}]$	1	266	Oxygen ligand→ Metal charge transfer
(IPblue)Cl	1	261	Electronic transitions centred on IPblue cation
	2	278	
	3	290	
	4	303	
	5	317	
	6	332	
	7	349	
Compound **7**	1	262	Electronic transition centred on IPblue cation
	2	270	Oxygen ligand→ Metal charge transfer (centred on POM cluster)
	3	279	Electronic transitions centred on IPblue cation
	4	288	
	5	303	
	6	317	
	7	332	
	8	349	

Table 11: Summary of absorbance peaks observed in the solution state UV/vis spectroscopy measurements for phosphotungstic acid, (IPblue)Cl, and compound **7** all dissolved in DMSO and recorded over the 900-200 nm wavelength range.

It was then decided to investigate the solid state UV/vis spectroscopic response of compound **7**, and its lone starting materials for comparison purposes. Once again, the technique of diffuse reflectance UV/vis spectroscopy was utilised to determine whether any intermolecular charge transfer phenomenon could be detected when the IP cation and POM anion are in closer proximity in the solid state. The measurements for each of the

starting materials and for compound **7**, were carried out over the 1300 to 190 nm wavelength range, comparisons between these spectra allowing clear identification of any emergent intermolecular charge transfer bands in the spectrum of **7**.
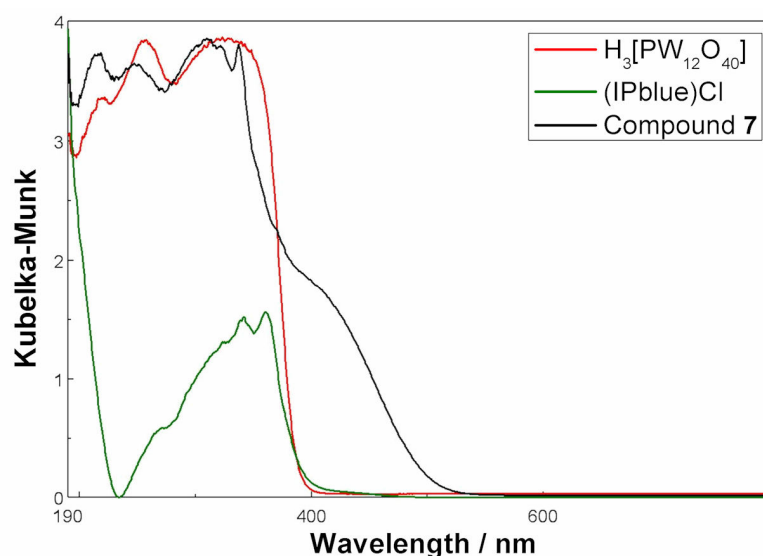
Figure 103: Overlaid diffuse reflectance UV/vis spectra for phosphotungstic acid, (IPblue)Cl, and compound **7** recorded over the 1300 to 190 nm wavelength range. Of particular note is the intermolecular charge transfer band at approximately 410 nm in the spectrum of compound **7** (black line). Colour code as shown in figure.

It can be seen from these results that, as expected when using the technique of diffuse reflectance spectroscopy, the strong absorbance bands which were observed during the solution state UV/vis measurements are suppressed.[279] These suppressed bands, between approximately 190 and 400 nm, are due to the IP cation-centred and POM anion-centred electronic transitions, whilst the strong band at approximately 410 nm is attributed to an intermolecular charge transfer from the aromatic IPblue cation to the fully oxidised POM anion (see Figure 103). The presence of this intermolecular charge transfer band in the solid state UV/vis measurement of compound **7**, but its absence from the solution state measurement could, as previously discussed during the investigation of compound **5**, indicate that either the closer proximity of the cation and anion in the solid state allows such intermolecular charge transitions to take place, or that such transitions might take place in the solution state as well, but are so weak that they cannot be detected.

In addition to these spectroscopic analyses, preliminary cyclic voltammetry studies have also been carried out in order to examine the redox processes of compound **7** in solution. In contrast to the results for compounds **5** and **6**, preliminary results for compound **7** have indicated the presence of five redox processes (one ill-defined) which have been attributed to electron processes on the tungsten centres of the POM anion. Due to the higher concentration of the singly-charged IPblue cations present (due to charge balance reasons), these redox processes are shifted to much more negative electrode potentials when compared with the shifts seen for compounds **5** and **6**. As these investigations are on-going these results will be discussed further in the Experimental, section 5.6.2.3.

3.8.4 Summary of the investigations using 2,3-dihydro-1*H*-imidazo[1,2-*f*]phenanthridinium (DIP) and imidazo-phenanthridinium (IP) as organic cations with Keggin [PW$_{12}$O$_{40}$]$^{3-}$ cluster anions

In summary, through the isolation and characterization of compounds **5**, **6** and **7** it has been shown that DIP and IP cations of varying steric bulk and geometry, and with different charge states, can be introduced into the POM reaction system using the Keggin cluster [PW$_{12}$O$_{40}$]$^{3-}$.

The structure of compound **5** has been shown as governed by electrostatic and H-bonding interactions rather than any ππ-stacking interactions between DIP cations. Each POM anion forms an electrostatic 1:1 relationship with a triply-charged DIP-1 cation; and the protonated diethylenetriamine chain of DIP-1 leads to the formation of an extended H-bonding network with the DMSO and H$_2$O molecules in the structure. The role of these H-bonding interactions in stabilizing the structure of **5** is revealed by viewing the lattice along the crystallographic *c*-axis. When viewing the lattice along this axis the alternating arrangement of DIP cations and POM anions within layers, which run parallel with the crystallographic *b*-axis, becomes evident. The H-bonding interactions are maximised through the orientation of the DIP cations within these layers, i.e. the aromatic head groups are enclosed within the layer structure, whilst the protonated tail groups are directed outwards towards the H-bonding solvent molecules (see Figure 71).

Compound **6** was, like compound **5**, also produced using a triply-charged DIP cation in reaction with phosphotungstic acid. However, although each $[PW_{12}O_{40}]^{3-}$ anion in the structure forms an electrostatic 1:1 relationship with a DIP-2 cation, the lattice structure is markedly different from that for compound **5** due to the steric bulk and geometry of the DIP-2 cation. In particular, in the unit cell of **6** the $[PW_{12}O_{40}]^{3-}$ anion is cupped by the DIP-2 cation, specifically by the two pendent DIP arms A and B, and is positioned in such a way as to have a slightly greater interaction with DIP-arm B. See Figure 77. Also $\pi\pi$-stacking interactions play a large role in stabilizing the structure of compound **6**, with two different types of $\pi\pi$-stacking interactions being identified when viewing the lattice along the crystallographic a-axis (see Figures 79 to 81).

In contrast to compounds **5** and **6**, compound **7** was synthesized through the reaction of a singly-charged imidazo-phenanthridinium cation, IPblue, with phosphotungstic acid. In the structure of **7** each triply-charged POM anion forms an electrostatic relationship with a columnar arrangement of three, singly-charged, $\pi\pi$-stacked IPblue cations (see Figure 90). Examination of the unit cell along the crystallographic b-axis then reveals an interesting packing arrangement based on two, interlocked tetrahedral motifs of the eight POM clusters and cation stacks. Each of these two idealised tetrahedral motifs are centred around a DMSO solvent molecule, and one of the tetrahedra is rotated with respect to its neighbour, through 90° along its C_2 axis which runs parallel to the crystallographic b-axis (see Figure 95 and 96). When extending the packing, these alternating, interlocked tetrahedral motifs can be seen to form layers running parallel with the crystallographic c-axis, and which then follow a repeating ABAB pattern within the crystallographic ac-plane (see Figure 94).

Investigations of the solution state and solid state UV/vis spectroscopic response of each of these compounds were carried out. These preliminary investigations have established that intermolecular charge transfer transitions occur in the solid state for all of the compounds **5** to **7**, and are also detected in the solution state for compound **6**. This may be attributed to the steric bulk of the DIP-2 cations in compound **6** leading to closer contact between these cations and POM anions in the solution state, when compared with the solution state anion-cation contact in compounds **5** and **7**.

Some preliminary cyclic voltammetry experiments using compounds **5** to **7** were carried out to study the redox activity of the dissolved compounds. These experiments revealed that the observed redox processes identified for each compound could be attributed to electron processes on the tungsten centres of the POM anions. Also, because of the presence of DIP or IP cations in these systems, these tungsten-centred redox processes were seen to be shifted to more negative electrode potentials when compared with the results for lone phosphotungstic acid. Due to the ongoing nature of these investigations, however, these results are discussed further in the Experimental, section 5.6.2.

Due to the use of the sterically demanding and geometrically interesting DIP-2 cation in the formation of compound **6,** SEM, EDX and powder XRD were used to examine the structure of the remaining inorganic framework after heating the sample to 1000 °C under an air atmosphere. After oxidation of the organic cations, the remaining tungsten oxide framework was observed to be composed of disc-like and multi-faceted tungsten oxide units, and appeared to possess a degree of porosity. In order to investigate this apparent porosity, BET measurements were then carried out. However, these measurements revealed the bulk structure to be non-porous, possibly due to the non-consistency of the WO_3 structure throughout the sample, or to the wide variation in depth of the 'pores'.

4   Conclusions and Outlook

4.1   Mass spectrometry as a tool to investigate the 'in-solution' self-assembly of polyoxometalate systems

In order to explore the key features of the self-assembly of complex polyoxometalate systems, the techniques of cryospray (CSI-) and electrospray mass spectrometry (ESI-MS) have been utilised to investigate, in detail, the species present within the reaction solutions from which $((n\text{-}C_4H_9)_4N)_{2n}(Ag_2Mo_8O_{26})_n$ (**1**)[81] and $((n\text{-}C_4H_9)_4N)_3[MnMo_6O_{18}((OCH_2)_3CNH_2)_2]$ (**2**)[92] are isolated. This approach has been further developed to allow real-time monitoring of the intensity changes of the detected species, and therefore, their concentrations, over the course of the reactions.

4.1.1   Examining the formation of a silver-linked polyoxometalate architecture using mass spectrometry and UV/vis spectroscopy

The technique of CSI-MS was first utilised in this manner to investigate the 'in-solution' rearrangement of molybdenum Lindqvist $[Mo_6O_{19}]^{2-}$ anions ($\{Mo_6\}$), in the presence of silver(I) cations, into the silver-linked β-octamolybdate structure $((n\text{-}C_4H_9)_4N)_{2n}(Ag_2Mo_8O_{26})_n$ (**1**).[81] Through this investigation the role of small isopolyoxomolybdate fragments and Ag^I ions in the assembly of the silver-linked β-octamolybdate structure **1** has been elucidated *via* the identification of the following anionic series:

(i) $[Mo_mO_{3m}]^-$ where m = 2, 3 or 5

(ii) $[HMo_mO_{3m+1}]^-$ where m = 2 to 6

(iii) $[H_7Mo_mO_{3m+2}]^-$ where m = 2 to 6

(iv) $[H_7Mo_mO_{3m+3}]^-$ where m = 2 to 5

(v) $[H_9Mo_mO_{3m+4}]^-$ where m = 2 to 6

(vi) $[AgMo_mO_{3m+1}]^-$ where m = 2 to 4

Anion series (vi), i.e. $[AgMo_mO_{3m+1}]^-$ where $m = 2$ to 4, is of particular interest because the $[AgMo_2O_7]^-$ and $[AgMo_4O_{13}]^-$ fragments of the $(Ag\{Mo_8\}Ag)$ synthon units, are of significance in understanding the formation of compound **1** from this reaction system. Specifically, detection of the $[AgMo_2O_7]^-$ fragment (peak at 410.7 m/z) supports the theory of rearrangement of the Lindqvist anion into $[AgMo_2O_7]^-$ building-block units, which are the smallest stable unit of the silver-linked POM chain of **1**. Then detection of the $[AgMo_4O_{13}]^-$ fragment (peak at 700.5 m/z), which is half the $(Ag\{Mo_8\}Ag)$ synthon unit, represents the next stepping stone in the final rearrangement into **1** (see Figure 104).

Also of interest from these results is the observation of mono-anionic series involving mixed oxidation state polyoxomolybdate species, from dimolybdate up to hexamolybdate fragments, which have been observed for the first time.[221] The observation of such building units is interesting as similar building-blocks, such as the $\{Mo^V_2O_8\}$ unit,[163, 222, 223] have been used as essential linker units to form mixed-valence POM structures such as $(Me_3NH)_2(Et_4N)Na_4[Na(H_2O)_3H_{15}Mo^V_{36}Mo^{VI}_6O_{109}((OCH_2)_3CCH_2OH)_7]$[224] and $(NH_4)_{12}[Mo_{36}(NO)_4O_{108}(H_2O)_{16}]$.[163]

In the higher mass range of these CSI-MS analyses, detection of the species $[(AgMo_8O_{26})TBA_2]^-$ (peak at 1776.6 m/z), $[(Ag_2Mo_8O_{26})(Mo_4O_{13})TBA_3]^-$ (peak at 2718.3 m/z), and $[(Ag_2Mo_8O_{26})(Mo_8O_{26})TBA_5]^-$ (peak at 3796.5 m/z), each with an increasing organic cation contribution concomitant with the increasing metal nuclearity, supports the previously proposed hypothesis[81] that the organic cations used in the synthesis do indeed play an important structure-directing role in promoting the mode of POM structure growth in solution (see Figure 104).
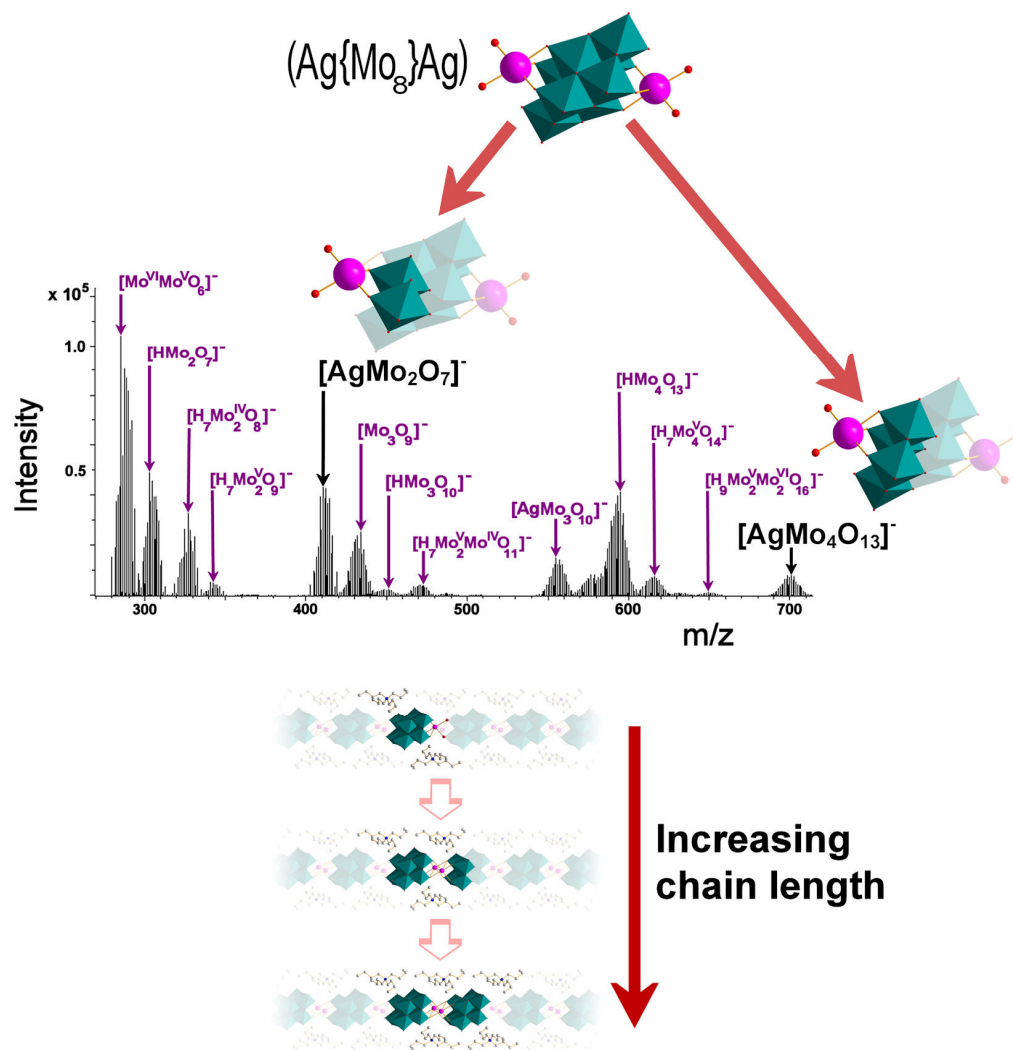
Figure 104: Top: The $[AgMo_2O_7]^-$ and $[AgMo_4O_{13}]^-$ fragments of the $(Ag\{Mo_8\}Ag)$ synthon of **1,** as observed in the mass spectrum of the reaction solution of **1**, are highlighted. Bottom: Illustration of the increasing chain length of fragments of **1** as observed in the higher mass range of the CSI-MS analyses carried out. Colour scheme: Mo, teal polyhedra; Ag, pink; O, red; C, grey; N, blue. All structures shown are formal representations based on crystallographic data.[81]

The rate of decrease in Lindqvist anion concentration, and therefore associated increase in $\{Mo_8\}$ anion concentration, for Reaction Mixtures **A-D,** were monitored *via* UV/vis spectroscopy. This correlation between decreasing Lindqvist anion and increasing $\{Mo_8\}$ anion concentration was supported by CSI-MS monitoring of Reaction Mix **A**, i.e. $TBA_2[Mo_6O_{19}]$ + AgF, over time. The use of CSI-MS in this way to monitor real-time, 'in-solution' rearrangements in a POM reactant solution represents a new approach to the application of mass spectrometry techniques in examining the self-assembly of POM compounds in solution.

The effect of the length of organic counter cation used in the reaction system on the rate of Lindqvist to (Ag{Mo$_8$}Ag) synthon rearrangement was examined *via* comparison of the 'pseudo' first order rate constants, with respect to [{Mo$_6$}], calculated over the first 75 min in the UV/vis spectroscopy experiment for each reaction mix. The general trend observed from these calculated rate constants was that the rate of decrease in the concentration of Lindqvist anions, and as a result, the inter-conversion of Lindqvist into β-octamolybdate anions, decreases as the carbon chain length of the alkylammonium cations increases.[225] These lower rates of inter-conversion when using a hexamolybdate reagent with a longer chain cation have been attributed to the steric bulk of these large organic groups hindering the rearrangement of Lindqvist anions, and hindering contact between the silver cations and molybdenum anions. In conclusion, therefore, these results support the previously proposed hypothesis that the steric bulk of the alkylammonium cations present in a reaction system influences the (Ag{Mo$_8$}Ag) synthon-containing POM structures which can be formed and then isolated in the solid state from these reaction mixtures.[81, 185]

4.1.2   Mass spectral investigations into the 'in-solution' formation of an organic-inorganic hybrid polyoxometalate

Following the mass spectral investigations described above into the formation of a silver-linked polyoxomolybdate system, this approach was extended to examine the formation of a complex organic-inorganic POM-hybrid system, i.e. ((n-C$_4$H$_9$)$_4$N)$_3$[MnMo$_6$O$_{18}$((OCH$_2$)$_3$CNH$_2$)$_2$] (**2**).[92]

The technique of ESI-MS was utilised in this investigation to enable real-time, 'in-solution' monitoring of the rearrangement of α-octamolybdate anions [α-Mo$_8$O$_{26}$]$^{4-}$ ({Mo$_8$}), and coordination of Mn(III) cations and TRIS groups, leading to the formation of **2**. The MS data recorded at the start of the reaction (after stirring the reaction solution at room temperature for 13 min) is dominated by peaks which can be assigned to

isopolyoxomolybdate fragments of the rearranging $[\alpha\text{-Mo}_8\text{O}_{26}]^{4-}$ anion (see top of Figure 105) and contains the ion series:

i) $[\text{H}_{m-2}\text{Mo}_m\text{O}_{3m}]^-$ where $m= 2$ or 3

ii) $[\text{Mo}_m\text{O}_{3m+1}]^{2-}$ where $m= 4$ or 5

iii) $[\text{Na}_n\text{H}_{1-n}\text{Mo}_m\text{O}_{3m+1}]^-$ where $m= 3$ or 4 and $n = 0$ or 1

iv) $[\text{H}_2\text{Mn}^{2+}\text{Mo}_m\text{O}_{3m+1}]-$ where $m = 3$ or 4

v) $[\text{Mo}_m\text{O}_{3m+1}\text{TBA}_1]^-$ where $m= 3$ to 5

vi) $[\text{Mo}_8\text{O}_{26}\text{TBA}_{3-n}\text{Na}_n]^-$ where $n= 0$ to 2

The dominance of these isopolyoxomolybdate fragments indicates that the $[\alpha\text{-Mo}_8\text{O}_{26}]^{4-}$ anion rearranges into these smaller fragment ions prior to further coordination with the manganese cations and TRIS groups. Indeed the first indications of this further coordination are illustrated by the presence of very low intensity peaks containing TRIS groups and manganese cations, e.g. $[\text{Mo}_2\text{O}_5((\text{OCH}_2)_3\text{CNH}_2)]^-$ (387.8 m/z), and $[\text{Mn}^{\text{III}}\text{Mo}_3\text{O}_8((\text{OCH}_2)_3\text{CNH}_2)_2]^-$ (706.7 m/z).
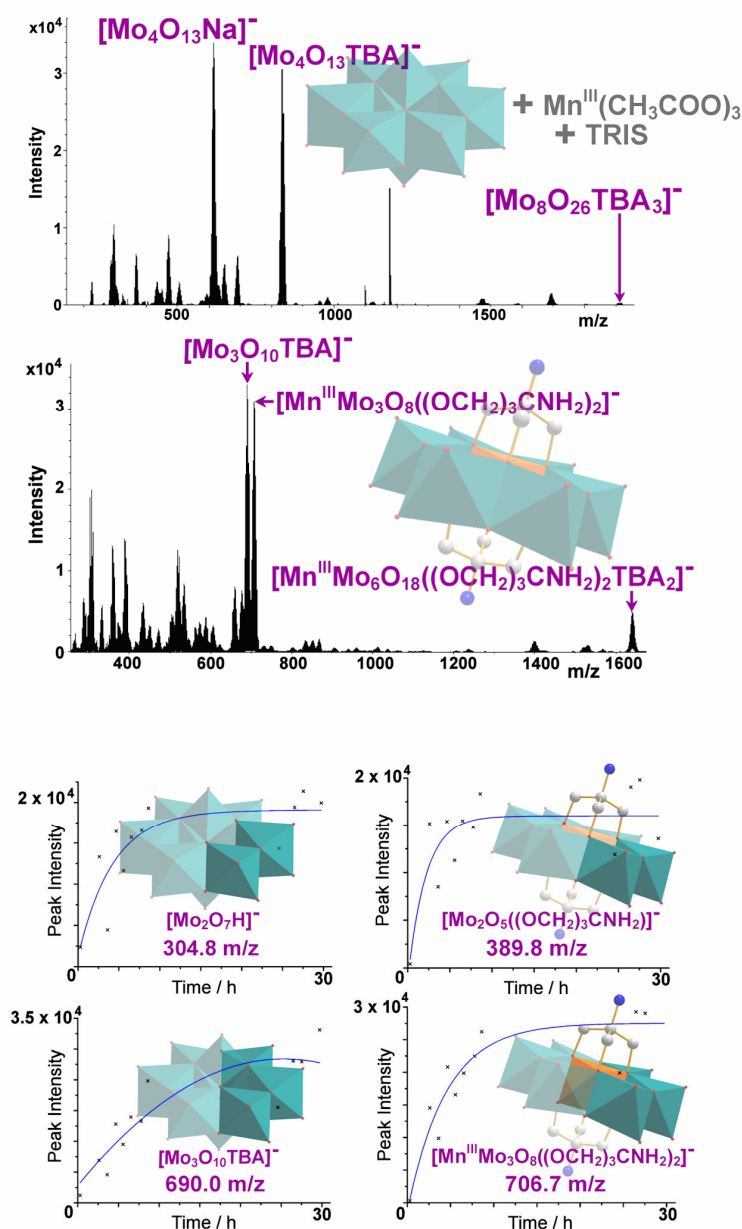
Figure 105: Top: ESI-MS spectra of the reaction solution of **2** collected: after stirring at room temperature for 13 min, and after refluxing at 80 °C for approximately 30 h. The [α-Mo_8O_{26}]$^{4-}$ anions, manganese(III) acetate and TRIS starting materials in the reaction solution are shown faded behind the first spectrum recorded. This spectrum is dominated by isopolyoxomolybdate species. The derivatized Mn-Anderson anion of **2**, i.e. [$MnMo_6O_{18}((OCH_2)_3CNH_2)_2$]$^{3-}$, is shown faded behind the final spectrum recorded. This spectrum is of greater complexity and contains a wide variety of fragment ion species. Bottom: Graphs showing the increasing peak intensity of the small fragments ions (listed in purple), when monitoring the reaction solution of **2** over 30 h using ESI-MS. The structures of these small fragments are shown faded behind each graph, and are formal representations based on crystallographic data.[92] Colour scheme: Mo, teal polyhedra; Mn, orange polyhedra; O, red; C, grey; N, blue. H atoms are omitted for clarity.

The MS data collected after refluxing for approx 7 h is of much greater complexity and the dominant peaks have been assigned to a wide variety of fragments, such as,

polyoxomolybdate fragments coordinated to Mn cations, e.g. $[Mn^{II}Mo^{VI}Mo^{V}O_7]^-$ (peak at 358.7 m/z); polyoxomolybdate fragments coordinated to TRIS, e.g. $[Mo_2O_5((OCH_2)CNH_2)]^-$ (peak at 389.8 m/z); or fragments of the product cluster **2**, e.g. $[Mn^{III}Mo_3O_8((OCH_2)_3CNH_2)_2]^-$ (peak at 706.7 m/z). This complexity of fragment ions identified, remained observable through to the final spectrum recorded after MS monitoring of this reaction solution for approximately 30 h (see lower spectrum at top of Figure 105), and the ion series identified were as follows:

i) $[H_{m-2}Mo_mO_{3m}]^-$ where $m = 2$ or 3

ii) $[HMo_mO_{3m+1}]^-$ where $m = 2$ or 3

iii) $[HMn^{2+}Mo_mO_{3m+2}]^-$ where $m = 2$ or 3

iv) $[Mo_mO_{3m-1}((OCH_2)_3CNH_2)]^-$ where $m = 2$ or 3

v) $[Mn^{(n+2)+}Mo_3O_{9+n}((OCH_2)_3CNH_2)H]^-$ where $n = 0$ or 1

vi) $[Mn^{3+}Mo_mO_{3m-1}((OCH_2)_3CNH_2)_2]^-$ where $m = 2$ to 5

vii) $[Mn^{3+}Mo_6O_{18}((OCH_2)_3CNH_2)_2TBA_{2-n}H_n]^-$ where $n = 0$ or 1

viii) $[Mo_mO_{3m+1}TBA_1]^-$ where $m = 3$ or 4

Additionally, by noting the changes in peak intensity of prominent peaks in the ESI-MS spectra over the time of this reaction, we were able to propose that the rearrangement of $[\alpha\text{-}Mo_8O_{26}]^{4-}$, occurs first *via* the formation of $[Mo_4O_{13}]^{2-}$ cluster species (i.e. $[Mo_4O_{13}Na_1]^-$ (614.6 m/z) and $[Mo_4O_{13}TBA]^-$ (833.8 m/z)) which are half-fragments of the $\{Mo_8\}$ clusters and the most prominent peaks in the first spectrum recorded (see top of Figure 105). It is proposed that this is followed by decomposition to smaller, stable isopolyoxomolybdate fragment ions containing just two, i.e. $[Mo_2O_7H]^-$, and three molybdenum centres, i.e. $[Mo_3O_{10}TBA]^-$; which subsequently coordinate with the tripodal TRIS ligands, i.e. $[Mo_2O_5((OCH_2)_3CNH_2)]^-$ (389.8 m/z); manganese ions, i.e. $[Mn^{III}Mo_3O_8((OCH_2)_3CNH_2)_2]^-$ (706.7 m/z) (see bottom of Figure 105); and further molybdate anionic units, to form the final Mn-Anderson-TRIS cluster of **2**, i.e. $[Mn^{III}Mo_6O_{18}((OCH_2)_3CNH_2)_2TBA_2]^-$ (1640.0 m/z).

In conclusion, these investigations have illustrated the power of CSI- and ESI-MS techniques in examining the self-assembly of POMs from their reaction solutions, not only on reaction conclusion, but in real-time. The application of these techniques to elucidate the 'in-solution' processes of ever more complex POM systems is now underway.

4.2 Investigating the encapsulation of high oxidation state heteroatoms within polyoxometalate clusters

Cronin *et al* have recently synthesized two tungsten-based Dawson clusters which encapsulate high oxidation state heteroanion templates, i.e. $[H_3W_{18}O_{56}(I^{VII}O_6)]^{6-}$[148] and $[H_3W_{18}O_{56}(Te^{VI}O_6)]^{7-}$[149], and which both possess catalytic activity towards the oxidation of alcohols. Following this work it was decided to investigate whether the analogous periodate-centred and tellurate-centred molybdenum analogues could also be produced. Although the isolation of these particular compounds continues to elude us, these investigations have allowed the isolation and characterization of two new molybdenum Anderson-based polyoxometalate structures, i.e. $Cs_{4.67}Na_{0.33}[IMo_6O_{24}]\cdot ca7H_2O$ (**3**), and $Na_4((HOCH_2CH_2)_3NH)_2[TeMo_6O_{24}]\cdot ca10H_2O$ (**4**).

4.2.1 Investigations into the encapsulation of periodate and tellurate heteroanion templates within polyoxomolybdate clusters

It was found that addition of periodic acid to an aqueous solution of sodium molybdate, followed by acidification to pH 1.8 using hydrochloric acid, and subsequent addition of an aqueous caesium chloride solution, led to the isolation of colourless, block, single crystals of $Cs_{4.67}Na_{0.33}[IMo_6O_{24}]\cdot ca7H_2O$ (**3**).
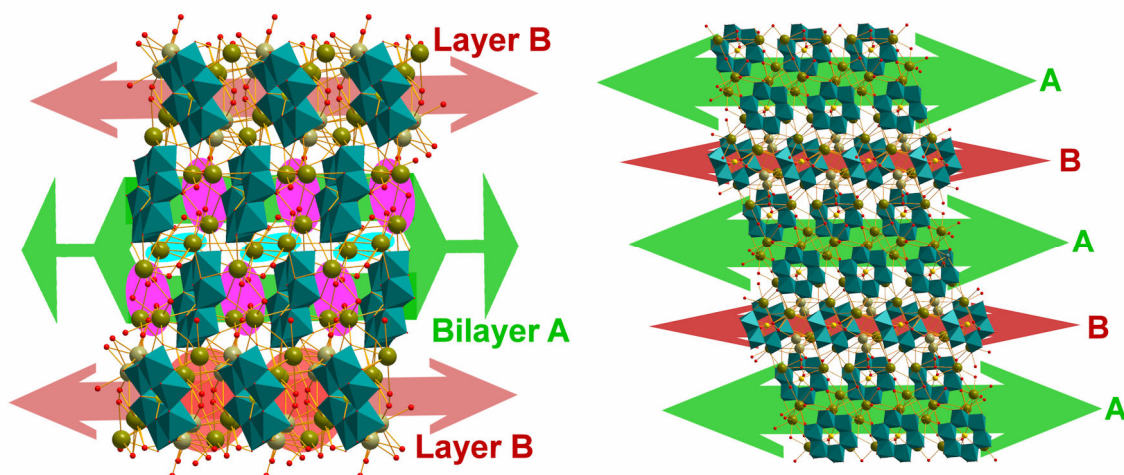
Figure 106: Left: Representation of **3** when viewed along the crystallographic *b*-axis. The green arrow highlights the two offset cluster arrays which make up bilayer A. The pink ellipsoids highlight the three coordinating caesium cations in the intra-layer voids, and the light blue ellipsoids highlight the two coordinating caesium cations between the offset cluster arrays. The red arrows highlight layer B, and the orange ellipsoids highlight the six coordinating caesium cations and four, partially-occupied sodium cations (disordered with caesium cations) between the clusters in this layer. Right: Representation of **3** when viewed along the crystallographic *a*-axis. The repeating ABAB pattern of bilayer A and layer B are still observable when viewing the lattice along this axis, however, when viewing in this direction the cluster layers run parallel with the crystallographic *b*-axis and the ABAB pattern extends within the crystallographic *bc*-plane. Colour scheme: Mo, teal polyhedra; I, gold; Cs, green; Na, grey; O, red.

Analysis of the crystal structure of **3** has revealed a closely-packed arrangement of periodate-centred molybdenum Anderson clusters which form ABAB layered cluster arrangements, when viewing along both the crystallographic *a*- and *b*-axes (see Figure 106). Layer A is composed of a bilayer of offset POM cluster arrays, where three coordinating caesium cations and H-bonding water molecules separate the clusters and reinforce each of these 'sub-layers'; then two further caesium cations reinforce the bilayer arrangement by coordinating between adjacent clusters from each 'sub-layer' (see left of Figure 106). Layer B is formed by an array of POM clusters which are offset and oriented at an angle of 25.5° with respect to the clusters which make up bilayer A. The structure of this layer is again reinforced by cation coordination and H-bonding interactions. In more detail, coordinating caesium cations; partially-occupied sodium cations (disordered with caesium cations); and H-bonding solvent H_2O molecules, occupy the spaces between the clusters so further stabilizing this cluster layer (see left of Figure 106).

When investigating the polyoxomolybdate structures formed on using $\{Te^{VI}O_6\}$ as a heteroanion template, the new molybdenum Anderson-based structure $Na_4((HOCH_2CH_2)_3NH)_2[TeMo_6O_{24}]\cdot ca10H_2O$ (**4**) was isolated. Examination of the crystal structure of **4** has revealed that the main building-blocks of the structure are the $[TeMo_6O_{24}]^{6-}$ anions and two coordinated cation arrangements, each of which is composed of a $\{Na_2\}$ dimer and a coordinated TEAH$^+$ cation. In more detail, within the unit cell of **4,** two of these $\{Na_2\}$ dimer and TEAH$^+$ cation motifs are seen to be coordinated to a central Anderson cluster, one situated on each face, and which are related by a centre of inversion positioned at the tellurium atom in the centre of the POM cluster (see top left of Figure 107). Two of the μ_2-bridging H_2O ligands, from each of these $\{Na_2\}$ dimer units, then coordinate to the $\{Na_2\}$ dimers on neighbouring POM clusters, leading to the connection of four adjacent POM clusters to the central Anderson cluster (see top right of Figure 107). These clusters are aligned in an almost parallel fashion, and are tilted at an angle of 71.5° with respect to the central Anderson cluster.
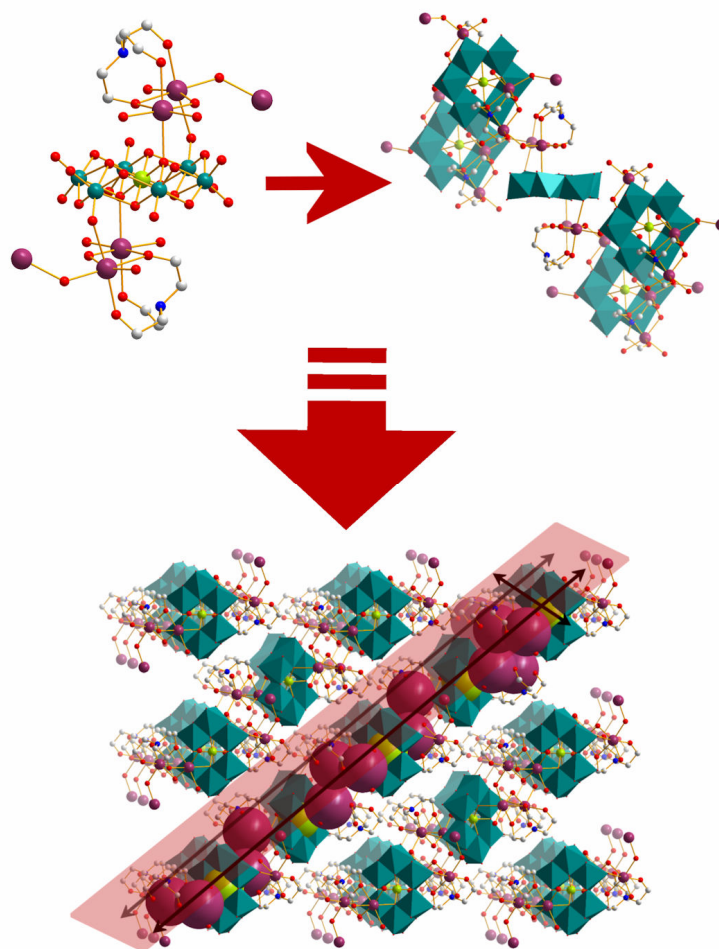
Figure 107: Top Left: Illustration of the coordinated cation arrangements in **4**, each of which is composed of a {Na$_2$} dimer and TEAH$^+$ cation, coordinated to opposing faces of the central [TeMo$_6$O$_{24}$]$^{6-}$ Anderson cluster. Top Right: Illustration showing the inter-connection, *via* the {Na$_2$} dimer units, of four clusters adjacent to the central Anderson cluster. Bottom: Representation of **4** when viewed slightly offset from the crystallographic *b*-axis. The space-filling representation highlights first the connection of the POM clusters into chains, which run at an angle of approximately 45° to the crystallographic *a*-axis; then second, the inter-connection of these chains *via* the {Na$_2$} dimer motifs, into layers of cluster chains extending along the crystallographic *b*-axis. These features are indicated using the black arrows and the red plane. Colour scheme: Mo, teal polyhedra; Te, light green; Na, purple; O, red; C, grey; N, blue. Solvent molecules and H atoms are omitted for clarity.

The inter-connection of these sub-structural motifs has led to some interesting packing arrangements within the overall crystal lattice of **4**. For example, when viewing the lattice along the crystallographic *b*-axis, the inter-connection of these structural motifs leads to the formation of a layered arrangement of inter-connected chains of POM clusters. These chains of POM clusters are observed to be formed *via* connection through the {Na$_2$} dimer units, and lie at approximately 45° to the crystallographic *a*-axis. Further inter-connection

between these cluster chains results in the formation of layers which extend along the crystallographic *b*-axis, then repeat in a co-linear fashion within the crystallographic *ac*-plane (see bottom of Figure 107).

In conclusion, two new molybdenum Anderson-based POM architectures have been synthesized, where the Anderson clusters in each are constructed around high oxidation state heteroanion templates, i.e. $\{I^{VII}O_6\}$ and $\{Te^{VI}O_6\}$, and the cations chosen for use in each system have led to formation of interesting packing arrangements in the solid state. Further work will continue to investigate the isolation of larger molybdenum cluster cages encapsulating these high oxidation state heteroanion templates, in the hope of developing stable, yet flexible cluster frameworks capable of structural rearrangement without decomposition on reduction of the central heteroanion template.

4.3 Investigations into the synthesis of new polyoxometalate architectures using pre-formed cluster building-blocks and large, photoactive organic cations

In order to investigate the synthesis of structurally interesting and potentially photoactive POM-organic compounds, three aromatic, organic molecules from a family of phenanthridinium-based molecules developed by Cronin *et al*[209, 210] have been used to synthesize three new POM architectures on reaction with phosphotungstic acid, i.e. (DIP-1)$[PW_{12}O_{40}]\cdot$5DMSO$\cdot ca$1H$_2$O (**5**); (DIP-2)$[PW_{12}O_{40}]$ $\cdot$5DMSO$\cdot ca$4H$_2$O (**6**); and (IPblue)$_3[PW_{12}O_{40}]\cdot$4DMSO (**7**). Following the successful isolation of these compounds, some preliminary UV/vis spectroscopy and cyclic voltammetry experiments have also been carried out to investigate the presence of any intermolecular charge transfer bands, and the redox processes of these compounds in solution, respectively.

4.3.1 Investigations using 2,3-dihydro-1*H*-imidazo[1,2-*f*]phenanthridinium (DIP) and imidazo-phenanthridinium (IP) as organic cations with Keggin [PW$_{12}$O$_{40}$]$^{3-}$ cluster anions

The successful isolation and characterization of compounds **5**, **6**, and **7**, has illustrated that DIP and IP cations of varying steric bulk and geometry, and with different charge states, may be introduced into the POM reaction system using the Keggin cluster, [PW$_{12}$O$_{40}$]$^{3-}$. Also each of these compounds were synthesized using similar experimental procedures, which allowed the isolation of single crystals suitable for single crystal X-ray diffraction.

4.3.1.1 (DIP-1)[PW$_{12}$O$_{40}$]·5DMSO·*ca*1H$_2$O (**5**)

In compound **5** each [PW$_{12}$O$_{40}$]$^{3-}$ anion forms an electrostatic 1:1 relationship with a triply-charged DIP-1 cation; and the presence of the protonated diethylenetriamine chain of DIP-1 leads to the formation of an extended H-bonding network with the DMSO and H$_2$O molecules in the structure. Indeed, of particular interest in this structure is the way these H-bonding interactions are maximised through the layer arrangement of cations and anions, when viewing the lattice along the crystallographic *c*-axis.
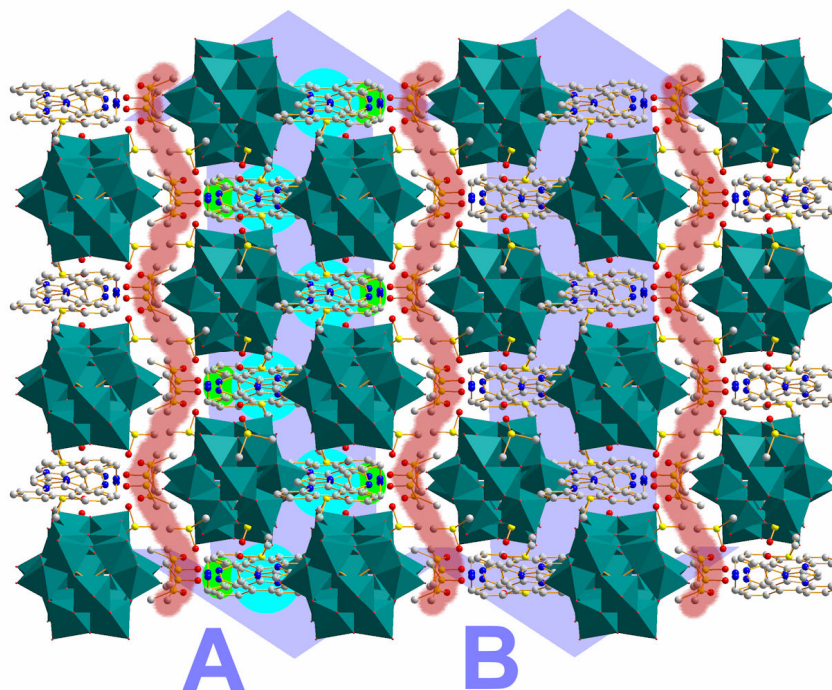
Figure 108: Representation of **5** when viewed along the crystallographic *c*-axis. The POM clusters and DIP cations are aligned together into layers which are highlighted with light purple arrows. These layers run parallel with the crystallographic *b*-axis and form a repeating ABAB pattern within the crystallographic *ab*-plane. Within one of these layers the light blue circles highlight the aromatic head groups of the DIP cations which are enclosed within the layer, whilst the light green ellipsoids highlight the protonated tail groups of the DIP cations which are directed outwards towards the H-bonding solvent molecules. The DMSO solvent molecules within the inter-layer voids are arranged in an anti-parallel fashion in order to maximise the H-bonding interactions with the tail groups of the DIP cations. This leads to the appearance of wave-like layers of these DMSO solvent molecules in the inter-layer voids, which are highlighted in red. Colour scheme: W, teal polyhedra; P, pink; O, red; C, grey; N, blue; S, yellow. Solvent H_2O molecules and H atoms are omitted for clarity.

When viewing along this crystallographic axis the inorganic clusters and DIP cations are aligned together into layers running parallel with the crystallographic *b*-axis, alternating between inorganic and organic components as you move along the length of the layer (see light purple arrows in Figure 108). These layers are then arranged into a repeating ABAB pattern within the crystallographic *ab*-plane. In order to maximise the H-bonding interactions with the DMSO and H_2O molecules lying within the inter-layer voids, each DIP in these inorganic-organic layers is positioned so that the aromatic head group is enclosed within the layer, whilst the protonated tail group is directed outwards towards the H-bonding solvent molecules. A wave-like layer of anti-parallel DMSO molecules can

then be seen within each inter-layer void, running parallel to the crystallographic b-axis, as a result of these H-bonding interactions (see Figure 108).

4.3.1.2 (DIP-2)[PW$_{12}$O$_{40}$] 5DMSO·ca4H$_2$O (**6**)

Compound **6** was also produced using a triply-charged DIP cation in reaction with phosphotungstic acid, therefore, each $[PW_{12}O_{40}]^{3-}$ anion in the structure forms an electrostatic, 1:1 relationship with a sterically bulky DIP-2 cation. Indeed, in the unit cell of **6,** the $[PW_{12}O_{40}]^{3-}$ anion can be seen to be cupped, within the more sterically crowded face of the DIP-2 cation, by the two DIP arms A and B, and is positioned in the matrix in such a way as to have a slightly greater interaction with DIP-arm B than DIP-arm A. See top left of Figure 109.

When viewing the crystal lattice along the crystallographic a-axis, the $[PW_{12}O_{40}]^{3-}$ cluster anions can be seen to be arranged into layers composed of two anti-parallel arrays of clusters, which run parallel with the crystallographic c-axis, and follow a repeating ABAB pattern within the crystallographic bc-plane. It is also noticeable that the DIP-2 cations form an organic 'sub-lattice' within the greater lattice structure. This organic 'sub-lattice' is comprised of two layers of DIP-2 cations arranged in an anti-parallel fashion, which run parallel with the crystallographic b-axis, and follow a repeating ABAB pattern within the crystallographic bc-plane. This repeating ABAB pattern of organic sub-structure both intersects the anti-parallel layers of the inorganic clusters, and plays a role in separating these layers into their inorganic ABAB pattern parallel to the crystallographic c-axis, by occupying part of the void space between these layers (see top right of Figure 109).
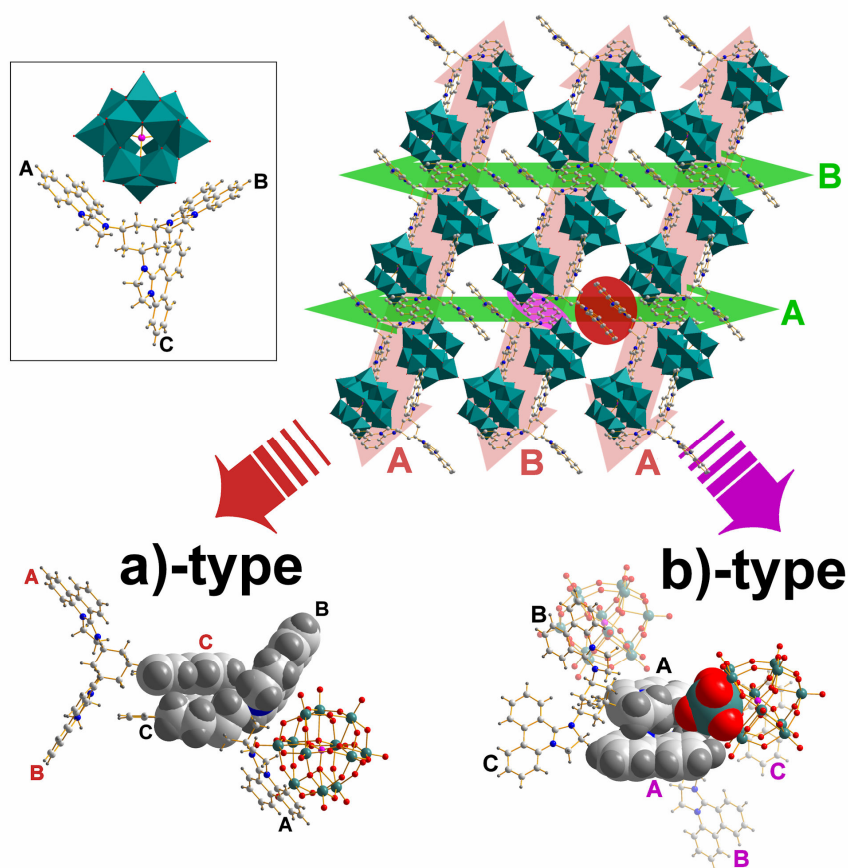
Figure 109: Top Left: Illustration of one DIP-2 cation and the closest POM cluster anion within the unit cell of **6**. The anion can be seen to be cupped within the more sterically hindered face of the DIP-2 cation, by DIP-arm A and DIP-arm B. Top Right: Representation of **6** when viewed along the crystallographic *a*-axis. The faded red arrows highlight the cluster layers within the structure. These layers are composed of two anti-parallel cluster arrays, which run parallel with the crystallographic *c*-axis. The green arrows highlight the anti-parallel arrangements DIP-2 cations into organic layers which run parallel with the crystallographic *b*-axis. The red circle highlights one of the a)-type ππ-stacking interactions, and the purple ellipsoid highlights one of the b)-type ππ-stacking interactions. Solvent molecules and H atoms are omitted for clarity. Bottom Left: Illustration of the a)-type ππ-stacking interaction established between DIP-arm C moieties from adjacent DIP-2 cations. The space-filling representation illustrates the steric clash, therefore the closest packing, between the adjacent cations. Bottom Right: Illustration of the b)-type ππ-stacking interaction established between DIP-arm A moieties from adjacent DIP-2 cations. The space-filling representation illustrates the steric clash, therefore the closest packing, between the ππ-stacking cations and the adjacent POM cluster. Colour scheme: W, teal polyhedra; P, pink; O, red; C, light grey; N, blue; H, dark grey. Solvent molecules are omitted for clarity.

Of particular interest in compound **6** is the arrangement of ππ-stacking interactions between the DIP-2 cations of the structure. In detail, two different sets of ππ-stacking interactions hold the organic 'sub-lattice' of DIP-2 cations together: a) between the DIP pendent moieties pointing into the void spaces between the inorganic layers; and b)

between the DIP pendent moieties intersecting the anti-parallel layers of inorganic clusters. See top right of Figure 109.

The a)-type $\pi\pi$-stacking interactions are established between DIP-arm C pendent moieties of DIP-2 cations from each alternating inorganic ABAB cluster layer, and involve two of the three aromatic rings of each DIP arm (see bottom left of Figure 109). In contrast, the b)-type $\pi\pi$-stacking interactions are established between DIP-arm A moieties from adjacent DIP-2 cations, and only a small portion of the delocalised aromatic ring systems of the DIP arms are overlaid, so indicating this is a weaker interaction than the a)-type form (see bottom right, Figure 109). Despite both DIP-arms C and A establishing $\pi\pi$-stacking interactions, the remaining DIP pendent arm of the DIP-2 cation, i.e. DIP-arm B, does not establish any such interaction. This is because, as can be seen by viewing the lattice along the crystallographic b-axis, no part of the DIP-arm B moieties of adjacent cations are overlaid with one another.

4.3.1.3 $(IPblue)_3[PW_{12}O_{40}]\cdot 4DMSO$ (**7**)

Following the isolation of compounds **5** and **6** using triply-charged DIP cations in reactions with phosphotungstic acid, it was decided to pursue this reaction strategy further using a more planar, singly-charged imidazo-phenanthridinium cation. Therefore, (IPblue)Cl was chosen for reaction with phosphotungstic acid and this led to the successful isolation and characterization of compound **7**.

Examination of the unit cell of compound **7** reveals that each triply-charged POM anion forms an electrostatic relationship with a columnar arrangement of three, singly-charged, $\pi\pi$-stacked IPblue cations (see top of Figure 110). When viewing the unit cell along the crystallographic b-axis each of these $\pi\pi$-stacks is seen to run parallel to the crystallographic c-axis, and there is a torsion angle of approximately 180° between the IP cation in closest contact with the POM cluster and the last cation in each of these three-cation stacks.

Another feature of particular interest when studying the unit cell of **7,** is the arrangement of the eight POM clusters into two tetrahedral motifs, each of which is centred around a

DMSO solvent molecule. When viewing the unit cell along the crystallographic *b*-axis these idealised tetrahedra are seen to be positioned in a co-linear fashion parallel to the crystallographic *c*-axis. However, one of the tetrahedra is rotated, with respect to the neighbouring tetrahedron, through 90° along its C_2 axis which runs parallel to the crystallographic *b*-axis (highlighted in green, centre left of Figure 110). On extending the packing and viewing the crystal lattice along the crystallographic *b*-axis, these alternating tetrahedral arrangements of POM clusters form layers which run parallel with the crystallographic *c*-axis, and then follow a repeating ABAB pattern within the crystallographic *ac*-plane (see bottom of Figure 110).
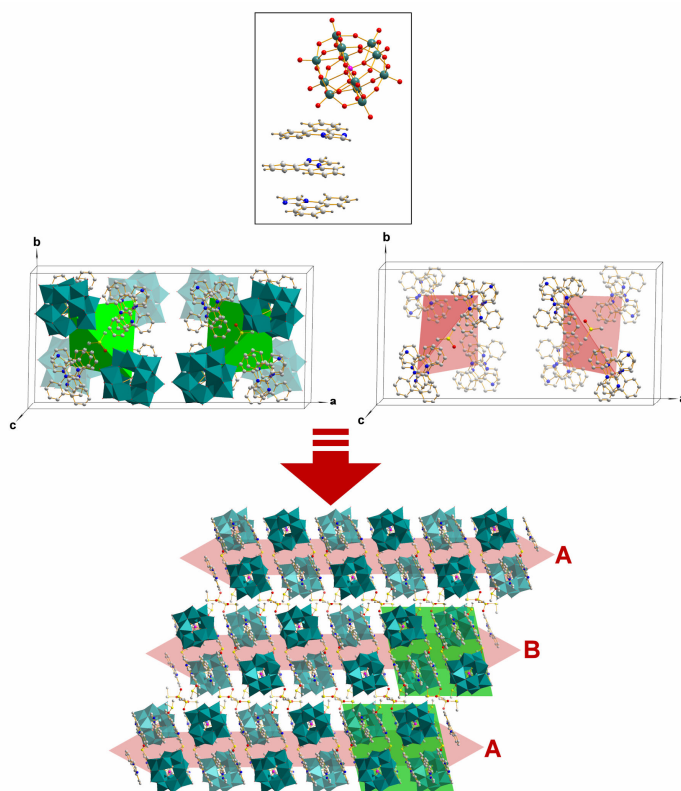
Figure 110: Top: Illustration of part of the unit cell of **7** showing one POM cluster anion and the closest π-stacking arrangement of three IPblue cations. Solvent molecules are omitted for clarity. Centre Left: Illustration of the unit cell of **7**, showing the vertex positions of the interlocked inorganic (POM clusters) and organic tetrahedra (three IPblue cation-stacks). For clarity, only the inorganic tetrahedra are highlighted in green. Centre Right: Illustration of the unit cell of **7**, showing only the organic tetrahedra (highlighted in red) whose vertices are formed by the eight, three-cation π-stacks. The solvent molecules (apart from the DMSO molecule in the centre of each tetrahedron); and H atoms are omitted from both central figures for clarity. Bottom: Representation of **7** when viewed along the crystallographic *b*-axis. The idealised, interlocked inorganic and organic tetrahedra (shown in the centre left figure) are highlighted with green parallelograms, and form alternating layers which run parallel with the crystallographic *c*-axis (highlighted with faded red arrows). H atoms are omitted for clarity. Colour scheme: W, teal polyhedra; P, pink; O, red; C, grey; N, blue; H, dark grey; S, yellow.

Intriguingly, further examination of the lattice reveals, not only these tetrahedral packing arrangements of inorganic POM building-blocks, but also a corresponding tetrahedron-based organic sub-structure as well. These organic sub-structures are composed of an arrangement of eight, three-cation π-stacks into two tetrahedral motifs (highlighted in red, centre right of Figure 110), each of which is centred around a DMSO solvent molecule. Indeed these organic tetrahedra are interlocked with those composed from the inorganic POM clusters and so are centred around the same DMSO solvent molecule (see centre left of Figure 110). As a result of the interlocking nature of these organic and inorganic tetrahedra, when viewing the crystal lattice along the crystallographic *b*-axis, these alternating, interlocked tetrahedral arrangements can be seen to form layers running parallel with the crystallographic *c*-axis. As described previously, these co-linear layers are then arranged into a repeating ABAB pattern within the crystallographic *ac*-plane (see bottom of Figure 110).

4.3.1.4   Further characterization of compounds **5**-**7**

Investigations of the solution state and solid state UV/vis spectroscopic response of compounds, **5**, **6** and **7** were carried out. These preliminary investigations established that intermolecular charge transfer transitions occur in the solid state for all of these compounds, and are also detected in the solution state for compound **6**. A possible explanation for this may be that the steric bulk of the DIP-2 cations in compound **6** leads to closer contact between these cations and POM anions in the solution state, when compared with the solution state contact between the less sterically demanding DIP-1 (compound **5**) or IPblue cations (compound **7**), and the POM anions.

Some preliminary cyclic voltammetry experiments using compounds **5** to **7** have been carried out to study the redox activity of the dissolved compounds in comparison with their lone starting materials. These experiments led to the finding that, in all of the compounds investigated, the redox processes identified can be attributed to electron processes on the tungsten centres of the POM anions. Also the presence of the DIP and IP cations has been observed to cause these redox processes to shift to more negative electrode potentials when compared with the lone phosphotungstic acid starting material. However, as these investigations are ongoing they are discussed further in the Experimental, section 5.6.2.

Finally, due to the use of the sterically demanding and geometrically interesting DIP-2 cation in the formation of compound **6,** SEM, EDX and powder XRD were used to examine the structure of the remaining inorganic framework after heating the sample to 1000 °C under an air atmosphere. Under these conditions, it was found that a tungsten oxide framework was produced that was composed of disc-like and multi-faceted tungsten oxide units.

In conclusion, these investigations have led to the synthesis and characterization of three new POM architectures incorporating phenanthridinium-based organic cations of varying steric bulk, geometry and charge. Also, preliminary UV/vis spectroscopy experiments have shown these compounds to possess emergent photoactivity, in the form of intermolecular charge transfer bands between the DIP or IP cations, and POM anions. Future work will now focus on the development of further POM architectures using different organic cations from this family of phenanthridinium-based molecules and different POM clusters to provide the inorganic framework of these structures.

5 Experimental

5.1 Materials

All reagents and solvents were supplied by Sigma Aldrich Chemical Company Ltd., Thermo Fisher Scientific, and Lancaster Chemicals. Unless stated otherwise, the materials were used without further purification.

5.2 Instrumentation

The mass spectrometry and UV/vis spectroscopy instrumentation, used in the analysis of polyoxometalate systems **1** and **2**, and the instrumentation used to analyse and characterize compounds **3** to **7** are given below:

Cryospray (CSI-) and electrospray mass spectrometry (ESI-MS): All MS data for the analysis of polyoxometalate reaction systems **1** and **2** was collected using a Q-trap, time-of-flight MS (MicrOTOF-Q MS) instrument supplied by Bruker Daltonics Ltd. This instrument was equipped either with an electrospray or cryospray source, both of which were supplied by Bruker Daltonics Ltd. and the detector was a time-of-flight, micro-channel plate detector.

UV/vis spectroscopy: Solution state UV/vis spectra were collected using a Shimadzu PharmaSpec UV-1700 UV/vis spectrophotometer in transmission mode. Quartz cuvettes with 1.0 cm optical path length were used. Solid state UV/vis spectra were collected using a Jasco V-670 UV/vis spectrophotometer equipped with a diffuse reflectance integrating sphere.

Fourier-transform infrared (IR) spectroscopy: All samples were prepared as KBr discs and IR spectra were collected in transmission mode using a JASCO FT-IR-410 spectrometer or a JASCO FT-IR 4100 spectrometer. Wavenumbers ($\tilde{\nu}$) are given in cm^{-1} with their intensities denoted as vs = very strong, s = strong, m = medium, w = weak, b = broad.

^{1}H- and ^{13}C-Nuclear magnetic resonance spectroscopy (^{1}H- and ^{13}C-NMR): ^{1}H-NMR and ^{13}C-NMR spectroscopy were performed on a Bruker DPX 400 spectrometer using the solvent signal as internal standard.

Single crystal X-Ray diffraction: All single crystal data collections were recorded at 150 K on the following instruments: Oxford Diffraction Gemini Ultra S (λ (Mo$_{K\alpha}$) = 0.71073Å and λ (Cu$_{K\alpha}$) = 1.5405 Å) equipped with a graphite monochromator. Bruker AXS Apex II (λ (Mo$_{K\alpha}$) = 0.71073 Å) equipped with a graphite monochromator.

Powder X-Ray diffraction (XRD): Powder XRD patterns were collected on a Bruker AXS D8 powder diffractometer (λ (Cu$_{K\alpha}$) = 1.5405 Å) equipped with a graphite monochromator. All data was collected in capillary mode at room temperature.

Elemental analysis (EA): Carbon, nitrogen and hydrogen content of materials were determined by the microanalysis services within the Department of Chemistry, University of Glasgow using an EA 1110 CHNS, CE-440 Elemental Analyser.

Thermogravimetric analysis (TGA): Thermogravimetric analyses were carried out using a Q500 Thermogravimetric Analyzer supplied by TA Instruments. These analyses were carried out under nitrogen or air flow at a heating rate of 5 °C min^{-1}.

Flame atomic absorption spectrometry (FAAS): FAAS was performed at the Environmental Chemistry Section, Department of Chemistry, University of Glasgow on a Perkin-Elmer 1100B Atomic Absorption Spectrophotometer.

Flame photometry: Flame photometry was performed for sodium content evaluation at the Environmental Chemistry Section, Department of Chemistry, University of Glasgow on a Sherwood M410 Flame Photometer.

Scanning electron microscopy (SEM): Scanning electron microscopy was carried out using a Hitachi S-4700 SEM instrument and a FEI/Philips XL-30 ESEM system using acceleration voltages of 10-20 kV. Samples were dispersed in ethanol and directly deposited on clean silicon wafers.

Energy-dispersive X-ray spectroscopy (EDX): Energy-dispersive X-ray analysis was carried out using the FEI/Philips XL-30 ESEM system equipped with an EDAX Sapphire EDX detector and using acceleration voltages of 20 kV.

Cyclic voltammetry (CV): CV analyses were carried out using a Voltalab model GPZ 301 electro-analysis system. The electrolyte used in all measurements was $((n\text{-}C_4H_9)_4N)PF_6$ (0.2 mol L^{-1}), the solvent was DMSO, and all samples were of approximately 10^{-3} mol L^{-1}. The standard three-electrode arrangement was employed, i.e. a Pt mesh auxiliary electrode, 3 mm glassy carbon working electrode, and Ag/AgCl reference electrode. All potentials are quoted relative to the Ag/AgCl reference electrode.

5.3 CSI-MS and UV/vis spectroscopic investigations into the formation of a silver-linked β-octamolybdate architecture

5.3.1 Synthesis and characterization of precursors

5.3.1.1 Synthesis of $((n\text{-}C_4H_{19})_4N)_2[Mo_6O_{19}]$ used in the production of reaction solution **1** and Reaction Mixture **A** for CSI-MS and UV/vis spectroscopic monitoring

$((n\text{-}C_4H_{19})_4N)_2[Mo_6O_{19}]$ (also referred to as $TBA_2[Mo_6O_{19}]$) was synthesized according to literature procedures[121] and its purity was confirmed using IR analysis.

5.3.1.2 Synthesis of $((n\text{-}C_5H_{11})_4N)_2[Mo_6O_{19}]$ used in the production of Reaction Mixture **B** for UV/vis spectroscopic monitoring

This method follows that reported by Cronin *et al*[83]: $Na_2MoO_4 \cdot 2H_2O$ (2.40 g, 10.0 mmol) was dissolved in 50 ml water then the pH reduced to approximately pH 2 by the addition of concentrated HCl (37 %). $(C_5H_{11})_4NBr$ (1.25 g, 3.3 mmol) was dissolved in 10 mL water, which was then added dropwise to the sodium molybdate solution with stirring. The mixture was left stirring at room temperature for 1 h resulting in the formation of a yellow precipitate. The precipitate was collected, washed with H_2O, then EtOH:H_2O (50:50), then Et_2O, and left to dry in a dessicator. The yellow solid was then recrystallized from a

minimum amount of acetonitrile, yielding yellow needle crystals of $((n\text{-}C_5H_{11})_4N)_2[Mo_6O_{19}]$. Yield: 1.64 g (1.1 mmol, 66.3 % based on Mo). Elemental analysis in weight % for $C_{40}H_{88}N_2Mo_6O_{19}$ (calculated values in brackets): C 32.51 (32.53), H 6.02 (6.01), N 1.97 (1.90).

5.3.1.3 Synthesis of $((n\text{-}C_6H_{11})_4N)_2[Mo_6O_{19}]$ used in the production of Reaction Mixture **C** for UV/vis spectroscopic monitoring

This method has been adapted from that reported by Cronin et al[83]: $Na_2MoO_4\cdot2H_2O$ (2.40 g, 9.9 mmol) was dissolved in 50 ml water then the pH reduced to approximately pH 2 by the addition of concentrated HCl (37 %). $(C_6H_{13})_4NBr$ (1.35 g, 3.1 mmol) was dissolved in 10 mL water, which was then added dropwise to the sodium molybdate solution with stirring. The mixture was left stirring at room temperature for 1 h resulting in the formation of a yellow, sticky solid in the flask. To wash this yellow solid, 60 mL of water was added to the flask and the flask was sonicated for 15 min. The water was decanted off and the flask washed again with fresh water. The yellow solid was dissolved in a minimum amount of acetonitrile and left open to recrystallize. Yield: 0.25 g (0.16 mmol, 9.7 % based on Mo). Elemental analysis in weight % for $C_{48}H_{104}N_2Mo_6O_{19}$ (calculated values in brackets): C 37.68 (36.28), H 6.88 (6.60), N 1.94 (1.76).

5.3.1.4 Synthesis of $((n\text{-}C_7H_{15})_4N)_2[Mo_6O_{19}]$ used in the production of Reaction Mixture **D** for UV/vis spectroscopic monitoring

This method follows that reported by Cronin et al[83]: $Na_2MoO_4\cdot2H_2O$ (2.04 g, 8.4 mmol) was dissolved in 50 ml water then the pH reduced to approximately pH 2 by the addition of concentrated HCl (37 %). $(C_7H_{15})_4NBr$ (1.62 g, 3.3 mmol) in a mixture of 20 mL water and 10 mL acetonitrile was then added dropwise to the sodium molybdate solution with stirring. The mixture was left stirring at room temperature for 4 h resulting in the formation of a yellow, sticky solid in the flask. The mixed solvent was decanted and fresh water was added to the flask in order to wash the yellow solid. The flask was then

sonicated for 15 min and heated until it became opaque. The solvent was decanted off again, and the yellow solid dissolved in a minimum amount of acetonitrile then left open to recrystallize at 0 °C. Yellow needle crystals of $((n\text{-}C_7H_{15})_4N)_2[Mo_6O_{19}]$ were collected. Yield: 0.4 g (0.24 mmol, 16.7 % based on Mo). Elemental analysis in weight % for $C_{56}H_{120}N_2Mo_6O_{19}$ (calculated values in brackets): C 39.54 (39.54), H 7.13 (7.11), N 1.58 (1.65).

5.3.2   Sample preparations for CSI-MS analyses

5.3.2.1   Sample preparation of reaction solution **1**

Silver(I) fluoride (28 mg, 0.22 mmol) suspended in methanol (3 mL) by sonication, was added to a solution of $TBA_2[Mo_6O_{19}]$ (150 mg, 0.11 mmol) in acetonitrile (4 mL). When left to stir overnight at room temperature, a cloudy white suspension was formed. Filtration of this solution produced a clear colourless solution. (i.e. This is the first stage of the synthesis of $TBA_{2n}[Ag_2Mo_8O_{26}]_n$ (**1**).[81]) From this solution 20 μL was removed and made up to 2 mL with acetonitrile to produce a 1×10^{-4} mol L^{-1} dilution suitable for MS testing.

5.3.2.2   Sample preparation for real-time, CSI-MS monitoring of Reaction Mixture **A**

Silver(I) fluoride (28 mg, 0.22 mmol) suspended in methanol (3 mL) by sonication, was added to a solution of $TBA_2[Mo_6O_{19}]$ (150 mg, 0.11 mmol) in acetonitrile (4 mL). This solution was stirred, protected from light, for 5 min at room temperature then filtered. The solution was then kept in the dark throughout the experiment. The reaction was timed from when the first 20 μL aliquot of this solution was made up to 2 mL with acetonitrile to produce the first 1×10^{-4} mol L^{-1} dilution suitable for MS testing. The time of removal of each 20 μL aliquot to make up MS dilutions was noted throughout this experiment, with the final dilution made up approximately 3 h 15 min (i.e. approximately 195 min) after the first dilution.

5.3.2.3   Sample preparations for UV/vis spectroscopy monitoring of Reaction Mixtures **A**
          – **D**

Reaction Mixture **A**: Silver(I) fluoride (28 mg, 0.22 mmol) suspended in methanol (3 mL)
by sonication, was added to a solution of $TBA_2[Mo_6O_{19}]$ (150 mg, 0.11 mmol) in
acetonitrile (4 mL). This solution was stirred, protected from light, for 5 min at room
temperature then filtered. From this solution 126 µL was removed and made up to 4 mL
with acetonitrile:methanol (40:30) solvent to produce a $5x10^{-4}$ mol L^{-1} dilution suitable for
UV/vis spectroscopy testing.

This preparation method was repeated replacing the $TBA_2[Mo_6O_{19}]$ with $((n-C_5H_{11})_4N)_2[Mo_6O_{19}]$ (162 mg, 0.11 mmol), $((n-C_6H_{13})_4N)_2[Mo_6O_{19}]$ (175 mg, 0.11 mmol),
or $((n-C_7H_{15})_4N)_2[Mo_6O_{19}]$ (187 mg, 0.11 mmol), to produce Reaction Mix **B**, **C**, or **D**
respectively for UV/vis spectroscopic, time-monitored experiments.

In order to calculate the molar absorption coefficient values for each tetraalkylammonium
hexamolybdate compound used in the UV/vis spectroscopy experiments, the method
described above was repeated for each alkylammonium hexamolybdate solution, in the
absence of silver(I) fluoride.

5.3.3   CSI-MS experimental and analyses

The following parameters were consistent for all CSI-MS scans given below. The
calibration solution used was Agilent ES tuning mix solution, Recorder No. G2421A,
enabling calibration between approximately 100 m/z and 3000 m/z. This solution was
diluted 60:1 with MeCN. Samples were introduced into the MS *via* direct injection at 180
µL/h. The cryospray settings were set with the sprayer nitrogen gas temperature at -40 ºC
and the drying nitrogen gas temperature at -20 ºC. The ion polarity for all MS scans
recorded was negative, with the voltage of the capillary tip set at 4000 V, end plate offset
at -500 V, funnel 1 RF at 300 Vpp and funnel 2 RF at 400 Vpp. Other MS parameters,

which were set to specific values for each scan, are given below in tabular format (see Table 12).

MS Parameter	Scan of Mass Range		
	50-1500m/z	1500-2600m/z	2500-6000m/z
Hexapole RF / Vpp	400	700	700
Ion Energy / eV/z	-5	-5	-5
Low Mass / m/z	600	400	400
Collision Energy / eV/z	-100	-20	-30
Collision Cell RF / Vpp	500	1200	1500
Transfer Time / μs	120	150	150
Pre-pulse Storage Time / μs	5	40	40
Summation	5000	30000	30000
Time of Acquisition / min	1	3	3
Active focus	ON	OFF	OFF

Table 12: CSI-MS parameters used in data acquisition for the reaction solution **1** and Reaction Mix **A**, within each mass range shown.

All data was processed using the Bruker Daltonics Data Analysis 3.4 software, whilst simulated isotope patterns were investigated using Bruker Isotope Pattern software and Molecular Weight Calculator 6.45.

All theoretical peak assignments were determined *via* comparison of the experimentally determined isotopic patterns for each peak, with simulated isotopic patterns. For relatively small POM fragments, e.g. up to approximately $[Mo_6O_{19}]^{2-}$, the isotopic pattern is quite distinct and comparison between experimental and simulated patterns is more meaningful (see Figure 31 in Results and Discussion, section 3.2.2.1) than for larger fragments where the isotopic pattern takes on a Gaussian shape and it cannot be said with certainty that the suggested peak is unequivocally correct.

Real-time CSI-MS monitoring experiments: For all data acquisitions in these experiments the CSI-MS method parameters used were as given in the parameter table above (Table 12) for the mass ranges 50-1500 m/z and 1500-2600 m/z. These parameters were consistent for all CSI-MS scans.

5.3.4   CSI-MS spectra of reaction solution 1

The spectra shown below represent the CSI-MS data of reaction solution **1,** acquired within each mass range monitored, i.e. 50-1500 m/z, 1500-2600 m/z, 2500-6000 m/z. See Figures 111 to 113.
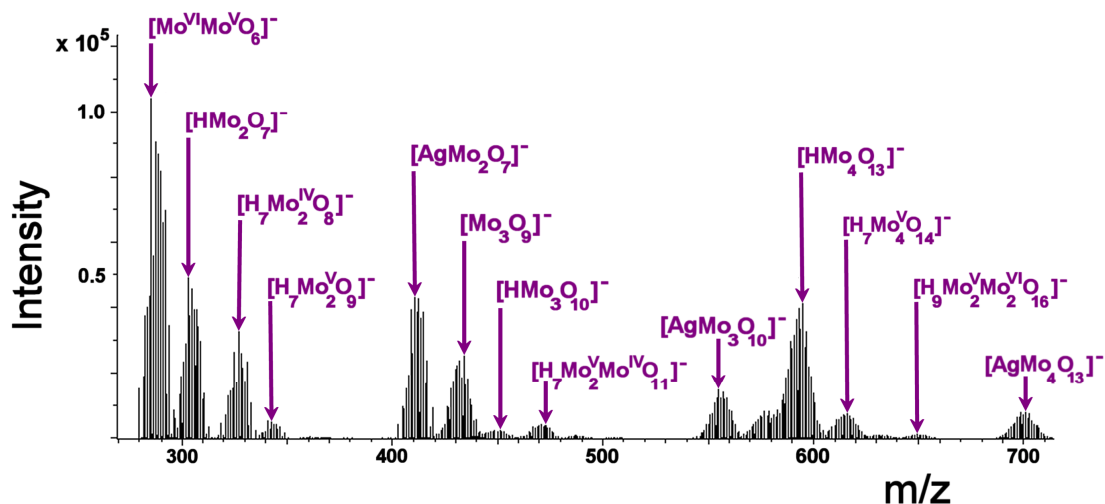
Figure 111: CSI-MS data collected from the reaction solution from which ((n-$C_4H_9)_4N)_{2n}(Ag_2Mo_8O_{26})_n$ (**1**) crystallizes. This data was collected over the 50–1500 m/z acquisition range. The six mono-anionic series identified within these results are highlighted. All labelled species have been assigned *via* comparison of the experimental isotope patterns with simulated isotopic envelopes.
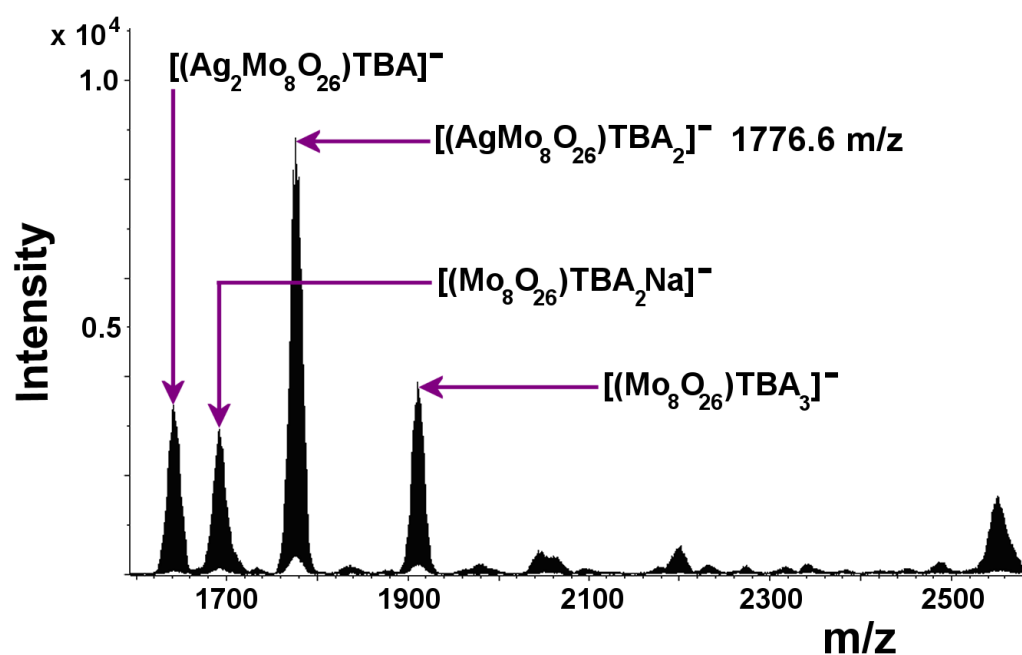
Figure 112: CSI-MS data collected from the reaction solution from which $((n\text{-}C_4H_9)_4N)_{2n}(Ag_2Mo_8O_{26})_n$ (**1**) crystallizes. Data collected over the 1500–2600 m/z range. Species attributed to peaks *via* comparison with simulated isotopic envelopes are labelled.
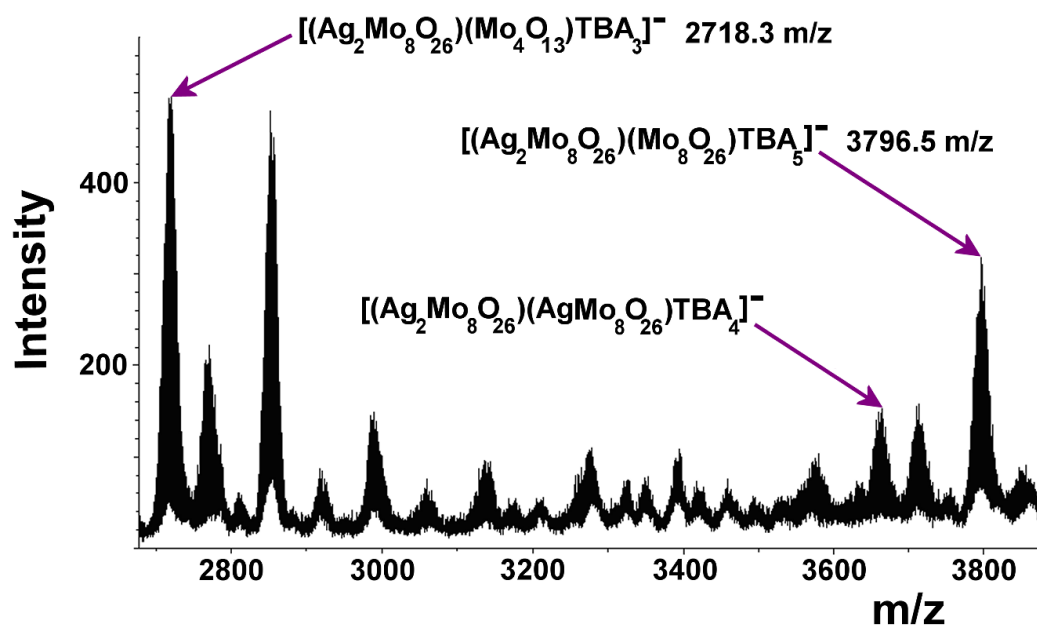
Figure 113: CSI-MS data collected from the reaction solution from which $((n\text{-}C_4H_9)_4N)_{2n}(Ag_2Mo_8O_{26})_n$ (**1**) crystallizes. Data collected over the 2500-6000 m/z range. Species attributed to peaks *via* comparison with simulated isotopic envelopes are labelled.

5.3.5 CSI-MS spectra of Reaction Mix A monitored over time

Figures 114 to 119 given below show the CSI-MS spectral data acquired at the beginning, middle and end points of the CSI-MS kinetic monitoring experiments of the reaction solution of $TBA_2[Mo_6O_{19}]$ + AgF, i.e. Reaction Mix **A**.

Tables 13 and 14 show the m/z values and peak assignments (where applicable) of some of the peaks shown in these spectra. Table 13 applies to the peaks labelled in red numbers for mass spectra collected over the mass range 50-1500 m/z, whereas Table 14 applies to the peaks labelled in blue numbers for mass spectra collected over the mass range 1500–2600 m/z.

Peak Number	m/z	Peak Assignment
1	285.8	$[Mo^{VI}Mo^{V}O_6]^-$
2	410.7	$[AgMo_2O_7]^-$
3	433.7	$[Mo_3O_9]^-$
4	556.6	$[AgMo_3O_{10}]^-$
5	594.4	$[HMo_4O_{13}]^-$
6	700.5	$[AgMo_4O_{13}]^-$
7	1122.6	$[TBA(Mo_6O_{19})]^-$

Table 13: The m/z values and peak assignments corresponding to the red peak numbers in Figures 114, 116 and 118 are shown.

Peak Number	m/z	Peak Assignment
1	1526.8	Not assigned
2	1556.3	Not assigned
3	1643.2	$[(Ag_2Mo_8O_{26})TBA]^-$
4	1776.6	$[(Ag_2Mo_8O_{26})TBA_2]^-$
5	1910.0	$[(Mo_8O_{26})TBA_3]^-$
6	2199.8	Not assigned
7	2485.6	Not assigned

Table 14: The m/z values and peak assignments corresponding to the blue peak numbers in Figures 115, 117 and 119 are shown.
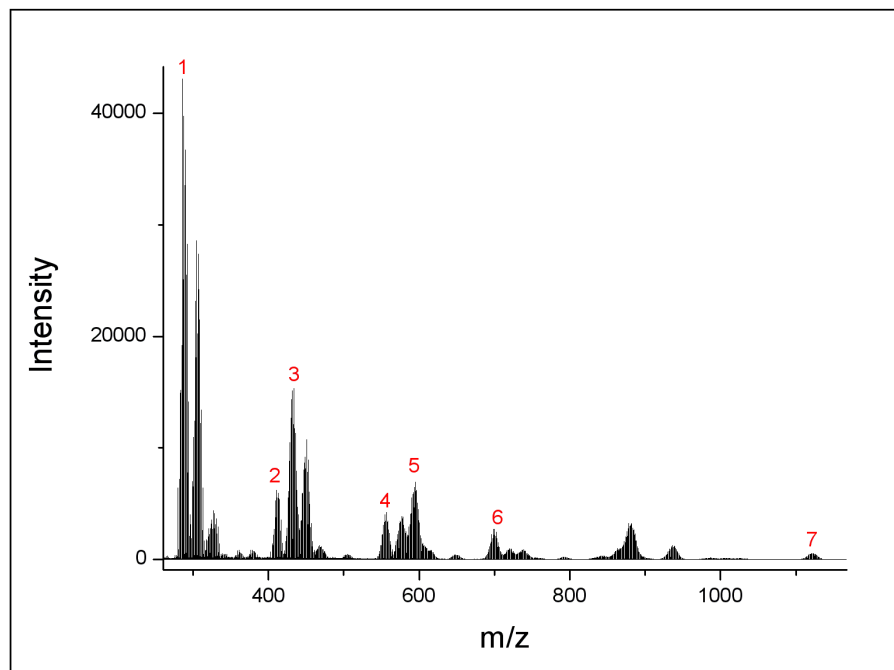
Figure 114: CSI-MS data acquired at the beginning of the CSI-MS kinetic monitoring of the reaction solution of $TBA_2[Mo_6O_{19}]$ + AgF, i.e. Reaction Mix **A**. In detail, this spectrum was acquired using MS dilution 1 of Reaction Mix **A**, approximately 1 min after this dilution was made up. Data collected for 1 min over the 50–1500 m/z range.
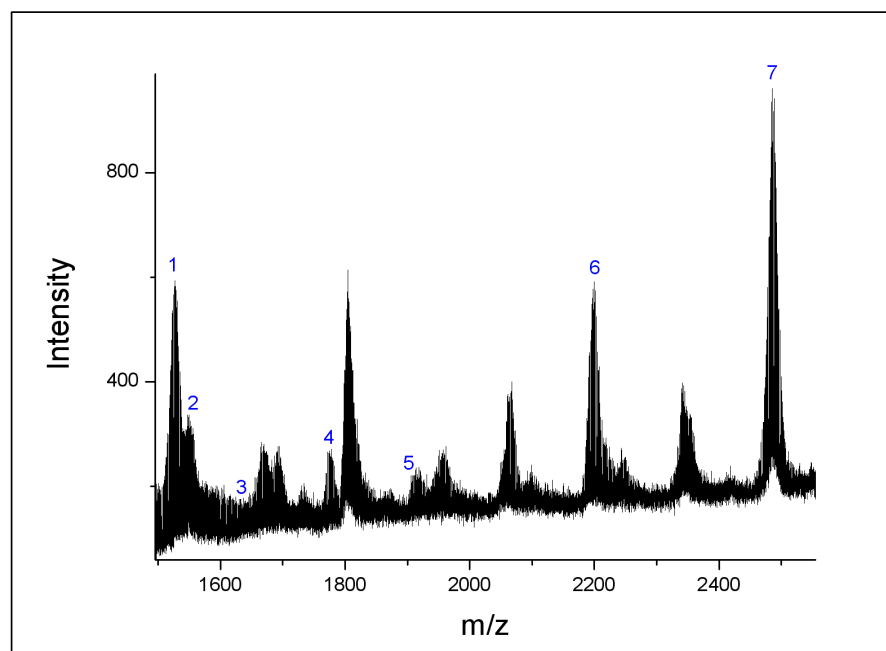
Figure 115: CSI-MS data acquired at the beginning of the CSI-MS kinetic monitoring of the reaction solution of $TBA_2[Mo_6O_{19}]$ + AgF, i.e. Reaction Mix **A**. In detail, this spectrum was acquired using MS dilution 1 of Reaction Mix **A**, approximately 3 min after this dilution was made up. Data collected for 3 min over the 1500–2600 m/z range.
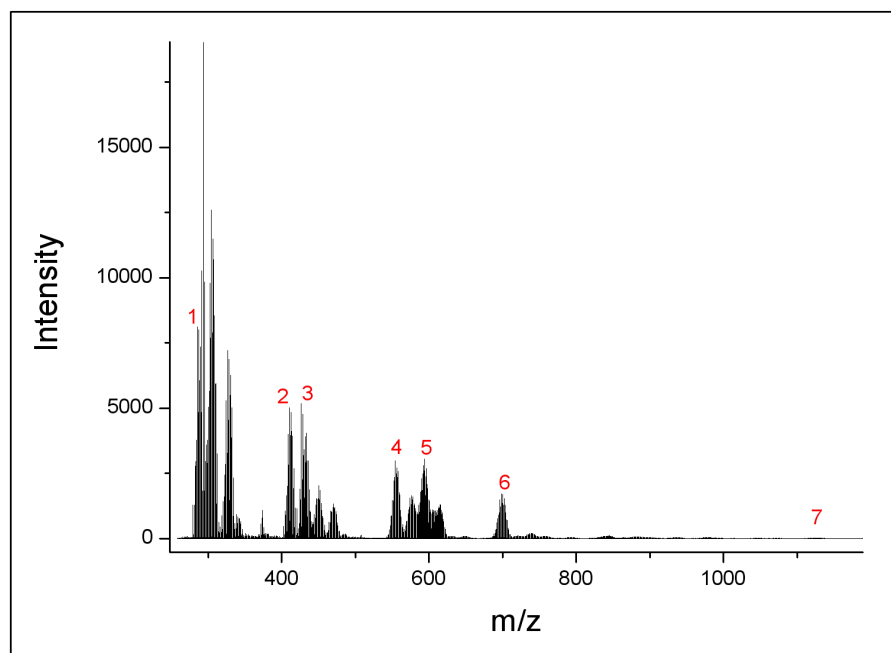
Figure 116: CSI-MS data acquired approximately half-way through the CSI-MS kinetic monitoring of the reaction solution of $TBA_2[Mo_6O_{19}]$ + AgF, i.e. Reaction Mix **A**. In detail, this spectrum was acquired using MS dilution 6 of Reaction Mix **A**, approximately 86 min after MS dilution 1 was made up. Data collected for 1 min over the 50–1500 m/z range.
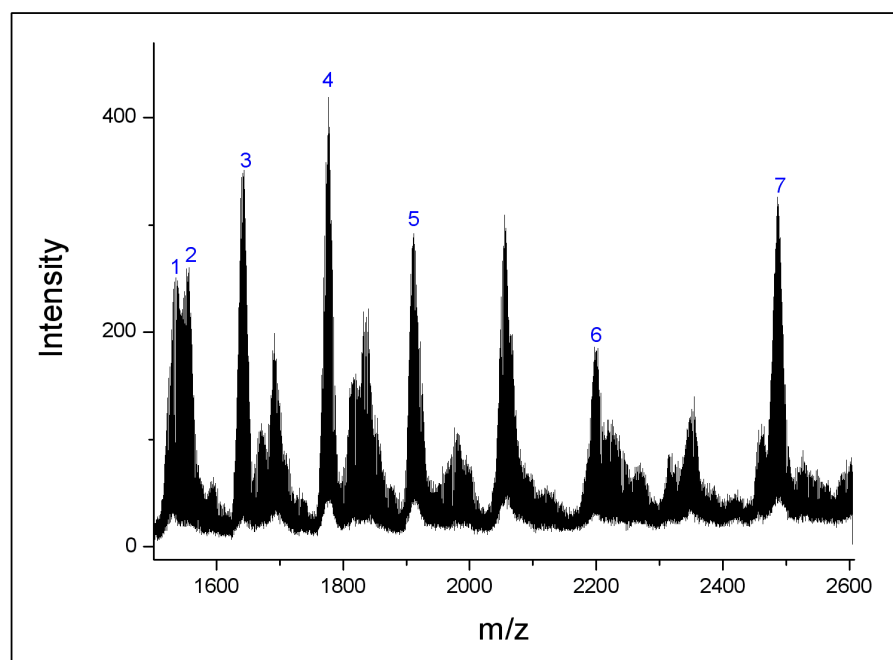
Figure 117: CSI-MS data acquired approximately half-way through the CSI-MS kinetic monitoring of the reaction solution of $TBA_2[Mo_6O_{19}]$ + AgF, i.e. Reaction Mix **A**. In detail, this spectrum was acquired using MS dilution 6 of Reaction Mix **A**, approximately 87 min after MS dilution 1 was made up. Data collected for 3 min over the 1500–2600 m/z range.
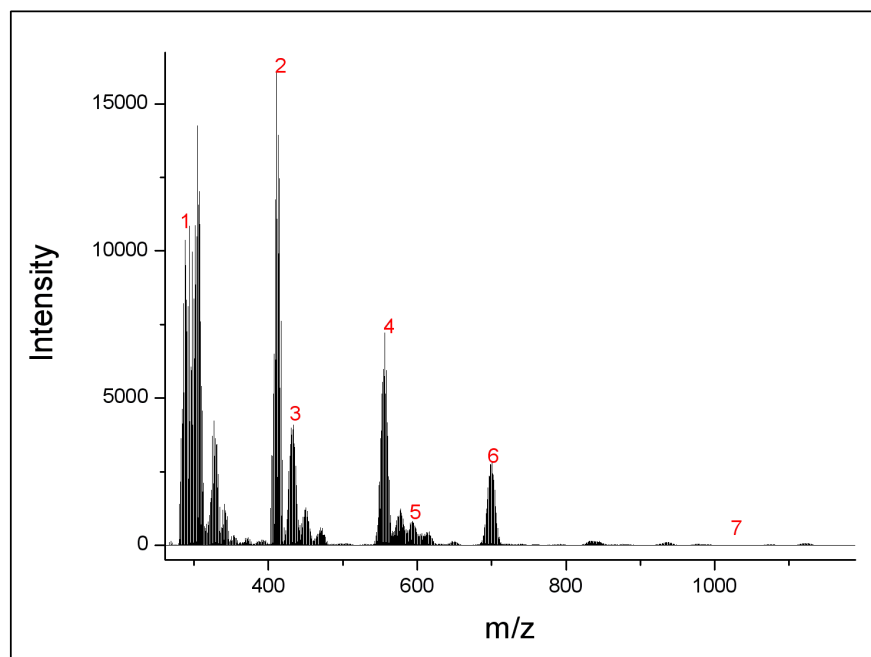
Figure 118: CSI-MS data acquired at the end of CSI-MS kinetic monitoring of the reaction solution of TBA$_2$[Mo$_6$O$_{19}$] + AgF, i.e. Reaction Mix **A**. In detail, this spectrum was acquired using MS dilution 12 of Reaction Mix **A**, approximately 194 min after MS dilution 1 was made up. Data collected for 1 min over the 50–1500 m/z range.
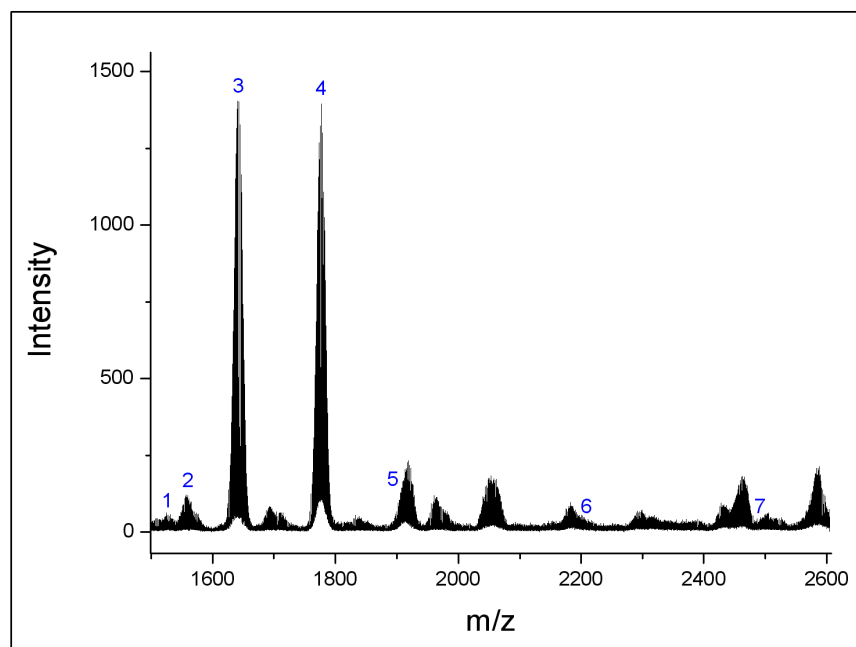
Figure 119: CSI-MS data acquired at the end of CSI-MS kinetic monitoring of the reaction solution of TBA$_2$[Mo$_6$O$_{19}$] + AgF, i.e. Reaction Mix **A**. In detail, this spectrum was acquired using MS dilution 12 of Reaction Mix **A**, approximately 195 min after MS dilution 1 was made up. Data collected for 3 min over the 1500–2600 m/z range.

Tables 15 to 17 below show the raw data extracted from all the CSI-MS spectra recorded in this way during this CSI-MS kinetic monitoring experiment in order to investigate the fate of the species $[TBA(Mo_6O_{19})]^-$, $[(AgMo_8O_{26})TBA_2]^-$, and $[(Ag_2Mo_8O_{26})TBA]^-$ over time. The graphs shown in Figure 32 in Results and Discussion, section 3.2.2.2, have been generated using this raw data.

Raw Data File Name	MS Dilution Number	Time of actual sampling (s)	Relative time of sampling (s)	m/z	Intensity
EW3-66A	1	80	0	1122.6	542
EW3-66D	2	1058	978	1123.6	118
EW3-66G	3	2024	1944	1123.6	185
EW3-66J	4	3000	2920	1122.6	47
EW3-66M	5	4123	4043	1122.6	64
EW3-66Q	6	5148	5068	1122.6	18
EW3-66T	7	6196	6116	1122.6	45
EW3-66W	8	7277	7197	1122.6	37
EW3-66Z	9	8223	8143	1122.7	5
EW3-66AC	10	9319	9239	1122.6	7
EW3-66AF	11	10516	10436	1122.6	6
EW3-66AI	12	11627	11547	1122.6	68

Table 15: The time of sampling and absolute intensities recorded for the peak at 1122.6 m/z (attributed to $[TBA(Mo_6O_{19})]^-$) during the CSI-MS kinetic monitoring of the reaction of $TBA_2[Mo_6O_{19}]$ + AgF, i.e. Reaction Mix **A**, are shown. This raw data has been used to generate the graph in Figure 32 which shows the MS monitored decrease in the intensity of the $[TBA(Mo_6O_{19})]^-$ species over time.

Raw Data File Name	MS Dilution Number	Time of actual sampling (s)	Relative time of sampling (s)	m/z	Intensity
EW3-66B	1	165	0	1776.6	257
EW3-66E	2	1145	980	1776.6	206
EW3-66H	3	2112	1947	1776.6	194
EW3-66K	4	3092	2927	1776.6	251
EW3-66N	5	4214	4049	1776.6	279
EW3-66R	6	5239	5074	1776.6	419
EW3-66U	7	6288	6123	1776.6	673
EW3-66X	8	7389	7224	1776.6	768
EW3-66AA	9	8394	8229	1776.6	1254
EW3-66AD	10	9410	9245	1776.6	993
EW3-66AG	11	10606	10441	1776.6	1948
EW3-66AJ	12	11714	11549	1776.6	1395

Table 16: The time of sampling and absolute intensities recorded for the peak at 1776.6 m/z (attributed to $[(AgMo_8O_{26})TBA_2]^-$) during the CSI-MS kinetic monitoring of the reaction of $TBA_2[Mo_6O_{19}]$ + AgF, i.e. Reaction Mix **A**, are shown. This raw data has been used to generate the graph in Figure 32 which shows the MS monitored decrease in the intensity of the $[(AgMo_8O_{26})TBA_2]^-$ species over time.

Raw Data File Name	MS Dilution Number	Time of actual sampling (s)	Relative time of sampling (s)	m/z	Intensity
EW3-66B	1	165	0	1643.2	161
EW3-66E	2	1145	980	1643.2	146
EW3-66H	3	2112	1947	1643.2	103
EW3-66K	4	3092	2927	1643.2	162
EW3-66N	5	4214	4049	1643.2	197
EW3-66R	6	5239	5074	1643.2	351
EW3-66U	7	6288	6123	1643.2	509
EW3-66X	8	7389	7224	1643.2	634
EW3-66AA	9	8394	8229	1643.2	1054
EW3-66AD	10	9410	9245	1643.2	848
EW3-66AG	11	10606	10441	1643.2	1424
EW3-66AJ	12	11714	11549	1643.2	1403

Table 17: The time of sampling and absolute intensities recorded for the peak at 1643.2 m/z (attributed to $[(Ag_2Mo_8O_{26})TBA]^-$) during the CSI-MS kinetic monitoring of the reaction of $TBA_2[Mo_6O_{19}] + AgF$, i.e. Reaction Mix **A** are shown. This raw data has been used to generate the graph in Figure 32 which shows the MS monitored decrease in the intensity of the $[(Ag_2Mo_8O_{26})TBA]^-$ species over time.

5.3.6   UV/vis spectroscopy of Reaction Mixtures A-D

The spectral data collected in order to determine the molar absorption coefficient values for each alkylammonium hexamolybdate used in this study was recorded over the wavelength range of 500 to 190 nm, using the same concentration hexamolybdate solutions (acetonitrile:methanol (40:30) solvent) as used when investigating the Reaction Mixtures **A-D**. The collection of kinetic data involved the recording of the absorbance count at 355 nm at 20 s intervals over a period of 75 min after the UV dilution of each reaction mixture was placed in the instrument. The wavelength of 355 nm was chosen for these kinetic monitoring experiments in order to avoid overlap of species, as shown on the left of Figure 121 below.
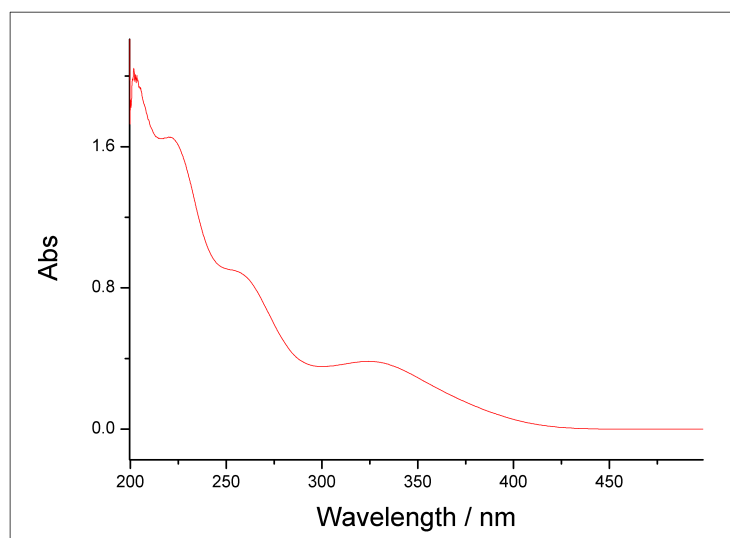
Figure 120: UV spectrum of a low concentration tetrapentylammonium hexamolybdate solution in acetonitrile:methanol (40:30) solvent to allow observation of the peak maxima.
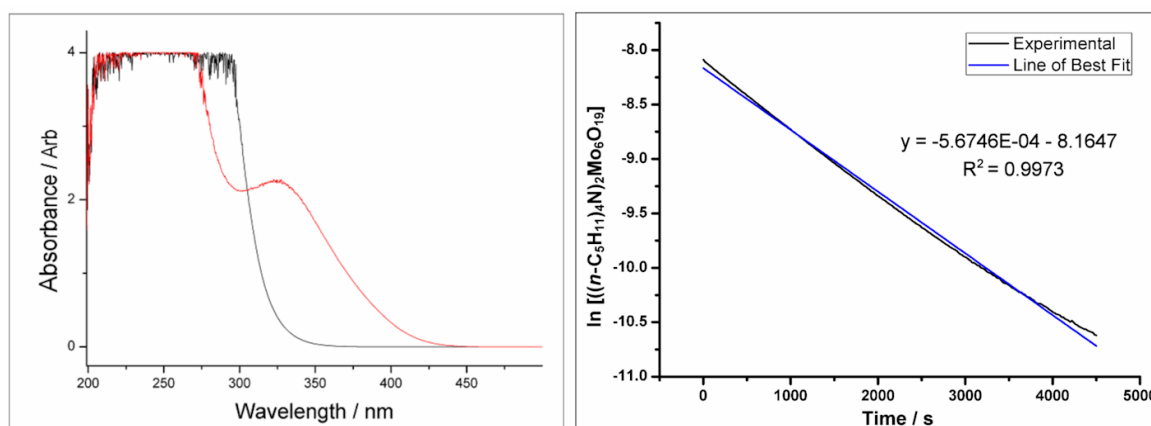
Figure 121: Left: Example UV/vis spectra illustrating the decrease in absorbance at 355 nm before and after kinetic monitoring of the reaction between $((n\text{-}C_5H_{11})_4N)_2[Mo_6O_{19}]$ + AgF in acetonitrile:methanol (40:30) solvent. The red line corresponds to $((n\text{-}C_5H_{11})_4N)_2[Mo_6O_{19}]$ in acetonitrile:methanol (40:30) solvent, whilst the black line corresponds to the same concentration of $((n\text{-}C_5H_{11})_4N)_2[Mo_6O_{19}]$ + AgF in acetonitrile:methanol (40:30) solvent after reaction completion. Right: Graph generated using the UV/vis data from the kinetic monitoring of the reaction of $((n\text{-}C_5H_{11})_4N)_2[Mo_6O_{19}]$ + AgF. The graph shows $-d(\ln[\{Mo_6\}])/dt$ over the first 75 min of the reaction, where the experimental data is shown in black and the line of best fit is shown in blue. The linear equation for this line is shown in the figure, and the absolute value of the calculated gradient is equal to the rate constant (k), i.e. 5.67×10^{-4} s^{-1}.

5.3.7   UV/vis spectroscopic data for Reaction Mixtures A-D

The graph showing $-d(\ln[\{Mo_6\}])/dt$ for the kinetic monitoring of $((n\text{-}C_5H_{11})_4N)_2[Mo_6O_{19}]$ + AgF over the first 75 min of the reaction, is included on the right of Figure 121. The absolute value of the calculated gradient (i.e. in this case, 5.67×10^{-4} s^{-1}) is the rate constant (k). Comparison of the rate constants for each alkylammonium cation tested are shown in Table 18 below and this reveals the general trend that the rate of decrease in the concentration of Lindqvist anions decreases as the carbon chain length of the alkylammonium cations increases. However, it should be noted that the absolute figures of these rate constants will vary according to changes in experimental parameters such as temperature variation, filtration time prior to kinetic monitoring, and the human error introduced by the time needed in the solution preparation process.

Reaction Mix	Length of alkylammonium cation carbon chain	AgF + {Mo$_6$} soln	
		$-d(\ln[\{Mo_6\}])/dt = k / s^{-1}$	R^2
A	4	5.06E-04	1.0000
B	5	5.67E-04	0.9973
C	6	4.58E-04	0.9994
D	7	3.50E-04	0.9999

Table 18: Calculated 'pseudo' first order rate constants for Reaction Mix **A**-**D** using data from UV/vis spectroscopy studies monitoring the decrease of $[\{Mo_6\}]$ over the first 75 min of each reaction. The R^2 value for each plot of $-d(\ln[\{Mo_6\}])/dt$, i.e. rate constant, is also shown.

5.4   ESI-MS investigations into the formation of a derivatized, manganese Anderson polyoxomolybdate architecture

5.4.1   Synthesis and characterization

5.4.1.1   Synthesis of $((n\text{-}C_4H_{19})_4N)_4[\alpha\text{-}Mo_8O_{26}]$ used in the production of reaction solution **2** for real-time ESI-MS monitoring

$((n\text{-}C_4H_{19})_4N)_4[\alpha\text{-}Mo_8O_{26}]$ was synthesized according to literature procedures[121] and its purity was confirmed using IR analysis.

5.4.2   Sample preparations for ESI-MS analyses

5.4.2.1   Sample preparation of reaction solution **2**

The reaction solution of $((n\text{-}C_4H_9)_4N)_3[MnMo_6O_{18}((OCH_2)_3CNH_2)_2]$ (**2**) was prepared following the method given by Hasenknopf *et al*[92] though scaled down by a factor of ten and monitored over 30 h:

$((n\text{-}C_4H_9)_4N)_4[\alpha\text{-}Mo_8O_{26}]$ (0.80 g, 0.37 mmol), $Mn(CH_3CO_2)_3\cdot2H_2O$ (0.15 g, 0.56 mmol) and $(HOCH_2)_3CNH_2$ (0.16 g, 0.13 mmol) were mixed in 15 mL of acetonitrile (stop-clock started at this point). This mixture was stirred for 13 min at room temperature then the first 100 μL aliquot for MS testing was removed (see details of MS dilutions below). The mixture was then set-up to reflux at 80 °C (started reflux at 23 min on stop-clock) with 100 μL aliquots removed for MS testing approximately hourly for the first 8 hours of reaction, then hereafter hourly once again between 24 and 30 h reaction time.

MS Dilutions: Each 100 μL aliquot of reaction solution **2** was made up to 10 mL with MeCN. Then 1 mL of this solution was made up to 5 mL with MeCN for direct injection into the ESI-MS system. The time on the stop-clock was noted when starting each MS data acquisition.

5.4.3   ESI-MS experimental and analyses

The following parameters, see Table 19, were consistent for all ESI-MS data collections. The calibration solution used was Agilent ES tuning mix solution, Recorder No. G2421A, enabling calibration between approximately 100 m/z and 3000 m/z. This solution was diluted 60:1 with acetonitrile. Samples were introduced into the MS *via* direct injection at 180 μL/h. The electrospray source was used with the drying nitrogen gas temperature at approx +100 ºC and the ion polarity for all MS data collections recorded was negative. All other MS parameters are given below in tabular format.

MS Parameter	Setting during Data Collection
Mass Range / m/z	50-3000
End Plate Offset / V	-1700
Funnel 1 RF / Vpp	300
Funnel 2 RF / Vpp	400
Hexapole RF / Vpp	400
Capillary / V	4500
Collision Energy / eV	-10
Collision Cell RF / Vpp	500
Transfer Time / μs	120
Pre-pulse Storage Time / μs	10
Summation	5000
Time of Acquisition / min	2
Active focus	OFF

Table 19: ESI-MS parameters used in each data acquisition of the reaction solution of **2**.

All data was processed using the Bruker Daltonics Data Analysis 4.0 software, whilst simulated isotope patterns were investigated using Bruker Isotope Pattern software and Molecular Weight Calculator 6.45. As for the earlier CSI-MS experiments, all theoretical peak assignments were determined *via* comparison of the experimentally determined isotopic patterns for each peak, with simulated isotopic patterns.

5.4.4   ESI-MS analyses of reaction solution 2 monitored over time

Table 20 below shows the noted time intervals at which ESI-MS data was acquired over the 30 h of monitoring the formation of **2**. Spectrum Number 1 is shown in Figure 122, Spectrum Number 7 is shown in Figure 123, and Spectrum Number 12 is shown in Figure 124. Peak intensity information from these spectra, and the time at which each was recorded (in hours), were used to produce Figures 40 to 43 in Results and Discussion, section 3.3.1.2.

ESI-MS Spectrum Number	Time on Stop-clock / min	Time on Stop-clock / h
1	17.70	0.3
2	156.07	2.6
3	216.68	3.6
4	279.80	4.7
5	334.15	5.6
6	391.17	6.5
7	467.37	7.8
8	516.28	8.6
9	1475.17	24.6
10	1587.97	26.5
11	1652.17	27.5
12	1783.95	29.7

Table 20: ESI-MS data acquisition at each noted time interval over the 30 h of monitoring reaction solution **2**, three outlying spectra have been removed.
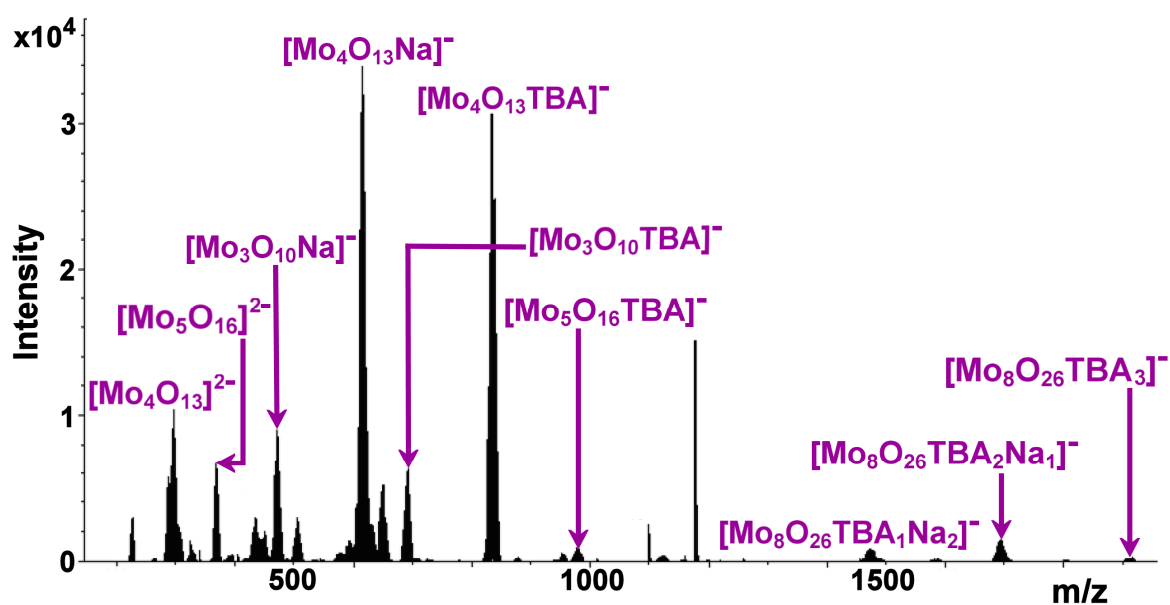
Figure 122: ESI-MS spectrum collected after stirring the reaction solution of **2** at room temperature for 13 min (i.e. ESI-MS Spectrum Number 1 in Table 20).
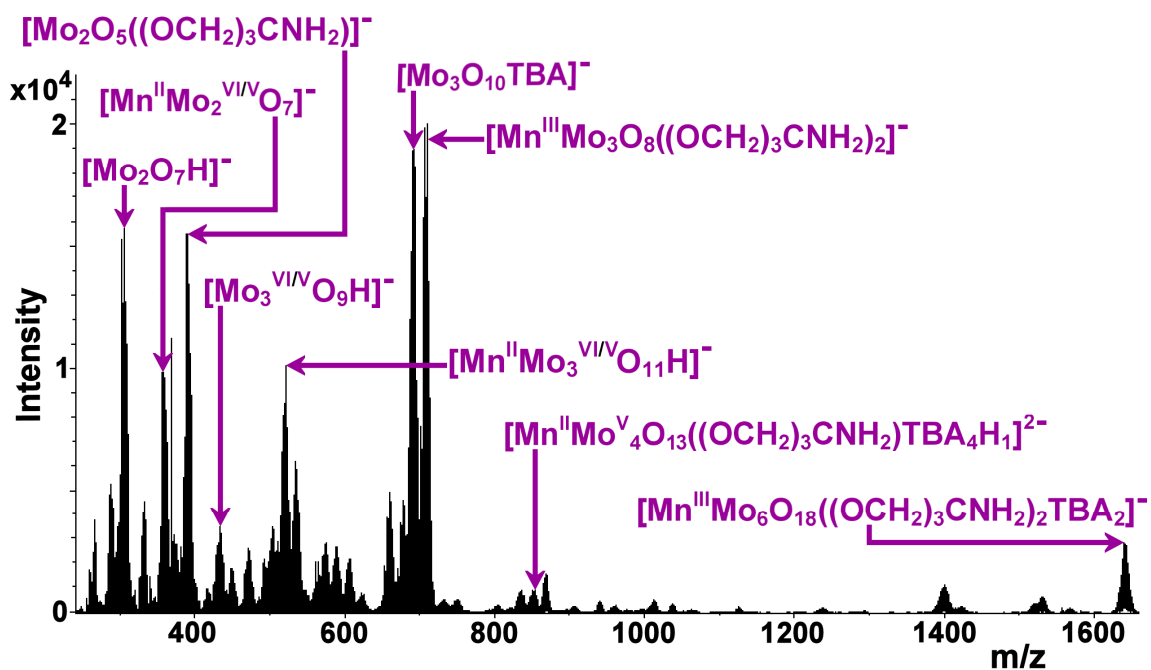
Figure 123: ESI-MS spectrum collected after refluxing the reaction solution of **2** at 80 °C for approximately 7 h (i.e. ESI-MS Spectrum Number 7 in Table 20).
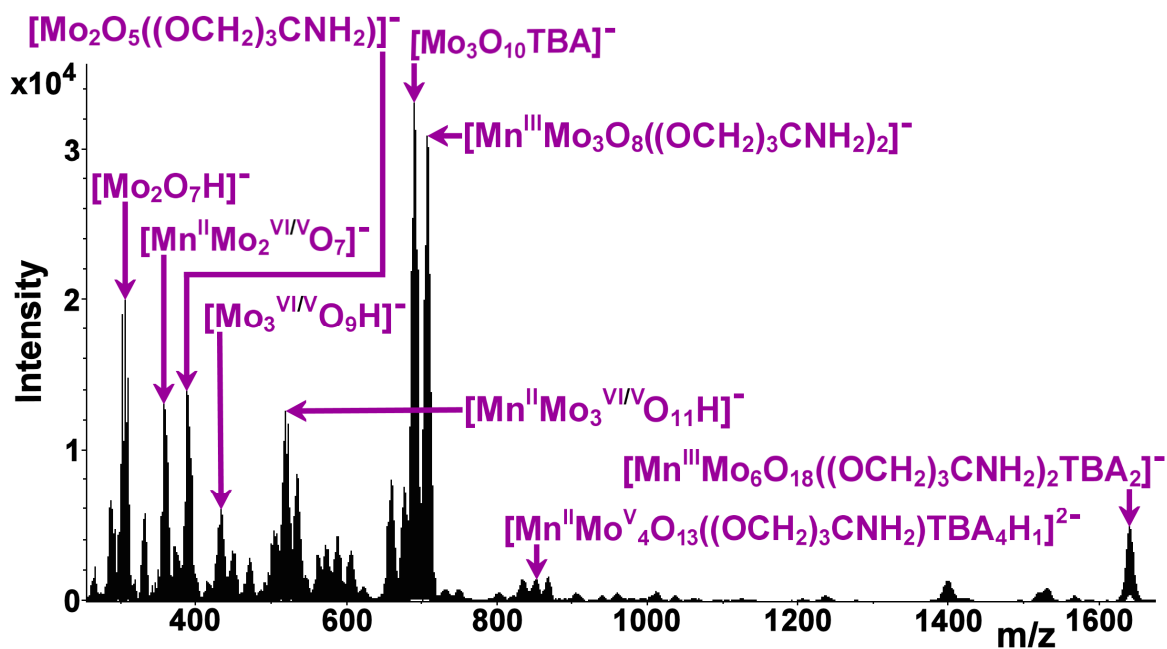
Figure 124: ESI-MS spectrum collected after refluxing the reaction solution of **2** at 80 °C for approximately 30 h (i.e. ESI-MS Spectrum Number 12 in Table 20).

5.5 The synthesis and characterization of new polyoxomolybdate architectures with high oxidation state heteroanion templates

5.5.1 Synthesis and characterization of compounds 3 to 4

5.5.1.1 Synthesis of compound **3**: $Cs_{4.67}Na_{0.33}[IMo_6O_{24}] \cdot ca7H_2O$

Aqueous solutions of the starting materials were made up as follows: $Na_2MoO_4 \cdot 2H_2O$ (8.0 g, 33 mmol) was dissolved in 40 mL water, CsCl (4.0 g, 24 mmol) was dissolved in 20 mL water, and H_5IO_6 (0.40 g, 1.8 mmol) was dissolved in 40 mL water. The H_5IO_6 solution was added to the Na_2MoO_4 solution and the pH was reduced to approximately 1.8 using 6 mol L^{-1} HCl. The CsCl solution was then added dropwise with stirring. The white precipitate formed was filtered off, and colourless block crystals of **3** suitable for single crystal X-ray diffraction, crystallized from the filtrate on diffusion of MeOH. Yield: 2.65 g (1.44 mmol, 26.0 % based on Mo).

Elemental analysis in weight % for $Cs_{4.67}Na_{0.33}[IMo_6O_{24}] \cdot ca7H_2O$ to confirm the absence of methanol solvent from the compound and aid assignment of water content (calculated values in brackets): C 0 (0), H 0.83 (0.77), N 0 (0).

TGA analysis (see Figure 125) shows three distinct weight losses when heating 35.0590 mg of **3**, under an air atmosphere, at 5 °C min^{-1}, from room temperature up to 800 °C. The first two weight losses, i.e. 6.30 % and 0.99 %, add to give a total weight loss of 7.30 %. This weight loss corresponds to the loss of seven solvent water molecules, when the formula of the compound is $Cs_{4.67}Na_{0.33}[IMo_6O_{24}] \cdot ca7H_2O$ (calculated: 6.85 %). The remaining weight loss of 9.58 % is due to cluster decomposition to a metal oxide.
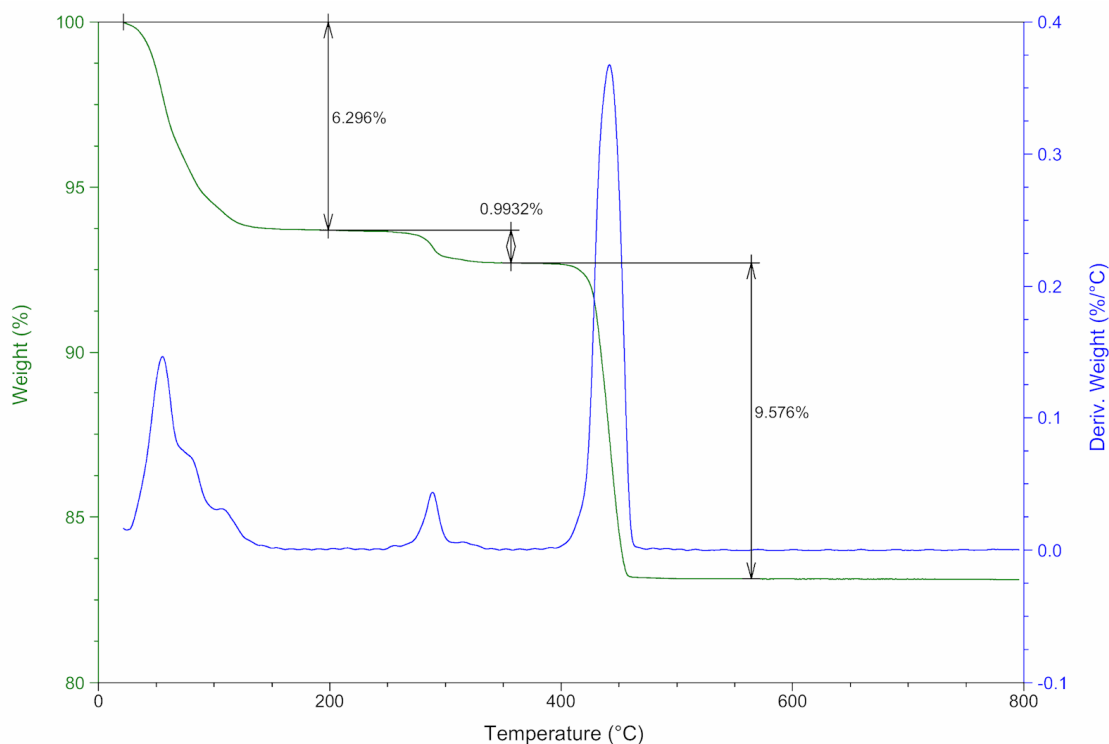
Figure 125: TGA analysis of **3**.

FAAS analysis in weight % for $Cs_{4.67}Na_{0.33}[IMo_6O_{24}] \cdot ca7H_2O$, to confirm the Mo and Cs content of **3** (calculated values in brackets): Mo 33.2 (31.3), Cs 26.9 (33.7).

Flame photometry in weight % for $Cs_{4.67}Na_{0.33}[IMo_6O_{24}] \cdot ca7H_2O$ analysis to confirm the Na content of **3** (calculated value in brackets): Na 1.5 (0.4).

The differences between the experimental and theoretical values for these analyses can be explained as follows. The theoretical values given above are calculated based on the caesium to sodium ratio assigned using the X-ray diffraction data from a single crystal of **3**. However, on collecting the bulk crystalline product of **3** on which to carry out the other analyses described here (i.e. EA, TGA, FAAS, flame photometry, and IR) the best theoretical fit for the FAAS and flame photometry analyses was found when the formula is $Cs_4Na_1[IMo_6O_{24}] \cdot ca7H_2O$. i.e. Calculated weight % values for FAAS analysis of Mo and Cs content, when using this formula are: Mo 32.6, Cs 30.1. Calculated weight % value for flame photometry analysis of Na content, when using this formula is: Na 1.3. This formula also provides calculated values within an acceptable range of the experimentally determined EA and TGA data. i.e. Calculated weight % for elemental analysis of H content, when using this formula is 0.80%. Calculated weight % for the loss of seven

solvent water molecules in the TGA analysis of **3**, when the formula of the compound is $Cs_4Na_1[IMo_6O_{24}] \cdot ca7H_2O$ is 7.14 %.

This phenomenon can be explained by the process of crystallization of the bulk product of **3** over time, where **3** initially crystallizes preferentially with a higher caesium content, then gradually crystallizes with a lower caesium content, and therefore higher sodium content, over time as the concentration of caesium ions in the solution decreases. Indeed this was observed on repeating this experiment and collecting the product in separate batches, where the later batch showed increased Na content by flame photometry.

Characteristic IR-bands[246] (in cm^{-1}): 3418 (m, b), 1617 (m), 939 (vs), 892 (vs), 682 (vs), 625 (vs), 475 (m).

5.5.1.2 Synthesis of compound **4**: $Na_4((HOCH_2CH_2)_3NH)_2[TeMo_6O_{24}] \cdot ca10H_2O$

Aqueous solutions of the starting materials were prepared as follows: $Na_2MoO_4 \cdot 2H_2O$ (20 g, 83 mmol) was dissolved in 50 mL water, $((CH_3CH_2OH)_3NH)Cl$ (16 g, 86 mmol) was dissolved in 50 mL water, and $Te(OH)_6$ (1.3 g, 5.6 mmol) was dissolved in 10 mL water. The $Te(OH)_6$ solution was added to the sodium molybdate solution followed by dropwise addition of the triethanolamine hydrochloride solution with stirring. The pH was then reduced to approximately 6.1 using 6 mol L^{-1} HCl. The white precipitate was filtered off and colourless rod and block crystals of **4**, suitable for single crystal X-ray diffraction, crystallized from the filtrate on diffusion of ethyl acetate. Yield: 899 mg (0.54 mmol, 3.9 % based on Mo). (Crude product yield: 6.85 g (4.13 mmol, 29.9 % based on Mo))

Elemental analysis in weight % for $Na_4((HOCH_2CH_2)_3NH)_2[TeMo_6O_{24}] \cdot ca10H_2O$ (calculated values in brackets): C 8.54 (8.68), H 3.00 (3.16), N 1.63 (1.69).

TGA analysis (see Figure 126) shows five distinct weight losses when heating 33.4240 mg of **4**, under an air atmosphere, from room temperature up to 560 °C. The first weight loss, i.e. 10.52 %, corresponds to the loss of ten solvent water molecules, when the formula of the compound is $Na_4((HOCH_2CH_2)_3NH)_2[TeMo_6O_{24}] \cdot ca10H_2O$ (calculated: 10.85 %).

The remaining four weight losses add to give a combined weight loss of 25.03 % (i.e. 10.71 + 4.30 + 5.71 + 4.31 = 25.03 %), which can be assigned to the oxidation of the organic cations from the compound and cluster decomposition with loss of Te (calculated: 25.79 %).
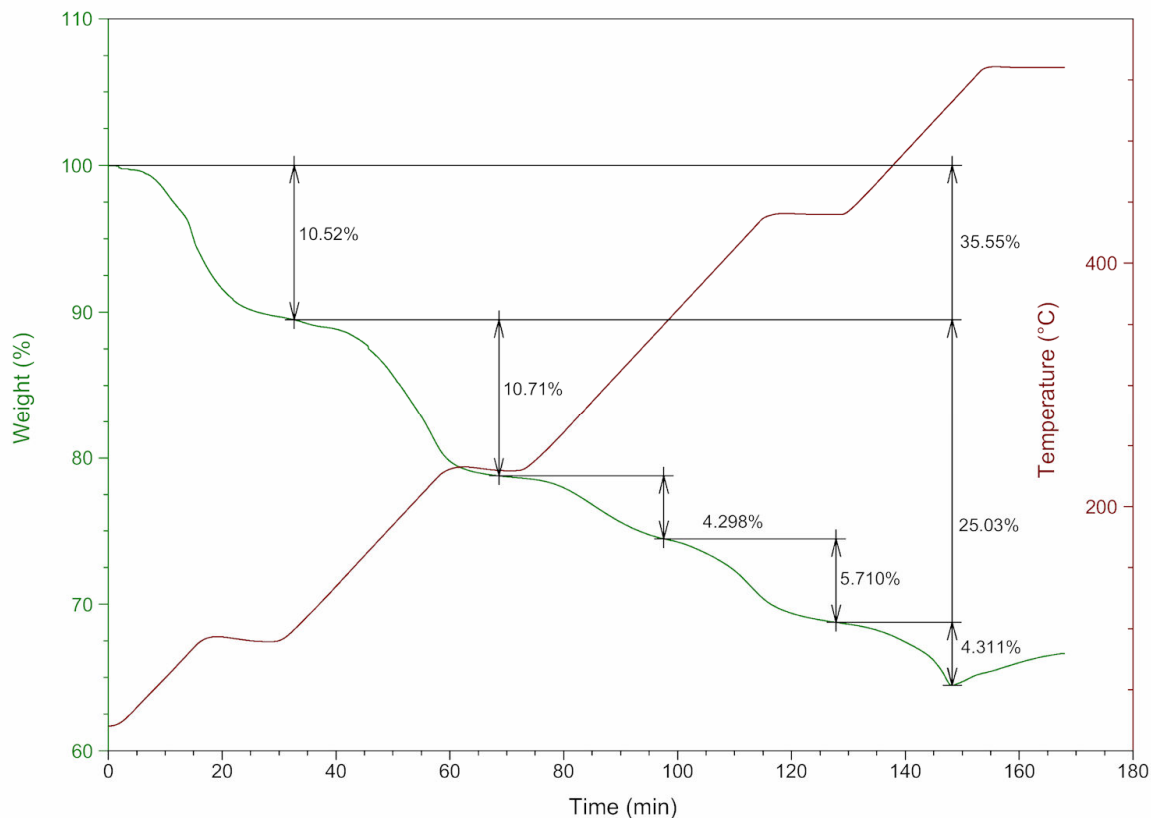
Figure 126: TGA analysis of **4**.

FAAS analysis in weight % for $Na_4((HOCH_2CH_2)_3NH)_2[TeMo_6O_{24}]\cdot ca10H_2O$, to confirm the Mo and Te content of **4** (calculated values in brackets): Mo 35.6 (34.7), Te 7.6 (7.7).

Flame photometry in weight % for $Na_4((HOCH_2CH_2)_3NH)_2[TeMo_6O_{24}]\cdot ca10H_2O$ analysis to confirm the Na content of **4** (calculated value in brackets): Na 5.2 (5.5).

Characteristic IR-bands[242] (in cm^{-1}): 3456 (vs, b), 1619 (m), 1470 (w), 1449 (w), 1407 (m), 1097 (w), 1062 (w), 1030 (m), 1005 (w), 929 (s), 899 (s), 669 (s), 614 (s), 446 (m).

5.6 The synthesis and characterization of new polyoxotungstate architectures with 2,3-dihydro-1*H*-imidazo[1,2-*f*]phenanthridinium (DIP) and imidazo-phenanthridinium (IP) cations

5.6.1 Synthesis and characterization of precursors

1-[2-(2-amino-ethylamino)-ethyl]-2,3-dihyro-1*H*-imidazo[1,2-*f*]phenanthridinium tribromide (also written as (DIP-1)Br$_3$),[209, 273, 274] *cis*-1,3,5-tri(2,3-dihydro-1*H*-imidazo[1,2-*f*]phenanthridinium)cyclohexane tribromide (also written as (DIP-2)Br$_3$),[209] and 1*H*-imidazo[1,2-*f*]phenanthridinium chloride (also written as (IPblue)Cl)[278] were synthesized according to literature procedures and their identities confirmed using ^{1}H and ^{13}C NMR, and IR analyses.

5.6.2 Synthesis and characterization of compounds 5 to 7

5.6.2.1 Synthesis of compound **5**: (C$_{19}$H$_{25}$N$_4$)[PW$_{12}$O$_{40}$]·5DMSO·*ca*1H$_2$O also written as (DIP-1)[PW$_{12}$O$_{40}$]·5DMSO·*ca*1H$_2$O

A solution of H$_3$[PW$_{12}$O$_{40}$]·xH$_2$O (201 mg, 70 µmol) in 2 mL water was prepared. To this solution was added, with stirring, 1-[2-(2-amino-ethylamino)-ethyl]-2,3-dihyro-1*H*-imidazo[1,2-*f*]phenanthridinium tribromide (115 mg, 0.21 mmol) in 20 mL water. The resulting yellow-orange precipitate was re-dissolved in hot DMSO. Yellow needle-like crystals of (DIP-1)[PW$_{12}$O$_{40}$]·5DMSO·*ca*1H$_2$O (**5**), suitable for single crystal X-ray diffraction, crystallized from this solution within 2 weeks. Yield: 194 mg (54.0 µmol, 77.6 % based on W).

Elemental analysis in weight % for the dehydrated material (C$_{19}$H$_{25}$N$_4$)[PW$_{12}$O$_{40}$]·5DMSO (calculated values in brackets): C 9.84 (9.74), H 1.26 (1.55), N 2.25 (1.57).

TGA analysis (see Figure 127) shows four distinct weight losses when heating 24.5120 mg of **5**, under an air atmosphere, at 5 °C min^{-1}, from room temperature up to 1000 °C. The first two weight losses, i.e. 3.68 % and 5.66 %, add to give a total weight loss of 9.34 %.

This weight loss corresponds to the loss of four DMSO molecules when the formula of the compound is $(C_{19}H_{25}N_4)[PW_{12}O_{40}]\cdot 4DMSO$ (calculated: 8.93 %). The weight loss of 8.34 % corresponds to the oxidation of the DIP-1 cations from the compound (calculated: 8.84 %). The remaining weight loss of 2.07 % could be due to decomposition of the cluster as the phosphate heteroanions are removed as volatile P_2O_5.
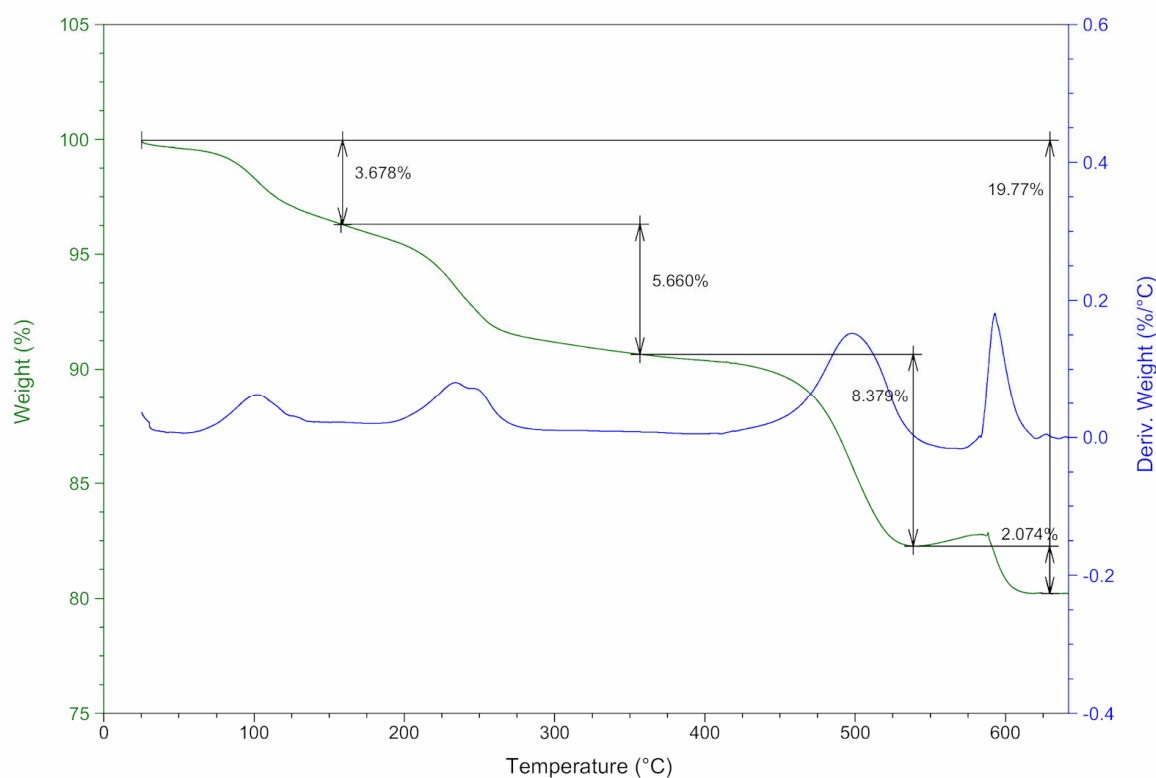
Figure 127: TGA analysis of **5**.

Characteristic IR-bands[264, 274] (in cm^{-1}): 3454 (s, b), 1611 (m), 1576 (m), 1550 (m), 1453 (m), 1393 (w), 1306 (m), 1268 (w), 1081 (s), 981 (s), 897 (s), 804 (s), 595 (w), 516 (m).

Characteristic solution state UV/vis absorption maxima for **5**, (DIP-1)Br$_3$, and $H_3PW_{12}O_{40}$, dissolved in DMSO and recorded over the 900-200 nm wavelength range are shown in Table 21 and Figure 128.

Compound	Peak Maxima Numbering	Wavelength of Absorption / nm	Associated Electronic Transition
$H_3[PW_{12}O_{40}]$	1	266	Oxygen ligand → Metal charge transfer
$(DIP-1)Br_3$	1	258	Electronic transitions centred on DIP-1 cation
	2	272	
	3	308	
	4	343	
	5	359	
	6	377	
Compound **5**	1	265	Oxygen ligand → Metal charge transfer (centred on POM cluster)
	2	310	Electronic transitions centred on DIP-1 cation
	3	343	
	4	360	
	5	378	

Table 21: Absorbance peak maxima observed in the solution state UV/vis spectroscopy measurements of $H_3PW_{12}O_{40}$, $(DIP-1)Br_3$, and compound **5**, as shown in Figure 128.
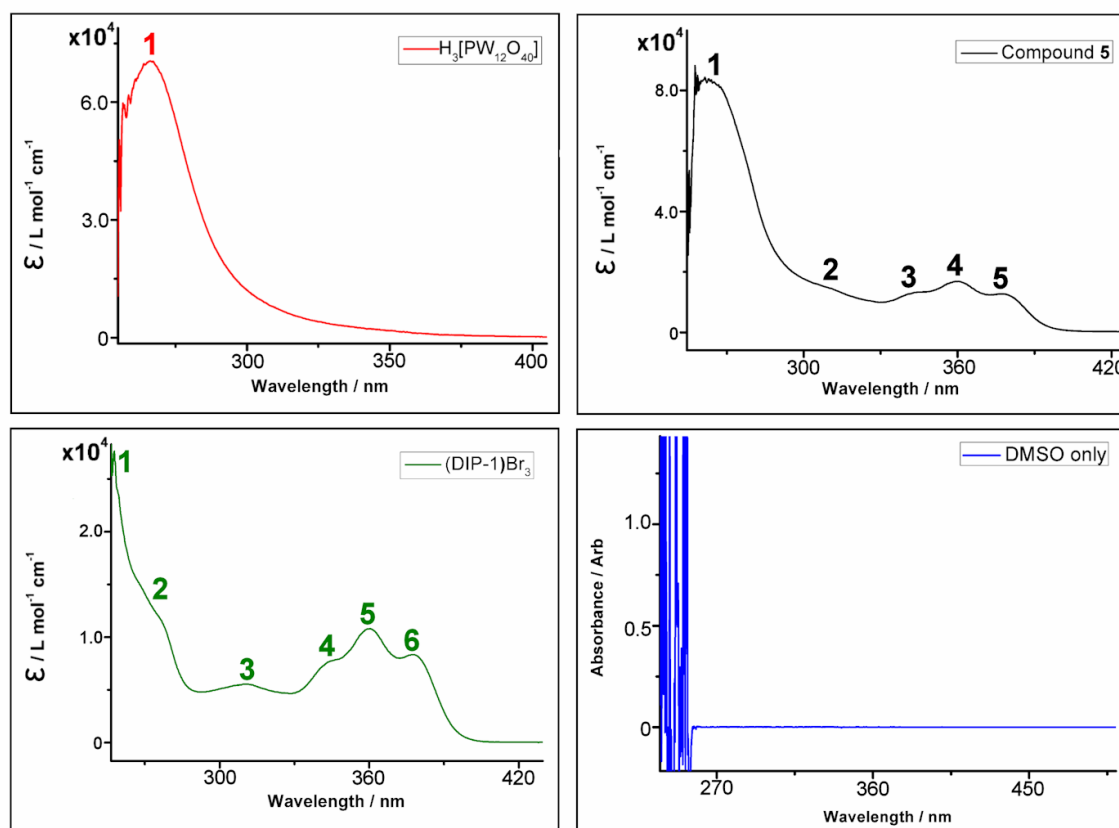
Figure 128: Solution state UV/vis spectra of $H_3PW_{12}O_{40}$ (1.6 x 10^{-5} mol L^{-1}) (top left), (DIP-1)Br$_3$ (3.8 x 10^{-5} mol L^{-1}) (bottom left), compound **5** (1.7 x 10^{-5} mol L^{-1}) (top right), and DMSO solvent only (bottom right). All compounds are dissolved in DMSO and the spectra recorded between 900 and 200 nm, with the DMSO beginning to absorb at approximately 255 nm. Peak maxima are highlighted with numbers which relate to Table 21.

Diffuse reflectance UV/vis spectra of **5**, (DIP-1)Br$_3$ and $H_3PW_{12}O_{40}$ are shown overlaid in Figure 129. The intermolecular charge transfer band at approximately 460 nm in the spectrum of **5** is particularly prominent, and indicates charge transfer from the DIP-1 cation to the fully oxidised POM anion.
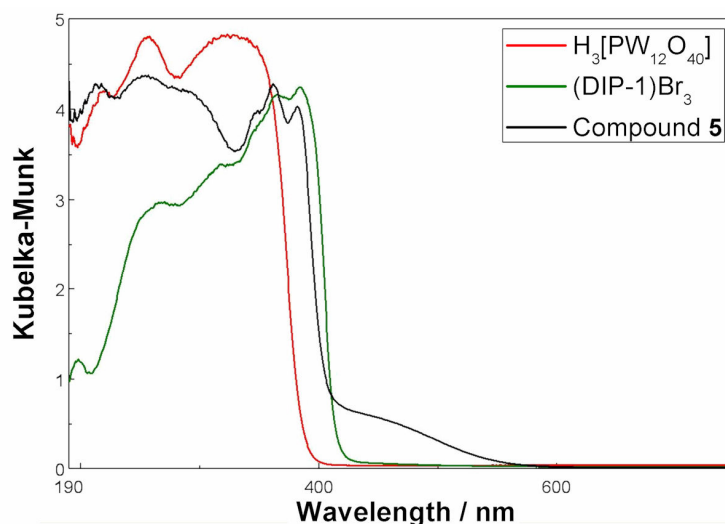
Figure 129: Overlaid diffuse reflectance UV/vis spectra for $H_3PW_{12}O_{40}$, (DIP-1)Br_3, and compound **5**. Colour code as shown in figure.

Preliminary cyclic voltammetry experiments have been carried out on solutions of **5**, (DIP-1)Br_3, and $H_3PW_{12}O_{40}$, each compound being dissolved in DMSO. Although DMSO is not the preferred solvent with which to carry out such experiments due to the restricted electrode potential window, the use of this solvent was unavoidable as compound **5** could not be dissolved in any other solvent. The voltammograms of (DIP-1)Br_3 did not show any clear, high intensity peaks to allow assignment of redox processes; whereas the voltammograms for **5** and $H_3PW_{12}O_{40}$ each show three redox processes. These can be attributed to electron processes on the tungsten centres of the POM anion[283-285] and are shifted to more negative electrode potentials in **5** due to the presence of the DIP-1 cation (see Figure 130 and Table 22). Further investigations are ongoing into these results.
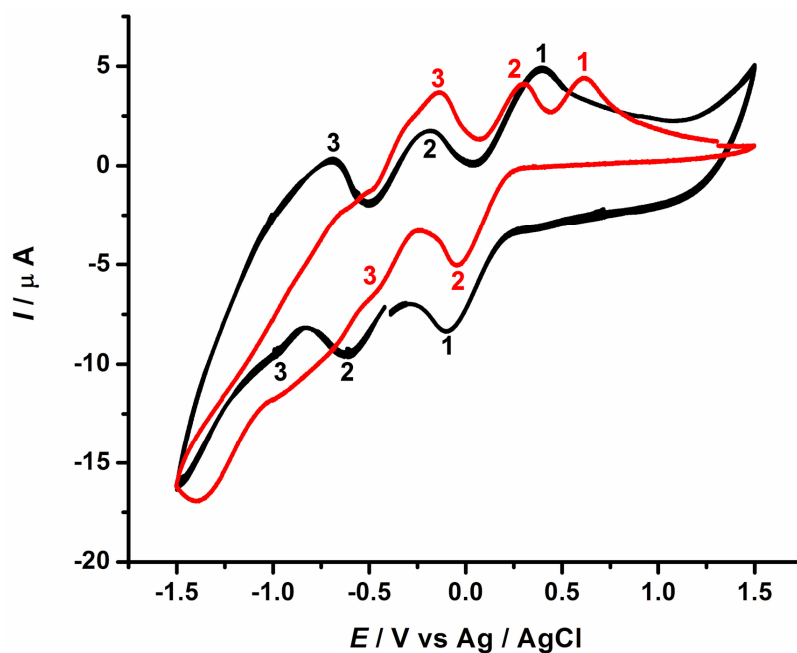
Figure 130: Overlaid cyclic voltammograms of compound **5** in DMSO (black line) and $H_3PW_{12}O_{40}$ in DMSO (red line) showing redox processes 1-3 for each compound (scan rate at 50 mV s^{-1}).

Redox Process	Oxidation Peak Potential / V vs Ag/AgCl	Reduction Peak Potential / V vs Ag/AgCl	Average Peak Potential / V vs Ag/AgCl	Reversibility of peak
Compound **5**				
1	0.395	-0.0992	0.15	Quasi-reversible
2	-0.185	-0.613	-0.40	Quasi-reversible
3	-0.686	-0.942	-0.81	Quasi-reversible
$H_3PW_{12}O_{40}$				
1	0.620	-	-	Irreversible
2	0.304	-0.0412	0.13	Quasi-reversible
3	-0.135	-0.468	-0.30	Quasi-reversible

Table 22: Electrochemical data obtained by cyclic voltammetry experiments shown in Figure 130 on compound **5** in DMSO (black text) and $H_3PW_{12}O_{40}$ in DMSO (red text). Scan rate at 50 mV s^{-1}.

5.6.2.2 Synthesis of compound **6**: $(C_{51}H_{45}N_6)[PW_{12}O_{40}]\cdot 5DMSO\cdot ca4H_2O$ also written as (DIP-2)$[PW_{12}O_{40}]\cdot 5DMSO\cdot ca4H_2O$

A solution of $H_3[PW_{12}O_{40}]\cdot xH_2O$ (490 mg, 0.17 mmol) in 100 mL water was prepared. To this solution was added, with stirring, *cis*-1,3,5-tri(2,3-dihydro-1*H*-imidazo[1,2-*f*]phenanthridinium)cyclohexane tribromide (500 mg, 0.51 mmol) in 45 mL DMSO. The

resulting orange-brown precipitate was recrystallized from hot DMSO, yielding orange needle-like crystals of (DIP-2)[PW$_{12}$O$_{40}$]·5DMSO·ca4H$_2$O (**6**) suitable for single crystal X-ray diffraction. Yield: 296 mg (72.6 μmol, 42.6 % based on W).

Elemental analysis in weight % for the dehydrated material (C$_{51}$H$_{45}$N$_6$)[PW$_{12}$O$_{40}$]·5DMSO (calculated values in brackets): C 18.97 (18.27), H 1.45 (1.89), N 2.38 (2.10).

TGA analysis (see Figure 131) shows five distinct weight losses when heating 32.6600 mg of **6**, under an air atmosphere, at 5 °C min^{-1}, from room temperature up to 1000 °C. The first two weight losses, i.e. 1.77 % and 6.54 %, add to give a total weight loss of 8.31 %. This weight loss corresponds to the loss of four DMSO molecules when the formula of the compound is (C$_{51}$H$_{45}$N$_6$)[PW$_{12}$O$_{40}$]·4DMSO (calculated: 7.95 %). The following three weight losses, i.e. 1.40 %, 1.92 % and 14.92%, add to give a total weight loss of 18.24 % which corresponds to the oxidation of the DIP-2 cations from the compound (calculated: 18.88 %).
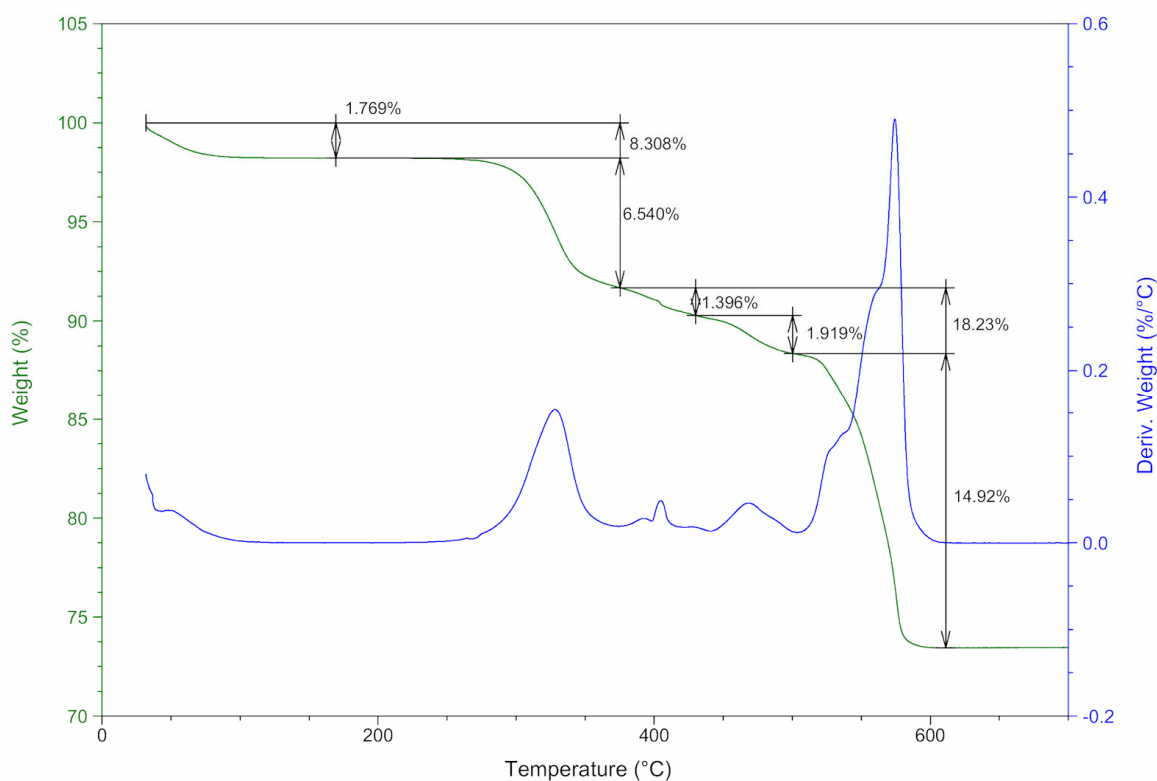

Figure 131: TGA analysis of **6**.

Characteristic IR-bands[209, 264] (in cm^{-1}): 3435 (m, b), 1611 (m), 1572 (s), 1532 (s), 1454 (m), 1385 (w), 1301 (m), 1264 (m), 1170 (w), 1079 (vs), 976 (vs), 896 (vs), 813 (vs), 747 (s), 716 (s), 667 (m), 511 (m).

Characteristic solution state UV/vis absorption maxima for **6**, (DIP-2)Br$_3$, and H$_3$PW$_{12}$O$_{40}$, dissolved in DMSO and recorded over the 900-200 nm wavelength range are shown in Table 23 and Figure 132. Two intermolecular charge transfer bands are identified at approximately 421 and 440 nm in the spectrum of **6**. Further detailed investigations are ongoing into these results.

Compound	Peak Maxima Numbering	Wavelength of Absorption / nm	Associated Electronic Transition
H$_3$[PW$_{12}$O$_{40}$]	1	266	Oxygen ligand → Metal charge transfer
(DIP-2)Br$_3$	1	258	Electronic transitions centred on DIP-2 cation
	2	273	
	3	310	
	4	345	
	5	362	
	6	381	
Compound **6**	1	257	Electronic transitions centred on DIP-2 cation, (possibly overlaying POM-centred oxygen ligand → metal charge transfer)
	2	275	
	3	306	Electronic transitions centred on DIP-2 cation
	4	345	
	5	362	
	6	381	
	7	421	DIP-2 → POM cluster (Intermolecular charge transfer)
	8	440	DIP-2 → POM cluster (Intermolecular charge transfer)

Table 23: Absorbance peak maxima observed within the solution state UV/vis spectra of H$_3$PW$_{12}$O$_{40}$, (DIP-2)Br$_3$, and compound **6,** as shown within Figure 132.
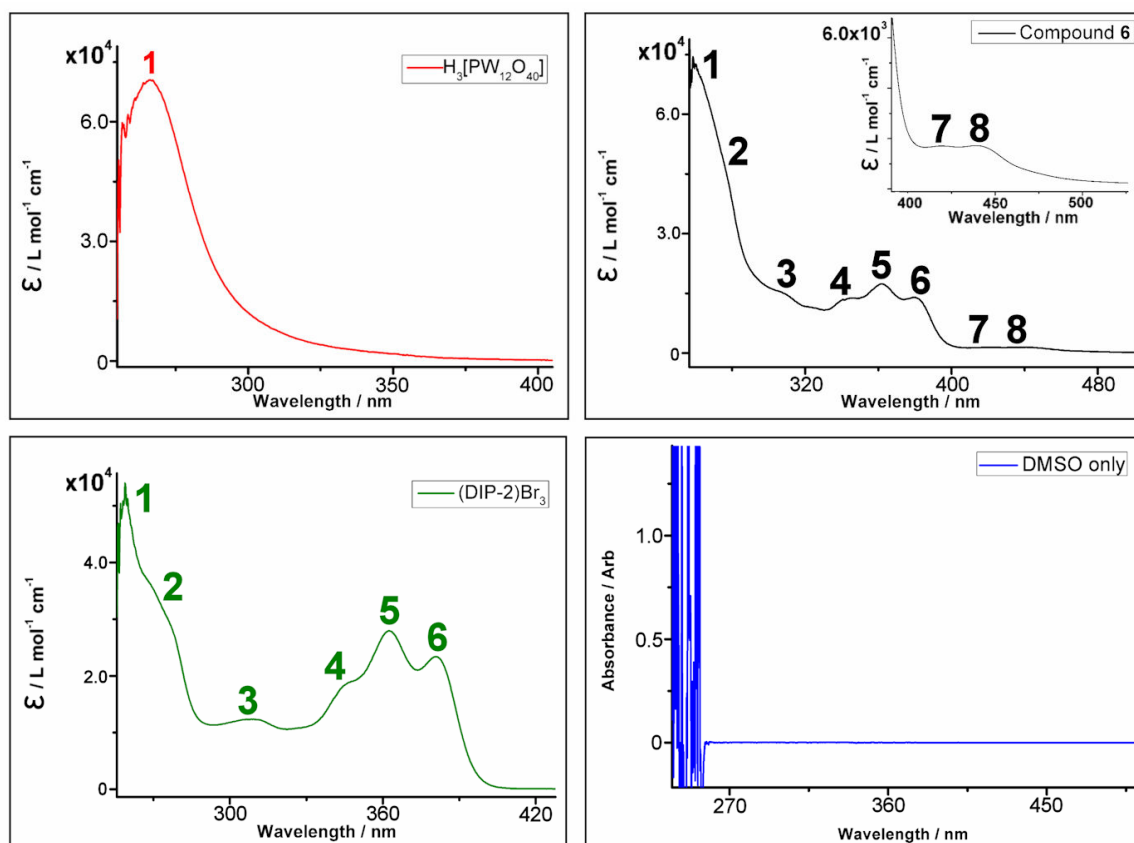
Figure 132: Solution state UV/vis spectra of $H_3PW_{12}O_{40}$ (1.6 x 10^{-5} mol L^{-1}) (top left), (DIP-2)Br$_3$ (2.6 x 10^{-5} mol L^{-1}) (bottom left), compound **6** (1.5 x 10^{-5} mol L^{-1}) (top right), and DMSO solvent only (bottom right). Inset graph for compound **6** is at higher concentration (1.7 x 10^{-4} mol L^{-1}) to show peak maxima 7 and 8. All compounds are dissolved in DMSO and the spectra recorded between 900 and 200 nm, with the DMSO beginning to absorb at approximately 255 nm. Peak maxima are highlighted with numbers which relate to Table 23.

Diffuse reflectance UV/vis spectra of **6**, (DIP-2)Br$_3$ and $H_3PW_{12}O_{40}$ are shown overlaid in Figure 133. An intermolecular charge transfer band at approximately 448 nm can be identified in the spectrum of **6**, and indicates charge transfer from the DIP-2 cation to the fully oxidised POM anion.
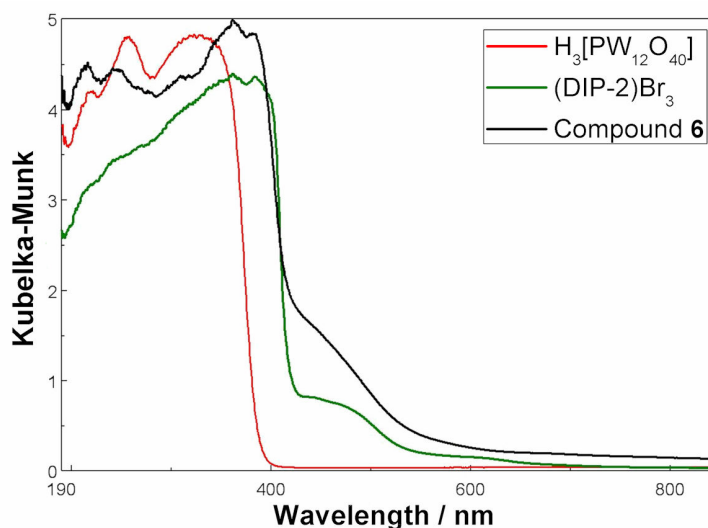
Figure 133: Overlaid diffuse reflectance UV/vis spectra for $H_3PW_{12}O_{40}$, (DIP-2)Br_3, and compound **6**. Colour code as shown in figure.

Preliminary cyclic voltammetry experiments have been carried out on solutions of **6**, (DIP-2)Br_3, and $H_3PW_{12}O_{40}$, with each compound dissolved in DMSO. Although DMSO is not the preferred solvent with which to carry out such experiments due to the restricted electrode potential window, the use of this solvent was unavoidable as compound **6** could not be dissolved in any other solvent. Although the voltammograms of (DIP-2)Br_3 did not show any clear, high intensity peaks to allow assignment of redox processes, the voltammograms for **6** and $H_3PW_{12}O_{40}$ each show three redox processes (however, the reduction peak of redox process 3 for compound **6** cannot be observed due to the electrode potential limit of the solvent window). These redox processes can be attributed to electron processes on the tungsten centres of the POM anion[283-285] and two of these processes are shifted to more negative electrode potentials in **6** due to the presence of the DIP-2 cation (see Figure 134 and Table 24). Further investigations are ongoing into these results.
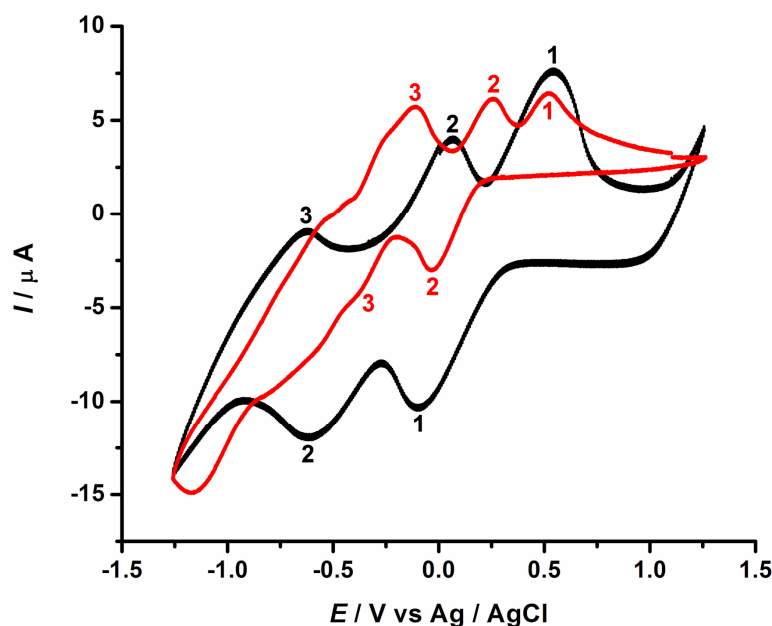
Figure 134: Overlaid cyclic voltammograms of compound **6** in DMSO (black line) and $H_3PW_{12}O_{40}$ in DMSO (red line) showing redox processes 1-3 for each compound (scan rate at 50 mV s^{-1}).

Redox Process	Oxidation Peak Potential / V vs Ag/AgCl	Reduction Peak Potential / V vs Ag/AgCl	Average Peak Potential / V vs Ag/AgCl	Reversibility of peak
Compound **6**				
1	0.541	-0.102	0.22	Quasi-reversible
2	0.0615	-0.615	-0.277	Quasi-reversible
3	-0.622	- (due to solvent limit)	-	- (due to solvent limit)
$H_3PW_{12}O_{40}$				
1	0.620	-	-	Irreversible
2	0.304	-0.0412	0.13	Quasi-reversible
3	-0.135	-0.468	-0.30	Quasi-reversible

Table 24: Electrochemical data obtained by cyclic voltammetry experiments shown in Figure 134 on compound **6** in DMSO (black text) and $H_3PW_{12}O_{40}$ in DMSO (red text). Scan rate at 50 mV s^{-1}.

SEM, EDX and powder XRD analysis were carried out on samples of **6** after heating under an air atmosphere at 5 °C min^{-1}, from room temperature to 1000 °C, i.e. so removing first the solvent through evaporation then the organic cations through oxidation. EDX and powder XRD data were collected to confirm the WO_3 composition of the remaining 'porous' framework material observed in the SEM images (see Results and Discussion, section 3.8.2.2). See Figure 135 and 136.
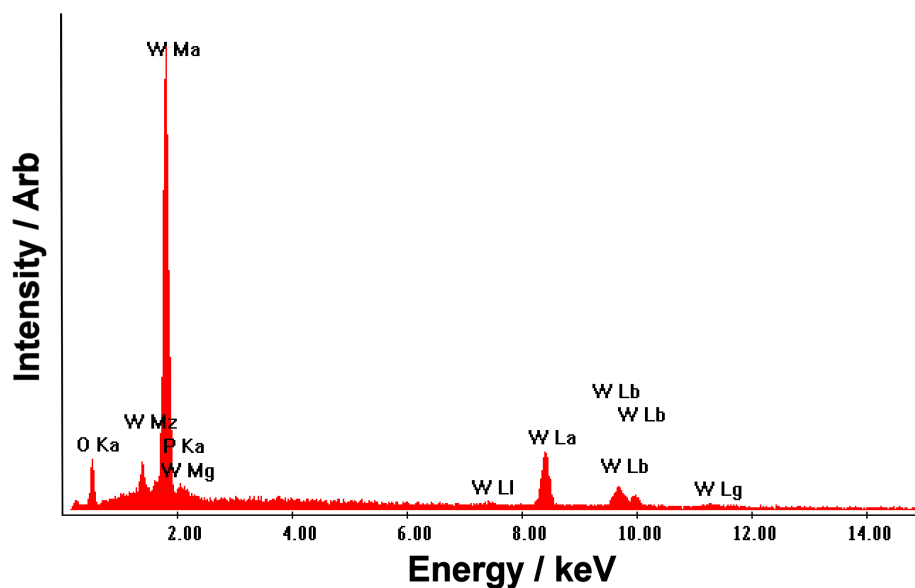
Figure 135: EDX data acquired from an area of the compound **6** sample after preparation for SEM analysis, i.e. after heating at 5 °C min^{-1}, under an air atmosphere, from room temperature to 1000 °C. This data confirms the composition of the remaining sample framework as WO_3.
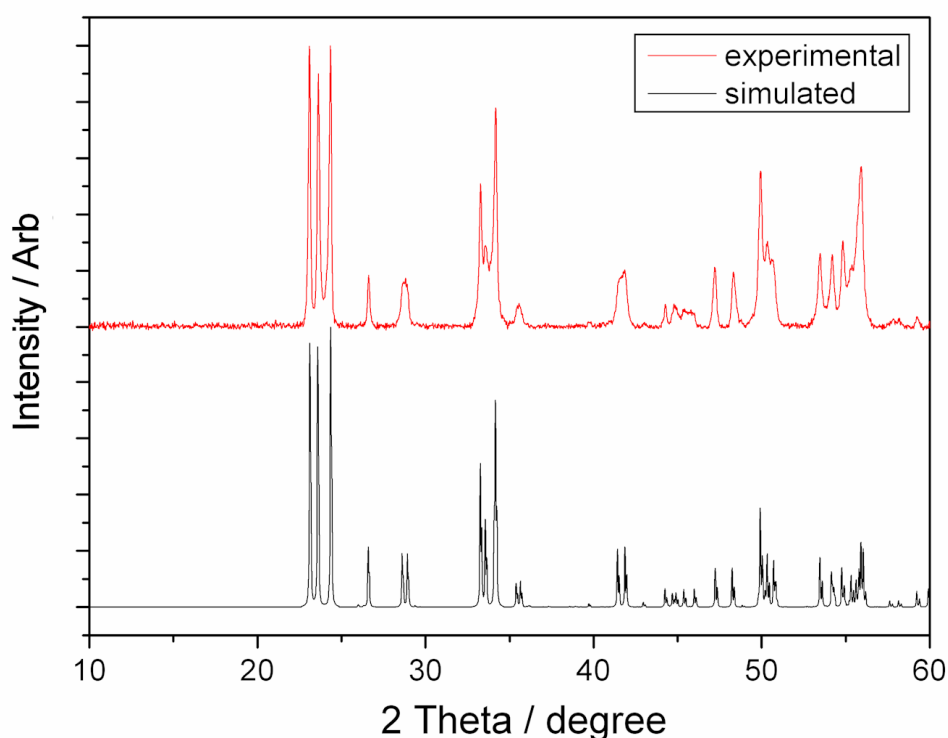
Figure 136: Powder XRD data collected of the compound **6** sample after preparation for SEM analysis, i.e. after heating at 5 °C min^{-1}, under an air atmosphere, from room temperature to 1000 °C (red line). Comparison of this data with a simulated powder pattern of WO_3[286] (black line) confirms the composition of the remaining sample framework as WO_3.

5.6.2.3 Synthesis of compound **7**: $(C_{15}H_{11}N_2)_3[PW_{12}O_{40}]\cdot4DMSO$ also written as $(IPblue)_3[PW_{12}O_{40}]\cdot4DMSO$

A solution of $H_3[PW_{12}O_{40}]\cdot xH_2O$ (162 mg, 56 µmol) in 5 mL water was prepared. To this solution was added, dropwise with stirring, 1*H*-imidazo[1,2-*f*]phenanthridinium chloride (50 mg, 0.20 mmol) in 2 mL water. The resulting orange precipitate was recrystallized from hot DMSO, yielding yellow needle-like crystals of $(IPblue)_3[PW_{12}O_{40}]\cdot4DMSO$ (**7**) suitable for single crystal X-ray diffraction. Yield: 120 mg (31.2 µmol, 55.5 % based on W).

Elemental analysis in weight % for $(C_{15}H_{11}N_2)_3[PW_{12}O_{40}]\cdot3DMSO$ showing loss of one solvent DMSO (calculated values in brackets): C 16.26 (16.25), H 1.34 (1.36), N 2.12 (2.23).

TGA analysis (see Figure 137) shows six distinct weight losses when heating 26.1020 mg of **7**, under an air atmosphere, at 5 °C min^{-1}, from room temperature up to 1000 °C. The first two weight losses, i.e. 5.82 % and 1.33 %, add to give a total weight loss of 7.15 %. This weight loss corresponds to the loss of three DMSO molecules when the formula of the compound is $(C_{15}H_{11}N_2)_3[PW_{12}O_{40}]\cdot3DMSO$ (calculated: 6.22 %). The remaining four weight losses, i.e. 2.27 %, 7.71 %, 3.66 % and 4.04 %, add to give a total weight loss of 17.69 % which corresponds to the oxidation of the IPblue cations from the compound (calculated: 17.45 %).
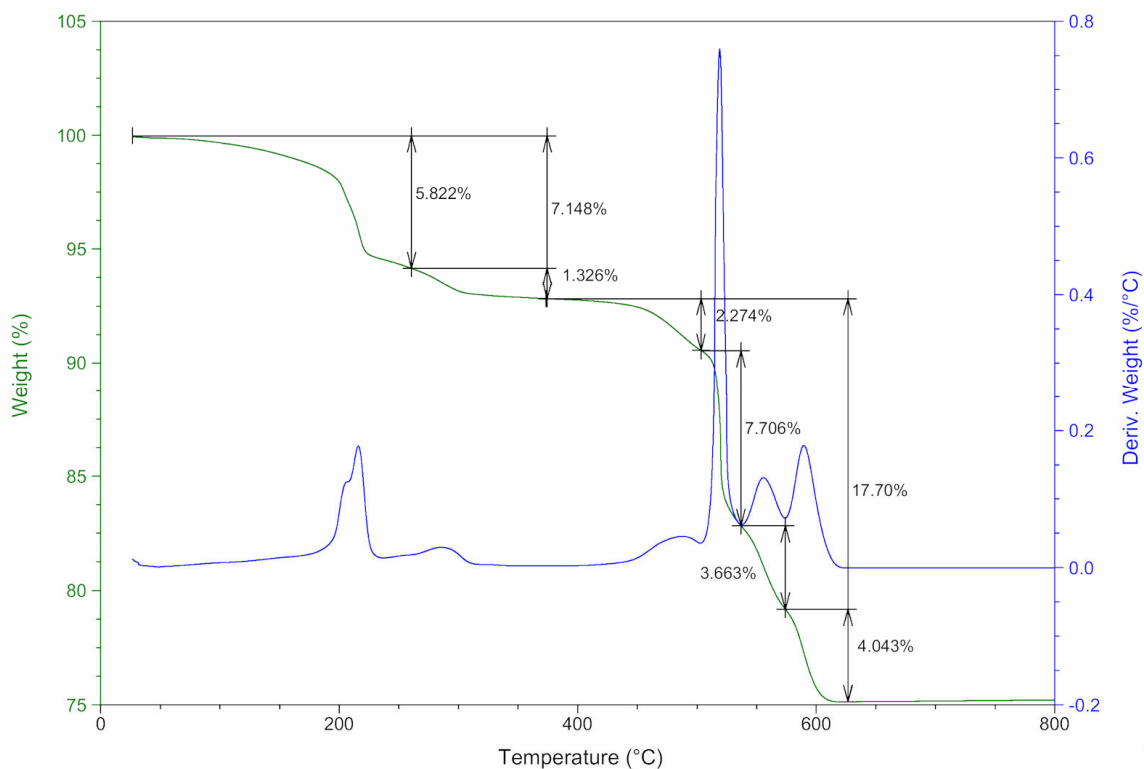
Figure 137: TGA analysis of **7**.

Characteristic IR-bands[264, 278] (in cm^{-1}): 3435 (m, b), 1631 (m), 1561 (m), 1534 (w), 1472 (w), 1435 (m), 1412 (w), 1334 (w), 1314 (w), 1079 (vs), 1017 (s), 977 (vs), 895 (vs), 810 (vs), 755 (s), 692 (s), 614 (m), 595 (m), 510 (m).

Characteristic solution state UV/vis absorption maxima for **7**, (IPblue)Cl, and $H_3PW_{12}O_{40}$, dissolved in DMSO and recorded over the 900-200 nm wavelength range are shown in Table 25 and Figure 138. Further detailed investigations are ongoing into these results.

Compound	Peak Maxima Numbering	Wavelength of Absorption / nm	Associated Electronic Transition
$H_3[PW_{12}O_{40}]$	1	266	Oxygen ligand→ Metal charge transfer
(IPblue)Cl	1	261	Electronic transitions centred on IPblue cation
	2	278	
	3	290	
	4	303	
	5	317	
	6	332	
	7	349	
Compound **7**	1	262	Electronic transition centred on IPblue cation
	2	270	Oxygen ligand→ Metal charge transfer (centred on POM cluster)
	3	279	Electronic transitions centred on IPblue cation
	4	288	
	5	303	
	6	317	
	7	332	
	8	349	

Table 25: Absorption peak maxima observed within the solution state UV/vis spectra of $H_3PW_{12}O_{40}$, (IPblue)Cl, and compound **7**, as shown in Figure 138.
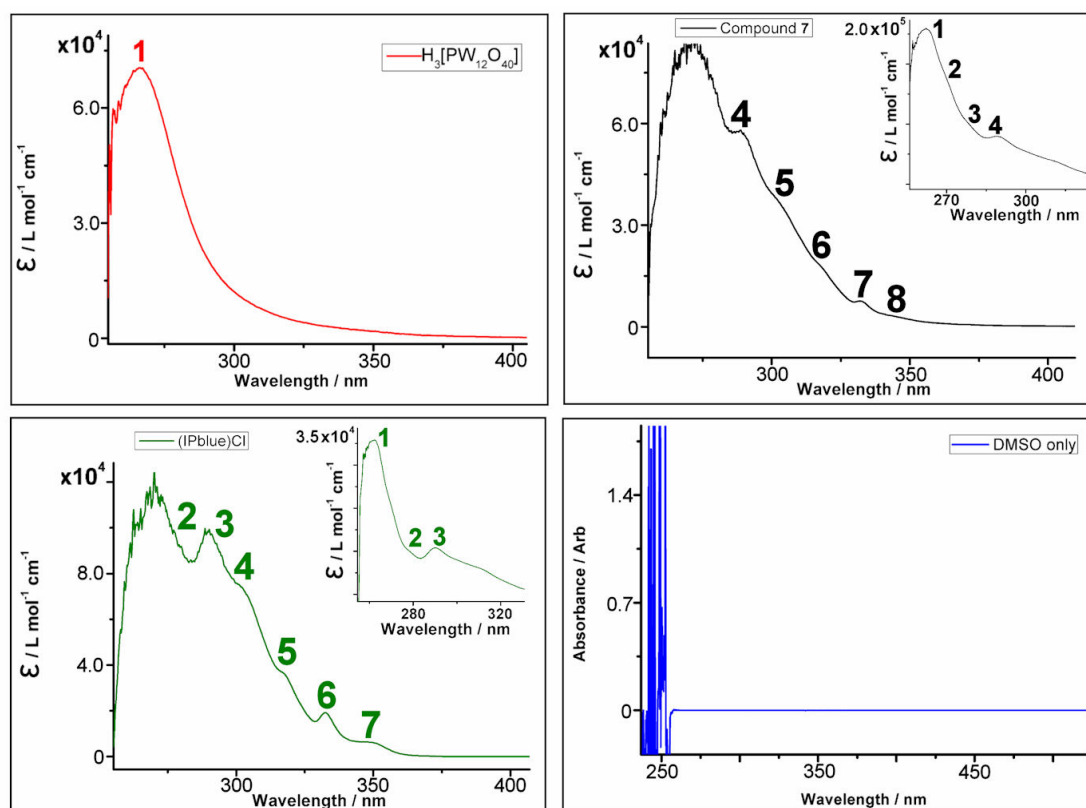
Figure 138: Solution state UV/vis spectra of $H_3PW_{12}O_{40}$ (1.6×10^{-5} mol L^{-1}) (top left), (IPblue)Cl (2.6×10^{-4} mol L^{-1}) (bottom left), compound **7** (3.8×10^{-5} mol L^{-1}) (top right), and DMSO solvent only (bottom right). Inset graph for (IPblue)Cl is at lower concentration (2.6×10^{-5} mol L^{-1}) to show peak maxima 1-3 more clearly. Inset graph for compound **7** is at lower concentration (3.7×10^{-6} mol L^{-1}) to show peak maxima 1-4 more clearly. All compounds are dissolved in DMSO and the spectra recorded between 900 and 200 nm, with the DMSO solvent beginning to absorb at approximately 255 nm. Peak maxima are highlighted with numbers which relate to those in Table 25.

Diffuse reflectance UV/vis spectra of **7**, (IPblue)Cl and $H_3PW_{12}O_{40}$ are shown overlaid in Figure 139. An intermolecular charge transfer band can be identified in the spectrum of **7** at approximately 410 nm. This indicates a charge transfer from the IPblue cation to the fully oxidised POM anion.
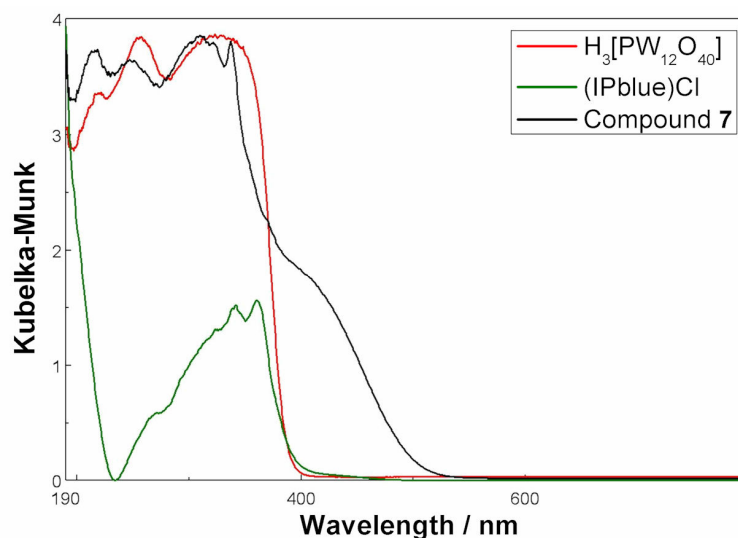
Figure 139: Overlaid diffuse reflectance UV/vis spectra for $H_3PW_{12}O_{40}$, (IPblue)Cl, and compound **7**. Colour as shown in figure.

Preliminary cyclic voltammetry experiments have been carried out on solutions of **7**, (IPblue)Cl, and $H_3PW_{12}O_{40}$, with each compound dissolved in DMSO. DMSO is not the preferred solvent with which to carry out such experiments due to the restricted electrode potential window, however, the use of this solvent was unavoidable as compound **7** could not be dissolved in any other solvent.

Unlike for the series of experiments carried out for compounds **5** and **6**, the voltammogram of the starting material (IPblue)Cl did show the presence of three redox processes (i.e. at reduction peak potentials *ca* -0.99 V, -1.6 V, and -1.8 V). However, only one of these processes (reduction peak potential *ca* -0.99 V) lies within the electrode potential window of the system when monitoring the electrochemical response of compound **7,** and this signal is overlaid by the higher intensity signals from the tungsten reductions. Therefore, the five redox processes (one ill-defined) seen in the voltammogram for **7** can be attributed to electron processes on the tungsten centres of the POM anion.[283-285] These redox couples can be seen to be shifted to much more negative electrode potentials than in the lone $H_3PW_{12}O_{40}$ sample, due to the presence of the IPblue cations (see Figure 140 and Table 26). Further investigations are ongoing into these results.
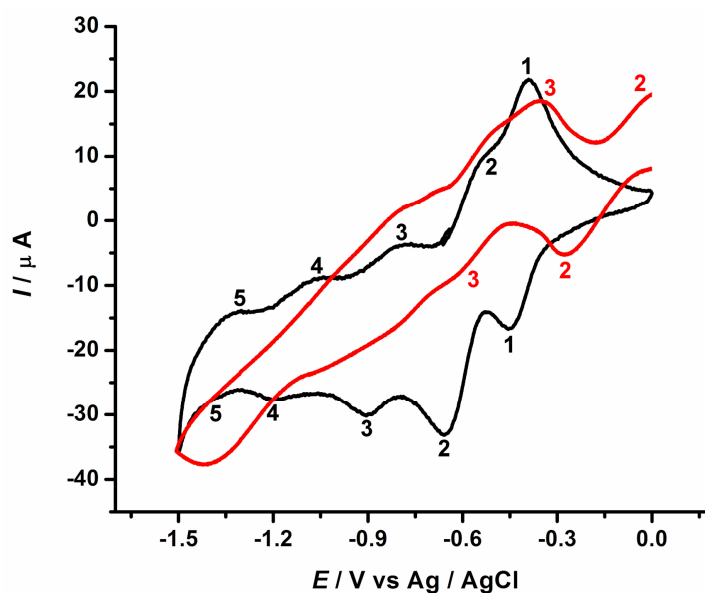
Figure 140: Overlaid cyclic voltammograms of compound **7** in DMSO (black line) and $H_3PW_{12}O_{40}$ in DMSO (red line) showing redox processes 1-5 for compound **7** and redox process 3 for $H_3PW_{12}O_{40}$ (scan rate at 50 mV s^{-1}).

Redox Process	Oxidation Peak Potential / V vs Ag/AgCl	Reduction Peak Potential / V vs Ag/AgCl	Average Peak Potential / V vs Ag/AgCl	Reversibility of peak
Compound **7**				
1	-0.390	-0.453	-0.42	Quasi-reversible
2	-0.539	-0.658	-0.60	Quasi-reversible
3	-0.794	-0.903	-0.85	Quasi-reversible
4	-1.06	-1.20	-1.1	Quasi-reversible
5	-1.31	(-1.39) Difficult to read due of solvent limit.	This is an ill-defined redox couple.	-
$H_3PW_{12}O_{40}$				
1	0.620	-	-	Irreversible
2	0.304	-0.0412	0.13	Quasi-reversible
3	-0.135	-0.468	-0.30	Quasi-reversible

Table 26: Electrochemical data obtained by cyclic voltammetry experiments shown in Figure 140 on compound **7** in DMSO (black text) and $H_3PW_{12}O_{40}$ in DMSO (red text). Scan rate at 50 mV s^{-1}

6   Crystallographic Section

Single crystal X-ray diffraction data for compounds **3** to **7** are presented in this thesis. Due to the large amount of tabulated data such as tables of bond lengths and angles, only the crystal data and structure refinement information, and ortep representations of these compounds are listed in this section. For additional data, the reader is referred to the supplementary data which is deposited with this thesis and can be obtained from the University of Glasgow. Structures were solved using Patterson or Direct methods with SHELXS-97 or SIR-92 using WinGX routines. Refinement was accomplished by full matrix least-squares on F^2 *via* SHELXL-97. All non-hydrogen atoms were refined anisotropically unless stated otherwise. Hydrogen atom positions were calculated using standard geometric criteria and refined using a riding model. All data manipulation and presentation steps were performed using WinGX. Details of interest about the structure refinement are given in the tables. The following quantities are given in the information for each structure and were calculated as follows:

$$\text{Goodness-of-fit (GooF)} = \left(\sqrt{\sum \frac{w(F_0^2 - F_c^2)^2}{(n-p)}} \right)$$

$$\text{Weighting scheme } w = \frac{1}{[\sigma^2(F_0)^2 + (AP)^2 + (BP)]}$$

$$\text{With } P = \frac{[\max(I_{obs,O}) + 2F_c^2]}{3}$$

and *p*: number of parameters; *n*: number of data; A, B: weighting scheme parameters

$$R1 = \frac{\sum ||F_0| - |F_c||}{\sum |F_o|}$$

$$wR2 = \sqrt{\frac{\sum[w(F_0^2 - F_c^2)^2]}{\sum w(F_0^2)^2}}$$

$$R(\text{int}) = \frac{\sum |F_0^2 - F_c^2(mean)|}{\sum |F_0^2|}$$

where both summations involve reflections for which more than one symmetry equivalent is averaged.

6.1 Crystal data and structure refinement for compound 3

Identification code	Compound **3**
Empirical formula	Cs4.67 Na0.33 I1 Mo6 H8 O28
Formula weight	1786.85
Temperature	150(2) K
Wavelength	0.71073 Å
Crystal system	Triclinic
Space group	*P*-1
Unit cell dimensions	a = 8.0130(2) Å $\quad$ α= 100.034(2)°.
	b = 10.5159(3) Å $\quad$ β= 94.587(2)°.
	c = 26.1210(6) Å $\quad$ γ = 97.692(2)°.
Volume	2135.82(9) Å^3
Z	3
Density (calculated)	4.176 g/cm^3
Absorption coefficient	9.635 mm^{-1}
F(000)	2404
Crystal size	0.3 x 0.4 x 0.4 mm^3
Theta range for data collection	2.78 to 26.00°.
Index ranges	-9<=h<=9, -12<=k<=12, -32<=l<=32
Reflections collected	30157
Independent reflections	8343 [R(int) = 0.0283]
Completeness to theta = 26.00°	99.7 %
Refinement method	Full-matrix least-squares on F^2
Data / restraints / parameters	8343 / 0 / 570
Goodness-of-fit on F^2	1.093
Final R indices [I>2sigma(I)]	R1 = 0.0285, wR2 = 0.0750
R indices (all data)	R1 = 0.0374, wR2 = 0.0770
Largest diff. peak and hole	1.606 and -1.768 e.Å^{-3}

Ortep representation of compound 3 at 50 % probability level
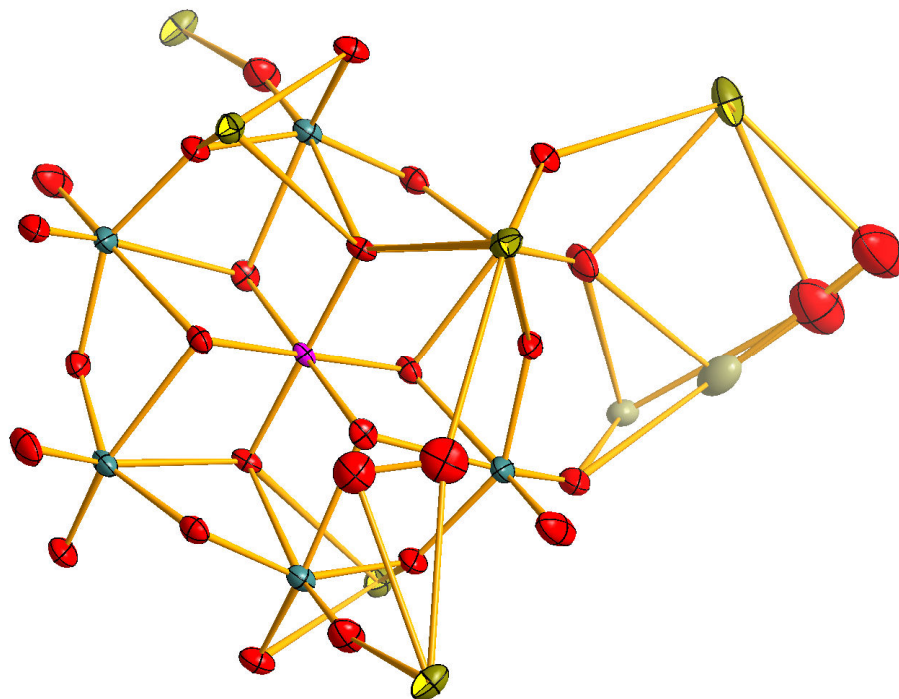
6.2 Crystal data and structure refinement for compound 4

Identification code	Compound **4**
Empirical formula	C12 H34 O31 N2 Na4 Te1 Mo6
Formula weight	1497.59
Temperature	150(2) K
Wavelength	0.71073 Å
Crystal system	Monoclinic
Space group	$P2_1/n$
Unit cell dimensions	$a = 13.3641(6)$ Å $\quad \alpha = 90°$.
	$b = 9.8141(4)$ Å $\quad \beta = 94.924(4)°$.
	$c = 17.0212(4)$ Å $\quad \gamma = 90°$.
Volume	2224.20(14) Å^3
Z	2
Density (calculated)	2.478 g/cm^3
Absorption coefficient	2.440 mm^{-1}
F(000)	1612
Crystal size	0.2 x 0.4 x 0.4 mm^3
Theta range for data collection	2.79 to 25.99°.
Index ranges	-16<=h<=16, -12<=k<=11, -15<=l<=20
Reflections collected	11437
Independent reflections	4287 [R(int) = 0.0414]
Completeness to theta = 25.99°	98.1 %
Refinement method	Full-matrix least-squares on F^2
Data / restraints / parameters	4287 / 0 / 286
Goodness-of-fit on F^2	1.109
Final R indices [I>2sigma(I)]	R1 = 0.0721, wR2 = 0.1848
R indices (all data)	R1 = 0.0790, wR2 = 0.1872
Largest diff. peak and hole	3.500 and -1.729 e.Å^{-3}

Ortep representation of compound 4 at 50 % probability level
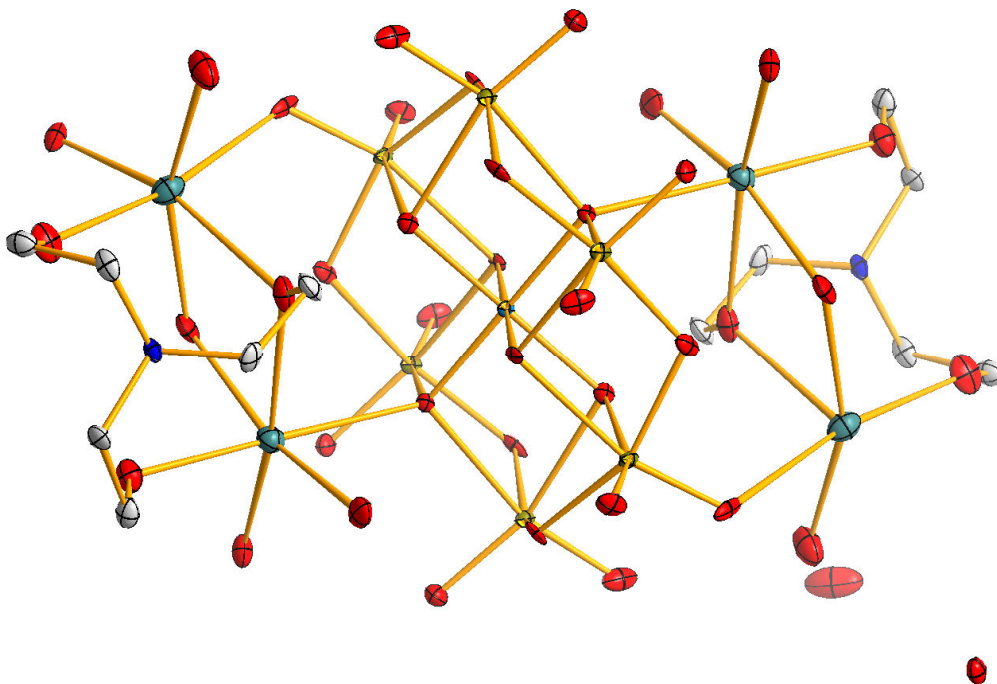
6.3 Crystal data and structure refinement for compound 5

Identification code	Compound **5**
Empirical formula	C29 H57 N4 O46 S5 P1 W12
Formula weight	3595.15
Temperature	150(2) K
Wavelength	1.54184 Å
Crystal system	Monoclinic
Space group	$P2_1/c$
Unit cell dimensions	a = 18.94390(10) Å α= 90°.
	b = 13.56420(10) Å β= 93.0780(10)°.
	c = 27.2546(2) Å γ = 90°.
Volume	6993.21(8) Å^3
Z	2
Density (calculated)	3.350 g/cm^3
Absorption coefficient	37.833 mm^{-1}
F(000)	6187
Crystal size	0.04 x 0.04 x 0.1 mm^3
Theta range for data collection	3.90 to 61.69°.
Index ranges	-18<=h<=21, -15<=k<=13, -25<=l<=31
Reflections collected	26284
Independent reflections	10164 [R(int) = 0.0335]
Completeness to theta = 61.69°	93.1 %
Refinement method	Full-matrix least-squares on F^2
Data / restraints / parameters	10164 / 4422 / 946
Goodness-of-fit on F^2	0.923
Final R indices [I>2sigma(I)]	R1 = 0.0297, wR2 = 0.0672
R indices (all data)	R1 = 0.0415, wR2 = 0.0695
Largest diff. peak and hole	1.879 and -1.334 e.Å^{-3}

ORTEP representation of compound 5 at 50 % probability level
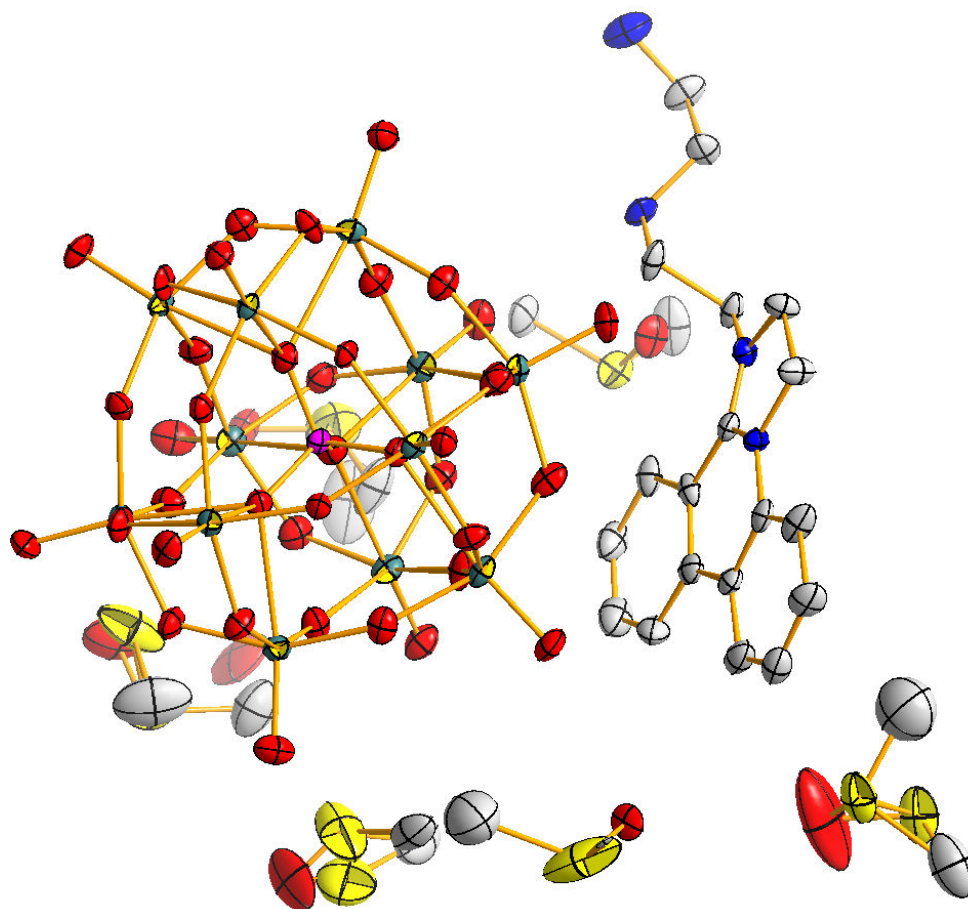
6.4 Crystal data and structure refinement for compound 6

Identification code	Compound **6**
Empirical formula	C61 H83 N6 O49 S5 P1 W12
Formula weight	4081.71
Temperature	150(2) K
Wavelength	0.71073 Å
Crystal system	Triclinic
Space group	P-1
Unit cell dimensions	a = 14.0249(9) Å α = 75.812(6)°.
	b = 17.5962(13) Å β = 70.004(6)°.
	c = 20.2941(12) Å γ = 88.572(6)°.
Volume	4553.3(5) Å^3
Z	2
Density (calculated)	2.811 g/cm^3
Absorption coefficient	15.265 mm^{-1}
F(000)	3472
Crystal size	0.04 x 0.04 x 0.1 mm^3
Theta range for data collection	3.21 to 23.26°.
Index ranges	-15<=h<=15, -19<=k<=19, -22<=l<=22
Reflections collected	28208
Independent reflections	12777 [R(int) = 0.0654]
Completeness to theta = 23.26°	97.5 %
Refinement method	Full-matrix least-squares on F^2
Data / restraints / parameters	12777 / 628 / 1177
Goodness-of-fit on F^2	0.848
Final R indices [I>2sigma(I)]	R1 = 0.0442, wR2 = 0.0877
R indices (all data)	R1 = 0.0938, wR2 = 0.0982
Largest diff. peak and hole	1.771 and -1.223 e.Å^{-3}

ORTEP representation of compound 6 at 50 % probability level
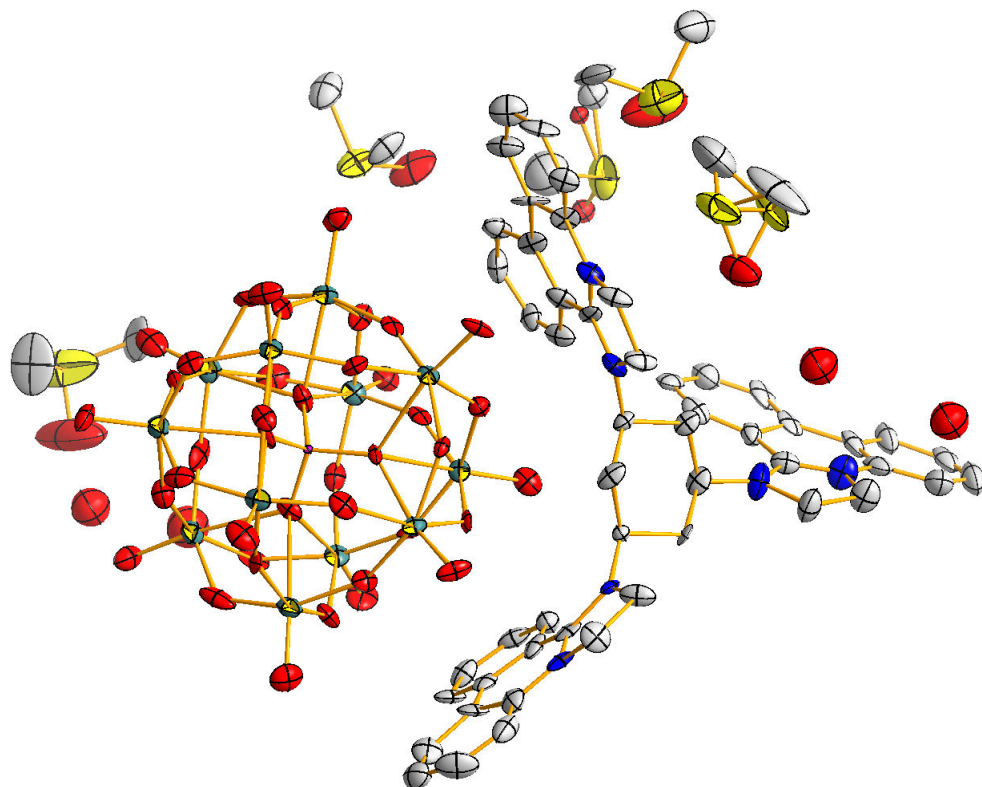
6.5 Crystal data and structure refinement for compound 7

Due to twinning, the atom displacement parameters could not be refined anisotropically.

Identification code	Compound **7**
Empirical formula	C53 H57 N6 O44 S4 P1 W12
Formula weight	3847.35
Temperature	150(2) K
Wavelength	0.71073 Å
Crystal system	Monoclinic
Space group	*C*2/c
Unit cell dimensions	a = 41.962(8) Å $\quad$ $\alpha= 90°$.
	b = 19.469(4) Å $\quad$ $\beta= 112.306(4)°$.
	c = 20.734(3) Å $\quad$ $\gamma = 90°$.
Volume	15672(5) Å^3
Z	6
Density (calculated)	2.381 g/cm^3
Absorption coefficient	13.255 mm^{-1}
F(000)	10386
Crystal size	0.05 x 0.05 x 0.15 mm^3
Theta range for data collection	1.05 to 24.07°.
Index ranges	-48<=h<=45, -20<=k<=22, -12<=l<=22
Reflections collected	28477
Independent reflections	11938 [R(int) = 0.0895]
Completeness to theta = 24.07°	96.2 %
Refinement method	Full-matrix least-squares on F^2
Data / restraints / parameters	11938 / 7 / 476
Goodness-of-fit on F^2	1.048
Final R indices [I>2sigma(I)]	R1 = 0.1473, wR2 = 0.3653
R indices (all data)	R1 = 0.2027, wR2 = 0.4080
Largest diff. peak and hole	14.324 and -10.158 e.Å^{-3}

ORTEP representation of compound 7 at 50 % probability level
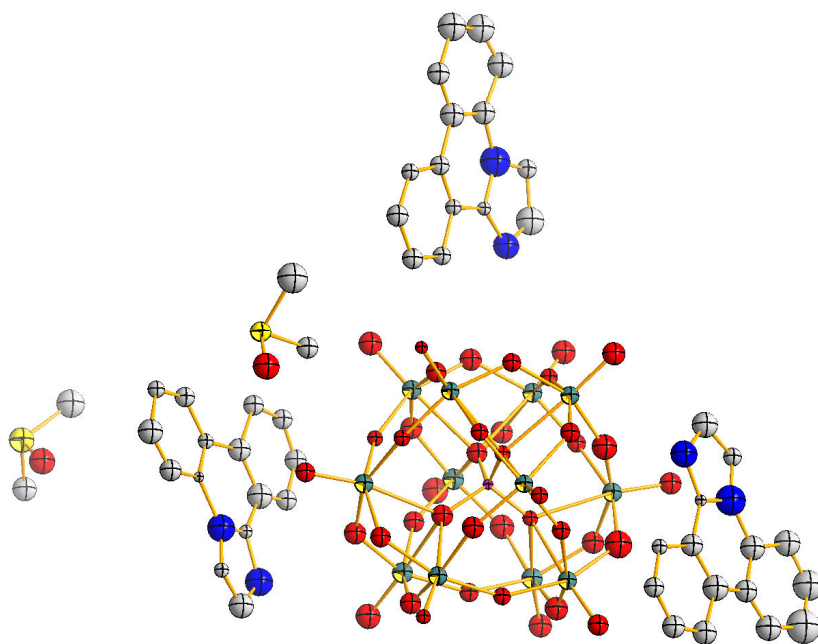
7 References

[1]   J.-M. Lehn, *Supramolecular Chemistry*, VCH Verlagsgesellschaft mbH, Weinheim, **1995**.

[2]   J. W. Steed, J. L. Atwood, *Supramolecular Chemistry*, John Wiley and Sons Ltd, Chichester, **2000**.

[3]   J. Berzelius, *Pogg. Ann.* **1826**, *6*, 369.

[4]   C. Marignac, *C. R. Acad. Sci.* **1862**, *55*, 888.

[5]   C. Marignac, *Ann. Chim.* **1862**, *25*, 362.

[6]   M. v. Laue, *Physikalische Zeitschrift* **1913**, *14*, 1075.

[7]   W. L. Bragg, *Nature* **1913**, *90*, 410.

[8]   A. Miolati, R. Pizzighelli, *J. Prak. Chem.* **1908**, *77*, 417.

[9]   L. Pauling, *J. Am. Chem. Soc.* **1929**, *51*, 2868.

[10]   J. F. Keggin, *Nature* **1933**, *132*, 351.

[11]   J. F. Keggin, *Proc. Roy. Soc. A* **1934**, *144*, 75.

[12]   D. E. Katsoulis, *Chem. Rev.* **1998**, *98*, 359.

[13]   J. T. Rhule, C. L. Hill, D. A. Judd, *Chem. Rev.* **1998**, *98*, 327.

[14]   P. Gouzerh, A. Proust, *Chem. Rev.* **1998**, *98*, 77.

[15]   T. Yamase, *Chem. Rev.* **1998**, *98*, 307.

[16]   A. Müller, F. Peters, M. T. Pope, D. Gatteschi, *Chem. Rev.* **1998**, *98*, 239.

[17]   L. Cronin, *Comprehensive Coordination Chemistry II, Vol. 7,* Elsevier, Amsterdam, **2004**.

[18]   M. T. Pope, *Heteropoly and Isopoly Oxometalates*, Springer-Verlag, Berlin, **1983**.

[19]   W. G. Klemperer, W. Shum, *J. Am. Chem. Soc.* **1976**, *98*, 8291.

[20]   D. -L. Long, E. Burkholder, L. Cronin, *Chem. Soc. Rev.* **2007**, *36*, 105.

[21]   D. Hou, G. S. Kim, K. S. Hagen, C. L. Hill, *Inorg. Chim. Acta* **1993**, *211*, 127.

[22]   J. Spandl, C. Daniel, I. Brudgam, H. Hartl, *Angew. Chem. Int. Ed.* **2003**, *42*, 1163.

[23]   M. I. Khan, Q. Chen, H. Hope, S. Parkin, C. J. O'Connor, J. Zubieta, *Inorg. Chem.* **1993**, *32*, 2929.

[24]   M. Piepenbrink, M. U. Triller, N. H. J. Gorman, B. Krebs, *Angew. Chem. Int. Ed.* **2002**, *41*, 2523.

[25]   G. Suss-Fink, L. Plasseraud, V. Ferrand, S. Stanislas, A. Neels, H. Stoeckli-Evans, M. Henry, G. Laurenczy, R. Roulet, *Polyhedron* **1998**, *17*, 2817.

[26]   V. W. Day, W. G. Klemperer, H. Chae, A. Yagasaki, *Abstr. Pap. Am. Chem. Soc.* **1989**, *197*, 116.

[27]   D. Hagrman, R. C. Haushalter, J. Zubieta, *Chem. Mater.* **1998**, *10*, 361.

[28]   Y. Q. Guo, X. L. Wang, Y. G. Li, E. B. Wang, L. Xu, C. W. Hu, *J. Coord. Chem.* **2004**, *57*, 445.

[29]   T. Yamase, M. T. Pope, *Polyoxometalate Chemistry for Nano-Composite Design*, Kluwer Academic, New York, **2002**.

[30]   Y. H. Du, A. L. Rheingold, E. A. Maatta, *J. Am. Chem. Soc.* **1992**, *114*, 345.

[31]   A. Proust, R. Thouvenot, M. Chaussade, F. Robert, P. Gouzerh, *Inorg. Chim. Acta* **1994**, *224*, 81.

[32]   J. B. Strong, R. Ostrander, A. L. Rheingold, E. A. Maatta, *J. Am. Chem. Soc.* **1994**, *116*, 3601.

[33]   T. R. Mohs, G. P. A. Yap, A. L. Rheingold, E. A. Maatta, *Inorg. Chem.* **1995**, *34*, 9.

[34]   Y. G. Wei, B. B. Xu, C. L. Barnes, Z. H. Peng, *J. Am. Chem. Soc.* **2001**, *123*, 4083.

[35] Y. G. Wei, M. Lu, C. F. C. Cheung, C. L. Barnes, Z. H. Peng, *Inorg. Chem.* **2001**, *40*, 5489.

[36] L. Xu, M. Lu, B. B. Xu, Y. G. Wei, Z. H. Peng, D. R. Powell, *Angew. Chem. Int. Ed.* **2002**, *41*, 4129.

[37] Q. Li, P. F. Wu, Y. Xia, Y. G. Wei, H. Y. Guo, *J. Organomet. Chem.* **2006**, *691*, 1223.

[38] H. T. Evans, *Inorg. Chem.* **1966**, *5*, 967.

[39] F. J. C. Rossotti, H. Rossotti, *Acta Chem. Scand.* **1956**, *10*, 957.

[40] F. Chauveau, *Bull. Soc. Chim. Fr.* **1960**, 810.

[41] J. Magee, E. Richardson, *J. Inorg. Nucl. Chem.* **1960**, *15*, 272.

[42] K. Schiller, E. Thilo, *Z. Anorg. Allg. Chem.* **1961**, *310*, 261.

[43] S. Nakamura, T. Ozeki, *J. Chem. Soc., Dalton Trans.* **2001**, 472.

[44] T. Yamase, T. Ikawa, *Bull. Chem. Soc. Jpn.* **1977**, *50*, 746.

[45] A. Don, T. J. R. Weakley, *Acta Crystallogr. Sect. B: Struct. Sci.* **1981**, *37*, 451.

[46] Y. Ohashi, K. Yanagi, Y. Sasada, T. Yamase, *Bull. Chem. Soc. Jpn.* **1982**, *55*, 1254.

[47] P. Román, J. M. Gutiérrez-Zorrilla, M. Martínez-Ripoll, S. García-Blanco, *Transition Met. Chem.* **1986**, *11*, 143.

[48] K. Sjöbom, B. Hedman, *Acta Chem. Scand.* **1973**, *A27*, 3673.

[49] K. G. Burtseva, T. S. Chernaya, M. I. Sirota, *Sov. Phys. Dokl.* **1978**, *23*, 784.

[50] J. Fuchs, E. P. Flindt, *Z. Naturforsch. B: Chem. Sci.* **1979**, *34*, 412.

[51] I. Paulat-Boeschen, *J. Chem. Soc., Chem. Commun.* **1979**, 780.

[52] B. Krebs, I. Paulat-Boeschen, *Acta. Cryst.* **1982**, *B38*, 1710.

[53] M. T. Pope, A. Müller, *Angew. Chem. Int. Ed. Engl.* **1991**, *30*, 34.

[54] K. Burgemeister, D. Drewes, E. M. Limanski, I. Kuper, B. Krebs, *Eur. J. Inorg. Chem.* **2004**, 2690.

[55] T. Yamase, Y. Yano, E. Ishikawa, *Langmuir* **2005**, *21*, 7823.

[56] D. -L. Long, C. Streb, P. Kögerler, L. Cronin, *J. Cluster Sci.* **2006**, *17*, 257.

[57] K. H. Tytko, B. Schonfel, B. Buss, O. Glemser, *Angew. Chem. Int. Ed. Engl.* **1973**, *12*, 330.

[58] D. Hagrman, P. J. Zapf, J. Zubieta, *Chem. Commun.* **1998**, 1283.

[59] R. S. Rarig, J. Zubieta, *Inorg. Chim. Acta* **2001**, *312*, 188.

[60] A. Bridgeman, *J. Phys. Chem. A* **2002**, *106*, 12151.

[61] C. D. Wu, C. Z. Lu, H. H. Zhuang, J. S. Huang, *Inorg. Chem.* **2002**, *41*, 5636.

[62] D. R. Xiao, Y. Hou, E. B. Wang, S. T. Wang, Y. G. Li, L. Xu, C. W. Hu, *Inorg. Chim. Acta* **2004**, *357*, 2525.

[63] D. G. Allis, E. Burkholder, J. Zubieta, *Polyhedron* **2004**, *23*, 1145.

[64] D. G. Allis, R. S. Rarig, E. Burkholder, J. Zubieta, *J. Mol. Struct.* **2004**, *688*, 11.

[65] Y. Q. Lan, S. L. Li, X. L. Wang, K. Z. Shao, D. Y. Du, H. Y. Zang, Z. M. Su, *Inorg. Chem.* **2008**, *47*, 8179.

[66] I. Lindqvist, *Arkiv. Kemi.* **1950**, *2*, 349.

[67] L. O. Atovmyan, Krasochk.On, *Zh. Strukt. Khim.* **1972**, *13*, 342.

[68] H. Vivier, J. Bernard, H. Djomaa, *Rev. Chim. Minérale* **1977**, *14*, 584.

[69] P. Román, J. M. Gutiérrez-Zorrilla, C. Esteban-Calderón, M. Martínez-Ripoll, S. García-Blanco, *Polyhedron* **1985**, *4*, 1043.

[70] S. L. Li, Y. Q. Lan, J. F. Ma, J. Yang, X. H. Wang, Z. M. Su, *Inorg. Chem.* **2007**, *46*, 8283.

[71] R. Z. Wang, J. Q. Xu, G. Y. Yang, W. M. Bu, Y. H. Xing, D. M. Li, S. Q. Liu, L. Ye, Y. G. Fan, *Polyhedron* **1999**, *18*, 2971.

[72]   W. B. Yang, C. Z. Lu, H. H. Zhuang, *J. Chem. Soc., Dalton Trans.* **2002**, 2879.

[73]   R. S. Rarig, J. Zubieta, *J. Solid State Chem.* **2002**, *167*, 370.

[74]   B. K. Koo, L. Bewley, V. Golub, R. S. Rarig, E. Burkholder, C. J. O'Connor, J. Zubieta, *Inorg. Chim. Acta* **2003**, *351*, 167.

[75]   J. H. Jia, J. H. Yu, Q. H. Pan, P. Chen, R. R. Xu, *Chem. J. Chin. Uni.* **2005**, *26*.

[76]   J. P. Wang, S. Z. Li, J. W. Zhao, J. Y. Niu, *Inorg. Chem. Commun.* **2006**, *9*, 599.

[77]   K. Pavani, S. E. Lofland, K. V. Ramanujachary, A. Ramanan, *Eur. J. Inorg. Chem.* **2007**, 568.

[78]   Z. H. Su, B. B. Zhou, Z. F. Zhao, X. Zhang, *Inorg. Chem. Commun.* **2008**, *11*, 334.

[79]   C. H. Tian, Z. G. Sun, J. Li, X. F. Zheng, H. D. Liang, L. C. Zhang, W. S. You, Z. M. Zhu, *Inorg. Chem. Commun.* **2007**, *10*, 757.

[80]   S. M. Chen, C. Z. Lu, Y. Q. Yu, Q. Z. Zhang, X. He, *Inorg. Chem. Commun.* **2004**, *7*, 1041.

[81]   H. Abbas, A. L. Pickering, D. -L. Long, P. Kögerler, L. Cronin, *Chem. Eur. J.* **2005**, *11*, 1071.

[82]   H. Abbas, C. Streb, A. L. Pickering, A. R. Neil, D. -L. Long, L. Cronin, *Cryst. Growth Des.* **2008**, *8*, 635.

[83]   H. Abbas, PhD Thesis, University of Glasgow (UK), **2006**.

[84]   J. Fuchs, H. Hartl, *Angew. Chem. Int. Ed. Engl.* **1976**, *15*, 375.

[85]   M. J. Schwing-Weill, F. Arnaud-Neu, *Bull. Soc. Chim. Fr.* **1970**.

[86]   S. Himeno, H. Niiya, T. Ueda, *Bull. Chem. Soc. Jpn.* **1997**, *70*, 631.

[87]   V. W. Day, M. F. Fredrich, W. G. Klemperer, W. Shum, *J. Am. Chem. Soc.* **1977**, *99*, 6146.

[88]   Y. P. Shi, G. L. Xue, H. M. Hu, F. Fu, J. W. Wang, *J. Coord. Chem.* **2006**, *59*, 1739.

[89]   Z. C. Xiao, Y. Zhu, Y. G. Wei, Y. Wang, *Inorg. Chem. Commun.* **2006**, *9*, 400.

[90]   Y. F. Qiu, L. Xu, G. G. Gao, W. J. Wang, F. Y. Li, *Inorg. Chim. Acta* **2006**, *359*, 451.

[91]   B. Hasenknopf, R. Delmont, P. Herson, P. Gouzerh, *Eur. J. Inorg. Chem.* **2002**, 1081.

[92]   P. R. Marcoux, B. Hasenknopf, J. Vaissermann, P. Gouzerh, *Eur. J. Inorg. Chem.* **2003**, 2406.

[93]   Y. -F. Song, D. -L. Long, L. Cronin, *Angew. Chem. Int. Ed.* **2007**, *46*, 3900.

[94]   Y. -F. Song, D. -L. Long, S. E. Kelly, L. Cronin, *Inorg. Chem.* **2008**, *47*, 9137.

[95]   J. Zhang, Y. -F. Song, L. Cronin, T. B. Liu, *J. Am. Chem. Soc.* **2008**, *130*, 14408.

[96]   Y. -F. Song, N. McMillan, D. -L. Long, S. Kane, J. Malm, M. O. Riehle, C. P. Pradeep, N. Gadegaard, L. Cronin, *J. Am. Chem. Soc.* **2009**, *131*, 1340.

[97]   M. T. Pope, *Comprehensive Coordination Chemistry, Vol. 3*, Pergamon Press, Oxford, **1987**.

[98]   K. Nomiya, T. Takahashi, T. Shirai, M. Miwa, *Polyhedron* **1987**, *6*, 213.

[99]   P. A. Lorenzo-Luis, P. Gili, A. Sánchez, E. Rodriguez-Castellón, J. Jiménez-Jiménez, C. Ruiz-Pérez, X. Solans, *Transition Met. Chem.* **1999**, *24*, 686.

[100] P. A. Lorenzo-Luis, P. Gili, *Recent Res. Dev. Inorg. Chem.* **2000**, *2*, 185.

[101] H. T. Evans, *Acta Cryst.* **1974**, *B30*, 2095.

[102] Q. Z. Zhang, Y. Q. Yu, S. M. Chen, X. He, Y. Yan, J. H. Liu, L. J. Chen, C. K. Xia, X. J. Xu, X. Y. Wu, C. Z. Lu, *Chin. J. Struct. Chem.* **2004**, *23*, 1269.

[103] A. Perloff, *Inorg. Chem.* **1970**, *9*, 2228.

[104] U. Lee, *Acta Crystallogr., Sect. C: Cryst. Struct. Commun.* **1994**, *50*, 1657.

[105] A. Rosenheim, *Z. Anorg. Allg. Chem.* **1916**, *96*, 139.

[106] A. LaGinestra, F. Gianetta, P. Fiorucci, *Gazz. Chim. Ital.* **1968**, *98*.

[107] J. Fuchs, I. Brudgam, *Z. Naturforsch., B: Chem. Sci.* **1977**, *32*, 403.

[108] Z. H. Xu, P. X. Xi, F. J. Chen, Z. Z. Zeng, *Transition Met. Chem.* **2008**, *33*, 237.

[109] Y. -F. Song, H. Abbas, C. Ritchie, N. McMillian, D. -L. Long, N. Gadegaard, L. Cronin, *J. Mater. Chem.* **2007**, *17*, 1903.

[110] F. Y. Su, B. B. Zhou, Z. F. Zhao, Z. H. Su, C. C. Zhu, *Cryst. Res. Tech.* **2009**, *44*, 447.

[111] H. Y. An, Y. G. Li, E. B. Wang, D. R. Xiao, C. Y. Sun, L. Xu, *Inorg. Chem.* **2005**, *44*, 6062.

[112] H. Y. An, Y. G. Li, D. R. Xiao, E. B. Wang, C. Y. Sun, *Cryst. Growth Des.* **2006**, *6*, 1107.

[113] Y. Liu, X. Zhang, P. Ma, *Huaxue Yanjiu* **2008**, *19*, 18.

[114] S. Favette, B. Hasenknopf, J. Vaissermann, P. Gouzerh, C. Roux, *Chem. Commun.* **2003**, 2664.

[115] G. M. Brown, M. R. Noespirlet, W. R. Busing, H. A. Levy, *Acta Crystallogr., Sect. B: Struct. Sci.* **1977**, *33*, 1038.

[116] L. C. W. Baker, J. S. Figgis, *J. Am. Chem. Soc.* **1970**, *92*, 3794.

[117] A. Tezé, G. Hervé, *J. Inorg. Nucl. Chem.* **1977**, *39*, 999.

[118] D. L. Kepert, *The Early Transition Elements*, Academic Press, New York, **1972**.

[119] M. T. Pope, *Inorg. Chem.* **1976**, *15*, 2008.

[120] M. Sadakane, D. Tsukuma, M. H. Dickman, B. Bassil, U. Kortz, M. Higashijima, W. Ueda, *Dalton Trans.* **2006**, 4271.

[121] A. Tezé, G. Hervé, *Inorganic Syntheses, Vol. 27*, John Wiley and Sons, New York, **1990**.

[122] G. Hervé, A. Tezé, *Inorg. Chem.* **1977**, *16*, 2115.

[123] S. T. Zheng, D. Q. Yuan, H. P. Jia, J. Zhang, G. Y. Yang, *Chem. Commun.* **2007**, 1858.

[124] L. Lisnard, P. Mialane, A. Dolbecq, J. Marrot, J. M. Clemente-Juan, E. Coronado, B. Keita, P. de Oliveira, L. Nadjo, F. Sécheresse, *Chem. Eur. J.* **2007**, *13*, 3525.

[125] K. Hayashi, H. Murakami, K. Nomiya, *Inorg. Chem.* **2006**, *45*, 8078.

[126] L. H. Bi, U. Kortz, B. Keita, L. Nadjo, *Dalton Trans.* **2004**, 3184.

[127] E. Coronado, C. Giménez-Saiz, C. J. Gómez-García, *Coord. Chem. Rev.* **2005**, *249*, 1776.

[128] J. M. Clemente-Juan, E. Coronado, *Coord. Chem. Rev.* **1999**, *195*, 361.

[129] J. M. Clemente-Juan, E. Coronado, J. R. Galán-Mascarós, C. J. Gómez-García, *Inorg. Chem.* **1999**, *38*, 55.

[130] M. Carraro, L. Sandei, A. Sartorel, G. Scorrano, M. Bonchio, *Org. Lett.* **2006**, *8*, 3671.

[131] R. H. Ingle, N. K. K. Raj, *J. Mol. Catal. A: Chem.* **2008**, *294*, 8.

[132] B. Dawson, *Acta Cryst.* **1953**, *6*, 113.

[133] M. T. Pope, *Encyclopedia of Inorganic Chemistry*, John Wiley and Sons, Chichester, **2005**.

[134] R. I. Maksimovskaya, G. M. Maksimov, G. S. Litvak, *Russ. Chem. Bull.* **2003**, *52*, 103.

[135] J. Zhang, A. M. Bond, P. J. S. Richardt, A. G. Wedd, *Inorg. Chem.* **2004**, *43*, 8263.

[136] C. Dablemont, C. G. Hamaker, R. Thouvenot, Z. Sojka, M. Che, E. A. Maatta, A. Proust, *Chem. Eur. J.* **2006**, *12*, 9150.

[137] L. L. Fan, E. Wang, Y. G. Li, H. Y. An, D. R. Xiao, X. L. Wang, *J. Mol. Struct.* **2007**, *841*, 28.

[138] B. B. Xu, L. Xu, G. G. Gao, Y. N. Jin, *Appl. Surf. Sci.* **2007**, *253*.

[139] L. Liu, L. X. Qiao, S. Z. Liu, D. M. Cui, C. M. Zhang, Z. J. Zhou, Z. L. Du, W. Y. Wong, *J. Polym. Sci., Part A: Polym. Chem.* **2008**, *46*, 3193.

[140] A. V. Ivanov, T. V. Vasina, V. D. Nissenbaum, L. M. Kustov, M. N. Timofeeva, J. I. Houzvicka, *Appl. Catal., A* **2004**, *259*, 65.

[141] M. N. Timofeeva, M. M. Matrosova, T. Reshetenko, L. B. Avdeeva, A. A. Budneva, A. B. Ayupov, E. A. Paukshtis, A. L. Chuvilin, A. V. Volodin, V. A. Likholobov, *J. Mol. Catal. A: Chem.* **2004**, *211*, 131.

[142] L. Ruhlmann, C. Costa-Coquelard, S. Sorgues, I. Lampre, *Macromol. Symp.* **2008**, *270*, 117.

[143] B. Hasenknopf, *Front. Biosci.* **2005**, *10*, 275.

[144] M. Inoue, T. Suzuki, Y. Fujita, M. Oda, N. Matsumoto, T. Yamase, *J. Inorg. Biochem.* **2006**, *100*, 1225.

[145] D. -L. Long, P. Kögerler, L. Cronin, *Angew. Chem. Int. Ed.* **2004**, *43*, 1817.

[146] D. -L. Long, H. Abbas, P. Kögerler, L. Cronin, *Angew. Chem. Int. Ed.* **2005**, *44*, 3415.

[147] D. -L. Long, P. Kögerler, A. D. C. Parenty, J. Fielden, L. Cronin, *Angew. Chem. Int. Ed.* **2006**, *45*, 4798.

[148] D. -L. Long, Y. -F. Song, E. F. Wilson, P. Kögerler, S. X. Guo, A. M. Bond, J. S. J. Hargreaves, L. Cronin, *Angew. Chem. Int. Ed.* **2008**, *47*, 4384.

[149] J. Yan, D. -L. Long, E. F. Wilson, L. Cronin, *Angew. Chem. Int. Ed.* **2009**, *48*, 4376.

[150] R. Contant, R. Thouvenot, *Can. J. Chem.* **1991**, *69*, 1498.

[151] Y. Q. Hou, C. L. Hill, *J. Am. Chem. Soc.* **1993**, *115*, 11823.

[152] M. Pohl, Y. Lin, T. J. R. Weakley, K. Nomiya, M. Kaneko, H. Weiner, R. G. Finke, *Inorg. Chem.* **1995**, *34*, 767.

[153] I. M. Mbomekalle, Y. W. Lu, B. Keita, L. Nadjo, W. A. Neiwert, K. I. Hardcastle, C. L. Hill, T. M. Anderson, *Eur. J. Inorg. Chem.* **2005**, 1547.

[154] Y. Sakai, A. Shinohara, K. Hayashi, K. Nomiya, *Eur. J. Inorg. Chem.* **2006**, 163.

[155] B. Godin, Y. G. Chen, J. Vaissermann, L. Ruhlmann, M. Verdaguer, P. Gouzerh, *Angew. Chem. Int. Ed.* **2005**, *44*, 3072.

[156] Y. Sakai, K. Yoza, C. N. Kato, K. Nomiya, *Chem. Eur. J.* **2003**, *9*, 4077.

[157] C. N. Kato, Y. Kasahara, K. Hayashi, A. Yamaguchi, T. Hasegawa, K. Nomiya, *Eur. J. Inorg. Chem.* **2006**, 4834.

[158] C. P. Pradeep, D. -L. Long, G. N. Newton, Y. -F. Song, L. Cronin, *Angew. Chem. Int. Ed.* **2008**, *47*, 4388.

[159] J. Li, I. Huth, L. M. Chamoreau, B. Hasenknopf, E. Lacôte, S. Thorimbert, M. Malacria, *Angew. Chem. Int. Ed.* **2009**, *48*, 2035.

[160] C. W. Scheele, *Sämtliche Physische und Chemische Werke, Vol. II* **1793**, reprint: Martin Sändig oHG, Wiesbaden, **1971**.

[161] F. A. Cotton, G. Wilkinson, C. A. Murillo, M. Bochmann, *Advanced Inorganic Chemistry*, John Wiley & Sons Ltd., **1999**.

[162] A. Müller, J. Meyer, E. Krickemeyer, E. Diemann, *Angew. Chem. Int. Ed. Engl.* **1996**, *35*, 1206.

[163] A. Müller, E. Krickemeyer, S. Dillinger, H. Bögge, W. Plass, A. Proust, L. Dloczik, C. Menke, J. Meyer, R. Rohlfing, *Z. Anorg. Allg. Chem.* **1994**, *620*, 599.

[164] A. Müller, W. Plass, E. Krickemeyer, S. Dillinger, H. Bögge, A. Armatage, A. Proust, C. Beugholt, U. Bergmann, *Angew. Chem. Int. Ed. Engl.* **1994**, *33*, 849.

[165]   P. Gouzerh, Y. Jeannin, A. Proust, F. Robert, *Angew. Chem. Int. Ed. Engl.* **1989**, *28*, 1363.

[166]   A. Müller, E. Krickemeyer, H. Bögge, M. Schmidtmann, C. Beugholt, P. Kögerler, C. Z. Lu, *Angew. Chem. Int. Ed.* **1998**, *37*, 1220.

[167]   A. Müller, M. Koop, H. Bögge, M. Schmidtmann, C. Beugholt, *Chem. Commun.* **1998**, 1501.

[168]   A. Müller, P. Kögerler, A. W. M. Dress, *Coord. Chem. Rev.* **2001**, *222*, 193.

[169]   A. Tsuda, E. Hirahara, Y.-S. Kim, H. Tanaka, T. Kawai, T. Aida, *Angew. Chem. Int. Ed.* **2004**, *43*, 6327.

[170]   J. Kepler, *Mysterium Cosmographicum*, **1596**.

[171]   A. Müller, E. Krickemeyer, H. Bögge, M. Schmidtmann, F. Peters, *Angew. Chem. Int. Ed.* **1998**, *37*, 3360.

[172]   A. Müller, S. Q. N. Shah, H. Bögge, M. Schmidtmann, P. Kögerler, B. Hauptfleisch, S. Leiding, K. Wittler, *Angew. Chem. Int. Ed.* **2000**, *39*, 1614.

[173]   A. Müller, S. Sarkar, S. Q. N. Shah, H. Bögge, M. Schmidtmann, S. Sarkar, P. Kögerler, B. Hauptfleisch, A. X. Trautwein, V. Schunemann, *Angew. Chem. Int. Ed.* **1999**, *38*, 3238.

[174]   A. Müller, E. Krickemeyer, S. K. Das, P. Kögerler, S. Sarkar, H. Bögge, M. Schmidtmann, S. Sarkar, *Angew. Chem. Int. Ed.* **2000**, *39*, 1612.

[175]   A. Müller, S. K. Das, S. Talismanov, S. Roy, E. Beckmann, H. Bögge, M. Schmidtmann, A. Merca, A. Berkle, L. Allouche, Y. S. Zhou, L. J. Zhang, *Angew. Chem. Int. Ed.* **2003**, *42*, 5039.

[176]   A. Müller, E. Krickemeyer, H. Bögge, M. Schmidtmann, B. Botar, M. O. Talismanova, *Angew. Chem. Int. Ed.* **2003**, *42*, 2085.

[177]   A. Müller, Y. S. Zhou, L. J. Zhang, H. Bögge, M. Schmidtmann, M. Dressel, J. van Slageren, *Chem. Commun.* **2004**, 2038.

[178]   A. Müller, D. Rehder, E. T. K. Haupt, A. Merca, H. Bögge, M. Schmidtmann, G. Heinze-Bruckner, *Angew. Chem. Int. Ed.* **2004**, *43*, 5115.

[179]   D. Volkmer, A. Du Chesne, D. G. Kurth, H. Schnablegger, P. Lehmann, M. J. Koop, A. Müller, *J. Am. Chem. Soc.* **2000**, *122*, 1995.

[180]   M. Bonchio, O. Bortolini, V. Conte, A. Sartorel, *Eur. J. Inorg. Chem.* **2003**, 699.

[181]   M. J. Deery, O. W. Howarth, K. R. Jennings, *J. Chem. Soc., Dalton Trans.* **1997**, 4783.

[182]   D. K. Walanda, R. C. Burns, G. A. Lawrance, E. I. von Nagy-Felsobuki, *J. Chem. Soc., Dalton Trans.* **1999**, 311.

[183]   D. K. Walanda, R. C. Burns, G. A. Lawrance, E. I. von Nagy-Felsobuki, *J. Cluster Sci.* **2000**, *11*, 5.

[184]   F. Sahureka, R. C. Burns, E. I. von Nagy-Felsobuki, *Inorg. Chim. Acta* **2002**, *332*, 7.

[185]   E. C. Alyea, D. Craig, I. Dance, K. Fisher, G. Willett, M. Scudder, *Cryst. Eng. Comm.* **2005**, *7*, 491.

[186]   J. Shiea, W. S. Wang, C. H. Wang, P. S. Chen, C. H. Chou, *Anal. Chem.* **1996**, *68*, 1062.

[187]   C. H. Wang, M. W. Huang, C. Y. Lee, H. L. Chei, J. P. Huang, J. Shiea, *J. Am. Soc. Mass Spectrom.* **1998**, *9*, 1168.

[188]   S. Sakamoto, M. Fujita, K. Kim, K. Yamaguchi, *Tetrahedron* **2000**, *56*, 955.

[189]   W. Henderson, J. S. McIndoe, *Mass Spectrometry of Inorganic and Organometallic Compounds*, John Wiley & Sons Ltd., Chichester, **2005**.

[190] C. Dablemont, A. Proust, R. Thouvenot, C. Afonso, F. Fournier, J. C. Tabet, *Inorg. Chem.* **2004**, *43*, 3514.

[191] C. Boglio, G. Lenoble, C. Duhayon, B. Hasenknopf, R. Thouvenot, C. Zhang, R. C. Howell, B. P. Burton-Pye, L. C. Francesconi, E. Lacôte, S. Thorimbert, M. Malacria, C. Afonso, J. C. Tabet, *Inorg. Chem.* **2006**, *45*, 1389.

[192] M. T. Ma, T. Waters, K. Beyer, R. Palamarczuk, P. J. S. Richardt, R. A. J. O'Hair, A. G. Wedd, *Inorg. Chem.* **2009**, *48*, 598.

[193] D. K. Walanda, R. C. Burns, G. A. Lawrance, E. I. von Nagy-Felsobuki, *Inorg. Chim. Acta* **2000**, *305*, 118.

[194] D. K. Walanda, R. C. Burns, G. A. Lawrance, E. I. von Nagy-Felsobuki, *Inorg. Chem. Commun.* **1999**, *2*, 487.

[195] F. Sahureka, R. C. Burns, E. I. von Nagy-Felsobuki, *Inorg. Chim. Acta* **2003**, *351*, 69.

[196] C. R. Mayer, C. Roch-Marchal, H. Lavanant, R. Thouvenot, N. Sellier, J. C. Blais, F. Sécheresse, *Chem. Eur. J.* **2004**, *10*, 5517.

[197] F. Sahureka, R. C. Burns, E. I. von Nagy-Felsobuki, *Inorg. Chem. Commun.* **2002**, *5*, 23.

[198] R. Colton, J. C. Traeger, *Inorg. Chim. Acta* **1992**, *201*, 153.

[199] J. L. Tuoi, E. Muller, *Rapid Commun. Mass Spectrom.* **1994**, *8*.

[200] T. C. Lau, J. Y. Wang, R. Guevremont, *J. Chem. Soc., Chem. Commun.* **1995**, 877.

[201] T. Waters, R. A. J. O'Hair, A. G. Wedd, *J. Am. Chem. Soc.* **2003**, *125*, 3384.

[202] T. Waters, R. A. J. O'Hair, A. G. Wedd, *Int. J. Mass Spectrom.* **2003**, *228*, 599.

[203] J. Gun, A. Modestov, O. Lev, D. Saurenz, M. A. Vorotyntsev, R. Poli, *Eur. J. Inorg. Chem.* **2003**, 482.

[204] S. Sakamoto, M. Yoshizawa, T. Kusukawa, M. Fujita, K. Yamaguchi, *Org. Lett.* **2001**, *3*, 1601.

[205] K. Saito, Y. Sei, S. Miki, K. Yamaguchi, *Toxicon* **2008**, *51*, 1496.

[206] M. Kunimura, S. Sakamoto, K. Yamaguchi, *Org. Lett.* **2002**, *4*, 347.

[207] S. J. Park, D. M. Shin, S. Sakamoto, K. Yamaguchi, Y. K. Chung, M. S. Lah, J. I. Hong, *Chem. Eur. J.* **2004**, *11*, 235.

[208] H. N. Miras, D. -L. Long, P. Kögerler, L. Cronin, *Dalton Trans.* **2008**, 214.

[209] A. D. C. Parenty, L. V. Smith, A. L. Pickering, D. -L. Long, L. Cronin, *J. Org. Chem.* **2004**, *69*, 5934.

[210] A. D. C. Parenty, K. M. Guthrie, Y. -F. Song, L. V. Smith, E. Burkholder, L. Cronin, *Chem. Commun.* **2006**, 1194.

[211] A. D. C. Parenty, Y. -F. Song, C. J. Richmond, L. Cronin, *Org. Lett.* **2007**, *9*, 2253.

[212] A. Müller, E. Beckmann, H. Bögge, M. Schmidtmann, A. Dress, *Angew. Chem. Int. Ed.* **2002**, *41*, 1162.

[213] G. J. T. Cooper, G. N. Newton, P. Kögerler, D. -L. Long, L. Engelhardt, M. Luban, L. Cronin, *Angew. Chem. Int. Ed.* **2007**, *46*, 1340.

[214] D. -L. Long, C. Streb, Y. -F. Song, S. Mitchell, L. Cronin, *J. Am. Chem. Soc.* **2008**.

[215] D. -L. Long, P. Kögerler, L. J. Farrugia, L. Cronin, *Angew. Chem. Int. Ed.* **2003**, *42*, 4180.

[216] D. -L. Long, H. Abbas, P. Kögerler, L. Cronin, *J. Am. Chem. Soc.* **2004**, *126*, 13880.

[217] A. L. Nolan, R. C. Burns, G. A. Lawrance, *J. Chem. Soc., Dalton Trans* **1996**, 2629.

[218] S. J. Angus-Dunne, J. A. Irwin, R. C. Burns, G. A. Lawrance, D. C. Craig, *J. Chem. Soc., Dalton Trans.* **1993**, 2717.

[219] M. Jansen, *Angew. Chem. Int. Ed.* **1987**, *26*, 1098.

[220] B. M. Gatehouse, P. Leverett, *J. Chem. Soc., Dalton Trans.* **1976**, 1316.

[221] Only the peaks that could be unambiguously fitted using simulated spectra were assigned. We are presently developing a fitting approach to more fully assign all the species.

[222] H. K. Chae, W. G. Klemperer, T. A. Marquart, *Coord. Chem. Rev.* **1993**, *128*, 209.

[223] A. Müller, J. Meyer, E. Krickemeyer, C. Beugholt, H. Bögge, F. Peters, M. Schmidtmann, P. Kögerler, M. J. Koop, *Chem. Eur. J.* **1998**, *4*, 1000.

[224] M. I. Khan, J. Zubieta, *J. Am. Chem. Soc.* **1992**, *114*, 10058.

[225] Comparison of the 'pseudo' first order rate constants reveals the general trend that the rate of decrease in the concentration of Lindqvist anions decreases as the carbon chain length of the alkylammonium cations increases. However, it should be noted that the absolute figures of these rate constants will vary according to changes in experimental parameters such as temperature variation, filtration time prior to kinetic monitoring, and the human error introduced by the time needed in the solution preparation process.

[226] M. I. Khan, Q. Chen, J. Zubieta, D. P. Goshorn, *Inorg. Chem.* **1992**, *31*, 1556.

[227] Q. Chen, D. P. Goshorn, C. P. Scholes, X. L. Tan, J. Zubieta, *J. Am. Chem. Soc.* **1992**, *114*, 4667.

[228] A. Müller, J. Meyer, H. Bögge, A. Stammler, A. Botar, *Z. Anorg. Allg. Chem.* **1995**, *621*, 1818.

[229] H. D. Zeng, G. R. Newkome, C. L. Hill, *Angew. Chem. Int. Ed.* **2000**, *39*, 1772.

[230] A. J. Wilson, W. T. Robinson, C. J. Wilkins, *Acta Crystallogr., Sect. C: Cryst. Struct. Commun.* **1982**, *39*, 54.

[231] L. Ma, S. C. Liu, J. Zubieta, *Inorg. Chem.* **1989**, *28*, 175.

[232] S. C. Liu, L. D. Ma, D. McGowty, J. Zubieta, *Polyhedron* **1990**, *9*, 1541.

[233] A. Müller, J. Meyer, H. Bögge, A. Stammler, A. Botar, *Chem. Eur. J.* **1998**, *4*, 1388.

[234] E. F. Wilson, H. Abbas, B. J. Duncombe, C. Streb, D. -L. Long, L. Cronin, *J. Am. Chem. Soc.* **2008**, *130*, 13876.

[235] M. Filowitz, R. K. C. Ho, W. G. Klemperer, W. Shum, *Inorg. Chem.* **1979**, *18*, 93.

[236] C. Rosu, M. H. Dickman, *Acta Crystallogr., Sect C: Cryst. Struct. Commun.* **1999**, *55*, 11.

[237] C. Rosu, C. J. Gómez-García, M. H. Dickman, M. Rusu, *Synth. React. Inorg. Met. –Org. Chem.* **1999**, *29*, 1123.

[238] C. Rosu, T. J. R. Weakley, *Acta Crystallogr. Sect. C: Cryst. Struct. Commun.* **2000**, *56*, E170.

[239] D. Honda, T. Ozeki, A. Yagasaki, *Inorg. Chem. Commun.* **2005**, *44*, 9616.

[240] H. T. Evans, *J. Am. Chem. Soc.* **1948**, *70*, 1291.

[241] P. A. L. Luis, P. Martín-Zarza, A. Sánchez, C. Ruiz-Pérez, M. Hernández-Molina, X. Solans, P. Gili, *Inorg. Chim. Acta* **1998**, *277*, 139.

[242] P. Gili, P. A. Lorenzo-Luis, P. Martín-Zarza, S. Domínguez, A. Sánchez, J. M. Arrieta, E. Rodriguez-Castellón, J. Jiménez-Jiménez, C. Ruiz-Pérez, M. Hernández-Molina, X. Solans, *Transition Met. Chem.* **1999**, *24*, 141.

[243] K. J. Schmidt, G. J. Schrobilgen, J. F. Sawyer, *Acta Crystallogr., Sect. C: Cryst. Struc. Commun.* **1986**, *42*, 1115.

[244] H. Ichida, A. Yagasaki, *J. Chem. Soc., Chem. Commun.* **1991**, 27.

[245] S. Konaka, Y. Ozawa, A. Yagasaki, *Inorg. Chem. Commun.* **2008**, *11*, 1267.

[246] A. M. Khenkin, R. Neumann, *Adv. Synth. Catal.* **2002**, *344*, 1017.

[247] H. Tsuji, K. Oshima, Y. Koyasu, *Chem. Mater.* **2003**, *15*, 2112.

[248] P. Beato, A. Blume, F. Girgsdies, R. E. Jentoft, R. Schlogel, O. Timpe, A. Trunschke, G. Weinberg, Q. Basher, F. A. Hamid, S. B. A. Hamid, E. Omar, L. M. Salim, *Appl. Catal., A* **2006**, *307*, 137.

[249] H. T. Evans, B. M. Gatehouse, *J. Chem. Soc., Dalton Trans.* **1975**, 505.

[250] H. T. Evans, *J. Am. Chem. Soc.* **1968**, *90*, 3275.

[251] L. Ouahab, *Molecular Engineering 3* **1993**, 183.

[252] L. Ouahab, *C. R. Acad. Sci. Ser. IIc: Chim.* **1998**, *1*, 369.

[253] E. Coronado, C. J. Gómez-García, *Chem Rev* **1998**, *98*, 273.

[254] M. Clemente-León, E. Coronado, C. J. Gómez-García, E. Martínez-Ferrero, *J. Cluster Sci.* **2002**, *13*, 381.

[255] C. M. Prosser-McCartha, M. Kadkhodayan, M. M. Williamson, D. A. Bouchard, C. L. Hill, *J. Chem. Soc., Chem. Commun.* **1986**, 1747.

[256] M. M. Williamson, D. A. Bouchard, C. L. Hill, *Inorg. Chem.* **1987**, *26*, 1436.

[257] C. L. Hill, D. A. Bouchard, M. Kadkhodayan, M. M. Williamson, J. A. Schmidt, E. F. Hilinski, *J. Am. Chem. Soc.* **1988**, *110*, 5471.

[258] J. Y. Niu, X. Z. You, C. Y. Duan, H. K. Fun, Z. Y. Zhou, *Inorg. Chem.* **1996**, *35*, 4211.

[259] D. Attanasio, M. Bonamico, V. Fares, P. Imperatori, L. Suber, *J. Chem. Soc., Dalton Trans* **1990**, 3221.

[260] X. M. Zhang, B. Z. Shan, C. Y. Duan, X. Z. You, *Chem. Commun.* **1997**, 1131.

[261] Y. S. Zhou, E. B. Wang, J. Peng, J. Liu, C. W. Hu, R. D. Huang, X. Z. You, *Polyhedron* **1999**, *18*, 1419.

[262] P. Le Maguerès, S. M. Hubig, S. V. Lindeman, P. Veya, J. K. Kochi, *J. Am. Chem. Soc.* **2000**, *122*, 10073.

[263] L. J. Zhang, Y. S. Zhou, Z. Yu, G. S. Fang, X. Z. You, *J. Mol. Struct.* **2001**, *570*, 83.

[264] J. A. F. Gamelas, A. M. V. Cavaleiro, E. D. Gomes, M. Belsley, E. Herdtweck, *Polyhedron* **2002**, *21*, 2537.

[265] D. Attanasio, F. Bachechi, *Adv. Mater.* **1994**, *6*, 145.

[266] D. Hagrman, P. J. Hagrman, J. Zubieta, *Angew. Chem. Int. Ed.* **1999**, *38*, 3165.

[267] R. Harada, Y. Matsuda, H. Okawa, T. Kojima, *Angew. Chem. Int. Ed.* **2004**, *43*, 1825.

[268] T. Kojima, T. Nakanishi, R. Harada, K. Ohkubo, S. Yamauchi, S. Fukuzumi, *Chem.Eur. J.* **2007**, *13*, 8714.

[269] C. Allain, S. Favette, L. M. Chamoreau, J. Vaissermann, L. Ruhlmann, B. Hasenknopf, *Eur. J. Inorg. Chem.* **2008**, 3433.

[270] A. Yokoyama, T. Kojima, K. Ohkubo, S. Fukuzumi, *Chem. Commun.* **2007**, 3997.

[271] A. D. C. Parenty, L. V. Smith, K. M. Guthrie, D. -L. Long, J. Plumb, R. Brown, L. Cronin, *J. Med. Chem.* **2005**, *48*, 4504.

[272] A. D. C. Parenty, L. V. Smith, L. Cronin, *Tetrahedron* **2005**, *61*, 8410.

[273] S. Srinivasachari, K. M. Fichter, T. M. Reineke, *J. Am. Chem. Soc.* **2008**, *130*, 4618.

[274] P. J. Kitson, PhD Thesis, University of Glasgow (UK), **2009**.

[275] F. Lions, K. V. Martin, *J. Am. Chem. Soc.* **1957**, *79*, 1572.

[276] A. Baeyer, *Ber. Deutsch. Chem. Ges.* **1886**, *19*.

[277] F. L. Urbach, J. E. Sarneski, L. J. Turner, D. H. Busch, *Inorg. Chem.* **1968**, *7*, 2169.

[278] A. D. C. Parenty, L. Cronin, *Synthesis-Stuttgart* **2008**, 155.

[279] K. Nishikida, E. Nishio, R. W. Hannah, *Selected Applications of Modern FT-IR Techniques*, CRC Press, **1996**.

[280] C. A. Hunter, J. K. M. Sanders, *J. Am. Chem. Soc.* **1990**, *112*, 5525.

[281] C. Janiak, *J. Chem. Soc., Dalton Trans.* **2000**, 3885.

[282] C. A. Hunter, K. R. Lawson, J. Perkins, C. J. Urch, *J. Chem. Soc., Perkin Trans. 2* **2001**, 651.

[283] M. T. Pope, G. M. Varga, *Inorg. Chem.* **1966**, *5*, 1249.

[284] B. Keita, L. Nadjo, *J. Electroanal. Chem.* **1987**, *230*, 267.

[285] B. Keita, L. Nadjo, *J. Electroanal. Chem.* **1987**, *227*, 77.

[286] B. O. Loopstra, H. M. Rietveld, *Acta Cryst.* **1969**, *B25*, 1420.